Thermal Conditions and Kinematics of Steep Bedrock Permafrost

Dissertation
zur
Erlangung der naturwissenschaftlichen Doktorwürde
(Dr. sc. nat.)

vorgelegt der

Mathematisch-naturwissenschaftlichen Fakultät

der

Universität Zürich

von

Andreas Hasler

von

Hasle BE

Promotionskomitee
Prof. Dr. Wilfried Haeberli (Vorsitz)
Dr. Stephan Gruber (Leitung der Dissertation)
Dr. Hansueli Gubler

Zürich, 2011

Abstract

Steep mountain flanks with heterogeneous micro-topography and surface characteristics are typical for high alpine mountain ranges. Permafrost, defined as the subsurface volume remaining at or below 0 °C throughout the year, modifies the hydrological and mechanical conditions of these flanks. Rock fall from permafrost bedrock and stability problems of high-alpine infrastructure raise the demand for understanding how these rock faces evolve in response to climate change and where most critical situations may emerge. Diverse studies address this topic and advances in the knowledge of the general permafrost distribution in steep rock faces and in the documentation and investigation of high-alpine rock instabilities have been made in the past decade. However, the processes linking climate change and rock fall are still poorly understood and empirical data is limited. This thesis addresses the corresponding knowledge gap. It is an exploratory study of the thermal, hydrological and mechanical processes in steep bedrock permafrost and its active layer.

A large part of the thesis focuses on distributed and extensive in-situ measurements of temperatures, rock movements and hydrological parameters. For this a data acquisition infrastructure based on wireless technology was developed within the consortium PermaSense, which was operated at two field sites (Matterhorn and Jungfraujoch, Swiss Alps) over the past 2–3 years and acquired datasets of novel quality and with new contents. The hydrothermal processes in fractured rock are, however, difficult to observe with field measurements alone. Therefore, laboratory experiments and numerical simulations of a single ice-filled cleft where set up and applied as complementary methods.

The main findings of these investigations are: i) a significant cooling effect with respect to snow-free surfaces in radiation-exposed rock faces caused by thin snow cover and air ventilation in clefts; ii) melt water warmed-up before percolation causes high erosion rates of the cleft ice but little warming of the surrounding rock; iii) two temporal patterns of rock movements have been described of which one is novel and restricted to the period with percolation of melt water into the cleft system. These findings are synthesized in a conceptual process model of climate-related rock fall in permafrost bedrock. This hypothetical model suggests that both, rock thermal conditions and melt-water production should be considered as drivers of warming-related rock fall.

The formulated hypotheses may be challenged or refined with the continuation of the present measurements and additional datasets of combined thermal and geotechnical investigations. Further, the deployment of the developed measurement infrastructure in an active instability may be a training case for a rock-fall monitoring and provide tools for future early-warning systems. More detailed analysis of the hydrothermal – mechanical interaction in rock clefts at subzero temperatures need to be considered to apply existing rock-mechanical models for permafrost bedrock. However, the application of such coupled numerical models to the field is limited to some case studies and requires a transfer to simple rules that may be applied based on the available information over large areas.

Zusammenfassung

Steile Bergflanken mit heterogener Mikrotopographie und Oberflächencharakteristik sind kennzeichnend fürs Hochgebirge. Permafrost, definiert als Untergrund der mehrjährig keine positiven Temperaturen aufweist, verändert die hydrologischen und mechanischen Eigenschaften dieser Bergflanken. Felsstürze aus Permafrostgebiet und Stabilitätsprobleme hochalpiner Infrastruktur begründen die Frage, welche Veränderungen solche Felswände angesichts des Klimawandels erfahren und wo dies zu kritischen Situationen führt. Studien zur Permafrost-Verbreitung sowie Dokumentationen und erste Untersuchungen hochalpiner Felsinstabilitäten haben im letzten Jahrzehnt wichtige Grundlagen geliefert. Die physikalischen Prozesse durch welche das Klima die Felsstabilität beeinflusst sind jedoch nur wenig verstanden und empirische Daten hierzu sind beschränkt. Die vorliegende Dissertation versucht diese Wissenslücke zu schliessen. Es handelt sich somit um eine explorative Studie zu thermischen, hydrologischen und mechanischen Prozessen in steilem Felspermafrost und dessen Auftauschicht.

Ein grosser Teil der Arbeit befasst sich mit räumlich verteilten in-situ Messungen von Temperaturen, Felsbewegungen und hydrologischen Parametern. Dazu wurde innerhalb des Konsortiums PermaSense eine Messinfrastruktur auf der Basis drahtloser Kommunikation entwickelt. Dieses System hat in zwei Messgebieten (Matterhorn und Jungfraujoch) während den letzten 3 Jahren Datensätze von neuartiger Qualität und unerwartetem Inhalt aufgezeichnet. Die hydrothermalen Prozesse in zerklüftetem Fels sind jedoch mit Feldmessungen schwierig einzugrenzen. Deshalb wurden zusätzlich Labor-Experimente und numerische Modellierungen einzelner eisgefüllter Klüfte aufgebaut und durchgeführt.

Die wichtigsten Befunde aus diesen Untersuchungen sind: i) ein deutlich kühlender Effekt in südexponierten Felswänden der durch eine dünne Schneedecke und Luftzirkulation in Klüften verursacht wird; ii) eine starke Eis-Erosion in eisgefüllten Klüften aber nur geringe Erwärmung des angrenzenden Felsens als Folge von versickerndem Schmelzwasser; iii) zwei zeitliche Muster von Felsbewegungen wurden festgestellt, eines davon ist neuartig und schränkt sich auf die Periode mit Schmelzwasser Versickerung. Diese Befunde wurden in einem konzeptionellen Prozessmodell der klimabedingten Felsstürze in Permafrostgebieten synthetisiert. Dieses hypothetische Modell betont, dass sowohl die allgemeinen thermischen Bedingungen sowie die Schmelzwasserproduktion als Auslöser von erwärmungsbezogenen Destabilisierungen berücksichtigt werden müssen.

Diese Hypothesen müssen mit der Fortführung der präsentierten Messungen oder anderen Daten von kombinierten thermisch-geotechnischen Messungen überprüft werden. Weiter könnte die Installation der entwickelten Messinfrastruktur in einer aktiven Felsinstabilität als Trainingsfall zur Überwachung von Felssturz-Anrisszonen dienen und Algorithmen für zukünftige Frühwarnsysteme liefern. Detaillierte Analysen der hydrothermalen – mechanischen Interaktionen in teilweise gefrorenen Felsklüften sind nötig um bestehende felsmechanische Modelle für Felspermafrost anzuwenden. Die Anwendung solcher Modelle ist jedoch limitiert auf Fallstudien und der Transfer zu vereinfachten Regeln aufgrund der verfügbaren Informationen ist Bedingung für die Verallgemeinerung auf höhere Skalen.

Acknowledgements

Even though a thesis is the representation of the scientific work of the author, such a project is not isolated and depends on the work and ideas of other persons. This is particularly true for this thesis, which wouldn't have been possible without the support of many colleagues, friends and institutions. For example, the unique datasets of the PermaSense field deployments, which provide an important basis for this study, couldn't be gathered without the interdisciplinary cooperation with computer scientists and the support of technicians and field-assistants. In the following I would like to express my sincere thanks to:

Stephan Gruber, the supervisor of this thesis, who motivated me with his enthusiasm for research and challenged my reasoning in many discussions. His various ideas indicated the direction of this research, often led to new perspectives and contained many advices how to address my research topic. On diverse field trips he was a powerful help and a great companion.

Wilfried Haeberli, who helped me to focus on the essential points in my argumentation and enhanced many drafts with his ideas and comments. Especially, he opened my eyes for a comprehensive perspective where current quantitative approaches may be blind for important processes. Further, Hansueli Gubler, who identified critical points and helped me to overcome them with his sound knowledge on measurement setup and environmental physics.

Igor Talzi and Christian Tschudin from the University Basel, who played a key role in starting the PermaSense project, developing concepts and prototypes and setting up a first generation of this infrastructure.

Jan Beutel from the ETH Zurich as the driving person to achieve the successful operation of the PermaSense technology at Matterhorn and Jungfraujoch. The combination of his technical knowledge with his enthusiasm for high-alpine environments, were a great advantage for this project. Within the group around Jan, Roman Lim and Mustafa Yuecel where my main contacts to identify and solve problems and they were the developers of many key components of the system. Further, Tonio Gsell, Andreas Meier, Christian Plessl, Lothar Thiele, and Matthias Woehrle contributed with their developments and analyses to the success of PermaSense. Congratulation to all of you!

Ivan Woodhatch and Hanspeter Brühlhart for their advice and skillful help for the production of the sensor hardware. Further, Peter Soland, Karoly Szeker, and Peter Robmann for the layout of the circuit board from the sensor rods, and Kurt Bössiger, Marcel Schaffner, and Grischa Martin for the production of the mechanical parts of the sensor nodes.

Marianne Font, Anthony Dubois, Jean-Louis Lagarde, and the whole staff from CNRS-M2C in Caen (FR) for their help with physical modeling and the possibility to work in their laboratory. The work with you in Caen was great an enrichment of my scientific skills!

Jeannette Noetzli and Lucas Girad for proof reading and discussing the manuscript. Thanks to their help, I hope, the reasoning of this thesis is understandable and retraceable.

Holger Frey, Stefanie Gubler, and Raymond Lebris, who were great office mates and the whole 3G-group for the inspiring environment at the Department of Geography, University Zurich.

Lorenz Boeckli, Noldi Matthis, Karl Stranski, Joel Fiddes, Paolo Pogliotti, and Luzia Fischer for their reliable and skillful assistance for the fieldwork under the challenging circumstances in steep rock faces.

Andreas Wyss from the Jungfrau Railways and Kurt Lauber from the Hörnli hut as well as the Air Zermat for their logistic support.

The Research Station Jungfraujoch (HSFJG) and their staff for the use of this infrastructure and their hospitality.

Hugo Raetzo, Andreas Goetz, and Dani VonderMuehll for their initiation, support and confidence related to the project PermaSense and this thesis.

The present study was funded by the Swiss Federal Office for the Environment (FOEN) and supported via PermaSense by the National Competence Center of Research – Mobile Information and Communication Systems (NCCR-MICS).

Contents

Part B: Publications

Methodical papers:

Research papers:

Appendix

List of Terms

GriaAlp	group on rock and ice avalanches in the Alps
GST	ground surface temperature
MAAT	mean annual air temperature
MAGT	mean annual ground temperature
MAGST	mean annual ground surface temperature
N	north
PERMOS	Swiss permafrost monitoring network
PermaSense	project for development and prototyping of a wireless data acquisition infrastructure for high alpine permafrost (this thesis is part of PermaSense)
S	south
SR	sensor type: sensor rod
TO	thermal offset
TC	sensor type: thermistor chain
TM	sensor type: temperature–moisture chain
WSN	wireless sensor network

Part A: Synopsis

1 Introduction

Steep bedrock permafrost is abundant in cold mountains and may increasingly be a source of hazards with permafrost degradation following climate change. This thesis focuses on the physical mechanisms linking climate and rock instabilities in these steep mountain flanks. It addresses key knowledge-gaps with process studies based on in-situ field measurements or model studies that build its central part. Finally, possible ways to link the results obtained and methods developed to future hazard mitigation are sketched.

1.1 Context and relevance

Permafrost is a widespread climate-driven thermal phenomenon also in high-alpine regions. The phenomenon, defined by continuous ground temperatures where water may exist as ice (≤0 °C), affects the hydrological and mechanical properties of the subsurface and is, hence, a governing factor of geomorphodynamics. A large proportion of the periglacial area of cold mountain ranges is steep bedrock because gently terrain often accumulates temperate glaciers with no underlying permafrost. Here, permafrost degradation can affect manmade infrastructure, cause more rock fall activity, or trigger natural disasters of larger scale via process chains (Haeberli et al., 1997). The hypothesis that climate-related rock destabilization is decisive to alpine geomorpodynamics is supported by a) the exceptional number of rock falls that occurred in the hot summer 2003 in the European Alps (Gruber et al., 2004a), b) the correlation of high regional rock fall activity with warm decades in the past century (Fischer, 2010; Ravanel and Deline, 2010) and c) the observation of ice in the rock fall deposits or at the failure surface reported from high-alpine rock falls (e.g. Dramis et al., 1995; Fischer et al., 2010; Gruber and Haeberli, 2007; Pirulli, 2009; Ravanel et al., 2010). The process interactions linking climate change, permafrost conditions and rock fall in high-alpine bedrock are currently poorly understood, because the complexity arising from diverse feedback mechanisms and the high spatial variability hinder empirical investigations and limit the validity of existing models. A better process understanding is needed to delimitate potential rock fall areas and to estimate timing (and magnitude) of events where critical situations are detected.

1.2 Previous work and problem statement

To develop a conceptual model as a concretization of the process understanding of the climate – permafrost – rock fall interaction (or parts of it), this thesis aims to identify and describe qualitatively and, where possible quantitatively, thermal, hydrological and mechanical processes. The main focus is hence on the basic research of permafrost science and periglacial

geomorphodynamics in steep bedrock. This is addressed with detailed studies of distributed field measurements or sensitivity studies by experimentation with simple models. However, some application-oriented conceptual and technological outcomes are aspired, too.

Climate – permafrost interaction in steep bedrock

In this thesis, the term *steep bedrock* assigns mountain flanks that are steeper than 40° and that are not covered by glaciers or large hanging glaciers. In such rock faces the distribution and temperature of permafrost is roughly controlled by the surface temperature, similar to permafrost in gentle terrain, but is influenced by larger lateral heat fluxes due to 3D-effects in the steep topography (Wegmann, 1998; Noetzli et al., 2007). Distributed rock surface temperatures are typically estimated by numerical models that simulate the energy exchange with the atmosphere (Gruber et al., 2004b). Such surface temperatures have been validated with systematic measurements in near-vertical (> 70°) bedrock (Gruber et al., 2003; Gruber et al., 2004b; Noetzli et al., 2007). However, the thermal effects of surface and near-surface characteristics, snow cover and water percolation in gentler sections remain largely unknown (Gruber and Haeberli, 2007). Because rock faces with average inclinations in the order of 40–70° are abundant in high alpine ranges further knowledge about the thermal effect of these characteristics is important for future estimates of the permafrost conditions and correspondingly to assess recent rock fall detachment zones with respect to their thermal conditions.

According to borehole temperature measurements alpine permafrost in Europe only experienced a slight warming (0.3–1.0 °C) in the upper tens of meters in the past two decades (Harris et al., 2009) or is even not (yet) significant (PERMOS, 2010). Hence, ground temperature does not simply follow atmospheric warming and is strongly influenced by the surface conditions making other climatic factors (e.g. winter snow fall) important. A more direct coupling to temperature rise is expected for near-vertical rock sections (Gruber et al., 2004b), but for steep bedrock no boreholes with longer timeseries exists. The direct dependency may be complicated for less steep rock faces similar to the situation in gentle terrain, but it may show other sensitivies. The empirical investigation of such modified climate-sensitivity of fractured, non-vertical rock is not a focal point of the present study, due to the lack of long-term data. Nevertheless, better process understanding may enable model analysis of these effects.

Climate – rock-fall interaction in steep bedrock

Fischer (2010) discusses different factors contributing to the stability of high-alpine slopes and arranges them in a continuum between *disposing factors* and *trigger factors.* Even though lithology, structure, and topography of rock slopes are dominating factors for the disposition of rock fall (Fischer et al., 2011), a direct climate impact acts via phenomena such as glaciers, ice faces, permafrost, and rock hydrology (Gruber et al., 2004a; Gruber and Haeberli, 2007; Fischer and Huggel, 2008). The effect of ice loss in steep faces and valley glacier retreat was assumed to play an important role in two case studies (Fischer et al., 2006; Fischer et al., 2010) and thermal, hydrological, and mechanical influence of covering hanging glaciers is suspected to be involved in the release of large rock-ice avalanches (Haeberli et al., 2004; Huggel, 2009). For

diverse rock falls liquid water was observed at the failure plane after the detachment despite the low mean annual air temperatures (Huggel, 2009). In situ measurements of pre-failure deformations in permafrost areas are limited to a time series measured at Jungfraujoch, Switzerland (Wegmann, 1998). Corresponding measurements of thermal and hydrological conditions for this event are not available. Further, no clear correlation with topographic or meteorological situations in which rock fall with volumes larger than 1000 m^3 occurred, was found (Noetzli et al., 2003; Huggel et al., 2010; Naegeli, 2010; Ravanel et al., 2010; Fischer et al., 2011). Therefore, an empirical identification of the process interactions that have triggered these events was not possible so far. Exceptional rock fall of rather small volumes throughout the Alps correlate with the hot and dry summer 2003. However, the early timing of their occurrence underlines a fast reaction to extreme climatic events (Gruber et al., 2004a). In the scope of this thesis are the thermal and hydrological (permafrost related) influencing factors, while the effects of glacier retreat and mechanical influence of hanging glaciers are not considered.

Diverse studies focus on physical processes that modify the geotechnical properties of cold bedrock: Ice formation processes are an efficient contribution to high-alpine rock weathering and cleft widening (Hallet et al., 1991; Matsuoka, 2001a; Murton et al., 2006) and the pore ice content influences the geotechnical properties of intact rock (Mellor, 1973). Changes in cleft-ice temperature and geometry affect the mechanical properties of discontinuities (Davies et al., 2001; Guenzel, 2008; Krautblatter, 2009) and the melt of cleft ice due to permafrost degradation affects the down-slope hydrological regime and the possibility to build up hydrostatic pressure within the previously ice-sealed cleft system (Haeberli et al., 1997). Krautbatter (2009) points out the temperature dependency of the total friction of rough fracture surfaces and formulates a mechanical model with frictional, cohesive and ductile terms. The transfer of such laboratory-based and theoretical knowledge to the natural situations still dues, because a conceptual model interlinking the thermal, hydrological and mechanical subsystems does not yet exist. Further, the small-scale temperature fields in fractured bedrock and the cleft characteristics are largely unknown and prohibit the setup of realistic temperature-dependent stability models. A key role for this process understanding and quantification accords to the hydrothermal processes in cold fractured rock, which influence both, the thermal and the mechanical properties along discontinuities. For these processes that include phase change between water and ice recent work on hydrothermal processes in scree slopes (Rist, 2007; Scherler, et al., 2010) provide an information basis.

1.3 Research questions

The overarching research question addressed in this thesis is:

- How is rock stability in permafrost areas linked to atmospheric conditions?

This question underlines the focus on basic process understanding. From the above-stated problems and research gaps, a series of sub-questions is deduced:

– What influence do surface and subsurface characteristics have on the thermal conditions in steep bedrock permafrost?

– How do hydrothermal processes affect the thermal, hydrological and mechanical properties in clefts at subzero temperatures?

– What is the mechanical response of fractured rock to meteorological events and which processes explain the resulting kinematics?

Further, two application-oriented questions refer to the transfer of the findings from process research and related methodical experiences to the mitigation of climate impact in high-alpine environments.

- How can we delimit rock fall hazard from permafrost areas in time and space?
- What technical and scientific means support a rock fall monitoring in critical situations?

1.4 Structure

Following the introduction, the approaches and corresponding characteristics of statements made in this thesis are motivated and outlined in Chapter 2 (methodology). Chapter 3 explains the conception and progress of the technical development of an infrastructure for distributed in-situ sensing in alpine environments. This chapter mainly refers to the two methodical publications (Publication I and II). The middle part (Chapter 4–6) discusses the main scientific results with respect to the three subquestions, because the different parts build on each other (Figure 1). Detailed reasoning and descriptions of the analysis methods of this part may be found in the publications that form the scientific core of this thesis (Publication III–V). The synthesis (Chapter 7) arranges the extended process understanding obtained, in a framework for climate driven rock instabilities (overarching research question) and sketches the application of these findings for hazard mitigation (application oriented questions). The thesis is concluded by a summary of progress, a list of the main outcomes and the future (research) perspectives (Chapter 8).

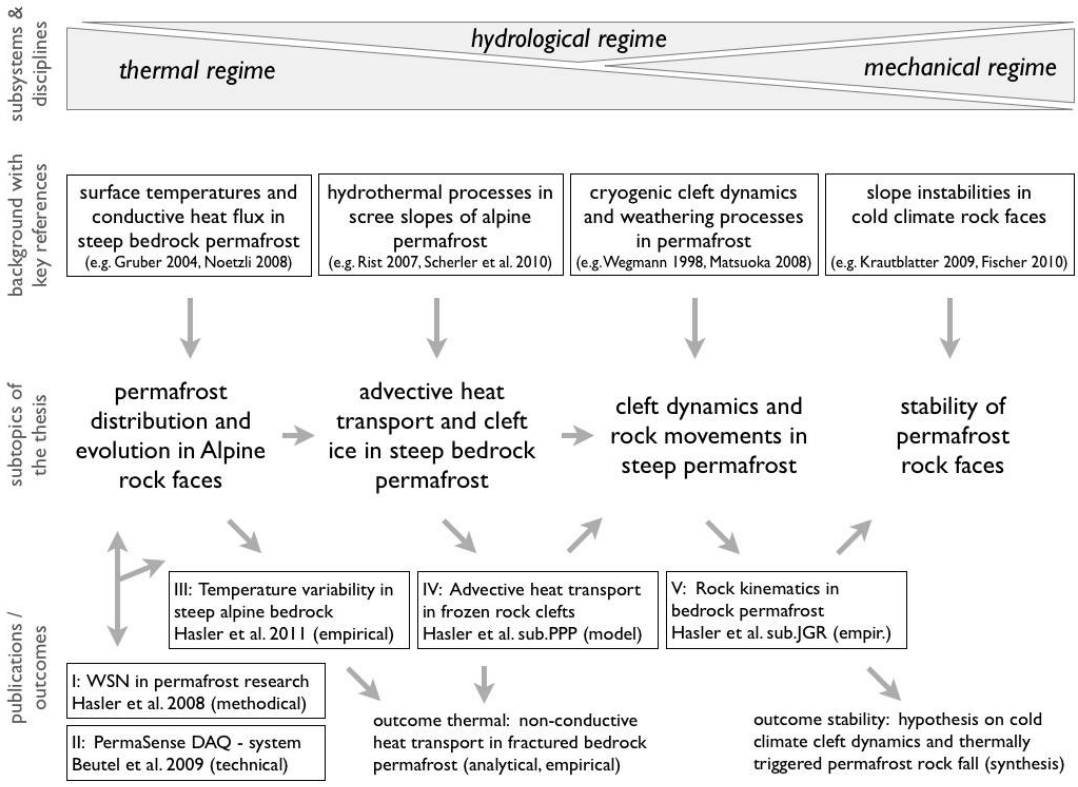

Figure 1: *Argumentation line of this thesis in a trans-disciplinary framework (geophysics, rock hydrology and rock mechanics).*

Figure 1 shows the main argumentation line of this thesis and puts Publication III–V into perspective. Following the main causality (excluding important feedback mechanisms), I arrange the publications from thermal to hydrological and finally mechanical processes. Hence, Figure 1 illustrates how one subtopic is based on findings of the others and should not be mistaken as a process framework, which will be presented later. The main outcomes can be classified into a) empirical – analytical findings on thermal conditions of steep bedrock permafrost and b) a synthesis on permafrost-related rock destabilization (Figure 1).

Chapter 4–7 have the character of an extended discussion where the findings of the publications are arranged in a larger framework and related to each other. Therefore I would like to stress two aspects of the structure of the following text: 1) No particular *background* or *methods* sections exist; this is contained in the respective chapters and reduced to a minimum needed for a broader discussion; in more detail it is described in the publications. 2) Empirical and technical contents that are not covered by the publications are rolled out to the appendix. This keeps the synopsis on a general level but makes it retraceable where referred to unpublished contents.

2 Methodology

Additionally to the exploratory character of this study, the addressed research object is of high complexity as it is typical for natural systems. For these reasons, the methodology of this thesis consists to large parts of empirical approaches to formulate process-models by abductive reasoning. The hypotheses on process interactions are qualitative (or semi-quantitative) models because of the inherent generalization even tough they are based on extensive data. Such a conceptual level is a precondition for quantitative model formulation and hypothesis testing in the future.

2.1 Science theory

Nature of the research object

Contrary to experimental physics where problems are investigated in a clearly defined, *reduced* frame, environmental science is especially challenged by the amount of possibly interacting variables. Most of the basic physical principles behind environmental phenomena are well established in the sense that they where "known and recognized" within the classical physics of the 19th century (Bak, 1996). Hence, the design of representative measurement setups, suitable analysis instruments and appropriate models is the key challenge in environmental science and not the detection of "new physical laws". This is in particular true for permafrost and geomorphodynamics in high mountains: Many interactions between physical variables and processes, large spans of interacting scales, short time series in relation to effects investigated, and variables that are difficult to explore empirically (causing logistically and technically challenging field work) characterise the research objects. An example is the topic of this study: The physical fields involved are thermodynamics, fluid dynamics, (structural-) mechanics and electromagnetism. Heat conduction in rock would be easy to predict in detail if rock was a homogeneous medium. But phase transitions of water in the micro pores of the rock modify its thermal behavior on a larger scale. Discontinuities in the rock are relevant for its mechanical and hydrological characteristics but will also influence the thermal field by fluid movements such as air and water circulation. The complexity[1] resulting from feedbacks between temperature, phase state, hydrology and mechanics within a spatial structure, underlines the limits of a strictly deterministic approach. *Nature* as a research object is therefore always addressed with a number of simplifications or at a higher level of abstraction (Harrison, 2009).

[1] Complexity is a (non-linear) behavior of systems with many degrees of freedom (Phillips, 2003). It is not predicted by the simple aggregation, even if behavior of constituents is known.

Science theoretical terms and approaches

"Science is the effort to assign to the chaotic variety of sensations a consistent theoretical system" (Einstein, 1940). As the title of Einsteins essay *The fundament of physics* indicates, and as we will see below, this excerpt represents a specific perspective of what science is. More general and possibly more appropriate for a wider range of science is the paraphrase that science is the comprehensible solving of a problem (Richards, 2009). Here, I will explain *how* I try to find answers to my research questions and *what kind of answers* these are. But first, some considerations are given about science theoretical traditions and their implications in the context of geosciences:

The different approaches of scientific knowledge generation or problem solving in geosciences are reflected by the various sciences theoretical concepts that underlie the discipline (Richards, 2009). Richards (2009) emphasizes the role that these traditions still have today: For example, the value of and confidence in comprehensible measurements and observations is based on the *Positivism* of the 18th century, and *Logical Empirism,* which defines the systematic intervention, is still practiced in experiments. The approaches of both traditions draw conclusions a posteriori from a case to the general (*induction*). *Critical Rationalism* (Popper, 1935) being the concept of a priori theorizing with logical *deduction* to hypothesis and with falsification as sole empirical prove, has sustainably influenced today's science. For geosciences this purely deductive theorizing from the general (axiom) to a case, has its limitation (see below). However, the relativity of current scientific understanding and its questioning as postulated by Popper is fundamental to the evolution of sciences. After Richards (2009), *Realism* came up with uncovering hidden structures within observations and *Modern Science* addressed observer effects and uncertainties in empirical methods.

Critical Rationalism as the predominant science theory of empirical–analytical sciences poses the following problem for an application to geoscience: It is vague in theorizing how axioms as the basis of theories emerge (intuition). The need for theories on a higher level of abstraction requires a reflection on how they may be established. The concept of *abduction* developed by Peirce in the beginning of the 20th century (Fann, 1970) is in this respect a synthesis of induction and deduction. Abduction theorizes the drawing from a case (observation) to a rule (theory). However, different abductive approaches exist and the term is generally used for an iterative approximation of a theory to the observations.

Natural science may be seen as a continuum ranging from *reductionism* to a *holistic understanding* of nature (Figure 2). Reductionism reduces the problem to be solved to a causality, consisting of a minimum number of elements. In its pure form, this is only aspired in physics where a phenomenon (or observation) is tried to be explained theoretically, based on a minimal number of laws or axioms. But many other disciplines apply theories on a higher level of abstraction where processes and variables are integrated or ignored. They are of a different quality than physical theories because they are not reduced to *first principles* but the reduction is rather in the incompleteness (abstraction) how the entire problem is taken into account. Here, this is referred to as *phenomenological reductionism*[2] (Figure 2). With more complex research

[2] This term is deduced from *phenomenological physics,* which means that a theory is induced to meat the observation (phenomenon). See e.g. (Einstein, 1936).

topics the explanatory power of reductionist theories decreases and a *heuristic* approach generating simple but robust "rule of tumbs" is more appropriate to understand and describe (instead of quantitatively explain) the phenomena (Figure 2). This allows the qualitative consideration of many influencing processes but with corresponding limitations in the prognostics. Such a *holistic understanding* as a qualitative mental model of the real world can be a basis for the formulation of quantitative hypotheses. Its strength is that it is less "blind" for processes that are important but not revealed by deductive approaches.

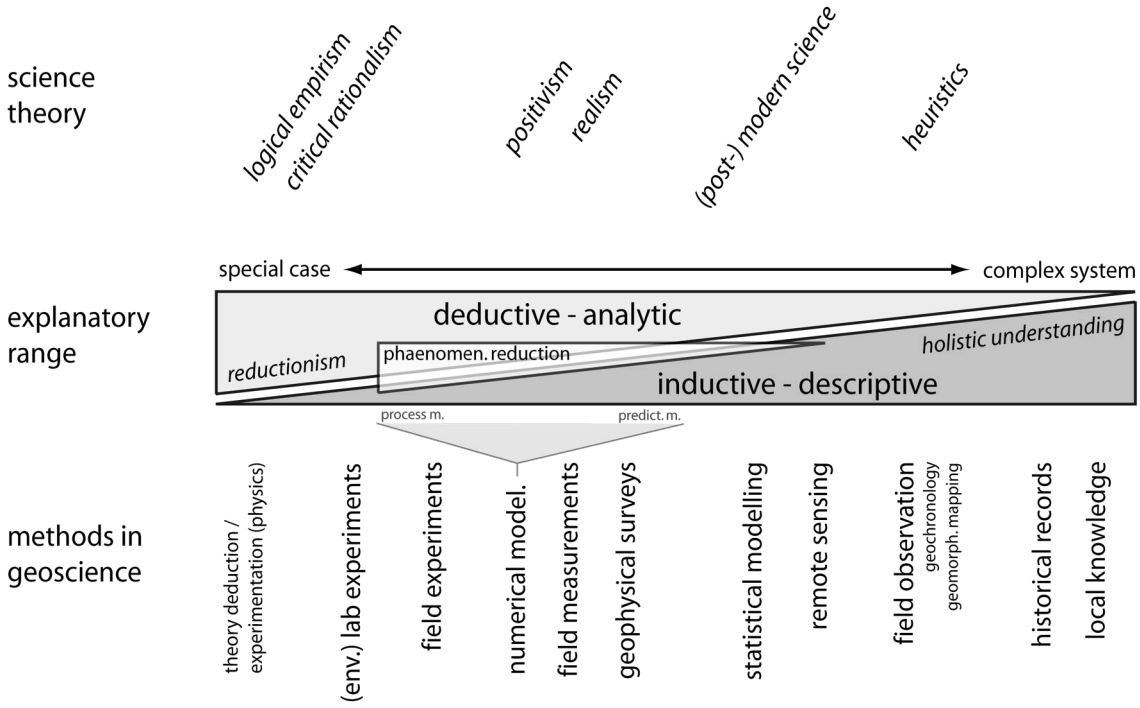

Figure 2: *Framework of methods in geosciences in a continuum between a clearly defined "special case" and a "complex system" as research object. Science theoretical concepts and methods are assigned to their approximate position in this continuum. Terms from science theory are used after (Richards, 2009) except "heuristics".*

Resuming the excerpt of Albert Einstein, we see the science theoretical difference to the postulate of critical rationalism: In geosciences we do not strictly assign a theoretical system to the empirical "sensations" but also act the other way around. Empirical description and speculations on explanations for unexpected findings as well as deduction from accepted principles and empirical testing are part of our scientific practice and theory.

Statement character and models

In geosciences there are often problems (or questions) that require directly or indirectly a (spatial) description or quantification of variables. As long as no generalization to a theoretical level takes place, the answering of this questions is not subject of an inductive process because they remain descriptive. In this study such *empirical statements* are made where the results of the field measurements are presented such as it is the case for the temperature and dilatation measurements at Matterhorn and Jungfraujoch. Without further interpretation they cannot be extrapolated in time or space (no prediction). The results of a hypothesis-generating induction

or abduction from empirical statements I name *empirics hypothesis*. These hypotheses do not have a strictly logical basis (different hypothesis are possible) but speculate about theoretical explanations of the empirical statements and can reveal the importance of hidden (and unexpected) processes (cf. Realism). This procedure is problematic if its speculative character is not clearly declared. The interpretation of our rock movement measurements is to one part such an abduction. In contrast, *empirical evidence* is understood as the result of a hypothesis-testing, which support the confidence in (but don't prove) a theory *(theoretical statement)*. The hypothesizing on explanations for empirical findings on the basis of existing (phaenomenological) theories or empirics hypothesis such as done for one part of the rock movements could be seen alternatively as a hypothesis testing (i.e. broader meaning of abduction). We may conclude, that any reference to empirical findings does not attribute a "true" or "false" to a theoretical explanation but rather a "consistent" or "inconsistent".

Models are theoretical statements and their implementations on empirical circumstances or systems (Harrison, 2009). *Conceptual models* do state qualitatively or semi-quantitatively our understanding of a system. In geoscience they may be based on theoretical considerations but they are not free of empirism because they are phenomenological. After their quantitative formulation in *mathematical models* they may be implemented in computers[3]. These quantitative formulations can emerge empirically (by induction) in case of *empirical* or *statistical models.* However, this depends on the selection of the explanatory variables (and the corresponding conceptual models). In contrast *physically oriented models* model physical processes explicitly and often time-dependent. This allows their use as *process models* or *prognostic models* (Figure 2). The former are used to learn about processes and sensitivities and are an important method for theory and model enhancement (abduction of process). The latter make statements about expected outcomes in result variables (prognostics). Both types of numerical models contain empirical statements within their parameterization (e.g. material parameters; a priori), their setup (geometry, scale; e.g. pore characteristics of rock) and their calibration (tuning parameters; a posteriori). As a consequence of this inductive part, the empirical data for parameter definition and the one for model validation (empirical evidence) need to be independent and the limits of model validity must be declared (Rykiel, 1996). A fundamentally different type of models are *physical models.* They are implementations of conceptual models in the laboratory (laboratory experiments), hence, they reproduce an empiry of reduced complexity based on our theoretical understanding. This allows exploring physical effects that are not addressed in mathematical formulations of the same system and supports parameterization or/and calibration of physically oriented models.

[3] The term *numerical model* is used for these computer implementations by some authors, while other restrict the term to models that use of numerical methods to solve the mathematical models.

2.2 Approaches used in this thesis

Krautblatter et al. (2011) state that a direct abduction from rock fall records of high-alpine areas to the controlling mechanisms is difficult due to the limited data. They identify four major fields in which research needs exist to develop a processual linkage between climate and rock fall hazard: 1) the thermal conditions of steep permafrost bedrock; 2) the appraisal of information of the characteristics and volume changes of rock faces by remote sensing methods; 3) the characterization and process understanding of bedrock instabilities; and 4) the flow propagation of rock and rock-ice avalanches (Krautblatter et al., 2011). The publication emerged from a workshop of an informal group on rock and ice avalanches in the Alps (GriaAlp), hence these four categories reflect to a part the fields of ongoing research activity in the Alps. The field of rock hydrology in bedrock permafrost, which would be an important element between 1) and 3), is for example not explicitly addressed because respective work does not exists. The focus of this thesis is, however on the process understanding of 1) and 3) and to minor extend to the hydrologic processes interlinking them. In respect to the processes controlling the thermal conditions 1), the small-scale variability of rock temperatures should be investigated, hence empirical data from the field is required (Krautblatter et al., 2011). The same is true for rock instabilities because the transfer from laboratory scale to the field and the application of existing rock mechanical models to permafrost field sites is problematic. Concerning the thermal influence of hydrological processes within fractured rock an isolation of the problem to a few controllable parameters was applied complementary to the field measurements. These two different approaches are outlined in the following subsections.

Field measurements and observations: abduction of conceptual models

For both, the thermal conditions in steep bedrock permafrost and driving mechanisms of rock movements, in-situ measurements are essential for a better process understanding because of the explorative character and the high complexity of driving processes. Temperature and kinematics of steep bedrock are therefore measured with direct methods, at high temporal resolution, and spatially distributed (Chapter 3). These extensive data sets and derived data (e.g. cross-correlations between different variables, annual means) are in a first step interpreted in terms of typical patterns (empirical statements). Subsequently, existing theories and concepts on (hydro-) thermal processes in permafrost and releasing mechanisms of rock fall are discussed, adapted and modified to fit with the observations. These abductions refer to specific subsystems (atmosphere – ground temperature and ground temperature – rock stability interactions) and differs from the abduction based on rock fall records (Noetzli et al., 2003; Huggel et al., 2010; Naegeli, 2010; Ravanel et al., 2010). The main difference is the closer link to the time dependent driving processes because the empirical data reveals the evolution of the parameters of interest such as temperatures and rock movements.

The results of these abductions are hypotheses that enhance our process understanding and quantification in the respective domains. In other terms, conceptual (semi-quantitative) models of processes are formulated. They need to be supported by future empirical evidences that may extend or limit the validity of these models. In Chapter 7 they are synthesised and introduced

into current conceptual models of the entire process chain of climate related high-alpine rock fall (Chapter 7). This transfer of the conceptual models to a more general level is not an up-scaling in terms of special dimensions, because the field observations address situations of the same order of magnitude. The comparison with field evidences from other studies (partly) justifies the drawing of analogies from the observed special case to the general. Further, the similar characteristics of many high-alpine rock faces regarding micro-topography and near-surface characteristics supports this induction. This generalization has two scientific consequences: a) The hypotheses are qualitative. b) Not in-situ measurements alone, but analyses of rock fall may be used to challenge these hypotheses. The hypotheses may be an attempt toward a delimitation of rock fall hazards in time and space (Chapter 7).

However, these hypotheses should not be mistaken with geomorphic concepts that interlink process and form and, hence, state the domains and efficiency of processes on a higher spatial and temporal level. The focus of this study is much more on low frequency events that may have a minor influence on landscape evolution. The relatively short time span compared to event frequency that are relevant for natural hazard, requires the consideration of feedback mechanisms and disequilibrium's (cf. Schumm and Lichty, 1965) and limits the applicability of frequency-magnitude relations. Further simple analogies between different scales appear to be problematic for the system investigated, because different subsystems may have different scaling.

Numerical and physical modeling: reduction and sensitivity study

In case of the hydrothermal processes that may influence the thermal, hydrological and mechanical conditions in clefts (rock fractures), in-situ measurements appear unsuitable to evaluate the controlling mechanisms: This is because of a) the lack of suitable instruments to measure diverse parameters such as flow path and rate, heat release and ice formation in fractured rock; b) the extreme spatial variability, variable flow paths (due to ice melt) and open systems with mass and energy is exchanged with the surroundings (cf. Harrison, 2009) concern the result parameters themselves (in contrast to temperature and slow rock kinematics). Some test-setups to measure the presence of liquid water and flow in-situ were not successful in this study, hence the respective field data is limited to the temperatures near a possible run-off in clefts and some manual water temperature measurements at the surface during snow melt (Appendix: Supplementary material).

In the laboratory or with computers, simplified (reduced) models of the situation in the field can be set-up and allow the control and observation of diverse parameters. In the present case, we confined the model to one single (artificial) cleft that we consider as a prototype of ice-filled clefts in permafrost bedrock. These reduced models are based on the definition of a conceptual model (Chapter 5) and imply corresponding assumptions about the field situation (Figure 3). Hence, it is to large parts a quantification of the conceptual model even though the dimensions and the heat input to the laboratory experiment was chosen based on initial model results and field evidences (Figure 3). The numerical model is formulated prior to the so-called stationary laboratory experiments that are used for calibration and validation of the numerical model (Figure 3; Chapter 5). Systematic variation of the driving parameters of the numerical model result in a quantification of the cleft ice erosion and the warming of the surrounding rock and

identifies the sensitivity on variable advection and scaling. These findings together with the results of more realistic (cyclic) laboratory experiments are generalized to semi-quantitative hypotheses on advective processes in bedrock permafrost. It supports the interpretation of the field measurements and may be a basis for future hydro-thermal modelling of cold fractured rock.

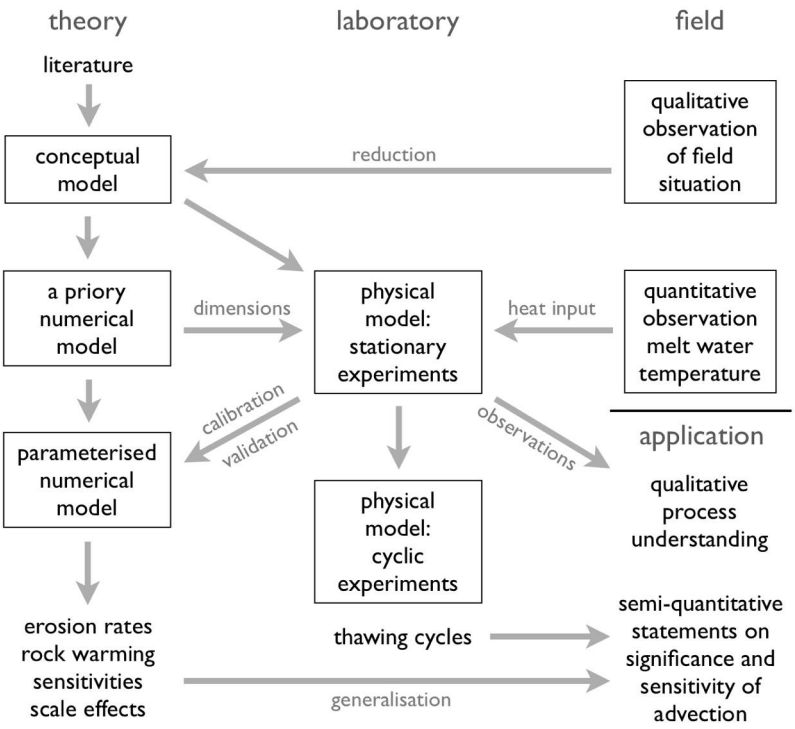

Figure 3: *Methods and reasoning of the studies on melt water advection in fractured rock.*

3 Distributed wireless sensing in harsh environments

Wireless Sensor Networks (WSNs) provide a valuable tool for distributed in-situ measurements of environmental parameters. Within the project PermaSense, we built a WSN to measure and observe temperature, geotechnical parameters and surface conditions in steep bedrock permafrost. The technical developments and customisations concern the entire chain from sensing over data transmission to data management. The technology was applied at two field sites in the Swiss-Alps and gathered time series of approximately two years, which are the basis for the field investigations in this study.

3.1 System design

Any data acquisition of in-situ measurements requires the following tasks: 1) physical sensing, 2) data logging, 3) data transmission, 4) pre-processing, and 5) archiving. In harsh environments, such as the potential starting zones of high-alpine rock fall, the performance of the first three tasks is challenging because of difficult access and environmental impact. In a joint project of computer- and geo-scientists (PermaSense) we designed and built a flexible data acquisition infrastructure based on new technologies to provide a powerful tool for scientific measurements and monitoring under extreme conditions. Diverse publications emerged from this interdisciplinary group documenting different stages of the development phase (Talzi et al., 2007; Publication I; Talzi et al., 2008; Publication II; Beutel et al., 2009). This section outlines the design of this acquisition system referring mainly to the two methodical Publications I and II and the Appendix A.1–4. The parts where the author substantially contributed are: i) definition of requirements of the system and sensor interface, ii) sensor development and selection, iii) mechanical design of the WSN hardware, and iv) management and processing of the measurement values (ii and iii are based on a consultancy report of Gubler (2006)).

Existing systems for distributed measurements based on individual miniature single-parameter loggers are time consuming in maintenance (Gruber et al., 2003) and wired systems are sensitive to environmental impacts such as boulder fall, avalanches or lightning. The data acquisition system developed within PermaSense (PermaDAQ) aims to meet the following key features: a) wireless communication allowing real-time system surveillance and remote data retrieval, b) ultra-low power operation for multi-year autonomous operation, c) precise sensing of diverse parameters, d) rugged hardware setup, and e) no configuration needed during installation work. However, wireless communication is sensitive to environmental conditions, first of all snow or ice cover on network nodes, and requires measures to deal with temporary connectivity loss. The translation of these features and their consequences into requirements of

a wireless sensor network (WSN) for use in high-alpine area is given in Publication I.

The wireless sensor network (WSN) and the data transmission to an internet server is sketched in Figure 4. This part of the acquisition system covers the tasks 1) to 3) (see above). The *sensor nodes* consist of an assembly of analog and/or digital sensors and a *network node* that triggers and logs the measurements and communicates within the local low-power WSN (cf. Appendix A.1). The measured values and system parameters are dynamically routed to an access point (*base station*) and from there via directional WLAN or LAN to the external data sink. Many hardware and software components are custom developments or adaptations of existing technologies (Publications I and II) because established components do not exist or are too power consuming. The basic communication component of the sensor nodes is the low-power WSN node *TinyNode* (Dubois-Ferrière et al., 2006). For the thermal monitoring a multiplexed sensor type was designed and produced: The so-called *sensor rods (SR), thermistor chains (TC)* or *temperature moisture chains (TM)* measure 4–8 temperatures and 0–4 electrical rock resistances (Publication I; Appendix A.1). The multiplexer electronics with reference resistors for analogue measurements is placed within these sensors to minimize thermal disturbance of the measurements (Appendix A.1). To allow the integration of a wide range of geotechnical and hydrological sensors in the WSN, we developed a *sensor interface board (SIB)* (Publication II). An overview of the applied sensors is given in Appendix A.1. The mechanical setup with protective elements against environmental impact of the sensor nodes and the architecture of the base station including additional sensors (weather station, automatic camera) are described in Publication II and by Beutel et al. (2009b).

The pre-processing and management of the data consists of general tasks for all data acquisition systems, such as conversion of raw data to physical values, safe storage and allocation of meta information. For the PermaSense system the capability to handle streaming data, the mapping (assign to location in the field) of different data packets, and divers checks of system behavior are additional tasks that require automated operation (Appendix A.2). A part of the meta data allocation and the conversion is performed automatically and the data is stored into a data base. Online tools to monitor the system operation and data status are available on the website http://data.permasense.ch/. The converted and mapped data can be accessed via this web site or directly via requests to the data base. Further processing such as data validation, filtering, and aggradation is currently implemented in offline data processing functions and not included in the automated pre-processing (Appendix A.2).

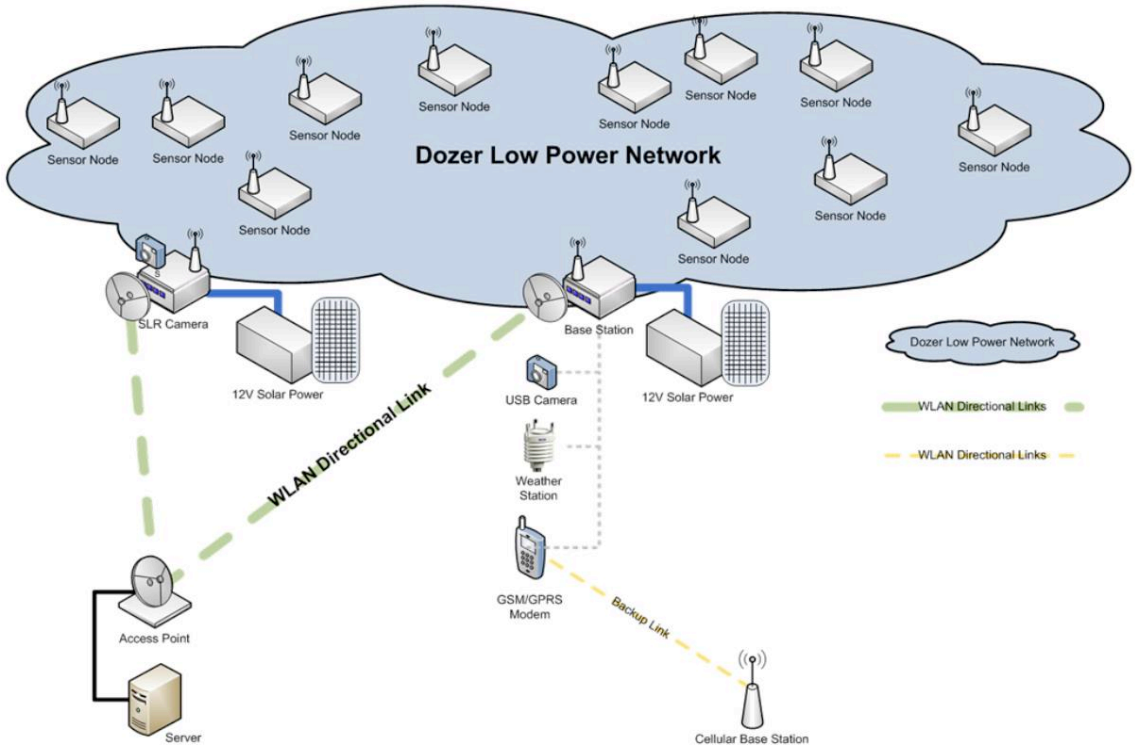

Figure 4: *Scheme of WSN and data transmission on the example of the Matterhorn deployment (figure by J. Beutel).*

3.2 Application at two field sites

The multifunctional WSN is operated at two permafrost field sites in the Swiss Alps and the corresponding data is analyzed in two publications (II and IV). Here a brief overview from a general perspective is given. Further descriptions are included in the thematical parts of this thesis (Chapter 4–6). A detailed description can be found in Publication I and II, whereas a recent extension of the Matterhorn site is described in Publication V.

The Jungfraujoch–Sphinx deployment

Figure 5 shows the installation at Jungfraujoch (3500 m a.s.l.). The separation of the network topology into two clusters (indicated with lines) and snow cover on many sensors were challenges from an algorithmic point of view during the first years of operation. Different surface characteristics and micro topographic situations are covered by this deployment but only two sensor types (SR, TC) are applied (Table 1). A first installation was performed in autumn 2006 and the WSN is operational since beginning of 2009.

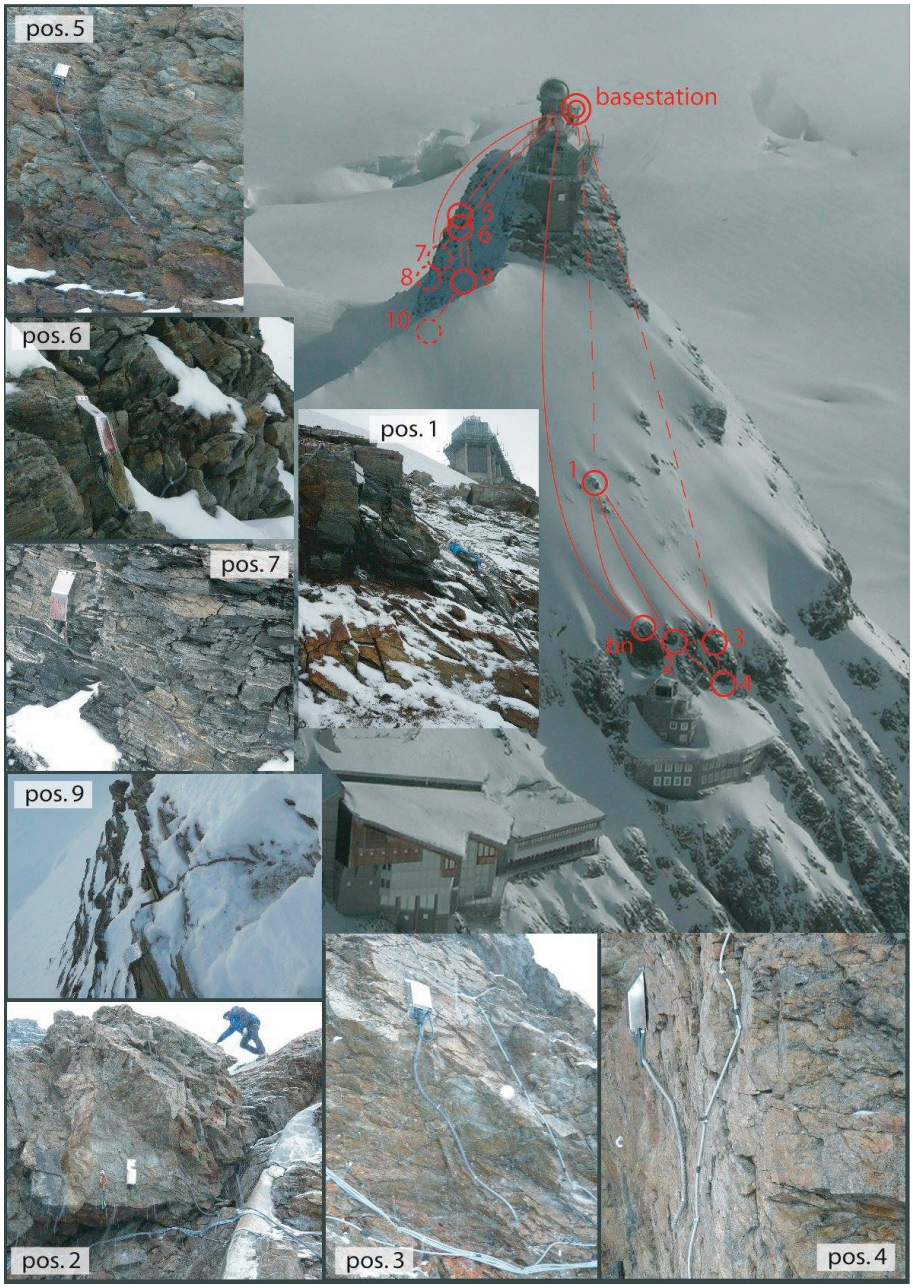

Figure 5: *Overview of the Jungfraujoch deployment and close-ups from all rock sensors (sensor rods). The circles indicate the locations of the sensor nodes; "bn" refers to a bridge node required for a stable connectivity to the basestation. The long cables beside the sensors 2–4 are not connected to the WSN (ERT-sounding).*

Table 1. Basic meta information for the Jungfraujoch field site.

location description				sensor node description		
location	feature	loc. orientation asp / °	slp / °	sensor node	no. temp. SR	TC
1	snow	215	30	jj01	4	
2	concave, wet	220	50	jj02	4	
3	convex, dry	190	80	jj03	4	
4	intact rock	200	75	jj04	4	
5	intact rock	330	85	jj05	4	
6	fractured	335	75	jj06	4	
7	limestone	330	75	jj07	4	
8	ice face	340	45	jj08		8
9	snow	330	40	jj09	4	
10	ice face	330	45	jj10		8

The Matterhorn–Hörnligrat deployment

At the Matterhorn field site the sensors are located at the north and south sides of a ridge similar to the Jungfraujoch deployment (Figure 6). They are at 3400–3550 m a.s.l in proximity of the detachment zone from a rock fall that occurred in summer 2003 (Publication V). At this field site many different sensor types are combined (Table 2; Appendix – Technical Documentation) at some locations two sensor nodes measure complementary parameters (locations 5/6, 7/8). Most of the sensor nodes gather data since summer 2008 except mh09, mh20, mh21, and mh22, which where installed in summer 2010.

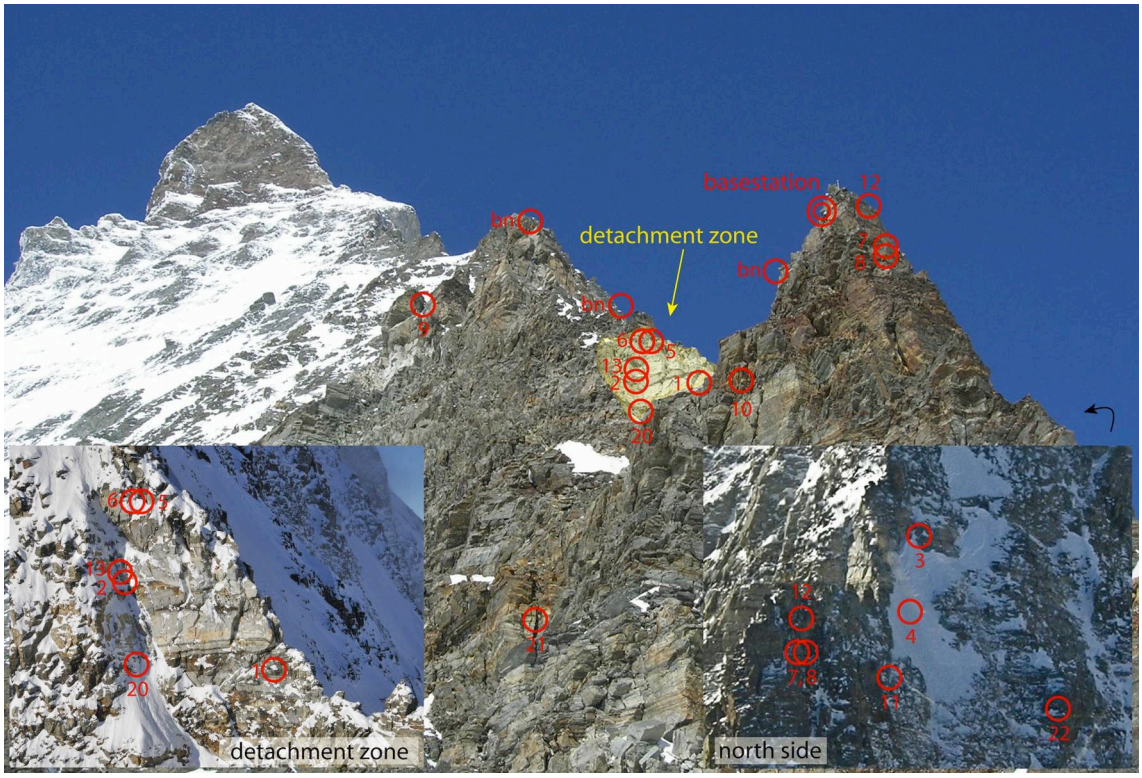

Figure 6: *Overview of the Matterhorn-Hörnligrat deployment. The circles indicate the locations of the sensor nodes; "bn" refers to bridge nodes (relay).*

Table 2. Basic meta information for the Matterhorn field site.

location description				sensor node description								
location	feature	loc. orientation		sensor	crackmeters (X/mm)			no. temperatures				others
		asp / °	slp / °	node	CR1	CR2	CR3	SR	TC	TM	Ts	
1	intense radiation	95	75	mh01	50				4		1	
2	concave, wet	80	50	mh02	50				8		1*	
3	north side	350	65	mh03	150				7		1	
4	saddle north	320	70	mh04	50				6		1	
5 / 6	top detachment	90	60	mh05						4		EP, WP
5 / 6	top detachment	90	60	mh06	100	200						
7 / 8	large tower	50	90	mh07						4		EP, WP
7 / 8	large tower	50	90	mh08	100	150						
9	leaning tower	80	70	mh09	100	200	200				1**	
10	south side	140	90	mh10				4			1	
11	north side	340	70	mh11				4			1	
12	tower west top	45	90	mh12				4			1	
13	same as mh02	80	70	mh13								SP
20	below mh02	70	70	mh20	100	150						
21	south low	70	85	mh21	100	150						
22	north low	70	85	mh22	100	150						

3.3 Technical outcomes

The interdisciplinary collaboration within PermaSense resulted in a consortium with significant experience and know-how on the design and operation of up-to-date data acquisition infrastructure in high-alpine environments. Beyond the aim of the initial PermaSense (Hasler and Gruber, 2009), new projects with enhancements and extensions of this technology (PermaSense III, X-Sense) emerged from this collaboration. Beside this consolidation of know-how, a number of technical outcomes can be listed as achievements of this project:

- Flexible and robust WSN for extreme climatic and environmental conditions.
- Sensor setup for high-precision monitoring of rock movements (±10 µm) and temperatures (±20 mK) (Appendix A.3).
- Enhanced data continuity due to efficient system monitoring tools (Appendix A.4).
- Basic data management infrastructure for real-time processing.

Possible further enhancements for a better usability are: i) the integration of data validation in data management infrastructure for better performance; ii) a real-time data visualization and processing; iii) a adaptive (case sensitive) sampling rate, e.g. for summer movements; iv) a data quality assessments in terms of network node interchangeability and system generated values (time stamp ect.); v) a deployment mode with connectivity and sensor value check to ease installation work. These outcomes and proposed enhancements are discussed in perspective of their application in rock instability research and monitoring in section 7.3.

4 Thermal conditions of steep bedrock permafrost

Energy exchange processes with the atmosphere drive the subsurface temperatures in steep bedrock. The surface and near-surface characteristics are the interface of this energy exchange and lead to significant spatial variability on a decimetre to decametre scale. The permafrost temperature of fractured bedrock in steep but rough rock faces are likely some degrees lower than current estimates that are based on rock surface temperatures measured in near-vertical, smooth rock sections. This difference is mainly caused by cleft ventilation and snow albedo and is expected to be largest for radiation-exposed faces with open fractures or long-lasting thin snow cover. The strong sensitivity of the albedo effect to spring and summer snowfall is relevant for climate impact on steep bedrock permafrost.

4.1 Surface temperatures in steep bedrock

Subsurface temperatures in intact near-vertical bedrock are directly coupled to the atmosphere due to the absence of snow cover and minor non-conductive effects in the near-surface layer. Correspondingly, ground surface temperatures (GSTs) measured in near-vertical rock walls with systematic aspect variation were used to validate energy balance models (Gruber et al., 2004b). Such physically oriented models are driven with meteorological data and capable to extrapolate the mean annual GST (MAGST) in time and space for locations with similar surface characteristics. They are applied to estimate the topographic distribution of permafrost in steep bedrock (FOEN, 2006; Noetzli and Gruber, 2009). For the field site at Matterhorn (3500 m a.s.l.) this estimate is +1 °C for the south face and –6 °C for the north face with 60° slope angle (Noetzli and Gruber, 2009). Gruber et al. (2004b) pointed out, that in non-vertical rock slopes snow and debris cover might lead to more complex thermal conditions and further investigations are needed to simulate temperatures realistically. A recent study on mountain permafrost in gently steep terrain reveals a large variability of the MAGST on heterogeneous surfaces within meters (Gubler et al., 2011). This underlines the necessity to consider small-scale variability for the estimation of rock face temperatures because these faces also often are extremely heterogeneous.

Publication III addresses this MAGST variability with spatially distributed rock temperature measurements. The small number of different measurement locations does not allow for a quantitative analysis, but the results show a possible range of the variability and provide a semi-quantitative understanding of the relevant processes: A thin but prevalent snow cover in steep faces at high elevation has a net cooling effect of several degrees in comparison with snow-free

bedrock (cf. also Pogliotti, 2011). In our measurements, this difference was in the order of 3 °C for the south faces at Matterhorn and Jungfraujoch (Figure 7). The roughness (micro topography) of the rock surface not only leads to snow retention, but also to local shading (e.g. jj03), which increases the small-scale temperature variability. Both effects reduce the influence of the incoming radiation on the surface energy balance. Snow retention has an additional cooling effect by latent energy consumption when melted by the warm rock. In our data, the systematic cooling effect of snow appears to be more effective than local shading (compare e.g. jj01 and jj03).

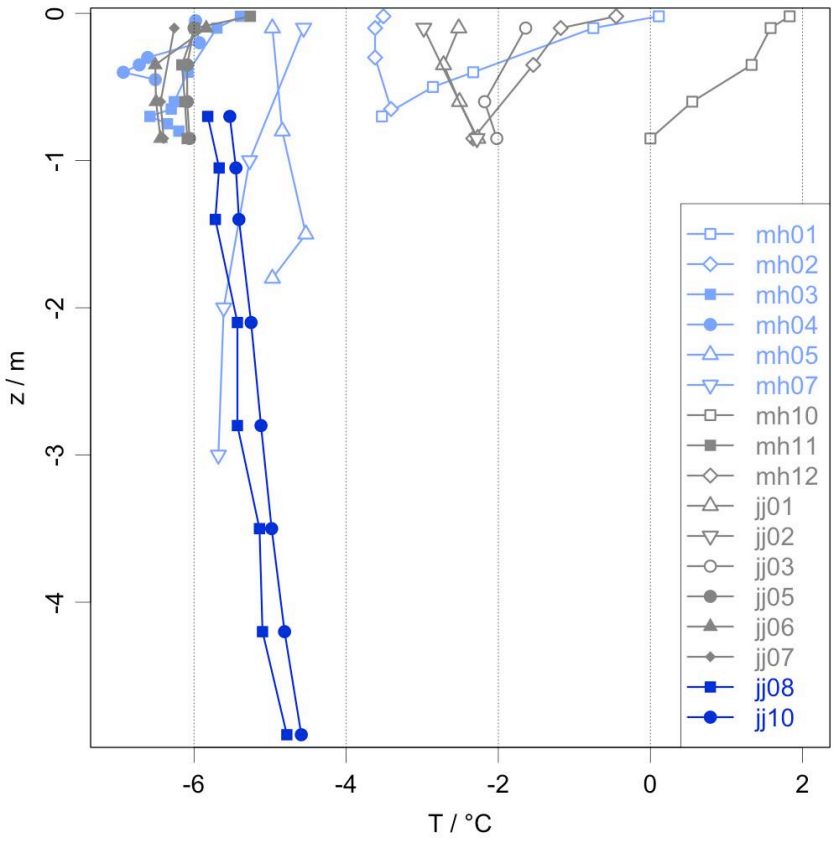

Figure 7: *Depth profiles of mean annual temperatures (MAT) in clefts (light blue), rock (grey), and ice (dark blue). Solid symbols stand for aspects NW to NE (shadow) and contour symbols for aspects E to SW (radiation-exposed); mh indicates Matterhorn and jj Jungfraujoch locations. The profiles mh02, mh05, jj01, and jj02 are often snow covered. Thermal variability is significantly smaller at shaded locations. Snow covered locations (mh02, mh05, jj01) are colder than snow free rock (mh01, mh10) with similar orientation (from Publication III).*

4.2 Near-surface processes and thermal offsets

Studies on the thermal conditions in a coarse debris near-surface layer describe a cooling of the subsurface due to air circulation in voids (e.g. Harris and Pedersen, 1998; Goering, 2003; Hanson and Hoelzle, 2004). A similar offset between MAGST and mean annual ground temperature at depth (MAGT) results from variable thermal conductivity of frozen and unfrozen ground material (Goodrich, 1978; Burn and Smith, 1988). This "thermal diode" effect is highly relevant for arctic soils with high water content and may also play a role in porous or fractured bedrock (Pogliotti et al., 2008). Further, the ventilation effect is expected to be important on debris covered (flatter) sections of high alpine rock faces (Gruber and Haeberli, 2007).

In Publication III we found that this ventilation effect is also significant in fractured bedrock: Cleft temperatures and offsets of the MAGT within the shallow boreholes (sensor rods, section 3) at Matterhorn, indicate cleft temperatures 2–4 °C and surrounding rock by 1–3 °C lower than GST (Figure 7; mh01, mh06/mh12). The effect is less pronounced at shadow locations and where clefts apertures are small (< 2 cm). Other non-conductive effects such as heat advection by percolating water or thermal diode effects could not demonstrate a significant effect on MAGT with our field data. However, Gerber (2010) demonstrates short-term and local thermal disturbance by advection in our field data (Appendix A.6). The hydro-thermal interactions and cleft ice evolution on a centimeter to decimeter scale are further discussed in Chapter 5. Thermal diode effects where estimated to be smaller than 0.5 °C in intact rock by some basic numerical experiments (Appendix A.7). In fractured rock with small cleft aperture this effect may be larger considering variable water content for the estimate of thermal conductivity.

4.3 Permafrost temperature and distribution

Permafrost temperature and distribution in steep bedrock is mainly determined by topography and corresponding meso-scale variability (decameter–km) in surface temperature (Wegmann, 1998; Gruber, 2005; Noetzli, 2008). Small-scale variability (dm–decameter) is important, because it systematically affects this general pattern and because it may be a key for the understanding of rock instabilities in steep bedrock. This potential role of heterogeneity for rock fall release will be discussed in Chapters 5 and 6. Here we focus on the findings that concern the general thermal conditions in steep bedrock.

Snow retention and ventilation in clefts both lower rock temperature (Figure 8). Both are most effective in radiation exposed faces, because they reduce the heating by short wave radiation. This is obvious for snow (higher albedo) but for the ventilation the dependency on radiation needs some explanation: Open clefts extend the surface available for sensible heat exchange but not for radiation. That is, the energy exchange between the atmosphere and the near-surface layer containing clefts (as an extreme case of roughness) is to a higher degree controlled by sensible heat fluxes than on flat surfaces. This shortcut of the atmosphere with the lower rock is shown in Figure 8. Radiation-exposed rock faces are in average cooled by ca. 1–3 °C when highly fractured (apertures > 2cm) or retaining snow due to their slope angle and surface roughness.

Based on these findings, permafrost distribution in Switzerland is expected to extend to lower elevations than current estimates (FOEN, 2006) in radiation exposed rock faces. This lowering could be in the order of 200–500 meters. For a rough estimate of the lower permafrost limit (Section 7.3) a lowering of 300 m was assumed. More important may be the altered climate sensitivity introduced by these effects. Salzmann et al. (2007) suggested a lower sensitivity of MAGST in south exposed rock faces compared to north faces based on surface energy balance modeling. The study, however, does not take into account snow and fracturing. The strong dependence of the here described snow cover effect from snowfall in the season with most irradiation (Publication III), may lead to an higher sensitivity on climate change in radiation-exposed rock faces.

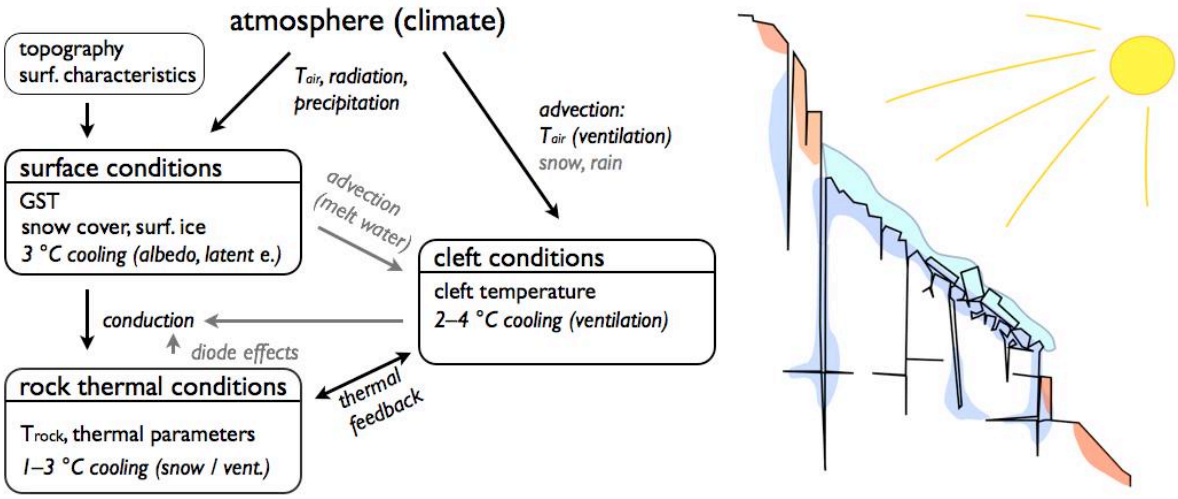

Figure 8: *Thermal conditions in radiation-exposed, steep, fractured bedrock. Left: Conceptual model of interactions between atmospheric conditions and rock temperatures at depth; estimations of the net cooling effects with respect to snow free surfaces are given (see Publication III); in grey, processes with a minor thermal influence (±1 °C) are indicated. Right: sketch of rock temperature variability with cooling below snow and beside clefts (blue) and warming at snow free rock surfaces (red).*

5 Cleft ice and hydrothermal processes

Water percolating into cold fractured bedrock can rapidly increase temperatures at depth by the release of latent heat due to ice aggradation (freezing). Advective sensible heat supplied by positive water temperatures can further warm rock and erode cleft ice (melting). For constant climatic conditions these two processes of ice aggradation and erosion may balance each other throughout the year. Studies conducted by numerical and physical modelling show that this equilibrium is highly sensitive to changes in the timing, magnitude and temperature of melt water production. Further these model results point out, that even cold permafrost is sensitive to advective thawing progression and can rapidly modify local thermal conditions within clefts.

5.1 Basic processes

Hydrothermal processes comprise sensible and latent heat exchange by water. For the active layer of permafrost soils in rather flat areas diverse studies on these effects exist (cf. Kane et al., 2001; Boike et al., 2008). The most important processes are latent heat release by percolating water, zero-curtain effects due to phase change of (often imobile) water, sensible heat transport by pore water flow and latent heat transport by water vapor (e.g. Boike et al., 1998; Ishikawa et al., 2006). Variable thermal conductivity (Goodrich, 1978) is important in many cases and often referred to as a non-conductive process but it does not fall under the above definition of hydrothermal processes. The importance of the hydrothermal processes depends on the hydraulic conditions and the pore characteristics of the respective active layer. For highly permeable active layers in alpine debris slopes two recent studies conclude that the existence of macro pores and the low saturation lead to percolation along preferential flow paths and to large latent heat input at depth during snow melt (Rist, 2007; Scherler et al., 2010). Similar enhanced warming at depth was observed in dry sandy active layers in Mongolia (Ishikawa et al., 2006). The active layer of steep fractured bedrock with open clefts is highly permeable too and is expected to experience a similar process. Additionally, the flow of water on warm rock surfaces prior to percolation may lead to large sensible heat input. The permafrost body is often considered as an aquiclude, but temperature measurements in a rock glacier prove that this is not strictly the case (Vonder Muehll, 1992). If similar permeable taliks (or unsaturated thawing coridors) exist in steep fractured bedrock permafrost is not clear. In Publication IV we consider the case of an ice-sealed permafrost table that leads to a lateral runoff of the percolating water, similar to the situation reported by Rist (2007).

Thermal interactions between water in cleft systems and rock have been addressed in the context of geothermal heat exploitation (e.g. Kohl et al., 1995) and nuclear waste storage (e.g.

Muralidhar, 1990). For the active layer in steep bedrock we assume such an unsaturated cleft system but we consider phase changes in addition. Models of the thermal erosion of intra- and sub-glacial channels (Röthlisberger, 1972; Nye, 1976) consider the heat flux and phase change at the interface between water flow and an ice body similar to situations in clefts. Their focus on energy fluxes, not explicitly resolving flow conditions, is adopted in Publication IV. However, in contrast to sub-glacial channels the internal heat production of the fluid becomes negligible compared to the advected sensible heat in rock clefts. The conceptual model of advective heat transport in fractured steep bedrock formulated in Publication IV is illustrated in Figure 9 with a single idealized cleft. The advected heat may be latent or sensible. The former is the case if aggradation occurs and the latter if the water is >0 °C. Conversely, the sensible heat transported to the ice level (z) by conduction or advection degrades the cleft ice and leads to latent heat absorption. If this melted water runs of, latent heat is exported out of the system. As the case in unfractured rock, heat input also results in a warming of the rock and corresponding changes in liquid water content (Figure 9).

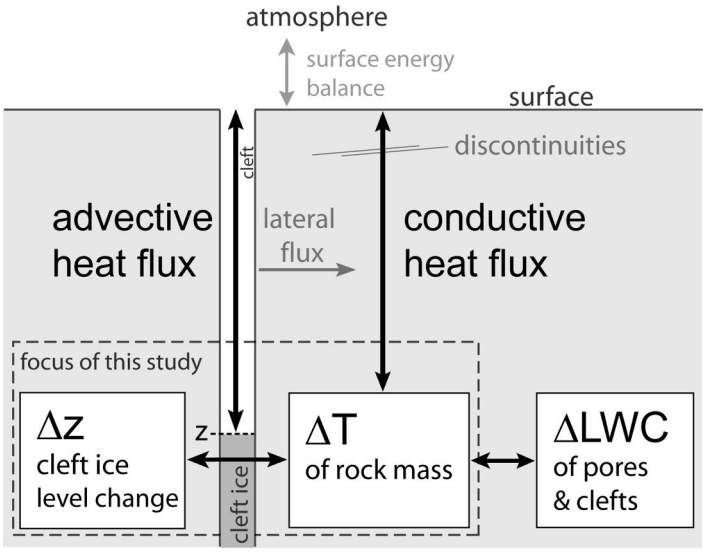

Figure 9: *Conceptual model of the hydrothermal processes in a partly frozen rock cleft (from Publication IV).*

5.2 Quantification in a single cleft

With laboratory experiments and numerical simulations, a first quantification of the heat fluxes resulting in ice erosion and rock warming was performed (Publication IV). This study suggests that the larger part of the sensible heat advected by water percolation from the surface to the cleft ice level results in latent heat consumption by erosion of the cleft ice (Figure 10). During the first minutes to hours (stabilization time) of this percolation, the rock is warmed due to latent heat released by ice aggradationand preconditions it for later erosion. This initial aggradation and depends on the rock temperature and the applied advective heat flux. From field measurements of snow melt water running over the rock surface (Appendix A.5) we know that the advective heat input is extremely variable and heterogeneous. The main controlling factors of advective heat input are the availability of melt water, incoming radiation and flow path length prior to percolation.

The numerical model was calibrated to fit the observed ice erosion rates. In the following both, rock warming and initial aggradations of cleft ice corresponded well with the observations from the laboratory. With a systematic variation of applied advective heat and the initial rock temperature (Figure 10; Trock) we postulate a simple dependency of the ice erosion rate (mm/min) after stabilization on these two variables:

$$\frac{dz}{dt} = 0.05 + 0.02 \cdot P_{wat} + 0.1 \cdot T_{rock} \quad (1)$$

P_{wat} is the released sensible heat of percolating cleft water per unit length (W/m) and T_{rock} the initial rock Temperature (°C). This approximation is valid for cleft widths in the order of 0.6–1 cm. For larger clefts similar heat input results in smaller erosion rates because more ice volume in the cleft needs to be eroded. The following relation for stable cleft ice conditions dependent of negative rock temperatures may be derived from (1):

$$P_{stab} = \frac{-0.1 \cdot T_{rock} - 0.05}{0.02} = -5 \cdot T_{rock} - 2.5 \quad (2)$$

P_{stab} is the heat input at which the ice level is approximately stable in Watt per unit length of the cleft (W/m). If the heat input is lager, erosion occurs, for smaller heat inputs aggradation prevails. Because this equilibrium is sensitive to small changes in cleft and ice geometry, (2) gives the order of magnitude where this equilibrium is but not an exact value. However, this equation may allow a estimate if the respective advective heat input results in significant ice erosion or not.

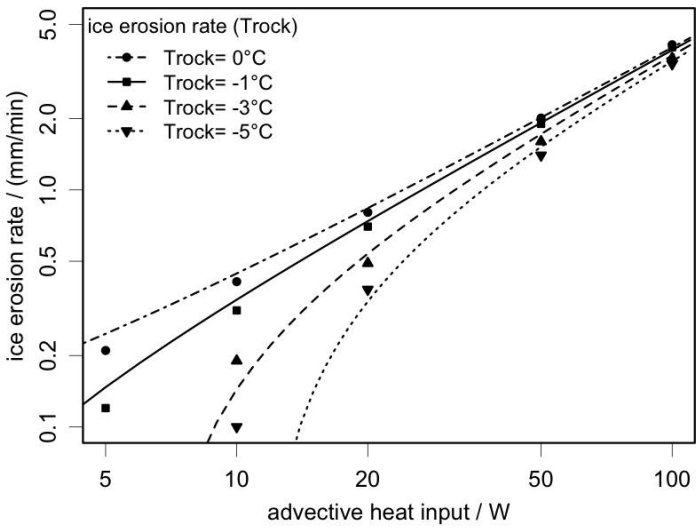

Figure 10 *Modeled ice erosion rates (points) with linear approximation according to (1) (lines) for different rock temperatures (legend) in an 8 mm wide and 0.5 m long cleft.*

A second set of experiments with variable advective heat input was performed to assess the effect of this more realistic advection (Publication IV). Short-term variability has almost similar effect as its temporal average with slightly more erosion and less heating of the surrounding rock. For long cycles in combination with a warming at the surface (conductive heat wave simulating thawing season) the timing of advective heat input is decisive for the ice erosion. This is because the amount of initial aggradation depends on the progression of the heat wave. For small heat inputs used in the laboratory, the ice level tends to stabilize at a level where aggradation and erosion of an entire cycle balance each other. However, if the heat input is large enough to cause net erosion even without the conductive heat wave, progressive erosion into the permafrost body may occur over the years.

5.3 Application to fractured steep bedrock

Scaling and generalization

To transfer these findings to the field two problems need to be considered: i) scaling of these processes; ii) generalization of the findings from laboratory to natural systems. The scaling issue was addressed in Publication IV with numerical experiments for clefts of large diameters on the basis of two different cleft sizes considered in the laboratory. For larger clefts more advective heat input for a similar erosion rate is needed. This scaling is almost proportional to length dimensions. Hence, the surface available for heating up melt water is proportional to the energy needed for the same absolute erosion if cleft length and width are up-scaled accordingly. For very large clefts not all the ice may be eroded and channels within the ice may develop. Further, in some cases percolating water may be trapped and slowly freeze.

For a network of fractures with various cleft sizes the basic processes correspond to the here described setting, but the feedbacks between small and large clefts as well as other geometric effects may lead to large variability of the efficiency of water advection within the cleft system. The model and parameterizations presented in Publication IV are, hence, not an instrument to predict cleft ice evolution generally but allow to asses the sensitivity on different meteorological and climatic conditions if combined with respective input data (Chapter 7).

Hydrothermal processes and their influence on near-surface temperatures

In the near-surface layer advective heat input by percolating water is combined with a conductive warming. In the shallow boreholes at Jungfraujoch we could detect latent heat release by the freezing of water after initial percolation. One example of this is given in the supplementary material (Appendix A.6). However, the thermal effect of this advection on the mean annual temperatures is small (compare publication III). This is because of the ice aggraded in the active layer is melted a few weeks after and, hence, has no large net effect on the temperatures. Within the clefts at Matterhorn, similar latent heat release in the early melting season can be observed (Appendix A.6). The effect of sensible heat release by warm water percolating into clefts was not detected in the field data. This effect is more difficult to distinguish from other thermal effects (conduction, warm air advection) and depends very much on the sensor position (very close to significant runoff).

The measurable thermal influence of advection of water percolating into the cleft system is, hence, a short-term and localized modification of the temperature field first of all (Figure 11). The erosion of the cleft ice instead consumes a large part of the applied energy. The net ice erosion (erosion–aggradation) depends on the near-cleft rock temperature (Figure 11). Significant disturbance of the ground temperatures attributed to water advection in rock was postulated by Krautblatter (2009) on the basis of indirect methods such as ERT-sounding. Such effects are likely where large amounts of melt water percolate in a cleft, however the geophysical method is sensitive on both, rock temperature and water table within the clefts.

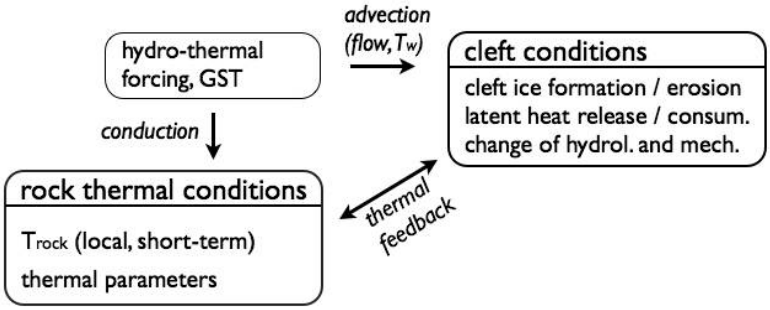

Figure 11: *Interaction between rock thermal conditions and cleft conditions if forced by hydro-thermal heat input and ground surface temperature.*

Hydrothermal processes and their influence on cleft conditions

Regarding the hydrological and mechanical cleft conditions the influence of hydrothermal processes may be far more important. If latent heat is released, the local warming may affect the temperature dependent mechanical strength of the cleft (Section 6). This is possibly not restricted to an ice level such as assumed in Publication IV and may be combined with the build up of hydrostatic pressure in the melt season. That would require an incompletely ice-sealed permafrost body. Three possible settings may be considered: 1) thin fractures between cleft ice and rock due to thermal contraction of rock and ice (ice wedging theory applied to rock); 2) fracture development due to gravitational creep processes; 3) hydro-thermally eroded channels that have no water retained to refreeze during cold season. The initial development of 3) may be combined with 1)+2). Observations of leakage of cold water (<1 °C) through minimal fissures in the laboratory indicate that the self sealing of water under pressure is limited to very small fissures in cold rock. This limit of ice sealing may be estimated with simple model studies comparable to the numerical modeling in Publication IV. However, the development of preferential flow paths within the ice may complicate this situation. Observations of enhanced water seepage in tunnels at Jungfraujoch (cf. Gruber and Haeberli, 2007) indicate the existence of water flow along clefts (*micro talik* if it remains unfrozen or *active drainage channel* if cleft walls are <0 °C if dry) in warm permafrost bedrock. The rock movements described in the next section point in a similar direction.

6 Kinematics of steep bedrock permafrost

Rock movements at Matterhorn (Swiss Alps) show two distinct temporal patterns: First, a previously-described cleft opening that is negatively correlated to temperature, and second, for some locations an enhanced opening and shearing during summer that is novel for kinematical measurements in permafrost bedrock. The fast reaction of both processes to the near-surface conditions points toward a high importance of thermo-mechanical stress propagation through the rock mass and hydro-thermal weakening of mechanical cleft strength.

6.1 Movement patterns in bedrock permafrost

A limited number of previous field studies on rock movements in bedrock permafrost and its active layer exist (Wegmann and Gudmundsson, 1999; Matsuoka, 2001a; Matsuoka, 2008; Nordvik et al., 2010;). All these publications report cleft expansions that are negatively correlated to (rock-) temperature, but on different time scales (diurnal to annual) and with differing superimposed linear trends. Similar movement patterns have been observed at some non-permafrost sites (Watson et al., 2004; Gischig et al., 2010). Some of these measurements where performed with crack dilatation measurements at the surface, similar to our setup (Matsuoka, 2001a; Matsuoka, 2008; Nordvik et al., 2010), while others applied extensometer and inclinometer measurements in boreholes or remote sensing methods. The inverse dependency on annual temperature fluctuations is common to all these datasets based on different methods and measured at different depths or at the surface.

At Matterhorn-Hörnligrat we recorded cleft dilatations and shearing since summer 2008 at six arbitrarily selected large clefts in and around the detachment zone from a rock fall event in summer 2003. This deployment was extended in summer 2010 to include cold and warm conditions at larger distance from the ridge (see Chapter 3 and Publication V). Even though these ten independent point measurements are a small sample in a system with many degrees of freedom, the similarities of these time series with each other and with earlier measurements in bedrock permafrost, however, supports an interpretation of this data as characteristic for permafrost bedrock: During most of the year, the cleft expansion is negatively correlated to the rock or cleft temperature with an occasionally increased expansion rate in autumn (Figure 12). Contrary, opening occurs at two clefts in summer when minimal cleft aperture would be expected according to this negatively temperature-correlated pattern. The initiation of this summer opening is synchronous with snow melt and stops with the first intense freezing (Figure 12). Significant shearing activity is restricted to this time span as well. The response of both movement types to the near-surface thermal conditions has a delay of hours to a few weeks.

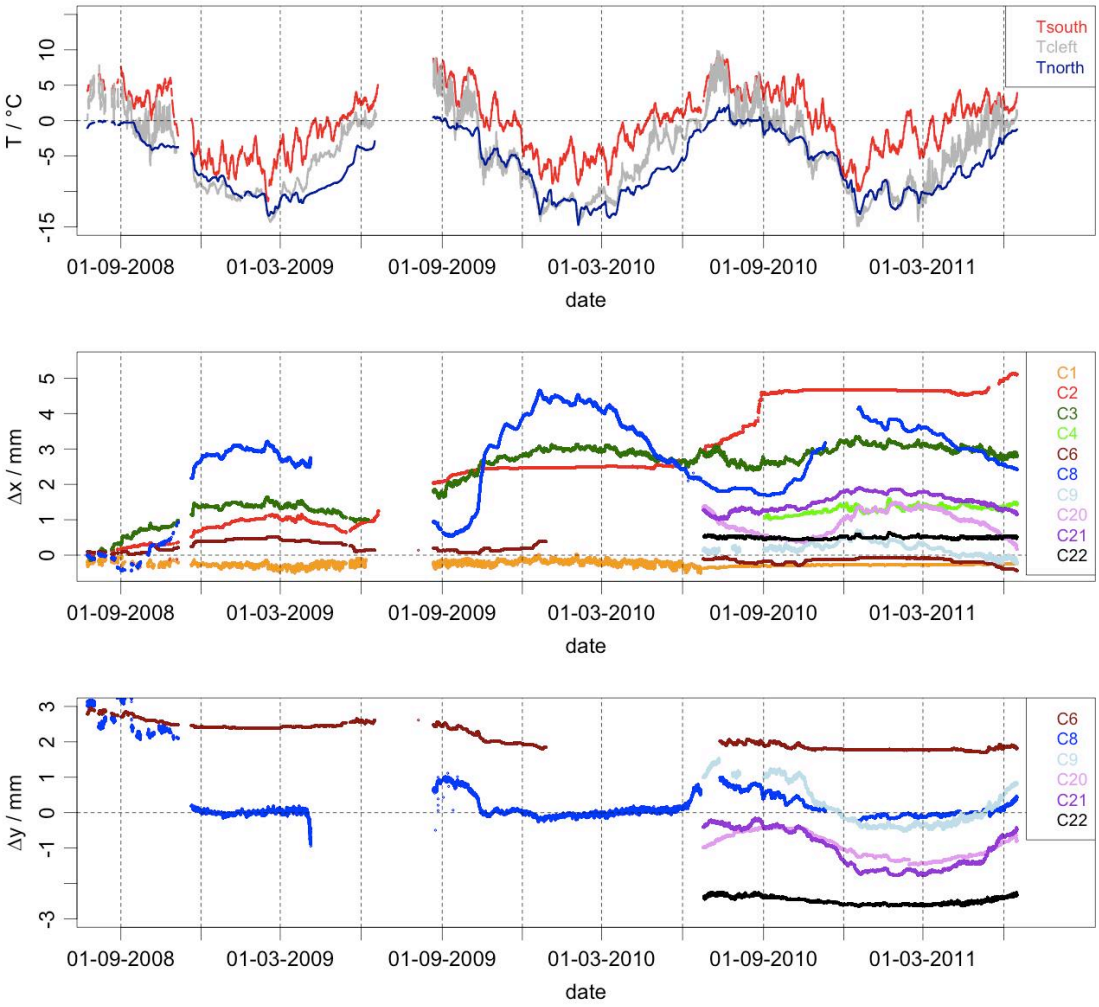

Figure 12: *Overview of the thermal conditions (T) and cleft movements (Δx = expansion and Δy = shearing for the different clefts C1 to C22) at Matterhorn-Hörnligrat. Update of Figure 6 in Publication V with latest 4 moths of data. This new data clearly supports the hypothesis of reduced shearing activity in winter (or enhanced activity in summer (Publication V)).*

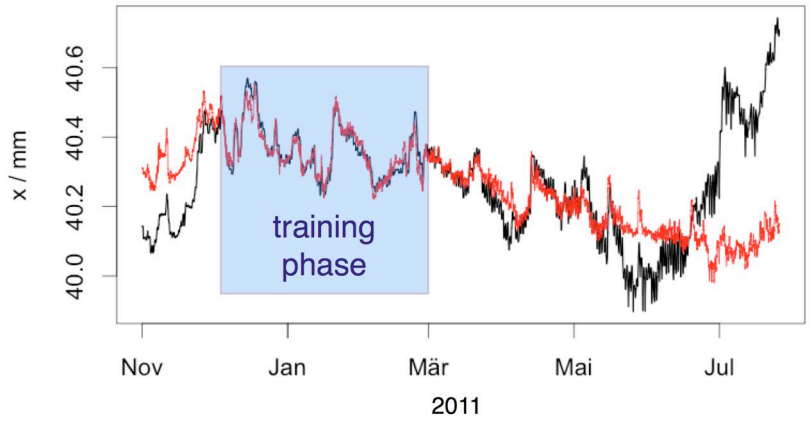

Figure 13: Example of cleft expansion prediction by a multiple linear regression model (for C3). Black: measured deformation; red: modelled deformation. The blue box indicates the time series that was used to fit the regression model. The difference between model and observation increases mid May when positive cleft temperatures occurred (compare Figure 12).

The negative correlation to rock temperatures at different depth may be analysed with a multiple linear regression model. A modification of the crackmeter regression model of Nordvik et al. (2010; Equation 6) with a smoothed temperature instead of a sinusoidal explanatory function may reveal a large temperature dependence of periglacial cleft movements:

$$y_{i,k} = \beta_{0,k} + \beta_{1,k} \cdot t_i + \beta_{2,k} \cdot T_{short\_k,t_i} + \beta_{3,k} \cdot T_{smooth\_k,t_i} + e_{i,k} \quad (3)$$

where $\beta_{0,k} - \beta_{3,k}$ are the unknown regression parameters for a cleft (k), t_i is the time, T_{short_k,t_i} is the high-pass filtered cleft temperature at t_i, T_{smooth_k,t_i} is the low-pass filtered (e.g., 30-days running mean) cleft temperature at t_i and $e_{i,k}$ is the residual. Instead of the filtered temperatures the use of surface temperatures and temperatures at some meters depth could provide comparable results. An example of such a statistical cleft expansion model is given in Figure 13.

6.2 Driving processes

In the problem statement of this thesis studies on temperature dependent geotechnical properties of rock and frozen clefts where listed. The findings and theories of these laboratory studies are the basis for the interpretation of the rock movements of the current study (Publication V). In Publication V we postulate that:

i) The negative temperature-correlation is caused by thermo-mechanical forcing and is reinforced by cryogenic processes during the freezing period.

ii) The enhanced movement in summer originates from hydro-thermally induced strength reduction in rock fractures containing perennial ice.

The first hypothesis i) suggests that ice segregation through the inter-cleft rock mass is not the driving process of seasonal cycles in periglacial rock movements such as assumed in earlier studies (e.g Wegmann and Gudmundsson, 1999). Empirically, this is based on the fast reaction of all cleft movements on signals in near-surface temperature record and the continuation of this negatively temperature-correlated cleft dilatation at some clefts during summer (strongly positive temperatures). Theoretically, the large expansion rates do not correspond with the low permeability of the rock types in the field (cf. Matsuoka, 2001b). This hypothesis also suggests to rethink the "field evidences" for ice segregation: Seismic/acoustic emissions in fractured rock (e.g. Amitrano et al., 2010) could possibly origin from thermally forced ruptures in the ice-cemented celfts and not from segregation such as the case in porous rock (Hallet, 1983, Hallet et al., 1991).

For the observed coincidence of enhanced shearing and summer expansions with melt water infiltration (Figure 12), hydrothermal influence on the cleft conditions (ii) is the most likely explanation. This may be explained by the latent heat release and hydrostatic pressure built-up in clefts sketched in Chapter 5. The detailed mechanism leading to the cleft strength decrease with temperature is rather not linked to strength reduction of the pure cleft ice alone (e.g. Davies et al., 2001; Ladanyi, 2006) because ductile deformation rates in ice are likely to exceed the observed deformation rates under gravity driven stresses. Instead, a temperature dependent weakening of the rock-rock contacts of clefts such as e.g. suggested by Krautblatter (2009) and

the hydrostatic influence are more likely explanations of this strength decrease (Publication V). However, short-term stresses (earth quakes, thermally induced stresses and stress peaks of a stick-slip cleft movement (Scholz and Engelder, 1976; Faillettaz et al., 2010) may be absorbed by ice infill. An understanding of the strength reduction of ice-cemented clefts with rock-rock contacts may be derived from an analogy with compressive triaxial experiments with ice saturated debris where friction at rock-rock contacts is an important determinant (Arenson and Springman, 2005). Tensile and shear strength experiments for such rock ice mixtures might give more insights in the future. Further situations with low ice content and significant rock-rock contacts (Ladanyi, 2006) may be combined with water supply in experimental setups.

Figure 14 sketches these process interactions between rock mass, cleft conditions and rock kinematics. Hypothesis i) is expressed by the stress change that results from thermal expansion of the rock mass (Figure 14). The resulting quasi elastic deformation depend on the geometrical setting of the discontinuities and the topography, however they show common patterns at different sites. Hypothesis ii) contains the strength reduction of the cleft (left side) and possibly the rock strength reduction of near-cleft rock (cleft surface) and inter-cleft rock bridges. The rock strength reduction is influenced by thermal feedbacks between cleft and rock mass (Figure 14): Advective heat input may cause a fast response of this rock strength and corresponding deformations. Positive feedbacks between deformations (cleft geometry change), hydraulic permeability of the clefts, and cleft strength reductions could be important for the acceleration during the thawing season.

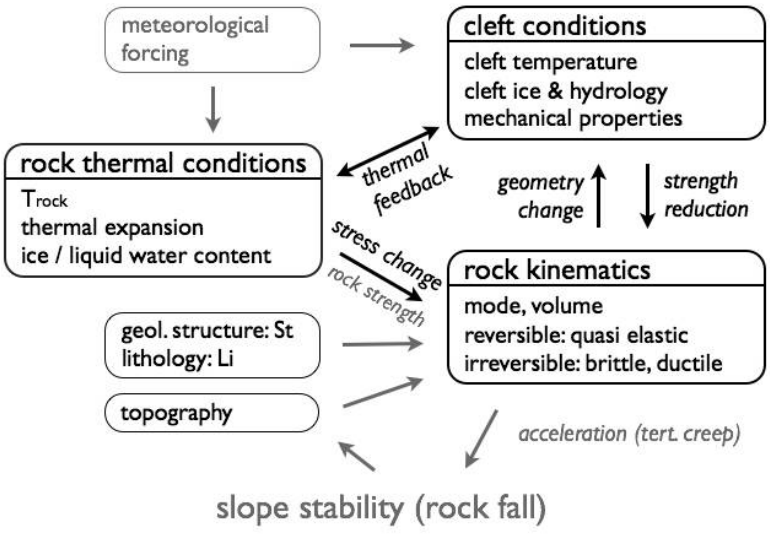

Figure 14: *Process interactions between thermal conditions in rock, temperature dependent cleft conditions and rock movements.*

7 Synthesis

The driving mechanisms of the enhanced opening and shearing observed in the field may be similar to those involved in the release of warming-related rock fall. In this chapter, process interactions proposed in the previous chapters are synthesised to a conceptual model of climate – rock fall interactions. Based on this, possible ways to delimitate permafrost-related rock fall in time and space are sketched. Finally, the possibilities to monitor critical rock sections with modern monitoring techniques developed within the project PermaSense are outlined.

7.1 Process interactions of permafrost-related rock instabilities

Within the three previous chapters the thermal conditions, the hydrothermal interactions and the mechanical response to meteorological forcing in steep bedrock permafrost and the active layer were sketched (Figure 8, 11, 13). Figure 15 is a synthesis of these figures and outlines possible interactions between climate and rock fall. The figure translates the influencing factors of slope stability and their interactions in high-alpine rock faces (Fischer and Huggel, 2008) to physical processes. Glacier debuttressing or additional loading by increased accumulation on hanging glaciers (e.g. more wet snowfall) are not represented in Figure 15. These situations can be detected by monitoring of glacier changes and are expected to have larger response times.

From Chapter 4 we conclude that ground surface temperatures (GST) and near-surface rock temperatures in steep bedrock are not influenced by air temperature and radiation alone, but are significantly lowered by air ventilation in clefts and snow-cover (Figure 15). From Chapter 5 we summarize that percolation of melt water into the cleft system causes local and short-term thermal anomalies and modifies of the cleft ice geometry and hydrological properties. Changes in melt water infiltration affect cleft systems even in cold permafrost and the thermal feedback from rock to cleft ice, e.g. self-sealing of cleft ice in cold rock (Gruber and Haeberli, 2007), is limited to situations with small flow rates. Hence, changes in surface conditions may be more important regarding the cleft conditions than trends in permafrost temperatures (Figure 15). The findings of Chapter 6 suggest that temperature fluctuations of rock masses drive reversible movements by thermal expansion and stress propagation (Gischig et al., 2010). Even though the geometrical setting (structure, topography) defines the spatial movement mode (sliding, toppling) resulting from the thermo-mechanical forcing (Figure 15), the cleft dilatation negatively correlated with temperature is typical for most records from permafrost areas (Chapter 6). In some cases these movements are not completely reversible and contribute to a long-term deformation that could precondition rock failure. In Chapter 6 a second movement regime for the period with presence of melt water and near-surface cleft temperatures ≥0 °C was

identified. The coincidence of irreversible opening with enhanced shearing activity during this periode led to the hypothesis that such regime change is caused by a reduction of the shear strength of the cleft (Figure 15). This strength reduction related to thawing might be the main trigger for rock fall during warm periods from bedrock permafrost and is not restricted to rock temperatures close to 0 °C but may occur even in cold rock if melt water input is exceptionally intense. The timing of exceptional rock fall in summer 2003 as well as the observed liquid water at the failure plain after rock fall events would be well explained by this hydrothermal mechanical interaction. Alternatively, the strength reduction of a cleft could also be caused by conductive warming of the rock (and clefts) from the surface (Figure 15), but this would involve large response times for failure planes at depth. Additionally, the changed topography after a rock fall event causes feedbacks on the surface conditions and stress field and may result in a series of events (Figure 15).

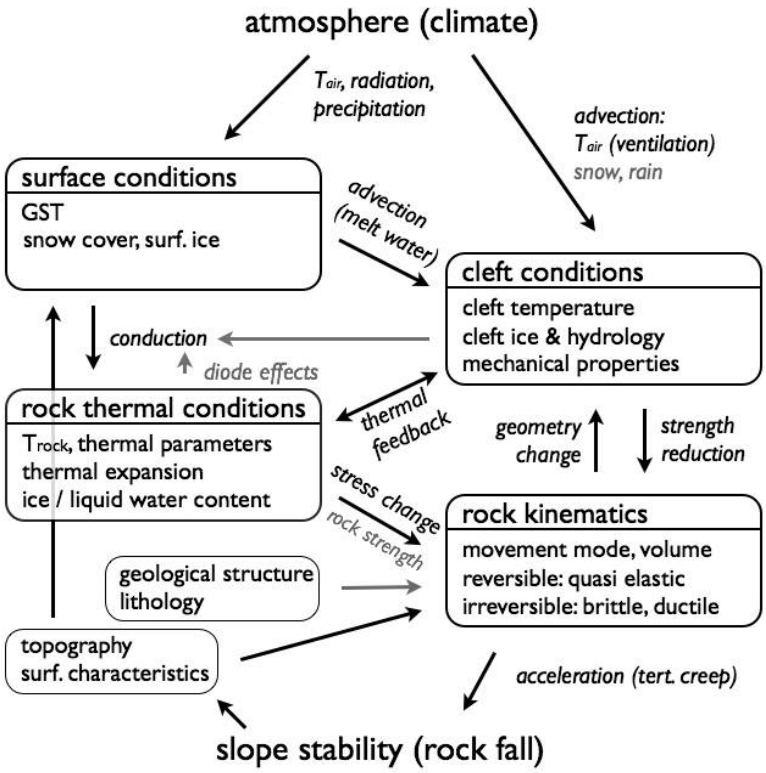

Figure 15: *Conceptual model of the interactions between climate and rock fall in steep bedrock permafrost. In grey are the processes not in the main focus of this study and may be of minor importance for permafrost-related rock fall.*

The sensitivity of the above described thawing-related failure mechanisms to repeated extreme climatic events (e.g. exceptionally warm summers) depends on the recovery of the hydrological cleft conditions and on the evolution of the rock fall predisposition. On one hand the release of most critical situations by a fist extreme event could lower the average rock fall hazard for further events. On the other hand, the drainage channels developed may increase the sensitivity to hydro-thermal triggering processes. Which one of the two effects currently

dominates is not known. Further, we might briefly consider an alternative explanation for the rock fall activity coinciding with extreme warm periods that is consistent with the above described conceptual model, but has not yet been mentioned: In the extreme summer 2003 in the Alps the near-surface layer (1–2 m) was at record temperature since very long time. Thermo-mechanical stresses forced by this surface layer may have been maximal for the past century and could be the cause for the cumulation of rock failures. The consequences from a new extreme hot summer may be different: The near-surface temperatures experienced in summer 2003 would have much less effect because the corresponding stresses have been experienced only a few years before. However, the recorded coincidence of enhanced opening and shearing with cleft temperatures ≥0 °C is not explained by this latter hypothesis.

Summarizing Figure 15, a direct coupling of the mechanical cleft conditions to surface conditions by water advection in melting periods is the main process interaction discovered. In contrast to this fast process, the change of permafrost temperatures modifies slowly the shear strength of ice-cemented clefts and the equilibrium between ice aggradation and erosion in clefts and affects the sensitivity to net cleft ice erosion. Where irreversible rock slope deformation occurs positive feedbacks between hydraulic permeability, cleft strength and rock movements have to be expected.

7.2 Delimitation of rock fall occurrence in time and space

Prototypes of rock fall events

Considering the above sketched systems we can distinguish between conductively controlled and advectively controlled events as *prototypes* of permafrost related rock fall events: a) Situations with little melt water influence with a slow propagation from GST to the mechanical conditions at depth by conductive warming of discontinuities. b) Situations with significant melt water influence with a fast (hydrothermal) signal propagation from the surface conditions to mechanical response within clefts at depths independent from rock temperature. These two prototypes would group the warming related rock falls in two populations with a spatio-temporal pattern that differs from rock fall caused by glacier retreat or other factors (Figure 16):

a) Conductively controlled population: Release timing depends on failure plane depth, hence autumn/winter (maximal thawing depth, permafrost degradation) or all-year activity in warm permafrost (> –1.5 °C) is expected. Rock fall can be roughly delimited in space but not in time.

b) Advectively controlled population: Rock fall occur at or closely after intense thawing events (mainly spring/summer) and is not limited to warm permafrost. Delimitation is possible in time but not in space.

Treating them separately allows to delimit their occurrence in time or space, what would not be possible for the basic population of rock falls in periglacial areas (Figure 16).

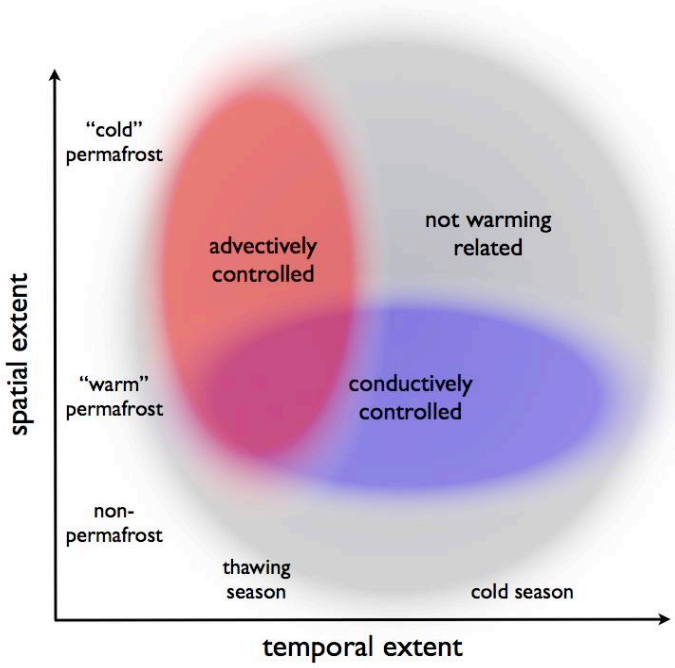

Figure 16: *Hypothetical scheme of two populations (red, blue) of thermally induced rock fall in permafrost areas. The third population (grey) are the remaining rock fall that are not warming related and that are here considered as not delimited in time and space.*

In summary, rock fall is expected all over the year at the lower permafrost limit but is limited to the thawing season in colder permafrost (Figure 16). In addition, there are events that are triggered by other factors (Fischer and Huggel, 2008) and do not obey this spatio-temporal pattern (Figure 16). Strong rainfalls as possible trigger is important in the sub-periglacial environment, which overlaps in the periglacial zone with hydrothermal effects. Rainfall can be excluded as possible triggers at high elevation in the cold season. Seismic triggers and stress changes due to temperature variations do not have these spatio-temporal limitation. They are less variable in time and space and can be seen as background noise to an increasing event frequency and spatio-temporal concentration of the events postulated here. Stress field modification due to glacier retreat or other changes of the surface ice are another important factors of rock fall release in permafrost areas (Fischer et al., 2006; Haeberli et al., 1997). Interactions of the surface ice with the thermal state of the adjacent rock combine this direct effect on the stress field with thermal releasing mechanisms. Events controlled by these complex interactions may also deviate the two sketched populations.

Approach for spatial delimitation

A first test of the above hypothesis with the PERMOS rock fall inventory considering all recoded rock fall events since the little ice age (1850) and larger than 1000 m^3 (PERMOS, 2010) reveals a dependency of the autumn and winter rock falls on aspect and elevation as a rough proxy for permafrost temperature (Figure 17). For the entire population no correlation between aspect and elevation is visible (Figure 17; top). However, autumn/winter events do not

occur in the northerly oriented slopes at high elevations (Figure 17; bottom). The two events that deviate from the expected pattern are likely not in permafrost (2100 m a.s.l., southeast and west). In the future analyses of rock fall inventories regarding the modeled permafrost limits or temperatures (Noetzli et al., 2003; Naegeli, 2010; Ravanel et al., 2010; Fischer et al., 2011) and the seasonal temperature evolution may support the proposed correlation of cold season rock fall with the lower permafrost limit. If this hypothesis holds true, this may allow to spatially delimit the probability of conductively controlled rock fall from steep high-alpine bedrock.

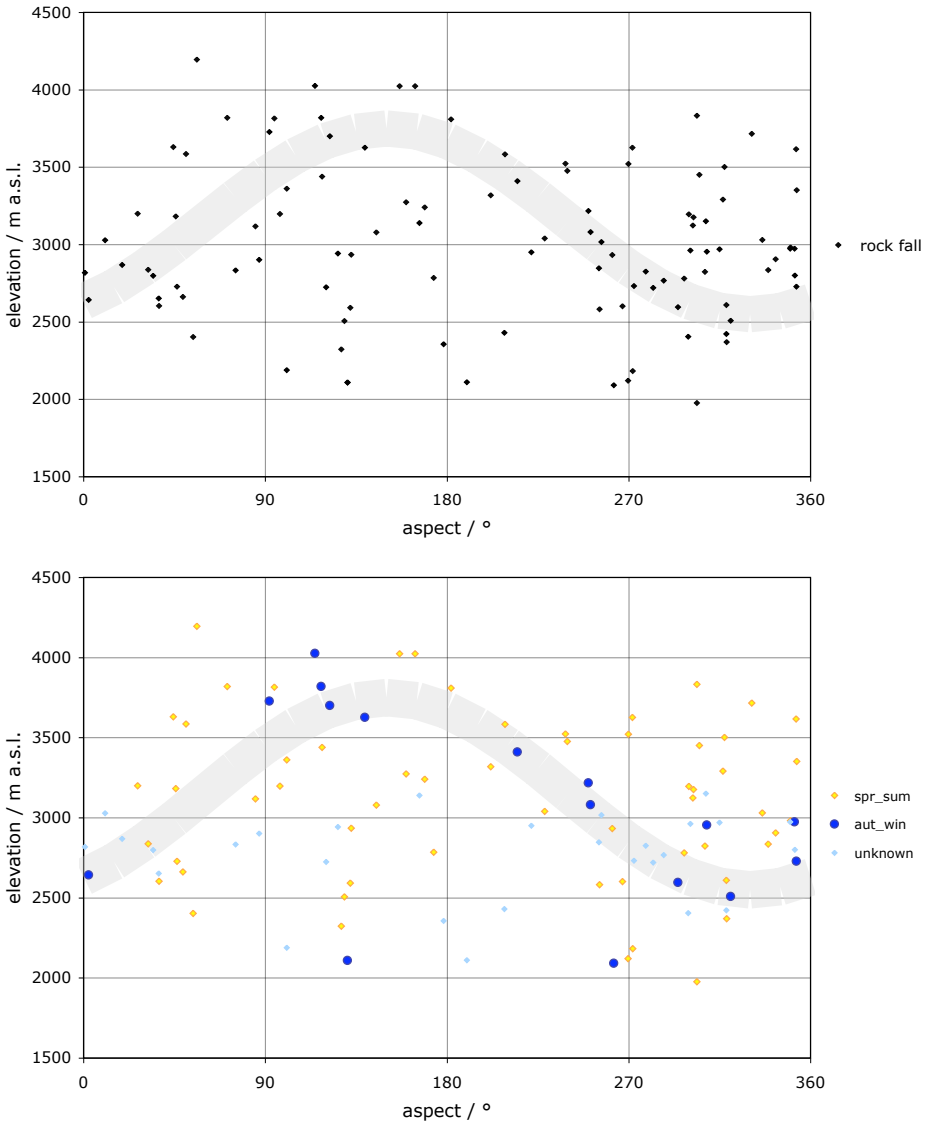

Figure 17: *Elevation-aspect distribution (degree clockwise) of Alpine rock falls (data from PERMOS 2010) and approximate lower permafrost limit (gray) for rock permafrost in the Alps (estimated according to Chapter 4 and Publication III). Top: basic population; bottom: separated by season; spr_sum = March to August; aut_win = September to February.*

Approach for temporal delimitation

The advectively controlled population can be delimited to the time during or after intense melt water production. Analysis of surface conditions near the release area may reveal typical temporal patterns prior to events. Looking at available temperature and precipitation time series from the pre-failure weeks and their inter-annual variation (Huggel, 2009; Fischer et al., 2010; Huggel et al., 2010) are attempts into this direction. However, the analysis of air temperatures is likely not sufficient because of the influence of radiation on snow melt. The comparison of boulder fall activity with in-situ surface temperature records showed a delay of 5–15 days with respect to snow melt in the releasing area (Matsuoka and Sakai, 1999). Even though the processes and time scales are not necessarily the same for larger rock masses, a similar analysis could be performed on the basis of distributed GST records: A set of GST time series from comparable topographic situations for different surface characteristics would provide a more realistic representation of the melt conditions in the release area even if they are extrapolated over large horizontal distances (compare e.g. Jungfraujoch and Matterhorn) than an extrapolation of air temperatures. The setup of GST measurements at variable surface types in rock faces within the past years allows a corresponding analysis for recent rock falls. Physically based models including snow cover and melt in steep rock (Pogliotti, 2011) will provide an additional basis for such analyses. Possibly, patterns in the deviation from the average seasonal evolution of the GST and snow-melt may be observed for pre-failure time periods. This would allow to delimit advectively controlled rock fall more precisely than when considering the whole warm period (spring, summer) as done in the previous chapter. However, a temporal delimitation based on these approaches is always of limited precision and contains uncertainties due to different reaction times and sensitivities caused by spatial heterogeneity.

7.3 In-situ monitoring of potential high-alpine rock fall

SAR interferometry (InSAR) is a remote sensing method for the detection of rock instabilities within large areas. Deformations larger than a few millimeters and of spatial extent of some decameters may be detected reliably with space-born sensors (Strozzi et al., 2010). Increased boulder fall activity, geomorphologic indications of accelerated deformation or changes in surface ice may be other signs for potential rock failures. Where critical situations are detected, a detailed monitoring of deformations and the ability of early warning of a failure is aspired for hazard mitigation. Currently the knowledge about pre-failure deformations in permafrost is limited and criteria for early warning do not exist. Based on the analysis of the cleft kinematics on Matterhorn and the stated conceptual model, possible ways for future monitoring and early warning are sketched in the following.

Pre-failure deformations

Thermally induced reversible (negatively temperature-correlated) rock movements appear to be typical in high alpine permafrost bedrock, but their amplitude and frequency depends on the local conditions. Movements that progressively deviate from this pattern may be interpreted as pre-failure deformations (Section 7.1) and their acceleration may be used to estimate the timing of an eventual failure. For non-permafrost rock instabilities empirical analysis of deformation

rates and model studies assess the characteristics of these accelerations (e.g. Ryan and Call, 1992; Crosta and Agliardi, 2003; Faillettaz et al., 2010). However, general rules such as applied for ice failure mechanisms (e.g. Haeberli, 1975; Pralong, 2005) are difficult to define for rock and of limited validity when only one single point is measured (Eberhardt et al. 2008). Pre-failure extensions from a rock fall event in permafrost (Jungfraujoch) show a significant acceleration in the last week before the event (Wegmann, 1998), but irregularities complicate a prediction of the failure (Figure 18). Therefore, algorithms and visualization tools that are able to distinguish pre-failure deformations from negatively temperature-correlated rock movements, and that handle irregularities in the acceleration are required for failure prediction. Today a fully automated procedure is not feasible and more data on pre-failure deformations in permafrost areas is needed to develop algorithms for such predictions.

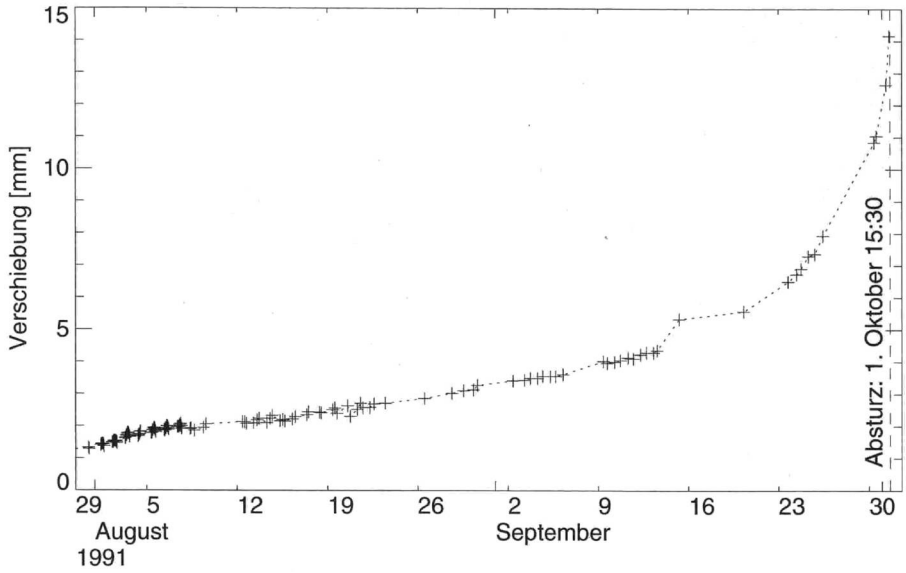

Figure 18: Progressive acceleration of the rock mass that failed on 1 October 1991 at Jungfraujoch (Figure 6.4 from Wegmann 1998; p. 35). The failing rock mass was constituted by an overhang with clefts parallel to the rock face. Some of these clefts showed water outflow during summer when snow melt occurred on the flatter sections above (Wegmann 1998).

Real time sensing and training of early warning

The PermaSense measurement infrastructure provides a tool to reliably monitor rock movements and other parameters at real-time (Chapter 3). The continued operation of the Matterhorn deployment over the coming years will provide data to analyze inter-annual variations of the deviation of thawing-related movements from the negatively temperature-correlated pattern. Further, changed sampling rates may provide more insight into the temporal mode of these movements (see below). The installation of such an infrastructure where rock masses are suspected to fail would be a training case for future early-warning systems, which can be sketched as follows:

1) Installation of 2-dimensional crackmeters at clefts selected by remote sensing methods and visual observation, and temperature measurements at the rock surface and within clefts.

2) Evaluation of the deviation from the negatively temperature-correlated pattern based on a statistical model of temperature-dependent movements (Equation 3; Figure 13).

3) Acquisition of high resolution movement mode of thawing-related movements (stick-slip mode) by adaptive sampling rate (<1 sec. for cleft temperatures >0 °C).

4) Real-time visualization and training of prediction algorithms based on the findings of 2) and 3) and possibly hydro-thermo-mechanical modeling.

5) Combination with periodic remote sensing (TerINSAR, LIDAR) and/or geodetic methods (for smaller movements) to obtain a spatial movement pattern.

Such a training installation should not be considered for early warning in a first year and its potential for the given case have to be evaluated after this training phase. With more experience, such a training phase may be shorter for following similar installations. The combination of scientific and practical use may lead to enhanced prediction capabilities for high-alpine rock fall and provide a method for future mitigation of rock fall in situations that have been recognized as critical.

8 Conclusion

This thesis contributes to an enhanced process understanding of the linkage between climate and rock fall release in steep bedrock permafrost by detailed studies of the thermal, hydrological and mechanical subsystems. The main findings relate to the thermal conditions and the kinematics of steep bedrock permafrost. Further, the methods applied provide means for in-situ measurements and monitoring in harsh environments. The hypotheses formulated need to be tested in the future and further methodical developments may provide measures to delimitate and monitor permafrost-related rock fall.

8.1 Summary of progress

Within the project PermaSense, which was the frame of this thesis, a data acquisition infrastructure for in-situ measurements has been developed. Here, substantial contributions relate to the definition of requirements (system specification and design), sensor development and data processing (Chapter 3). Field data acquired by this technology was used to analyze the thermal conditions and related rock movements at two permafrost field sites in the Swiss Alps. Based on this, hypotheses on the processes that control temperature and kinematics in steep high-alpine bedrock where formulated (Chapter 4 and 6). Complementary, laboratory experiments and numerical simulations of ice formation and erosion in clefts where conducted to provide first quantifications of hydrothermal processes in cold fractured bedrock (Chapter 5). The findings of these investigations were synthesized into a conceptual model of the processes that constitute the link between climate and rock fall, and the potential of their application for hazard mitigation was sketched (Chapter 7).

8.2 Outcomes

Main findings

In the following the findings of this thesis are outlined. Detailed lists of the results of individual parts may be found in the respective chapters and on the cover pages of the publications (Part B).

– Snow cover and clefts in steep high-alpine bedrock both have a cooling effect on the mean rock temperatures. For radiation exposed faces the net effect of these phenomena is on the order of 1–3 °C compared to near-vertical rock sections without snow.

– The thermal influence of percolating water is rather local and short-term but the effect on cleft ice and mechanical conditions is important and sensitive to changes of melting conditions at the surface.
– Movements of the rock masses beside clefts are negatively correlated with near-surface temperatures, which corresponds to other observations in permafrost bedrock. In contrast to earlier interpretations we attribute these movements mainly to the thermal dilatation of rock and related stresses.
– Thawing related movements that deviate from the known negative temperature-correlation where recorded at some locations. The fast reaction to melt initiation indicates hydro-thermal processes triggering these movements.

The conceptual model developed based on the above results suggests that rock fall release mechanisms are controlled by a reduction of the cleft strength, which may be caused directly by melt water percolation or indirectly by conductive warming of the cleft surrounding. As a consequence, most critical situations are expected when strong changes in melt water occur (temporal) or where the permafrost temperature is close to 0 °C (spatial).

Methodical outcomes

The methodical outcomes are related to the described technical developments (Chapter 3) and to the methods used for the geo-scientific analyses.

– The wireless sensor network (WSN) developed within PermaSense achieved stable operation and high data quality and provides a tool for flexible operation of a wide range of sensors.
– On-line data management tools and automated (off-line) data validation and visualization for the WSN data were developed.
– Analysis tools for near-surface temperature profiles, applicable to other temperature profiles.
– Model parameterization for cleft ice evolution in a single cleft may be used for future hydro-thermal modeling in fractured rock.
– A statistical model for the analysis of negatively temperature-correlated cleft movements in bedrock permafrost was formulated.

8.3 Perspectives

The findings of this thesis point toward the following open questions and research needs:

– The cooling effect of snow and clefts in steep bedrock should be considered for estimations of the permafrost distribution. For this a more general quantification of the effects may be achieved with numerical modeling studies (snow) and the analysis of temperature data from strongly fractured rock (clefts).
– The formulated hypotheses (Chapter 6) on rock kinematics in permafrost bedrock may be tested with a continuation of the field measurements at Matterhorn Hörnligrat. High-resolution records

of the thawing-related movements may reveal the temporal mode (stick-slip mode, slip velocity) of the movements and possibly allow conclusions on the driving mechanism.

– The strength reduction of (partly) ice-filled clefts including rock-rock contacts under the influence of water supply and temperature rise should be assessed. This may lead to a better understanding of the hydrothermal – mechanical interaction and provide a basis for a rock-mechanical parameterization of permafrost bedrock. Best means for such studies may be physical modeling.

– Investigations of the development of flow channels in thin rock fissures (or fissures in the cleft ice) at subzero temperatures will show in which situations fast hydrothermal interactions are expected within the permafrost body. Both, numerical modeling studies and physical modeling are possible ways here.

The methodology to transfer potential findings of the sketched process investigations to the field needs to be chosen based on the scale addressed: Coupled numerical models that simulate these processes will be limited to sensitivity and case studies. To be applied over larger areas the necessary input data (small scale heterogeneities) is missing and model uncertainties and calculating effort may strongly increase. Hence, simple and robust rules that can be applied to interpret empirical data and/or the results of hydrothermal models are promising. An example of such a simple rules are the sketched populations (Chapter 7) of rock fall. This may be tested by:

– Statistical analysis of rock fall based on the proposed spatial delimitation of the cold-season rock fall around the permafrost boundary.

The methodical outcomes regarding the WSN provide the possibility for a real-time monitoring of pre-failure deformations. After experiences with training cases such a system may be applied as monitoring and early-warning tool for rock fall of medium to large size with mid-term acceleration. For such an application further real-time processing and visualization and a dynamic sampling rate are necessary enhancements. The combination of in-situ measurements with other methods (e.g. remote sensing) may provide data sets with both, high temporal and high spatial resolution of harsh and remote environments in the future.

References

Amitrano, D. Arattano, M. Chiarle, M. Mortara, G. Occhiena, C. Pirulli, M. Scavia, C. 2010. Microseismic activity analysis for the study of the rupture mechanisms in unstable rock masses. *Natural Hazards and Earth System Sciences* 10. 831–841.

Arenson, LU. Springman, SM. 2005. Triaxial constant stress and constant strain rate tests on ice-rich permafrost samples. *Canadian Geotechnical Journal* 42(2). 412–430.

Bak, P. 1996. *How nature works: The science of self-organized criticality.* Copernicus, New York, USA.

Beutel, J. Gruber, S. Gubler, S. Hasler, A. Keller, M. Lim, R. Talzi, I. Thiele, L. Tschudin, C. Yücel, M. 2009. The PermaSense remote monitoring infrastructure. In *Proceedings of the International Snow Science Workshop 2009*, Davos, Switzerland.

Boike, J. Roth, K. Overduin, PP. 1998. Thermal and hydrologic dynamics of the active layer at a continuous permafrost site (Taymyr Peninsula, Siberia). *Water Resources Research* 34(3). 355–363.

Boike, J. Hagedorn, B. Roth, K. 2008. Heat and water transfer processes in permafrost-affected Soils: A review of field-and modeling-based studies for the Arctic and Antarctic. In *Proceedings of the Ninth International Conference on Permafrost*, Fairbanks, Alaska, USA. 149–154.

Burn, CR. Smith, CAS. 1988. Observations of the" thermal offset" in near-surface mean annual ground temperatures at several sites near Mayo, Yukon Territory, Canada. *Arctic* 41(2). 99–104.

Crosta, GB. Agliardi, F. 2003. Failure forecast for large rock slides by surface displacement measurements. *Canadian Geotechnical Journal* 40(1). 176-191.

Davies, MCR. Hamza, O. Harris, C. 2001. The effect of rise in mean annual temperature on the stability of rock slopes containing ice-filled discontinuities. *Permafrost and Periglacial Processes* 12(1). 137–144.

Dramis, F. Govi, M. Guglielmin, M. Mortara, G. 1995. Mountain permafrost and slope instability in the Italian Alps: the Val Pola landslide. *Permafrost and Periglacial Processes* 6(1). 73–81.

Dubois-Ferrière, H. Fabre, L. Meier, R. Metrailler, P. 2006. TinyNode: a comprehensive platform for wireless sensor network applications. In *Proceedings of the Fifth International Conference on Information Processing in Sensor Networks*, Nashville, Tennessee, USA. 358–365.

Eberhardt, E. Watson, AD. Loew, S. 2008. Improving the interpretation of slope monitoring and early warning data through better understanding of complex deep-seated landslide failure mechanisms. In *Proceedings of the Tenth International Symposium on Landslides and Engineered Slopes*, Xian, China. 39–51.

Einstein, A. 1936. Physik und Realität. In *Aus meinen späten Jahren.* Deutsche Verlags-Anstalt. Stuttgart, Deutschland.

Einstein, A. 1940. Das Fundament der Physik. In *Aus meinen späten Jahren.* Deutsche Verlags-Anstalt, Stuttgart, Deutschland.

Faillettaz, J. Sornette, D. Funk, M. 2010. Gravity-driven instabilities: Interplay between state- and velocity-dependent frictional sliding and stress corrosion damage cracking. *Journal of Geophysical Research* 115(B3). B03409.

Fann, KT. 1970. *Peirce's theory of abduction*. Martinus Nijhoff, The Hague, Netherlands.

Fischer, L. Kaeaeb, A. Huggel, C. Noetzli, J. 2006. Geology, glacier retreat and permafrost degradation as controlling factors of slope instabilities in a high-mountain rock wall: the Monte Rosa east face. *Natural Hazards and Earth System Sciences* 6(5). 761–772.

Fischer, L. Huggel, C. 2008. Methodical design for stability assessments of permafrost-affected high-mountain rock walls. In *Proceedings of the Ninth International Conference on Permafrost*, Fairbanks, Alaska, USA. 439–444.

Fischer, L. 2010. *Slope instabilities on perennially frozen and glacierised rock walls: multi-scale observations, analyses and modelling*. PhD Thesis. University of Zurich, Zurich, Switzerland.

Fischer, L. Amann, F. Moore, JR. Huggel, C. 2010. Assessment of periglacial slope stability for the 1988 Tschierva rock avalanche (Piz Morteratsch, Switzerland). *Engineering Geology* 116(1–2). 32–43.

Fischer, L. Purves, R. Huggel, C. Noetzli, J. Haeberli, W. 2011. On the influence of geological, topographic and cryospheric factors on slope instabilities: Statistical analyses of recent Alpine rock avalanches. *Natural Hazards and Earth System Sciences* submitted.

FOEN. 2006. Hinweiskarte Permafrost Schweiz, 1:50'000, Federal Office for the Environment, Bern, Switzerland.

Gerber, S. 2010. *Advektiver Waermetransport in den Felsflanken des Jungfraujochs*. Master Thesis. University of Zurich, Zurich, Switzerland.

Gischig, V. Moore, JR. Evans, KF. Loew, S. 2010. Seasonal changes of rock mass deformation rate due to thermal effects at the Randa rock slope instability, Switzerland. In *Proceedings of the 11th IAEG Congress*, Auckland, New Zealand.

Goering, DJ. 2003. Thermal response of air convection embankments to ambient temperature fluctuations. In *Proceedings of the Eighth International Conference on Permafrost,* Zurich, Switzerland. 291–296.

Goodrich, LE. 1978. Efficient numerical technique for one-dimensional thermal problems with phase change. *International Journal of Heat and Mass Transfer* 21(5). 615–621.

Gruber, S. Peter, M. Hoelzle, M. Woodhatch, I. Haeberli, W. 2003. Surface temperatures in steep Alpine rock faces — a strategy for regional-scale measurement and modelling. *Proceedings of the Eighth International Conference on Permafrost,* Zurich, Switzerland. 1. 325–330.

Gruber, S. Hoelzle, M. Haeberli, W. 2004a. Permafrost thaw and destabilization of Alpine rock walls in the hot summer of 2003. *Geophysical Research Letters* 31(13). L13504.

Gruber, S. Hoelzle, M. Haeberli, W. 2004b. Rock-wall temperatures in the Alps: modelling their topographic distribution and regional differences. *Permafrost and Periglacial Processes* 15(3). 299–307.

Gruber, S. 2005. *Mountain Permafrost: Transient spatial modelling, model verification and the use of remote sensing.* PhD Thesis. University of Zurich, Zurich, Switzerland.

Gruber, S. Haeberli, W. 2007. Permafrost in steep bedrock slopes and its temperature-related destabilization following climate change. *Journal of Geophysical Research* 112. F02S18.

Gubler, H. 2006. *PermaSense measurement concept for distributed permafrost sensors for rock-walls.* Unpublished report.

Gubler, S. Fiddes, J. Gruber, S. Keller, M. 2011. Scale-dependent measurement and analysis of ground surface temperature variability in alpine terrain. *The Cryosphere Discussion* 5. 307–338.

Guenzel, F. 2008. Shear Strength of Ice-Filled Rock Joints. In *Proceedings of the Ninth International Conference on Permafrost*, Fairbanks, Alaska, USA. 581–586.

Haeberli, W. 1975. Überwachung von Kalbungsflutwellen am Grubengletscher. *Schweizer Bauzeitung* 93(43). 694–696.

Haeberli, W. Wegmann, M. Vonder Muehll, D. 1997. Slope stability problems related to glacier shrinkage and permafrost degradation in the Alps. *Ecologae Geologicae Helvetiae* 90(3). 407–414.

Haeberli, W. Huggel, C. Kaab, A. Zgraggen-Oswald, S. Polkvoj, A. Galushkin, I. Zotikov, I. Osokin, N. 2004. The Kolka-Karmadon rock/ice slide of 20 September 2002: an extraordinary event of historical dimensions in North Ossetia, Russian Caucasus. *Journal of Glaciology* 50(171). 533–546.

Hall, K. 1997. Rock temperatures and implications for cold region weathering. I: New data from

Viking Valley, Alexander Island, Antarctica. *Permafrost and Periglacial Processes* 8(1). 69–90.

Hallet, B. 1983. The breakdown of rock due to freezing: a theoretical model. *Proceedings of the Fourth International Conference on Permafrost,* Fairbanks, Alaska, USA. 433–438.

Hallet, B. Walder, JS. Stubbs, CW. 1991. Weathering by segregation ice growth in microcracks at sustained sub-zero temperatures: Verification from an experimental study using acoustic emissions. *Permafrost and Periglacial Processes* 2(4). 283–300.

Hanson, S. Hoelzle, M. 2004. The thermal regime of the active layer at the Murtel rock glacier based on data from 2002. *Permafrost and Periglacial Processes* 15(3). 273–282.

Harris, SA. Pedersen, DE. 1998. Thermal regimes beneath coarse blocky materials. *Permafrost and Periglacial Processes* 9(2). 107–120.

Harris, C. Arenson, LU. Christiansen, HH. Etzelmüller, B. Frauenfelder, R. Gruber, S. Haeberli, W. Hauck, C. Hölzle, M. Humlum, O. 2009. Permafrost and climate in Europe: Monitoring and modelling thermal, geomorphological and geotechnical responses. *Earth Science Reviews* 92(3–4). 117–171.

Harrison, S. 2009. Environmental systems: Philsophy and applications in physical Geography. In *Key concepts in geography*. SAGE, New Dehli, India.

Hasler, A. Gruber, S. 2009. *PermaSense II: Zusammenfassender Schlussbericht an das Bundesamt für Umwelt.* Unpublished report.

Hinkel, KM. Outcalt, SI. 1993. Detection of nonconductive heat transport in soils using spectra analysis. *Water Resources Research* 29. 1017–1024.

Huggel, C. 2009. Recent extreme slope failures in glacial environments: effects of thermal perturbation. *Quaternary Science Reviews* 28(11-12). 1119–1130.

Huggel, C. Salzmann, N. Allen, S. Caplan-Auerbach, J. Fischer, L. Haeberli, W. Larsen, C. Schneider, D. Wessels, R. 2010. Recent and future warm extreme events and high-mountain slope stability. *Philosophical Transactions of the Royal Society A: Mathematical, Physical and Engineering Sciences* 368(1919). 2435.

Ishikawa, M. Zhang, Y. Kadota, T. Ohata, T. 2006. Hydrothermal regimes of the dry active layer. *Water Resources Research* 42(4). W04401.

Kane, DL. Hinkel, KM. Goering, DJ. Hinzman, LD. Outcalt, SI. 2001. Non-conductive heat transfer associated with frozen soils. *Global and Planetary Change* 29(3–4). 275–292.

Kaufmann, J. 2000. Experimental identification of damage mechanisms in cementitious porous materials on phase transition of pore solution under deicing salt attack. *Bericht-Eidgenossische Materialpruefungs-und Forschungsanstalt*, Duebendorf, Switzerland.

Kohl, T. Evansi, KF. Hopkirk, RJ. Rybach, L. 1995. Coupled hydraulic, thermal and mechanical considerations for the simulation of hot dry rock reservoirs. *Geothermics* 24(3). 345–359.

Krautblatter, M. 2009. *Detection and quantification of permafrost change in alpine rock walls and implications for rock instability*. PhD Thesis. Rheinischen Friedrich-Wilhelms-University Bonn, Bonn, Germany.

Krautblatter, M. 2010. Patterns of Multiannual Aggradation of Permafrost in Rock Walls with and Without Hydraulic Interconnectivity (Steintalli, Valley of Zermatt, Swiss Alps). In *Landform-Structure, Evolution, Process Control* 115: 199–219.

Krautblatter, M. Huggel, C. Deline, P. Hasler, A. 2011. Research perspectives for unstable high-alpine bedrock permafrost: measurement, modelling and process understanding. *Permafrost and Periglacial Processes* submitted.

Ladanyi, B. 2006. Creep of frozen slopes and ice-filled rock joints under temperature variation. *Canadian Journal of Civil Engineering* 33(6). 719–725.

Matsuoka, N. Sakai, H. 1999. Rockfall activity from an alpine cliff during thawing periods. *Geomorphology* 28(3–4). 309–328.

Matsuoka, N. 2001a. Direct observation of frost wedging in alpine bedrock. *Earth Surface Processes and Landforms* 26(6). 601–614.

Matsuoka, N. 2001b. Microgelivation versus macrogelivation: towards bridging the gap between laboratory and field frost weathering. *Permafrost and Periglacial Processes* 12(3). 299–313.

Matsuoka, N. 2008. Frost weathering and rockwall erosion in the southeastern Swiss Alps: Long-term (1994-2006) observations. *Geomorphology* 99(1–4). 353–368.

Mellor, M. 1973. Mechanical properties of rocks at low temperatures. In *Proceedings of the Second Conference on Permafrost*, Yakutsk, U.S.S.R. 334–344.

Mottaghy, D. Rath, V. 2006. Latent heat effects in subsurface heat transport modelling and their impact on palaeotemperature reconstructions. *Geophysical Journal International* 164(1). 236–245.

Muralidhar, K. 1990. Flow and transport in single rock fractures. *Journal of Fluid Mechanics* 215: 481–502.

Murton, JB. Peterson, R. Ozouf, JC. 2006. Bedrock fracture by ice segregation in cold regions. *Science* 314(5802). 1127.

Naegeli, B. 2010. *Felsstürtze und Permafrost – Ereignisanalyse und Abschätzung der Permafrostverhältnisse von Anrisszonen in den Alpen.* Master Thesis. University of Zurich, Zurich, Switzerland.

Noetzli, J. Hoelzle, M. Haeberli, W. 2003. Mountain permafrost and recent Alpine rock-fall events: a GIS-based approach to determine critical factors. In *Proceedings of the Eighth International Conference on Permafrost*, Zurich, Switzerland. 827–832.

Noetzli, J. Gruber, S. Kohl, T. Salzmann, N. Haeberli, W. 2007. Three-dimensional distribution and evolution of permafrost temperatures in idealized high-mountain topography. *Journal of Geophysical Research* 112: F02S13.

Noetzli, J. 2008. *Modeling transient three-dimensional temperature fields in mountain permafrost*. PhD Thesis. University of Zurich. Zurich, Switzerland.

Noetzli, J. Gruber, S. 2009. Transient thermal effects in Alpine permafrost. *The Cryosphere* 3(1). 85–99.

Nordvik, T. Blikra, LH. Nyrnes, E. Derron, MH. 2010. Statistical analysis of seasonal displacements at the Nordnes rockslide, northern Norway. *Engineering Geology*.

Nye, JF. 1976. Water flow in glaciers: jökulhlaups, tunnels and veins. *Journal of Glaciology* 17: 181–207.

PERMOS. 2010. Permafrost in Switzerland 2006/2007 and 2007/2008. Noetzli, J. and Vonder Muehll, D. (eds.). *Glaciological Report (Permafrost) No. 8/9 of the Cryospheric Commission of the Swiss Academy of Sciences*, Zurich, Switzerland.

Phillips, JD. 2003. Sources of nonlinearity and complexity in geomorphic systems. *Progress in Physical Geography* 27(1). 1.

Pirulli, M. 2009. The Thurwieser rock avalanche (Italian Alps): Description and dynamic analysis. *Engineering Geology* 109(1–2). 80–92.

Pogliotti, P. Cremonese, E. Morra di Cella, U. Gruber, S. Giardino, M. 2008. Thermal diffusivity variability in alpine permafrost rock walls. In *Proceedings of the Ninth International Conference on Permafrost*, Fairbanks, Alaska, USA 1427–1432.

Pogliotti, P. 2011. *Influence of Snow Cover on MAGST over Complex Morphologies in Mountain Permafrost Regions*. PhD Thesis. Università degli Studio di Torino, Turin, Italy.

Popper, KR. 1935. *Logik der Forschung: zur Erkenntnistheorie der modernen Naturwissenschaft*. Springer, Wien, Austria.

Pralong, A. 2005. On the instability of hanging glaciers. *Mitteilungen der Versuchsanstalt fur Wasserbau, Hydrologie und Glaziologie an der Eidgenossischen Technischen Hochschule Zurich*, Zurich, Switzerland.

Ravanel, L. Deline, P. 2010. Climate influence on rockfalls in high-Alpine steep rockwalls: The north side of the Aiguilles de Chamonix (Mont Blanc massif) since the end of the'Little Ice Age'. *The Holocene*: 1–9.

Ravanel, L. Allignol, F. Deline, P. Gruber, S. Ravello, M. 2010. Rock falls in the Mont Blanc Massif in 2007 and 2008. *Landslides* 7: 493–501.

Richards, K. 2009. Geography and the physical science tradition. In *Key Concepts in Geography*. SAGE, New Dehli, India.

Rist, A. 2007. *Hydrothermal processes within the active layer above alpine permafrost in steep scree slopes and their influence on slope stability*. PhD Thesis. University of Zurich,

Zurich, Switzerland.

Röthlisberger, H. 1972. Water pressure in intra-and subglacial channels. *Journal of Glaciology* 11(62). 177–203.

Ryan, TM. Call, RD. 1992. Applications of rock mass monitoring for stability assessment of pit slope failure. In *Rock Mechanics Proceedings of the 33rd Symposium,* Santa Fe, New Mexico, USA. 221–229.

Rykiel, EJ. 1996. Testing ecological models: the meaning of validation. *Ecological modelling* 90(3). 229–244.

Salzmann, N. Noetzli, J. Hauck, C. Gruber, S. Hoelzle, M. Haeberli, W. 2007. Ground surface temperature scenarios in complex high-mountain topography based on regional climate model results. *Journal of Geophysical Research* 112: F02S12.

Sass, JH. Lachenbruch, AH. Munroe, RJ. 1971. Thermal conductivity of rocks from measurements on fragments and its application to heat-flow determinations. *Journal of Geophysical Research* 76(14). 3391–3401.

Scherler, M. Hauck, C. Hoelzle, M. Stähli, M. Völksch, I. 2010. Meltwater infiltration into the frozen active layer at an alpine permafrost site. *Permafrost and Periglacial Processes* 21(4). 325–334.

Schumm, SA. Lichty, RW. 1965. Time, space, and causality in geomorphology. *American Journal of Science* 263(2). 110–119.

Scholz, CH. Engelder, JT. 1976. The role of asperity indentation and ploughing in rock friction--I: Asperity creep and stick-slip. *International Journal of Rock Mechanics and Mining Sciences and Geomechanics Abstracts*: 149–154.

Strozzi, T. Delaloye, R. Kääb, A. Ambrosi, C. Perruchoud, E. Wegmüller, U. 2010. Combined observations of rock mass movements using satellite SAR interferometry, differential GPS, airborne digital photogrammetry, and airborne photography interpretation. *Journal of Geophysical Research* 115(F1). F01014.

Talzi, I. Hasler, A. Gruber, S. Tschudin, C. 2007. PermaSense: investigating permafrost with a WSN in the Swiss Alps. In *Proceedings of the Fourth Workshop on Embedded Networked Sensors*, Cork, Ireland. 8–12.

Talzi, I. Schonborn, S. Tschudin, C. 2008. Providing data integrity in intermittently connected Wireless Sensor Networks. In *Fifth International Conference on Networked Sensing Systems, INSS 2008*, Kanazawa, Japan. 11–18.

Vonder Muehll, DS. 1992. Evidence of intrapermafrost groundwater flow beneath an active rock glacier in the Swiss Alps. *Permafrost and Periglacial Processes* 3(2). 169–173.

Watson, AD. Moore, DP. Stewart, TW. 2004. Temperature influence on rock slope movements at Checkerboard Creek. In *Proceedings of the Ninth International Symposium on Landslides,* London, A.A. Balkema Publishers. 1293–1298.

Wegmann, M. 1998. Frostdynamik in hochalpinen Felswänden am Beispiel der Region Jungfraujoch – Aletsch. PhD Thesis. Eidgenoessische Technische Hochschule Zuerich, Zurich, Switzerland.

Wegmann, M. Gudmundsson, G. 1999. Thermally induced temporal strain variations in rock walls observed at subzero temperatures. *Advances in Cold-Region Thermal Engineering and Sciences*: 511–518.

Part B: Publications

Paper I | WSN – requirements

Wireless sensor networks in permafrost research: concept, requirements, implementation, and challenges

Focus

This article outlines the potential and describes the requirements for wireless geotechnical sensing in steep high-alpine rock faces. It represents the stage of the technical developments after one and a half project years (autumn 2007). First experiences from two field deployments are discussed and next development steps are derived from them.

Main findings

- *No significant damage of the deployments due to rugged hardware design of sensors and network nodes*
- *System integration and application of custom designed sensors and sensor interface*
- *Need for algorithmic enhancements in the communication software and extensive testing with realistic conditions prior to field deployment*

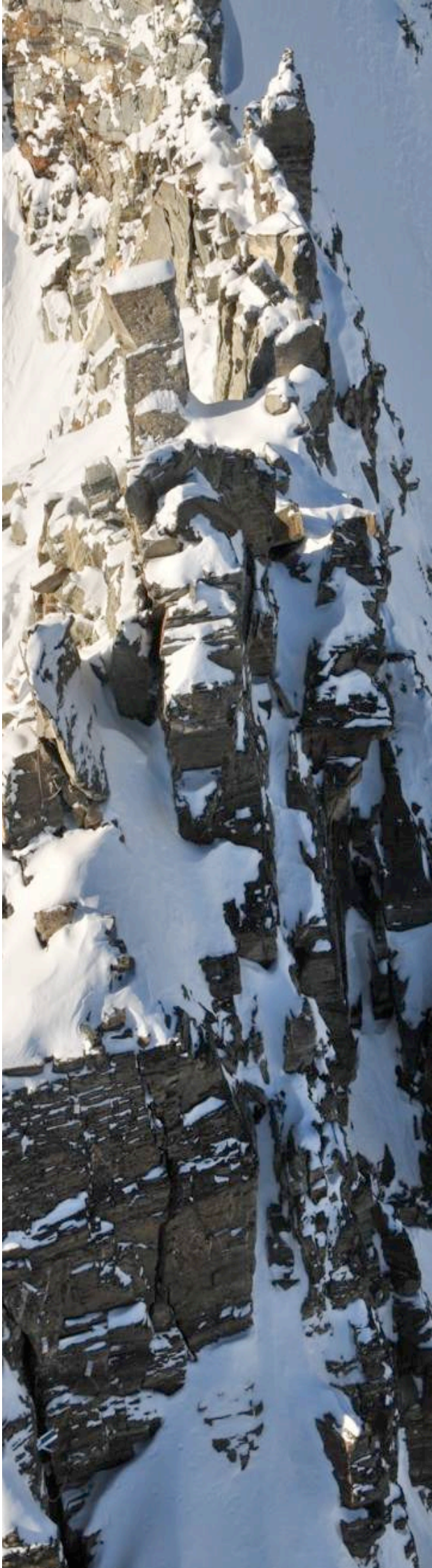

Citation

Hasler, A. Talzi, I. Beutel, J. Tschudin, C. Gruber, S. 2008. Wireless sensor networks in permafrost research: concept, requirements, implementation, and challenges. In Proceeding of the Ninth International Conference on Permafrost. Fairbanks, Alaska, USA. 669–674.

Wireless Sensor Networks in Permafrost Research – Concept, Requirements, Implementation and Challenges

Andreas Hasler
Glaciology, Geomorphodynamics, Geochronology; Geography Department, University of Zurich, Switzerland
Igor Talzi
Computer Science Department, University of Basel, Switzerland
Jan Beutel
Computer Engineering and Networks Laboratory, ETH Zurich, Switzerland
Christian Tschudin
Computer Science Department, University of Basel, Switzerland
Stephan Gruber
Glaciology, Geomorphodynamics, Geochronology; Geography Department, University of Zurich, Switzerland

Abstract

In a joint project of computer- and geo-scientists, wireless sensor networks (WSNs) are customized for permafrost monitoring in alpine areas. In this paper, we discuss requirements for a rugged setup of such a network that is adapted to operation in a difficult environment. The experiences with a first deployment at Jungfraujoch (Switzerland) show that beside hardware modifications of existing WSN-platforms, special emphasis should be given to the development of robust synchronization and low-power data routing algorithms. This results from the fact that standard software tools are not capable to deal with the high temperature fluctuations found in high-mountains without compromising the power consumption and the network topology. Enhancements resulted in a second deployment at Matterhorn (Switzerland), from where we expect results in the near future. Once the technology of WSN is a science grade instrument it will be a powerful tool to gather spatial permafrost data in near real-time.

Keywords: measurement; permafrost; PermaSense project; wireless sensor networks

Introduction

Spatially distributed measurements of permafrost parameters over long periods are time consuming in deployment and maintenance, vulnerable to environmental impacts, and create inhomogeneous data sets as no standard and easy applicable measurement devices exist. The project *PermaSense* addresses the development of a new generation of monitoring equipment for remote and harsh environments (Figure 1). In this paper, we present the design and implementation of a wireless sensor network (WSN) to measure temperatures, dilatation and diverse hydrological parameters in rock faces of Alpine permafrost.

A WSN generally consists of distributed *network nodes* with attached sensors, that communicate by local UHF radio within each other and that are up-linked by one (or several) *base stations* via mobile communication (e.g., UMTS, GPRS), internet or other data transfer systems to a *data sink server* (Figure 2). Each node contains a microprocessor, a radio transceiver, a sensor interface, some local memory, and an independent power supply. The network topology depends on the radio connectivity between the nodes. If data is transmitted via intermediate network nodes to the base station this is called *multi-hop* while a pure star-topology around the base station is called a *single-hop* network. Compared to existing logging systems using single radio-connected measurement devices, WSNs are designed to adapt their network topology dynamically according to the connectivity constraints, allowing to observe a larger area with multi-hop connection. While the dataflow is generally out of the network through the base station into the data sink, commands, network parameters, or even executable programs can potentially be pushed into the network.

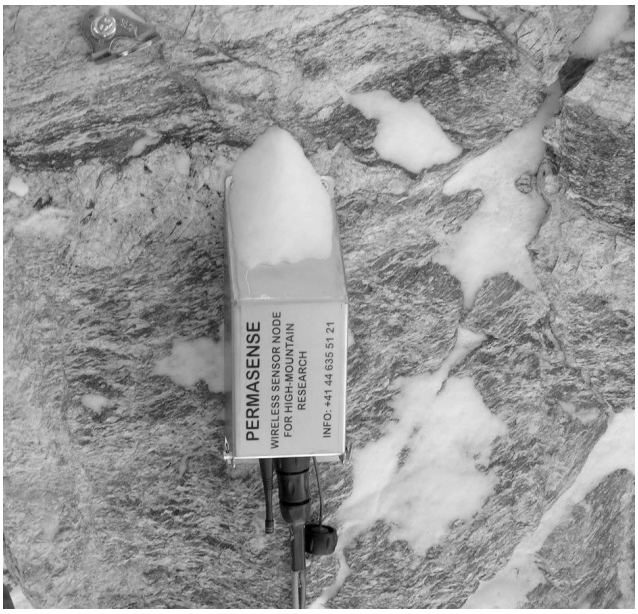

Figure 1: Network node at the field site Matterhorn – Hörnligrat

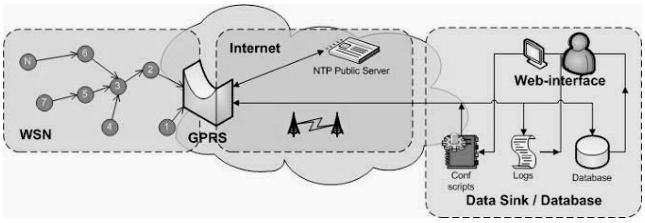

Figure 2: Framework of a WSN as used in our field deployments and testbed.

Based on experiences with our first deployment on Jungfraujoch (3500 m a.s.l., Swiss Alps) during winter and spring 2006/2007, we specify requirements for year-long, stand alone monitoring. WSN concepts and requirements for environmental use, and challenges for the implementation as well as the experiences from a second deployment generation are presented and discussed in this article.

Application of WSNs for Permafrost Research

Environmental wireless sensor networks

Environmental applications of WSN have emerged in the past years following the general developments in mobile communication (Hart & Martinez 2006). Depending on the monitored variables and processes the sensor networks differ in node size (e.g., from weather station to the futuristic "smart dust") as well as in spatial and functional extent of the network. In permafrost process research we are mainly interested in so-called *localized multifunctional sensor networks*. These systems are able to measure multiple parameters within an area of special interest. Despite the fast progress in the field of WSNs only a limited number of application projects exists so far. The Projects *Glacsweb* (Martinez et al. 2004), *SensorScope* (http://sensorscope.epfl.ch/index.php), or the *Volcano monitoring project* (Werner-Allen et al. 2006) are such examples. A larger overview of existing environmental sensor network projects is given by Hart & Martinez (2006).

Potential of WSNs

For permafrost research and other remote environmental applications of WSNs we identify the following potential:

- Once installed, maintenance and data acquisition is less time consuming with WSNs than with standard logging systems, particularly at difficult accessible locations. The nodes inform the operator about battery level and functioning.
- Data is available all year round at near real-time on a user interface. This is not only relevant for research, but can be very valuable for hazard monitoring.
- The data can be stored with redundancy and not only locally on the logger. In case of destruction or loss of a sensor node, the data measured until this event is saved.
- Measurements are synchronous and arrive at one central database. No extensive manual post-processing and homogenization of the data is needed.
- Interval and mode of measurements do not require being statically predefined. They can be controlled by remote commands from the user interface or can be context sensitive to other measurements of the network.

The project PermaSense

Wireless sensor networks have not yet been established for reliable, year-long operation under cold climate and high alpine conditions. In PermaSense computer- and geo-scientists upgrade in close cooperation the WSN platform *TinyNode* for permafrost research: Software for power efficient operation of an adaptive multi-hop network topology is currently under development and being tested. Robust and reliable deployment hardware was designed, sensor interface hardware was developed, and software integration of sensors is being implemented. Customized sensors were manufactured and compatible commercial sensors were evaluated and connected (Figure 3). A detailed description of the network software of our first deployment, based on TinyOS, is given by Talzi et al. (2007).

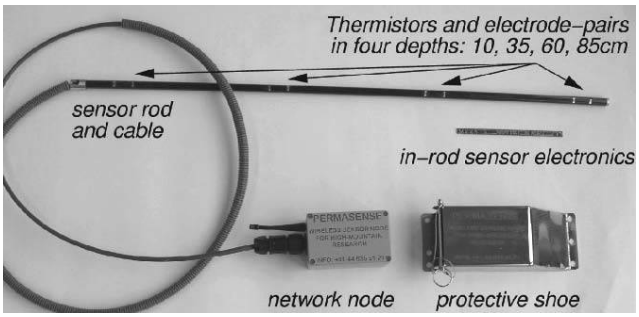

Figure 3: First generation network node and customized sensor rod that measures temperatures and DC-resistivity as an indicator of liquid pore water at four different depths; the electronics and battery (lithium-thionyl) of the network node are mounted in a waterproof aluminum housing (125x80x57 mm) and protected from ice and rock fall with a steel protective shoe: measurement electronics are in the tip of the sensor rod to minimize temperature fluctuation errors.

Requirements for a permafrost WSN

Similar to standard logging systems for permafrost purposes a WSN requires the following main features: Stable operation over a wide temperature range from -40 to 40 °C during at least one year or season, respectively (battery capacity). For analog measurements, a 12-bit analog-digital conversion (ADC) is generally sufficient as the resulting resolution for temperature measurements over the indicated range is 0.02 °C (a corresponding measurement accuracy can be reached with a zero-point calibration around 0 °C). If pressure sensors are applied, a vibration wire (VW) compatible ADC or frequency counter is of use. One or several digital interfaces (RS 232, RS 485 or SDI-12) for commercial sensors, allows the integration of divers sensor types into the network. For power intensive measurements (e.g., ERT), an incoming power supply line or solar panel control should be considered. All incoming and outgoing lines of this sensor interface should be

lightening protected if the system operates at exposed locations.

As permafrost parameters typically change with slow rates, a temporal resolution of the measurements of some minutes to hours is required. Rarely, continuous measurements are needed (e.g., acceleration sensors), which is not further considered in this article. The mechanical setup should correspond to the operating conditions (e.g., Figure 3).

WSN specific requirements:

- The scale of the spatial extent ranges from decameters up to several hundred meters (depending on WSN limitations). To provide connectivity in complex alpine topography a *multi-hop* system is preferable.
- Network topology is established automatically. A predefined topology is not applicable in practice and can not adapt itself to a temporal lack of connection caused by e.g. snow cover of the devices.
- Connectivity through snow and ice is better with lower radio frequencies (<1GHz).
- Ultra low power operation is supported. Sleeping cycles of the radio receiver and consequently synchronization of the wake periods are required.
- The measurements of different nodes are taken synchronically (in most cases an accuracy of seconds is sufficient) and time-stamped.
- Nodes with no connectivity to neighbors store measured data locally on the node (capacity: 6 months).
- Data transmission capacity considers payload of the measured data with some margins to catch up data transmission from temporally invisible nodes. Generally, measured data does not exceed 2kB per day.
- A *deployment mode* allows checking radio interconnectivity within the network during installation.
- A small form factor of the network node and a pluggable sensor interface ease the logistic effort for system maintenance.
- System health parameters (battery level, node temperature) inform the operator about network conditions and optimize the time of battery change.
- Command propagation into the network or context sensitivity allows to monitor periods of special interest in high resolution and to save power during less interesting periods.
- Data is stored in a database that provides metadata and has a safe backup strategy.
- A user interface supports the network maintenance (see above) and the database management.

Field Deployments

Energy balance models to estimate permafrost distribution and condition have recently been applied successfully to high mountain topography (Gruber et al. 2004). Especially for steep and compact rock faces with little snow cover, modeling results correspond well with surface temperature measurements. Also mean annual subsurface temperature distribution and permafrost bodies are simulated satisfyingly with a 3D heat-conduction model (Noetzli et al. 2008). However, in such models processes of non conductive heat transport are not considered despite their relevance for thawing depth and rate along fractures in the bedrock. The aim of our measurement site at Jungfraujoch is to quantify the spatial variability of thawing processes and heat transport in the near-surface layer.

1st Deployment: Jungfraujoch winter 2006/2007

The influence of surface characteristics, fracturing and melt water availability is measured by eight of the above described sensor rods in gently steep (40-70°) and fractured rock faces (general case in high alpine areas) around the Sphinx observatory at Jungfraujoch (ca. 3500m a.s.l., Figure 4, 5). Additionally, two thermistor chains are installed into the bordering ice faces.

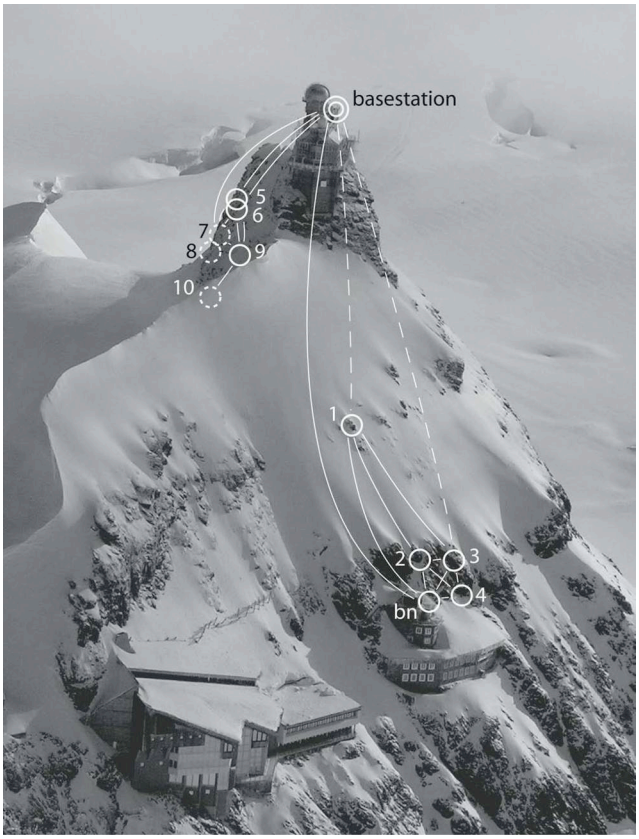

Figure 4: Deployment on Jungfraujoch (3500m a.s.l., Swiss Alps) consisting of ten sensor nodes with network topology; the base station is mounted on the Sphinx observatory; each circle depicts a network node with its corresponding number. Lines indicate good radio connectivity between nodes, dashed lines indicate unstable connectivity, dashed circles are hidden nodes, and *bn* is a bridge node introduced to provide stable connection to the base station; the network is divided into to two clusters on the north (left) and the south (right) facing slope of the ridge

Figure 5: Network node #4 and cable to the sensor rod, which is drilled one meter into the rock perpendicular to the surface. The network nodes can be easily exchanged and attached to the sensor by a waterproof plug.

The monitoring site consists of North and South faces of a ridge, which divides the network into two clusters with limited connectivity between them and differing thermal regimes (Figure 4). Resulting from this topology, the thermal clock drift requires synchronization algorithms that let the node times converge even with such temperature deviations.

The initial installation of the sensors took place in fall 2006 after four months of system design and hardware production. We set up a first network at the same time, which, however, has not been successful due to the short development time and insufficient testing of the network software and hardware. In addition, a stability problem of the measurement values appeared under field conditions. After a debugging and testing phase over winter 2006/2007 first valid data could be gathered in April 2007 (Figure 6). Yet no data transmission could be maintained over a period of more than two weeks. At this point, an extension of the project with the integration of network into a *testbed* prior to deployment was already planned for the second deployment in fall 2007. We decided to momentarily leave the network in a mode where data is stored locally to the node memory, and enhance and test the system for the second deployment.

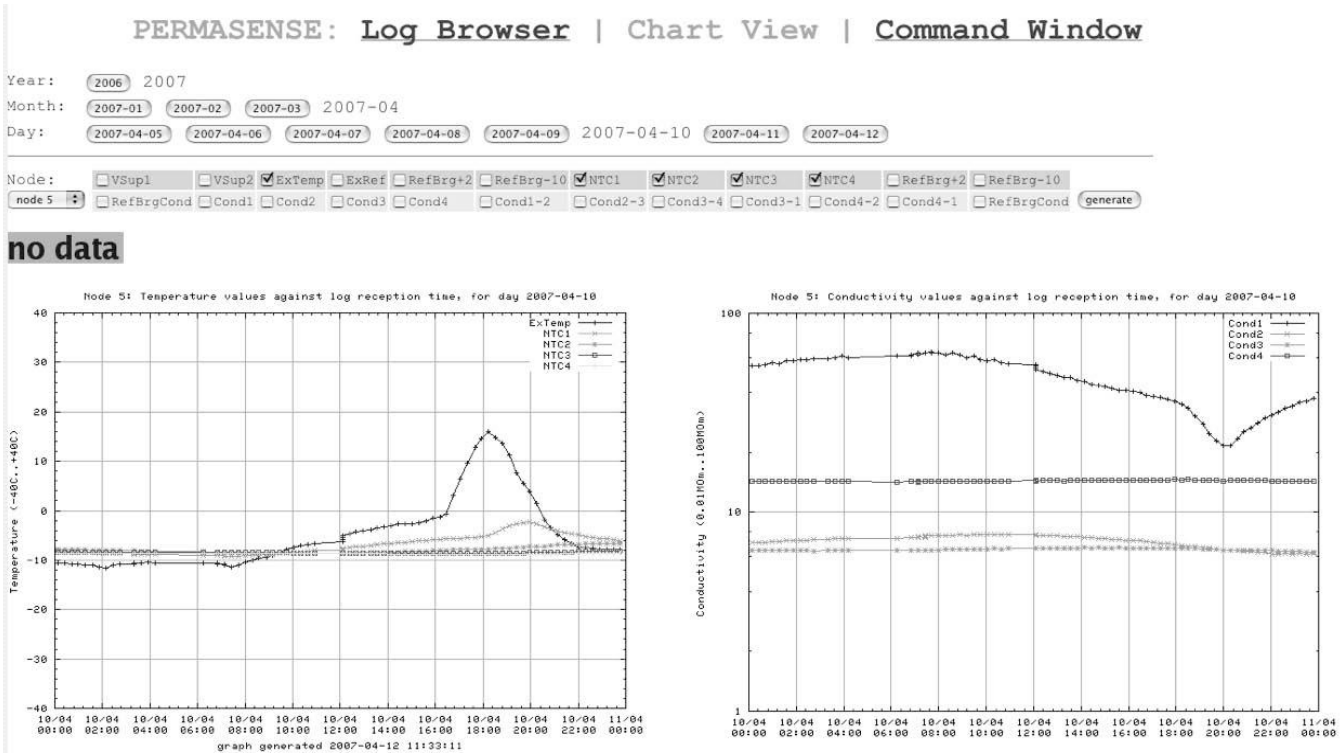

Figure 6: Screenshot of the user interface; direct visualization of one day of measurements from sensor rod #5 in the north facing slope of the Sphinx. On the left, temperatures of the sensor rod thermistors (NTC1–NTC4) and the node temperature are plotted; the right diagram shows the corresponding rock resistivities. At the near-surface level (NTC/Cond 1) the temperature signal is clearly visible in the resistivity values.

2nd Deployment: Matterhorn "Hörnligrat" (3400m a.s.l., Swiss Alps) in October 2007

Although public and research interests increased significantly following the hot Summer 2003, frost dynamics and natural hazards research in Alpine permafrost areas has been discussed already a decade ago (e.g., Haeberli et al. 1997, Wegmann 1998). Frost weathering and and rock fall activity is subject to year-long field observations and measurements (e.g., Matsuoka & Sakai 1999, Matsuoka 2001) and lab experiments (Murton et al., 2006). These lab experiments have shown that ice segregation takes place also in solid (but porous) rock. Field data gave clear evidence for the contribution of temperature fluctuation and water to near-surface weathering and pebble fall. However, a direct physical linkage between temperature and rock fall disposition has not yet been demonstrated in the field. Different concepts of this linkage are discussed in Gruber & Haeberli (2007). The second deployment of PermaSense addresses this issue, to gather data of cleft ice and rock stability interaction.

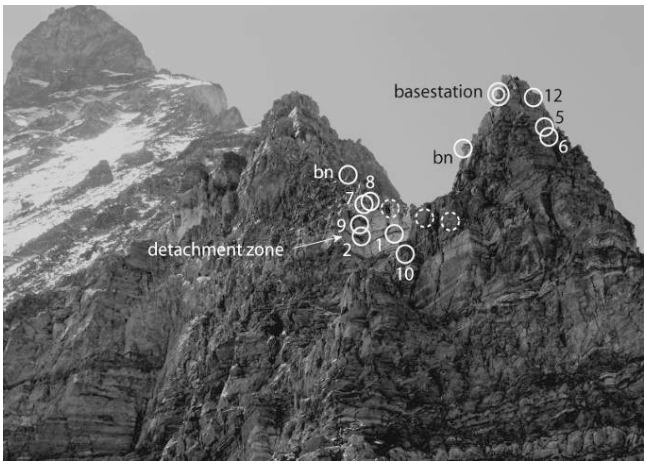

Figure 7: Deployment at Hörnligrat of the Matterhorn; circles with numbers mark sensor nodes, dashed circles are sensors on the back (north-western) side of the ridge, *bn* indicates bridge nodes.

The installation containing 13 sensor nodes with six sensor types, two bridge nodes, and one basestation was made on the north-east ridge of the Matterhorn, the Hörnligrat, in October 2007 (Figure 7). At this site, a rock fall of some 1000 m^3 occurred in July 2003. Massive ice was observed at the surface of the detachment zone (Figure 7) just after the event. This indicates the presence of stability-relevant ice-filled clefts in this area.

In addition to the sensors used on Jungfraujoch, we integrated commercial sensors with a newly designed *sensor interface board* (SIB) into our network. With these sensors we measure crack dilatation, water pressure, ice pressure and water movements in the clefts. Thermistor chains are mounted into clefts to measure temperature profiles together with the mentioned parameters. One node and SIB has a combination of this sensors attached resulting in a multiple sensor network node. The installation of more than one network node at one spot allows a flexible combination of sensors adapted to the situation in the field (Figure 8).

Figure 8: Installation site with multiple sensors: At the bottom two crack meters measure dilatation. Within the cleft potential water pressure and ice stress as well as temperatures at different depths are measured. The tube between the two nodes is the reference air pressure measurement.

Discussion of Experiences and Challenges of PermaSense

In the initial phase of PermaSense until April 2007 diverse problems where critical for the function of the WSN and subject of debugging. The quality of the measurements and the instable operation of the base station are two examples of this early stage and hardware related problems. Other system parts, such as the mechanical set up or the battery type appeared well adapted to the conditions met in the field over the winter and spring 2006/2007.

The network set up at Jungfraujoch in the end of April 2007 and the subsequent test runs at the test bed in Zurich showed to main topics remaining critical for stable long-term operation:

1. Time synchronization of the nodes.
2. Stability and power efficiency of the data routing.

As described above, the conditions in the field make time synchronization challenging due to large temperature fluctuations and deviations between installation spots. Short radio receiving slots compared to the sleeping intervals due

to power limitations, require a high quality of the synchronization. The fact that the clock quarts are generally optimized for 25°C and have high drifts at negative temperatures, makes a precise synchronization of a permafrost WSN even more challenging. Software based temperature drift compensation could be a possible way to go but needs extensive testing before application.

The currently used statically predefined data transmission slots, the radio communication as a power intense component is used in a rather inefficient way. To optimize power consumption and consequently increase battery life-time, a dynamic organization of the data transmission slots is promising. This could also increase the data transmission capacity in areas of the network where it is required and as consequence support a more stable data routing as well.

Conclusions

Based on the experiences gained from technology development and two high-mountain deployments, we can draw to the following main conclusions for the application of WSN in mountain permafrost research:

For a successful application of WSN in Permafrost research and to other environmentally challenging situations, an adapted software design and extensive testing of the network under realistic but well-monitored conditions are essential.

Due to large temperature fluctuations and large lateral temperature gradients in combination with complex network topologies and power limitations, synchronization of the nodes is a very challenging task. Major algorithmic work as well as specific testing is needed here.

The power efficiency and the duration of operation without battery exchange in the field can be increased significantly with further software development.

Once we succeed to overcome the current major problems, wireless sensor networks have the potential to become a powerful technology to gather spatially distributed field data in near-real time for permafrost research.

Acknowledgments

We like to thank Sandro Schönborn, Roman Lim, Mustafa Yücel for their contribution to PermaSense. The Project is partly financed by the Swiss Federal Office for the Environment (FOEN) and the National Competence Center for Research – Mobile Information and Communication Systems (NCCR-MICS). We also acknowledge the helpful technical advices of Hansueli Gubler, ALPUG, in the initial phase of PermaSense.

References

Gruber, S. & Haeberli, W. 2007. Permafrost in steep bedrock slopes and its temperature-related destabilization following climate change. *Journal of Geophysical Research* 112, doi:10.1029/2006-JF000547.

Gruber, S., Hoelzle, M. & Haeberli, W. 2004. Rock wall temperatures in the Alps: Modelling their topographic distribution and regional differences. *Permafrost Periglacial Processes* 15(3): 299–307.

Haeberli, W., Wegmann, M. & Vonder Muehll D. 1997. Slope stability problems related to glacier shrinkage and permafrost degradation in the Alps. *Eclogae Geologicae Helvetiae* 90: 407–414.

Hart, J.K. & Martinez, K. 2006. Environmental sensor networks: A revolution in the earth system science? *Earth-Science Reviews* 78: 177–191.

Martinez, K., Hart, J.K. & Ong, R. 2004. Environmental sensor networks. *Computer* 37 (8): 50–56.

Matsuoka, N. 2001. Direct observation of frost wedging in alpine bedrock. *Earth Surface Processes and Landforms* 26: 601–614.

Matsuoka, N. & Sakai, A. 1999. Rockfall activity from an alpine cliff during thawing periods. *Geomorphology* 28: 309-328.

Murton, J.B., Peterson, R. & Ozouf, J-C. 2006. Bedrock fracture by ice segregation in cold regions. *Science* 314: 1127–1129.

Noetzli, J., Hilbich, C., Hauck, C., Hoelzle, M., and Gruber, S. 2008. Comparison of Transient 2D Temperature Profiles with Time-Lapse Electrical Resistivity Data at the Schilthorn Crest, Switzerland. *Proceedings.of the Ninth International Conference on Permafrost.*

Talzi, I,. Hasler, A., Gruber, S. & Tschudin, C. 2007. PermaSense: Investigating permafrost with a WSN in the Swiss Alps. *In Proceedings for EmNets-07*: 8–12.

Wegmann, M. 1998. Frostdynamik in hochalpinen Feswänden am Beispiel der Region Jungfrau - Aletsch. Mitteilungen der Versuchsanstalt für Wasserbau, Hydrologie und Glaziologie an der ETH Zürich 161.

Werner-Allen, G., Lorincz, J., Johnson, J., Lees, J. & Welsh, M. 2006. Fidelity and yield in a volcano monitoring sensor network. *Proceedings of the 7th conference on USENIX Symposium on Operating Systems Design and Implementation* 7: 381–396.

Paper II | WSN – implementation

PermaDAQ: A scientific instrument for precision sensing and data recovery in environmental extremes

Focus

In this publication we describe the implemented system architecture of the second generation WSN of PermaSense in the third project year. A special focus is on the technical developments that meet the requirements of precise sensing and reliable operation with low power consumption.

Main findings

- *Successful operation of the WSN in the field with adapted communication protocols (Dozer)*
- *Precise and stable measurements by strict separation of operating phases and enhanced sampling routines*
- *Extended storage capacity for reliable operation (data acquisition) during connectivity loss and for post-deployment data validation*
- *Power tracing and optimization*

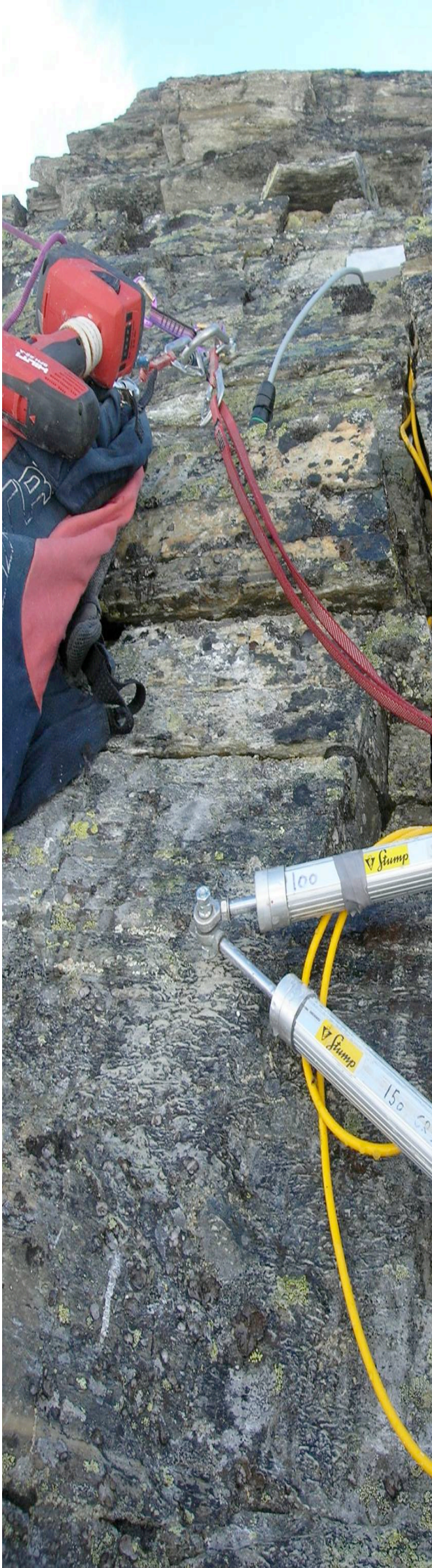

Citation

Beutel, J. Gruber, S. Hasler, A. Lim, R. Meier, A. Plessl, C. Talzi, I. Thiele, L. Tschudin, C. Woehrle, M. Yuecel, M. 2009. PermaDAQ: A scientific instrument for precision sensing and data recovery in environmental extremes. In Proceedings of the 2009 International Conference on Information Processing in Sensor Networks. IEEE Computer Society. 265–276.

PermaDAQ: A Scientific Instrument for Precision Sensing and Data Recovery in Environmental Extremes

Jan Beutel, Stephan Gruber[†], Andreas Hasler[†], Roman Lim, Andreas Meier, Christian Plessl[*], Igor Talzi[‡], Lothar Thiele, Christian Tschudin[‡], Matthias Woehrle, Mustafa Yuecel
Computer Engineering and Networks Lab, ETH Zurich, Zurich, Switzerland
[†]Physical Geography Division, Department of Geography, University of Zurich, Switzerland
[*]Paderborn Center for Parallel Computing, University of Paderborn, Germany
[‡]Computer Science Department, University of Basel, Switzerland
beutel@tik.ee.ethz.ch

ABSTRACT

The PermaSense project has set the ambitious goal of gathering real-time environmental data for high-mountain permafrost in unattended operation over multiple years. This paper discusses the specialized sensing and data recovery architecture tailored to meet the precision, reliability and durability requirements of scientists utilizing the data for model validation. We present a custom sensor interface board including specialized sensors and redundancy features for end-to-end data validation. Aspects of high-quality data acquisition, design for reliability by strict separation of operating phases and analysis of energy efficiency are discussed. The system integration using the Dozer protocol scheme achieves a best-in-class average power consumption of 148µA considerably exceeding the lifetime requirement.

Categories and Subject Descriptors

C.2.2 [**Network Architecture and Design**]: Distributed Networks; C.3 [**Special-Purpose and Application-Based Systems**]: Embedded Systems

General Terms

Design, Experimentation, Measurement, Reliability

Keywords

Architecture, Data Acquisition, Environmental Monitoring, Wireless Sensor Networks, Low-Power

IPSN '09 San Francisco, April 13-16,2009 , San Francisco, CA, USA

1. INTRODUCTION

The PermaSense project strives for collecting geophysical data in the high-altitude environment of the Swiss Alps with a wireless sensor network (WSN) running unattended for three years. The architecture aims to provide a long-term, high-quality wireless sensing and data recovery solution in extremely harsh environments with near complete recovery and near real-time delivery of the data. The observation periods targeted in conjunction with higher quality data than was previously feasible is expected to provide the relevant information for research and decision making, pioneering next generation early warning systems.

When using a sensor network as a scientific instrument for data gathering, the quality of data is of utmost importance. In PermaSense this is exacerbated by difficult access to the area under investigation and the labor intensive installation and maintenance of any sensing solution, wired or wireless. Current best practices require installation effort on the order of a man-day per sensor to achieve an accurate and well documented installation. Traditional WSN metaphors such as system-on-chip integration for cost reduction, smart clouds of redundant sensors or sensor placement scattered from a plane diminish in the light of such real world problems.

Based on a careful requirement analysis and close collaboration with the scientific partners, we have developed a specialized sensor interface board that integrates a TinyNode running Dozer [4] and is capable of acquiring data from a number of different sensors. The PermaDAQ system architecture is especially targeted at high precision measurements of slowly fluctuating quantities, reliable operation and an extremely tight energy budget. Powered from a single Li-$SOCL_2$ battery, an

average power consumption of 148µA is achieved based on a 2min measurement interval. This exceeds the lifetime requirement by a factor 2x and is competitive when compared with other recent WSN developments, e.g. railway bridges ∼166µA at 1sample/day [5]. Data acquisition accuracy is achieved by a strict separation of functions, minimizing possible interference from both electric effects and concurrently operating software components. Data quality is achieved using precision sampling and continuous, uninterrupted operation is warranted by storing data duplicates on non-volatile memory. This additional mechanism allows for buffering of data for delayed transmission on network outages and also for end-to-end data validation accross the whole chain of system components.

The contributions made in this paper are (i) an autonomous and robust sensor node architecture allowing high-precision data acquisition from a multitude of sensors, (ii) an extremely energy efficient integration with the Dozer communication protocol and (iii) and analysis of the performance w.r.t to sensing precision, effects of the environment and energy consumption.

2. SENSING IN ENVIRONMENTAL EXTREMES

2.1 Project Background – Scientific Relevance

PermaSense is a joint geo-science and engineering project with the aim to pioneer engineering as well as scientific use of next-generation sensing systems in harsh environmental conditions. The measurement strategy and system are designed for and immediately motivated by high-mountain permafrost research, but with the underlying aim to serve as prototype for future systems of wider applicability in research and hazard surveillance. In this context, the difficult environmental conditions at high elevation serve as a difficult benchmark for system robustness. In cold and steep mountain terrain, permafrost thaw can reduce the stability of slopes (e.g., frequency/magnitude relationships for large rock fall) in response to climate change [8]. [9] presents a more comprehensive introduction. Measurements in support of process research or model validation, however, are difficult to realize. Here, WSNs can help to provide higher quality data more effectively, e.g. by helping to optimize the resources for fieldwork, because the battery level and functioning of each sensor is monitored continuously and because small devices are easier to deploy. Additionally, the use of low-power and small WSN devices opens new and very valuable possibilities: Because the length of wiring installed is minimal, the susceptibility to lightning damage – a major limitation to the lifetime of such installations – is drastically reduced. Signals measured at different locations can be correlated precisely because time is known with much greater accuracy than with independent logging systems. Finally, continuous transmission of data enables information retrieval from "sacrificial sensors" that may be lost during a campaign measuring a destructive event.

Figure 1: Deployment sites Jungfraujoch (left) and Matterhorn (right) in high-alpine ambiance

The project started with an early prototype deployment (Jungfraujoch, 3500 m a.s.l.) in 2006/07 [17]. Based on the experience gained with this prototype, a thorough analysis, identification of shortcomings and misconceptions of the initial system design, a second-generation system architecture was developed. The new system was installed on a second field site (Matterhorn, 3450 m a.s.l.) in 2007/08 and is currently operationally and delivering sensor data in real-time[1].

2.2 PermaSense General Requirements

The refined requirements specification for the PermaSense system architecture is the following:

- About 25 nodes per site; node spacing ∼10-150m
- Minimum 3 years unattended lifetime
- Survival in harsh high-alpine environment (rock fall, avalanches, snow, ice, rime, lightning, storm)
- Ambient operating range -40 to +65℃, with max. 5℃per minute change rate
- Capable of sensing basic environmental parameters (temperature, electric conductivity, crack motion, ice stress, water pressure)
- ADC resolution >12 bits with 50ppm/℃ reference
- 1 to 60min adjustable sampling interval
- 99% data yield with max. 10 consec. samples lost
- Time synchronization to 1sec referenced to UTC
- 6 months autonomous storage capability
- No physical repairs or exchange of components
- No infrastructure support necessary

[1] See the data online at http://www.permasense.ch

2.3 PermaDAQ System Design Challenges

The two most prominent shortcomings of the first system developed [17] were limitations w.r.t the precision of the data acquisition and the ultra-low power design goal based on the TinyNode/TinyOS system design. These, and the high reliability requirement, both in terms of uninterrupted lifetime but also data integrity form the design challenges for the second generation architecture.

Precision Sensing – Emphasis is on the quality and accuracy of the sensing when used as a scientific instrument. Sensors, data acquisition, storage, data recovery and exact timing reconstruction have to be designed to increase accuracy and stability, even under severely adverse conditions. The altitude and fluctuations in environmental conditions, particularly in temperature, have a dramatic impact on the performance and reliability of the electrical components, e.g. oscillators or analog digital converters. Their characteristics deviate significantly at the limits of operating ranges. Radio communication interferes with precision measurements causing imprecise measurements. Since the effective quantitative changes observed are typically rather small, meticulous care is required to reduce measurement noise and to compensate for or identify dependencies, especially on temperature, in the system architecture.

Reliability in Harsh Environments – Long-term environmental monitoring relies on reliable and correct operation of all components that are linking the sensor to the data utilization or interpretation. Redundancy features that are reducing the risk of a single point of failure need to be incorporated in the system architecture as well as means for data replication and validation. Environmental conditions in high-alpine regions are very inhospitable. Sensors deployed there are subject to rock fall, avalanches humidity, deep snowcover, thunderstorm and lightening strokes in the immediate vicinity. Temperatures vary from -40℃ in wintertime to +60℃ if exposed to direct sunlight. Ice coating, rime and snow covering of the sensor nodes can interrupt wireless communication for longer periods of time. Some of the most interesting permafrost phenomena can be observed in exposed, steep rock walls in high-altitude mountains. Access to deployment sites is difficult; heavy equipment can only be brought in by airlifting with helicopters. This rough terrain demands that the deployment process for the sensor nodes is simple and does not require on-site programming, configuration or calibration. A robust mechanical design of nodes and sensors is important in order to protect from damage during deployment and operation.

Durability and Energy Constraints – A prime objective of PermaSense is to achieve multi-year continuous operation. This exceptionally long runtime is motivated by two factors: (i) Many geophysical phenomena in permafrost regions change at a rather slow rate but are superimposed with annual, daily and higher-frequency cycles, hence requiring long term measurements. (ii) The remote, high-alpine deployment area makes access to the sensor nodes difficult. Therefore a specialized power supply for the sensor nodes must be considered. The harshness of the environment, potentially prolonged coverage under a thick layer of snow, the size of the required panel, its resulting susceptibility to damage and especially the uncertain effectivity if nodes are deployed on a northerly exposition without the benefit of direct sunlight render a solar power supply impractical. A Li-$SOCl_2$ battery is optimized for slow discharge at low temperatures down to -40℃. The battery selected provides a capacity of approximately 8.2Ah under the expected operating conditions, resulting in an allowable current consumption of ∼300µA to reach the anticipated system lifetime. This current is about 2 orders of magnitude lower than a node's consumption when all components are active. Hence, it is important to exploit sophisticated and rigorous power-saving techniques to achieve this ultra-low duty cycle.

In order to build a reliable environmental monitoring system that is able to cope with these challenges, careful orchestration and optimization of all system components, i.e., sensors, sensor nodes, wireless communication, base station, database backend at the soft- and hardware level is needed. In Section 4, methods are presented for highly accurate data acquisition, despite of the strong fluctuations in environmental conditions. In Section 5, we discuss the measures taken to build a highly reliable system in order to prevent the need for field maintenance. Section 6 shows how we customize hard- and software to meet the tight energy budget.

3. THE PERMASENSE ARCHITECTURE

The PermaSense architecture features the tiered architecture paradigm established since Great Duck Island [16]. Figure 2 displays an overview of the tiers: sensors, wireless sensor network, base station and backend and their respective individual components. Each of these tiers is able to operate self-supported in case one of the other tiers experiences failures or maintenance outages effectively minimizing data loss.

The sensor network consists of Shockfish TinyNodes [6] running the ultra low-power Dozer protocol for multi-hop data gathering [4]. The TinyNodes are mounted on a sensor interface board (SIB) that contains all necessary circuitry for data acquisition, power management and system supervision. Additionally the nodes are equipped with external data storage using a 1GB flash memory SD card. The sensor nodes are powered from

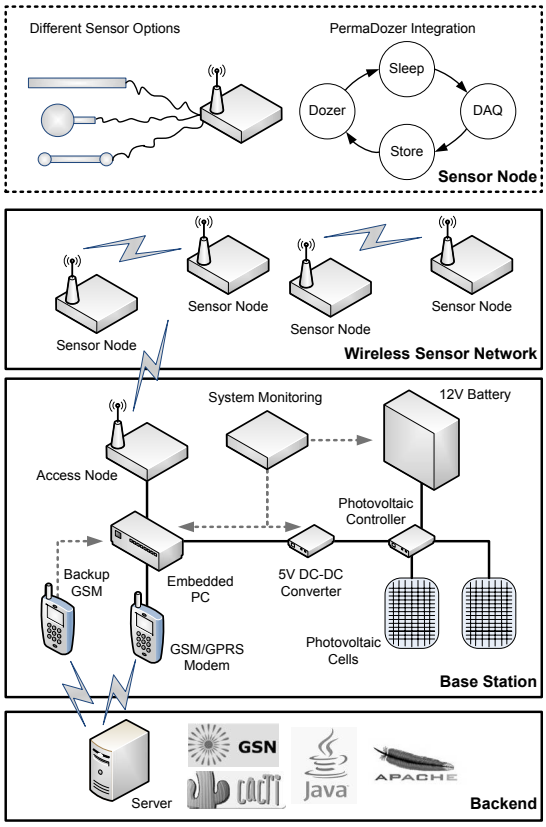

Figure 2: PermaSense System Architecture

a single non-rechargeable battery cell. The base station consists of an embedded PC platform connecting to a TinyNode used as access node to the sensor network and a data downlink (GPRS/EDGE) to the data backend.

Since it can be mounted in a shielded position, the base station is powered from a regenerative power supply using solar cells. The data backend consists of a server running GSN [1] as well as a number of control, supervision and management interfaces.

Constituting an obvious single point of failure and even worse, a component that is operated by an anonymous third party, the GSM/GPRS connection from the base station to the internet is an important reliability consideration for the whole system architecture. While multiple base stations and access nodes to the sensor network are an obvious way to circumvent any problems with reliable data transfers, they also add complexity and require to be installed and maintained. A backup using a second GSM/GPRS modem attached to the console of the base station is a simple yet effective method to remotely recover or reset a faulty base station or primary data link. This has been very successful and on several instances we have recovered and modified the base station software running at the deployment site.

In order to reduce the risk introduced by developing all necessary components from scratch, but also to lighten the workload and pressure on system development we made use of established solutions or adaptations of known and proven technologies wherever possible (cf. Table 1). In cases where no suitable solutions existed, a custom design specifically tailored to the given requirements of PermaSense was created.

Established Commodity Components
Base station embedded PC
Photovoltaic energy source
Online system monitoring and servicing
Adaptated/Partially Developed
Dozer multihop protocol
1 GB local storage extension
GSN data backend integration
Custom Developments Built from Scratch
Specialized sensors
Sensor interface board (SIB)
Data acquisition and storage integration
Mechanical component setup
Base station secondary communication

Table 1: Classification of technologies used according to the necessary development effort.

3.1 Dozer Operating Principles

To achieve reliable, high fidelity measurements the interference induced from other system components, e.g., radio communication or excessive processing demands needs to be observed with equal care as minimizing power and resource utilization. The Dozer protocol scheme [4] is optimally suited for this purpose as it leaves large windows for scheduling user tasks in between its periodic interaction with the radio for communication at a very low duty cycle of ∼0.1% and consuming only 0.082mW. A likely scenario is that a sensor node can be disconnected from radio connectivity for prolonged periods of time, e.g., when snowed in in winter. In this aspect, the scheme is very adequate as it actively reduces its duty cycle when connectivity is lost.

Dozer uses a TDMA-based link scheduling along a tree based routing structure. The tree structure is controlled by beacon messages originating at one or more sink nodes serving synchronization and data flow control purposes. Data is transported from children to parent on dedicated upload slots that follow a link based schedule. All data transfers are acknowledged. Rather than investing in complex collision avoidance schemes Dozer uses a precisely timed retransmission reducing excessive idle listening to a minimum. The adaptation of Dozer with the integration of custom data acquisition and storage in the dedicated processing window is called PermaDozer and is implemented in TinyOS (cf. Figure 2).

3.2 Custom Developments for PermaDAQ

3.2.1 Modular Architecture for Specialized Sensors

The PermaSense system architecture supports a number of sensors, predominantly oriented towards the acquisition of long-term, slowly fluctuating quantities. Currently the sensors supported are: (i) a sensor rod for profiling of temperature and electrical conductivity in solid rock, (ii) thermistor chains for profiling of temperatures inside cracks, (iii) crack meters consisting of a linear potentiometer for measuring movements, (iv) digital water pressure sensors to assess water flow in cracks, (v) analog earth pressure cells for assessing ice stress inside larger cracks and (vi) self potential sensors using analog differential conductivity measurements with electrodes mounted on the rock surface. To be able to consistently relate data acquired, calibration values and in-field sensor placement, each sensor contains an individual sensor identification chip that contains a unique serial ID. With the exception of the sensor rod, all these sensors are commercial and commonly used in geo-sciences.

3.2.2 Sensor Interface Board

A key deficiency of the first generation PermaSense prototype hardware [17] was the accuracy of the acquired sensor data, primarily due to the use of the internal AD converter and reference voltage circuit on the TinyNode's TI MSP430 microcontroller. Based on the experience with the first field deployment a dedicated sensor interface board was designed featuring precision AD channels, controllable voltage references, signal filtering and conditioning circuitry, ESD protection as well as in- and external power supplies and power management functions (cf. Figure 3 and Section 4.1 for details). With respect to other designs [18, 7, 2], this solution allows to switch dedicated power groups for all subsystems when not in use limiting power losses to leakage only.

3.2.3 Multi-Sensor Data Acquisition

Rather than designing a custom sensor node per sensor type, the PermaSense data acquisition architecture (PermaDAQ) is designed around a modular interface able to accommodate different combinations of sensors (cf. Figure 2). The key benefit of a modular solution is the ease and flexibility in the application at the expense of a more complex hardware and data acquisition routine. Furthermore, a single, multifunctional hard- and software is easier to maintain than a whole family of devices with varying function. A central part of this architecture is the DAQ routine that initializes the necessary components, calibrates the AD converter using the internal reference voltages, reads health information and then samples analog and digital sensor channels. Subsequently it returns into low-power sleep mode.

3.2.4 Storage Integration

All sampled data is stored locally on the sensor node. A custom buffering routine in the PermaDozer application takes care of archiving all generated data on a flash memory SD card present on every node. Since the SD card access is energy consuming, the data is first gathered in RAM before multiple data samples are written collectively to the SD card. The locally archiving of data allows for a delayed transmission of the data due to network outages. When snowed in, data is backlogged and subsequently flushed to the network upon restoration of reliable connectivity to the base station. The second and equally important purpose of the data storage is post-deployment validation. The data archived locally is used for checking sensor data integrity.

3.2.5 Mechanical Component Setup

The extreme exposure to the environment requires a robust, weatherproof enclosure, sufficient for protection from the elements and to withstand rock fall, avalanches and electrostatic discharge in the vicinity, i.e. lightning. Especially due to the latter, an absolute minimum of cabling is a stringent requirement. Furthermore, it is desirable that the whole mechanical setup is operable and maintainable in cold and wet weather using gloves, possibly even one-handed while suspended from a rope. Each sensor node is housed in a Rose+Bopla die-cast aluminum enclosure, using Souriau UTS series connectors and an outdoor antenna, all with a protection rating of IP68 which allows to sustain submergion in water. A stainless steel protective shoe adds additional protection, especially from rock falling from above as shown in Figure 4. The hanging mounting position minimizes the ingress of water through the antenna and connector as drops of water are not forming on the rubber seals instantly slipping down the cable(cf. Figure 5). Additionally a large 10g pack of silica gel is added inside every enclosure to absorb excess moisture. Silicon lubing of the antennas prior to mounting in the field reduces the risk of rime building up in bad/wet weather conditions.

3.2.6 Sensors for Subsurface Measurements

Many key permafrost processes can only be observed inside the rock walls. Therefore it was necessary to design custom sensors that are able to make observations below the surface. The main sensor employed by the PermaSense project is a long sensor rod that allows to measure profiles of temperature and electrical resistivity to discriminate the changing composition, i.e., the relative amounts of rock, ice, water and air, inside vertical rock walls. Each rod contains 4 thermistors and 4 electrode pairs equidistantly spaced that are connected to a multiplexer inside the sensor rod. Each sensor rod is inserted into a 1m deep hole drilled into the rock and at-

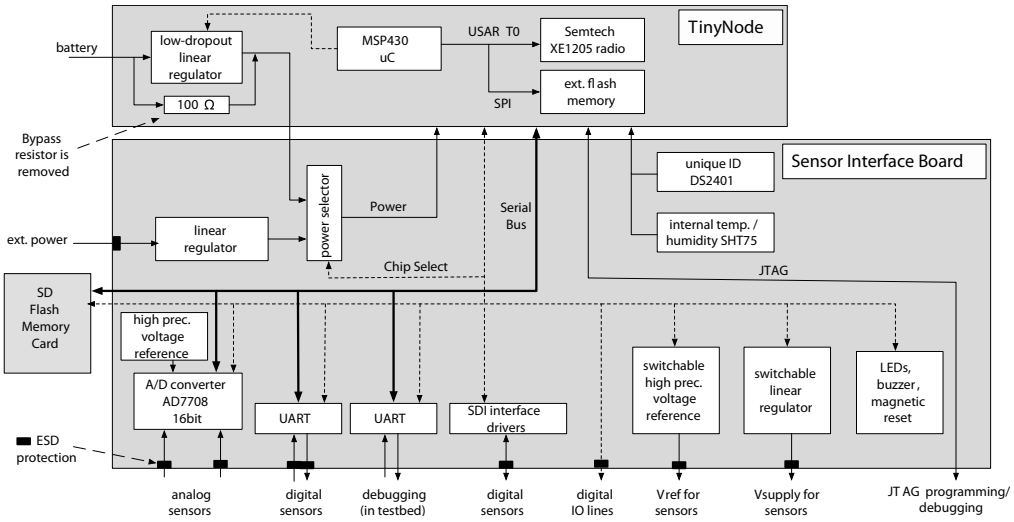

Figure 3: The SIB data acquisition architecture connects to a TinyNode over a single serial bus and uses GPIO pins to select dedicated power groups and address functional components.

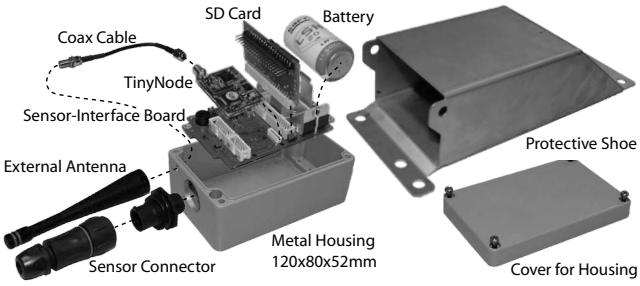

Figure 4: The sensor node is housed in an enclosure and mounted using a protective shoe.

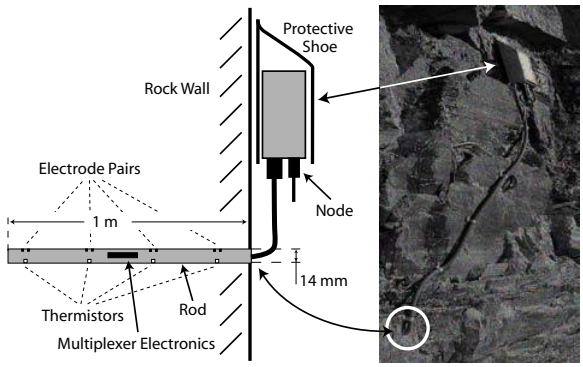

Figure 5: Sensor rod cross section diagram and a situation view from the mountain.

tached to a sensor node mounted nearby (cf. Figure 5). Calibration is done using a temperature controlled bath.

4. HIGH-QUALITY DATA ACQUISITION

4.1 Power Efficient Serial DAQ Architecture

The multitude of different sensors to be used in conjunction with the TinyNode and their precision requirements necessitate custom data acquisition hardware. The sensor interface board (SIB) is designed to allow flexible use of different sensors, both analog and digital; its supply can either be an internal battery or external 12V supply power source. Power consumption is minimized while components are not in use, which in the case of PermaSense is the predominant part of the time.

For this purpose all components are wired to a single serial bus using individual chip-select lines for selectively enabling these components (cf. Figure 3). The required 2.8V operating voltage is generated using the linear regulator on the TinyNode and distributed to the consumers on the SIB. Similarly to the multiplexing of the data bus, the power distribution to individual groups of consumers can be controlled in software.

The analog channels are sampled using an 8-channel Σ-Δ analog digital converter with 16-bit resolution (Analog Devices AD7708) and an external, temperature compensated precision voltage reference. An upgrade to a 24-bit ADC is possible if required. A number of features to aid testing, maintenance and deployment are integrated in the SIB: A unique serial ID allows to identify the individual hardware entity used, an additional UART allows synchronous debugging in a testbed setting, JTAG supports interactive debugging, LEDs can be enabled by individual jumpers to assure they are not accidentally powered on in a field deployment, a buzzer and magnetic reset (reed contact) allow to reset and check the booting sequence in the field and a temperature and humidity sensor is used to assess node health.

4.2 Increasing the Data Acquisition Accuracy

An initial implementation of the DAQ routines was designed in distinct phases of initialization, calibration, analog common ground and differential modes and digital measurements to ease future customization when optimizing for a single sensor type only, e.g., when only analog multiplexed is required. Each sensor measurement routine is furthermore preceded by a measurement of local node health parameters internal voltage, temperature and humidity inside the enclosure.

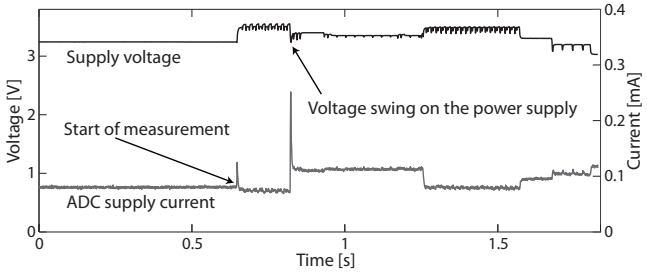

Figure 6: Detail measurement of the voltage supply swing in relation to the current consumed by the ADC causing imprecise measurements.

This DAQ routine functionally worked but showed considerable noise, especially on sensor types, such as the crack meter, that do not contain any higher frequency noise components (cf. the left on Figure 8). A more detailed analysis revealed some deficiencies in the actual drivers and routines, but more severely a direct connection to the stability and quality of the power supply. A detailed measurement was performed (cf. Figure 6) and the source of the considerable voltage swing on the supply voltage of the AD converter and reference voltage circuit on the SIB could be identified. Due to the bypass resistor present on the linear regulator on the TinyNode (100Ω as shown in Figure 3) the voltage generated is not fix but depends on the input voltage, i.e. the battery level and the actual current drawn. The TinyNode uses this feature to be able to shut down the regulator when entering sleep modes saving the quiescent current of 17µA versus 1µA in standby. The magnitude of this effect is especially prominent when the load is low and the battery level is high, i.e., when the regulator is not actually working, but the main current is drawn through the 100Ω bypass resistor. Only when the current exceeds the amount the bypass resistor is designed to handle, the regulator kicks in and actually supplies a regulated system voltage. Spontaneous peaks on the current being drawn, e.g., when turning on the radio transmitter add to the instability of this voltage, driving the critical data acquisition.

In order to resolve this issue, the bypass resistor was removed and the linear regulator forced on by an extra pull-up resistor. While at a first glance not deemed extremely severe, an increase in the sleep current consumption by 16µA is a considerable price to pay for the required data accuracy.

4.3 Strict Separation of Operating Phases

The reduction of all possible interference is of concern in the overall system integration of the PermaDozer application. If not accounted for properly a number of issues can lead to degraded performance: (i) Any consumer has influence on power quality and supply stability. (ii) Any switching of circuits causes noise on other circuits. This is especially prominent with RF interference from the radio on analog measurements, e.g. when coupled over a common ground plane. (iii) Exact timing is critical for many low-level software routines controlling critical hardware in real-time. Accurate and timely servicing of all interfaces in the order specified at design time and actively reducing any unnecessary interruption at run-time are the key requirements to achieve precision and reliability. Figure 6 shows an example of the ADC operation impacting voltage stability. If not separated clearly by the design, different components are bound to interfere which each other, degrading performance or even breaking the functionality.

The system model behind Dozer lends itself to an integration with a strict separation of the coarse grained operating phases responsible for different subsystems that would otherwise not be enforced in the event driven TinyOS operating model. Dozer supports a processing window in between its periodic interactions with the radio. All processing designed to be performed inside this window must be guaranteed to finish before the next communication phase commences. Therefore the DAQ routine runs (nearly) uninterrupted inside this window.

The separation and interleaving of the operating phases DAQ and Dozer is shown in Figure 7 for a network of three nodes (and one access node not displayed here). The DAQ routine is triggered every two minutes and is not synchronized across the network. The current peaks resembling Dozer beacons and data transfers depict the synchronization of the Dozer protocol scheme. With the improvement in power quality and strict separation of functions the data acquisition precision was improved by ∼24x (cf. Figure 8). This accuracy now leads to first results in the geo-science domain [10].

4.4 Exemplary Sensor Rod Data from the Field

An intermediate deployment using a logging only version of the software was used to gather first sensor data in the field and prove the SIB hardware design. This step was necessary both from a geophysical standpoint preliminary data analysis as well as from an engineering standpoint to see the performance of the system design

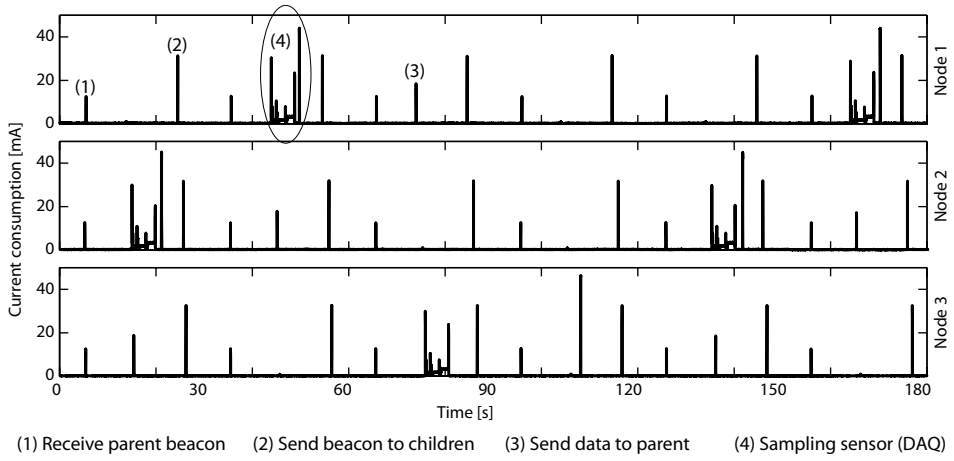

Figure 7: Power traces measured show periodic but asynchronous invocation of the DAQ routine (4) with subsequent data transfers (3) every 2min. Dozer beacon transfers (1) and (2), responsible for network synchronization are executed every 30sec.

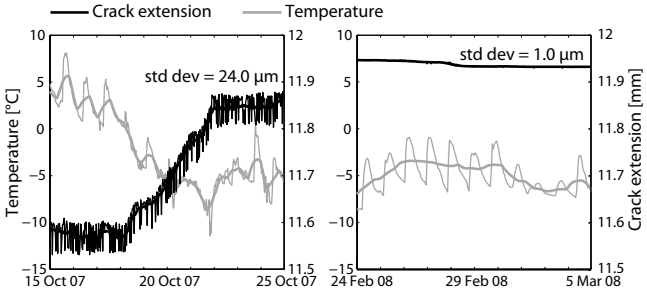

Figure 8: Improved accuracy and signal stability as a result of software refinement and stabilized power supplies. The difference in the two data sets shown is attributed to the measures described in Section 4.

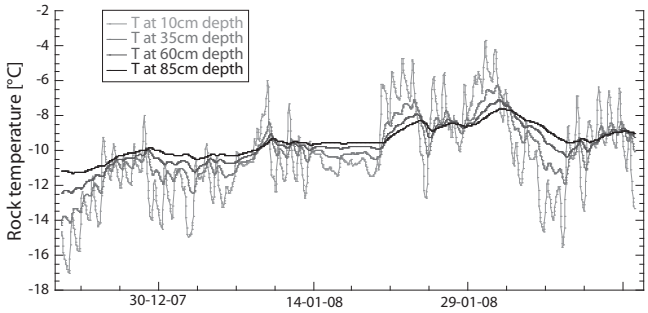

Figure 9: Example field data: As daily temperature cycles progress into the rock the signal is attenuated and phase shifted.

in a real operating case. Figure 9 shows example data generated using a sensor rod and SIB/TinyNode during the winter of 2006/2007 on Matterhorn. The strong peaks seen near the surface are attenuated and shifted as they protrude through the rock which is one of the phenomena that PermaSense is trying to observe in detail. This exemplary data is presented here as a proof of the validity and applicability of the system designed.

5. RELIABILITY – A LOOK UNDER THE HOOD

5.1 Energy Supply for Subzero Temperatures

Standard batteries, especially widely used NiMH and Li-Ion rechargeable cells have very bad characteristics in low temperatures. Their ability to deliver current close to the rated cell voltage diminishes quickly with the temperature dropping as well as the total capacity contained over a longer period of time. In contrast, specialized cell chemistries such as Li-$SOCl_2$ batteries exhibit good performance across a much wider temperature range at the cost of reduced peak discharge capability. Based on the expected peak current consumption of the SIB/TinyNode combination, a maximum form factor of a D-cell and the extremely high lifetime requirement under the given temperature constraint, a suitable Li-$SOCl_2$ cell (Saft LSH-20) was selected.

Nominal battery capacity [mAh]	13000
Nominal voltage [V]	3.6
Self discharge rate per year [%]	3%
Capacity at -40℃, 20mA discharge [mAh]	8200
Capacity at -40℃, 20mA, 3 years [mAh]	7462
Mean current available [mA]	**0.284**

Table 2: Power budget based on Saft LSH-20

The key characteristics can be seen in Table 2. Based on a self discharge rate of 3% per year and a nominal worst case capacity of 7462mAh the mean current available for the whole application was estimated to be 0.284mA. Of course there are a number of unknowns: (i) the peak discharge current (Table 4) is considerably higher than 20mA but again the average is much lower; (ii) temperature is expected to not always remain at -40℃; (iii) different sensors require different amounts of energy that can only be accounted for in average here and (iv) the actual discharge characteristics over such a long period of time are not available. This energy supply was selected from several competitors and deemed suitable for the formulated design goal of an average current consumption of ∼300 µA. As a safeguard against further adverse effects, e.g., peak currents, an optional super capacitor is integrated. So far the energy resources have been sufficient without this additional super capacitor.

5.2 Increasing the Storage Capabilities

The reliability constraint for PermaSense is a data yield of 99% with max. 10 consecutive samples being lost. While this primarily translates into an uptime requirement of the nodes and the network, it also requires correct dimensioning of the network and most importantly local storage when the communication system experiences failures. In general, such communication failures are attributed to poor connectivity, interference or system component failures. In the special case of high-alpine environmental monitoring the seasonal snow cover and the weather induced build-up of rime, e.g., on nodes and antennas, can mean that parts of the network are inaccessible for longer periods of time. During this time data sampling naturally must continue with local buffering and data delivery happening delayed when connectivity is restored. The specification lists 6 months of autonomous storage as a requirement.

Table 3 shows an approximate calculation of the data amounts generated by the data acquisition routine for a relaxed 30min DAQ interval, and also for 2, respectively 1min worst case calculations. Given that a single node only generates about 240MB and a network of 20 nodes only generates about 4.8GB of sensor data over a period of three years it seems feasible to equip both sensor nodes and the base station with sufficient storage resources using conventional flash memory technology. The cost on the bill of material is negligible and energy requirements can be kept low if bulk access methods are used and integration is performed with some care [15].

Using the worst case calculation with a 1min interval, single nodes are equipped with a 1GB storage resource leaving enough room for auxiliary timestamping and data structures. Since enough storage space for copies of all data acquired at every node is available,

DAQ Interval	1min	2min	30min
Byte/day/node	233280	116640	7776
TinyOS packets[a]/min	7.04	3.52	0.234
Mbyte/year/node	80.0	40.1	2.64
Mbyte/3years/20nodes	4805	2403	160

[a] 23 byte per TOS packet

Table 3: Estimation of the DAQ data volume

we store duplicates of all data, to be used for validation of the sensor data across the whole system. Remember that accurate and valid data is of primary importance when using a sensor network as a scientific instrument.

The sensor nodes use a stripped down FAT file system that allows for reading out the buffered data on every PC. The base station writes an additional copy to its flash disk, including an NTP synchronized time stamp, which allows backup and direct validation with the data contained in the final database.

5.3 Dimensioning the Networking Component

Dozer is based on a quasi-periodic, extremely low duty cycle that can be parameterized. Data gathering is initiated and controlled by beacon packets that contain synchronization as well as routing and flow control information. In agreement with the original Dozer publication [4] and further counseling with its authors a ratio of a maximum of 1:4 between the packet generation rate and the beacon rate has been used in the parameterization of the PermaDozer application. With the calculated load on the network, the Dozer protocol is parameterized to sample and generate data packets every 2min and Dozer beacons every 30sec. This beacon interval has been optimized and carefully tested by its original authors to account for temperature drift that would eventually lead to de-synchronization and loss of connectivity. Each beacon period is capable of transmitting 20 data packets. In the case of flushing data backlogged on a node, a maximum of 10 packets is submitted to the network queue per beacon period as not to excessively overload the network. This has been found to be robust and offer sufficient performance for this application. The discussion in this paper is based on this 2min and 30sec case. Effects of varying network traffic, topology etc. have been neglected.

5.4 Internal Node Health Indicators

The protection from the elements and sufficient energy are key to a durable and lasting outdoor sensor network deployment [16]. In order to continuously assess node health and to be able to schedule repair or replacement of faulty node hardware well in advance every enclosure contains an individual node health indicator that measures ambient temperature, humidity and the

battery voltage. Figure 10 shows such health data over a period of one month for a node mounted on a vertical rock wall, facing south, exposed to considerable temperature variability on clear weather conditions. Especially notable is the stress induced by the large daily temperature variation. The system voltage is extremely stable and the low humidity values around 10% suggest that the enclosure and connector are in good condition. This indicator is invaluable should any moisture protrude inside the enclosure causing permanent damage.

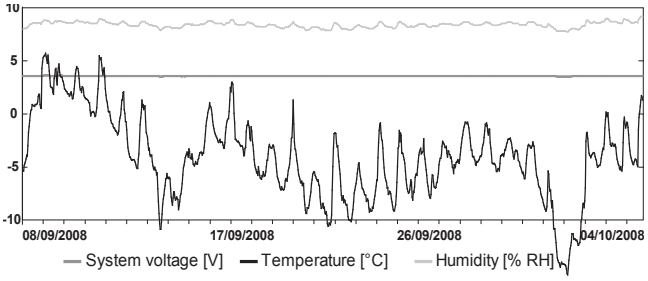

Figure 10: The system voltage shows exceptional stability over strong variation in temperature.

6. ENERGY EFFICIENT DESIGN

The PermaDAQ data acquisition architecture is a complex system composed of a number of individual consumers (e.g., radio, microcontroller, memory, data acquisition, sensors, debugging) each with their own characteristics and operating modes. Due to the complexity and interaction of system components, it is not possible to calculate the power consumption of the complete system in detail in advance, but only simple estimations based on individual values derived from datasheets. However in order to be able to assess the lifetime of a sensor node a detailed analysis of the power consumption and the contribution of the different subsystems is required. Measurements characterizing the operating modes sleep, data acquisition (DAQ) and communication (Dozer), are shown in Table 4. Additionally, average power consumption over a 10min period is shown for partial implementations (DAQ only, Dozer only) as well as the complete PermaDozer application. Measurements have been performed using a fixed 3.6V power supply and a 12 node tabletop network. A detailed power trace of several nodes in operation is shown in Figure 7.

The important fact to note is that with a total power consumption of 148µA the required goal of ∼300µA has been achieved if not surpassed. An analysis of the individual components contributing to this power consumption is calculated as follows: Both partial implementation values contain the same system overhead for running the system core but differ in contribution in their respective function. This overhead is calculated as the

Operating Mode Characterization	**[mA]**
Sleep	0.026
DAQ active[a]	2.086
Dozer RX idle	13.64
Dozer RX	14.2
Dozer TX	54.6
Measured Average Values	**[mA]**
DAQ only (2min)	0.110
Dozer only (30sec/2min)[b]	0.072
PermaDozer total (30sec/2min)	**0.148**

[a] Averages power consumption measured over a complete DAQ routine execution without attached sensor
[b] Dozer only includes communication, not including network initialization and access to flash memory

Table 4: Power consumption for individual modes as well as the aggregate duty cycle for PermaDozer, measured at 3.6V

difference between the two partial values and the total: $P_{SYS} = P_{DAQ} + P_{DOZER} - P_{TOTAL}$. In an approximation this system overhead can be split into a contribution of the lowest achievable power state (sleep) and a functional overhead. The individual contributions in mA for the contributions of P_{SYS} (sleep + overhead) 23.0%, P_{DAQ} 51.4% and and P_{DOZER} 25.7% leading to the total of 0.148mA are presented in Figure 11.

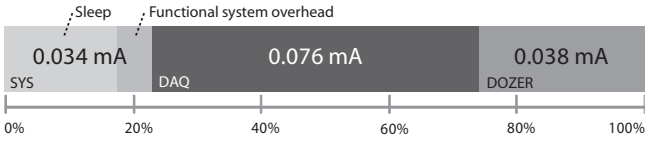

Figure 11: 0.148mA total power consumption is split into contributions for SYS (with sleep and overhead), DAQ and DOZER at a ratio 1:2:1.

Surprising is the high contribution of the sensing routine. This is in strong contrast to the common belief that the dominant cost of low-power wireless sensing systems is in the communication [13, 12]. Not the general assumptions on the relation of the energy cost for communication and computation are wrong or have changed, but past discussion has been focusing mainly on the power consumption of the individual subsystems in isolation, and not in an integrated context. In the given system context, especially with a complex and time consuming DAQ routine (cf. Figure 12), the overall picture changes which can be seen in the ratio of 1:2:1 for P_{SYS}, P_{DAQ} and P_{DOZER} respectively. It is neither the modular design nor poor engineering of the DAQ routine that causes such a high contribution: The cause is in the fundamentals of sensing itself. The dominant time of the DAQ routine is spent waiting for power

hungry components to initialize, reference voltages and frequencies to stabilize and on refining precision on elaborate interleaved measurements of analog channels and references in order to achieve the precision required. Related sensor network projects [18], although operating at a different performance point, have also noted this dominant contribution of the ADC power consumption.

It is worth to note, that although meticulous care has been taken to reduce sleep consumption to an absolute minimum, the influence on overall power performance is significant and further reduction should be pursued. The contribution of sleep, including the 16 µA introduced by the stability enhancement described in Section 4.2 are visible in the leftmost grey bar in Figure 11.

Figure 12 shows the complete DAQ routine measured for different types of sensors. Depending on the sensor type used and especially the duration of the SIB-sensor interaction the average power consumption of the DAQ part alone can vary by as much as 250%. In the case of some sensors, e.g., electrodes used for conductivity measurements on the rock surface (not shown here), the power consumption is additionally dependent on the actual material and environmental conditions encountered at the specific location. As a result, the type of sensor and its respective energy requirement must also be considered in the discussion of the total power budget.

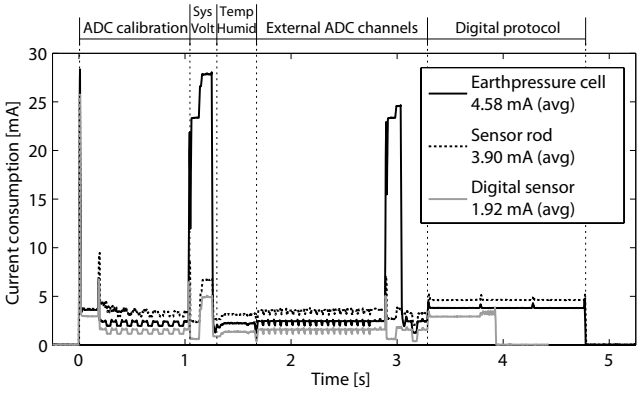

Figure 12: Detailed operating mode characterization of the multifunctional DAQ routine for different sensors shows significant difference depending on the sensor type used.

7. RELATED WORK

There is an extensive body of work on environmental monitoring deployments [14]. We concentrate our discussion on representative deployments targeting the three criteria for the PermaSense project.

Great Duck Island (GDI) [16] is one of the earliest long-term sensor network deployments monitoring a wildlife habitat for a period of 123 days. While the tiered architecture proposed then is a standard followed by most other systems and much of the initial experience gained remains a valuable contribution, both the sensing requirements and the environmental constraints of GDI are rather relaxed compared to PermaSense. Custom, high-quality sensing, the extreme environmental conditions and required longevity require additional measures to be taken both for node and system reliability.

Similar in terms of extreme environmental conditions and longevity is the Glacsweb project [11] monitoring subsurface phenomena in the Briksdalsbreen glacier. Sensor nodes are submerged inside the glacier, flowing along within the ice at different depths. Sensor data is gathered over multiple years, with intermediate data storage accommodating for periods of communication loss. Ranging between sensor nodes determines node positions. The main difference is the quality of sensor data and the non-retrievable nodes. Glacsweb probes merely pressure and resistivity using a simple microcontroller, while PermaSense supports a number of novel high quality sensors with precision data acquisition hardware providing data of diverse permafrost related phenomena.

Sensorscope [3] is a prominent environmental monitoring project in the Swiss Alpes. It differs in its goals, as the deployments are targeted for shorter term measurement campaigns. Instead of accuracy of individual sensors, the system design strives for generating models by high spatial density of inexpensive sensors in parts following the original Smart Dust paradigm. All nodes are powered by solar cells and hence do not require the strict conservation of energy like PermaSense.

From a data acquisition quality perspective, the closest project to PermaSense is volcano monitoring [18], which requires high fidelity data sampled at a very high rate (100Hz). As a result of the combination of energy required to transmit the high data rate, the choice of the Telos platform and the use of a standard, small form factor battery, the deployments are not designed for a long lifetime, i.e., requiring several battery changes over a project lifetime of 19 days.

8. CONCLUDING REMARKS

PermaSense is an ambitious project opening new horizons in the otherwise well-travelled domain of WSNs for environmental monitoring. Particulars are the high reliability, accuracy requirements, the extremes of the environment targeted as well as the longevity. Contrary to many first generation efforts PermaSense builds on the refinement of proven technology in practice, rather than dominantly building from scratch. In this sense the PermaDAQ architecture with the sensor interface board (SIB) and PermaDozer integration presented in this paper evolved based on the large body of related work and own prototypical experience and of course also failures.

This practical and requirement driven approach has lead to a number of successes that are described here. The mechanical setup designed has shown to work extremely well, significantly simplifying deployment and maintenance. So far no mechanical damage to nodes has been observed and servicing of a 15 node deployment with the exchange of nodes is performed in under two hours.

A strict design for testability and many redundancy features are key to success with respect to accurate, timely and complete data recovery from the field. The field site on Matterhorn has been operating continuously since being equipped in mid July 2008. An analysis of the network performance and especially the sensor data is not the focus of this paper. Temporary servicing of individual components during the initial deployment phase has resulted in no significant data losses. The preliminary analysis presented suggests that the accuracy improvements made will lead to substantial scientific results in the near future. The storage component introduced further enhances reliability by allowing delayed transmission and precision by support of post-deployment data validation – a necessity should WSNs be more widely adopted as a scientific instrument. The power consumption goal set or the operable PermaDAQ architecture has been more than achieved leaving enough slack to guarantee the required lifetime.

9. ACKNOWLEDGMENTS

The work presented was supported by NCCR-MICS, a center supported by the Swiss National Science Foundation under grant number 5005-67322 and the Swiss Federal Office for the Environment (FOEN). We are grateful for the support of the International Foundation High Altitude Research Stations Jungfraujoch and Gornergrat (HFSJG). Additionally we thank our collaborators for the tireless help and advice given: N. Burri, P. von Rickenbach (Dozer), H. Gubler (sensor rods), S. Schoenborn (data analysis), R. Schmid (SIB), A. Salehi (GSN), C. Guntermann and J. Hunziker (storage).

10. REFERENCES

[1] K. Aberer, M. Hauswirth, and A. Salehi. A middleware for fast and flexible sensor network deployment. In *Proc. 32nd Int'l Conf. Very Large Data Bases (VLDB '06)*, pages 1199–1202. ACM Press, New York, 2006.

[2] A. Arora, P. Dutta, S. Bapat, V. Kulathumani, H. Zhang, V. Naik, V. Mittal, H. Cao, M. Demirbas, M. Gouda, Y. Choi, T. Herman, S. Kulkarni, U. Arumugam, M. Nesterenko, A. Vora, and M. Miyashita. A line in the sand: a wireless sensor network for target detection, classification, and tracking. *Computer Networks*, 46(5):605 – 634, 2004.

[3] G. Barrenetxea, F. Ingelrest, G. Schaefer, M. Vetterli, O. Couach, and M. Parlange. Sensorscope: Out-of-the-box environmental monitoring. In *Proc. 7th Int'l Conf. Information Processing Sensor Networks (IPSN '08)*, pages 332–343. IEEE CS Press, Los Alamitos, CA, 2008.

[4] N. Burri, P. von Rickenbach, and R. Wattenhofer. Dozer: ultra-low power data gathering in sensor networks. In *Proc. 6th Int'l Conf. Information Processing Sensor Networks (IPSN '07)*, pages 450–459. ACM Press, New York, April 2007.

[5] K. Chebrolu, B. Raman, N. Mishra, P.K. Valiveti, and R. Kumar. Brimon: a sensor network system for railway bridge monitoring. In *Proc. 6th Int'l Conf. Mobile Systems, Applications, and Services (MobiSys 2008)*, pages 2–14, New York, NY, USA, 2008. ACM Press, New York.

[6] H. Dubois-Ferrière, L. Fabre, R. Meier, and P. Metrailler. Tinynode: a comprehensive platform for wireless sensor network applications. In *Proc. 5th Int'l Conf. Information Processing Sensor Networks (IPSN '06)*, pages 358–365. ACM Press, New York, 2006.

[7] P. Dutta, J. Taneja, J. Jeong, X. Jiang, and D. Culler. A building block approach to sensornet systems. In *Proc. 6th ACM Conf. Embedded Networked Sensor Systems (SenSys 2008)*, pages 267–280. ACM Press, New York, November 2008.

[8] S. Gruber and W. Häeberli. Permafrost in steep bedrock slopes and its temperature-related destabilization following climate change. *Journal of Geophysical Research*, 112(F02S18), 2007.

[9] S. Gruber and W. Häeberli. Mountain permafrost. In R. Margesin, editor, *Permafrost Soils*, Biology Series, page 348pp. Springer, Berlin, 2008.

[10] A. Hasler, I. Talzi, J. Beutel, C. Tschudin, and S. Gruber. Wireless sensor networks in permafrost research - concept, requirements, implementation and challenges. In *Proc. 9th Int'l Conf. on Permafrost (NICOP 2008)*, volume 1, pages 669–674, June 2008.

[11] K. Martinez, P. Padhy, A. Elsaify, G. Zou, A. Riddoch, J. K. Hart, and H. L. R. Ong. Deploying a sensor network in an extreme environment. In *Proc. Int'l Conf. Sensor Networks, Ubiquitous, and Trustworthy Computing (SUTC 2006)*, volume 1, pages 186–193. IEEE, Piscataway, NJ, June 2006.

[12] G.J. Pottie and W.J. Kaiser. Wireless integrated network sensors. *Communications of the ACM*, 43(5):51–58, May 2000.

[13] J.M. Rabaey, M.J. Ammer, J.L. da Silva Jr., D. Patel, and S. Roundy. PicoRadio supports ad hoc ultra-low power wireless networking. *IEEE Computer*, 33(7):42–48, July 2000.

[14] K. Römer and F. Mattern. The design space of wireless sensor networks. *IEEE Wireless Communications*, 11(6):54–61, December 2004.

[15] L. Selavo, A. Wood, Q. Cao, T. Sookoor, H. Liu, A. Srinivasan, Y. Wu, W. Kang, J. Stankovic, D. Young, and J. Porter. LUSTER: wireless sensor network for environmental research. In *Proc. 5th ACM Conf. Embedded Networked Sensor Systems (SenSys 2007)*, pages 103–116. ACM Press, New York, November 2007.

[16] R. Szewczyk, J. Polastre, A. Mainwaring, and D. Culler. Lessons from a sensor network expedition. In *Proc. 1st European Workshop on Sensor Networks (EWSN 2004)*, volume 2920 of *Lecture Notes in Computer Science*, pages 307–322. Springer, Berlin, January 2004.

[17] I. Talzi, A. Hasler, S. Gruber, and C. Tschudin. PermaSense: investigating permafrost with a WSN in the Swiss Alps. In *Proc. 4th IEEE Workshop on Embedded Networked Sensors (EmNetS-IV)*, pages 8–12. ACM Press, New York, 2007.

[18] G. Werner-Allen, K. Lorincz, J. Johnson, J. Lees, and M. Welsh. Fidelity and yield in a volcano monitoring sensor network. In *Proc. 7th Symp. Operating Systems Design and Implementation (OSDI '06)*, pages 27–27, Berkeley, CA, 2006. USENIX Association, Berkeley, CA.

Paper III | Thermal conditions

Temperature variability and offset in steep alpine rock and ice faces

Focus

Temperature data from two permafrost field sites is analysed in respect to variability and thermal offsets. The 17 shallow temperature profiles considered span different surface and near-surface characteristics and comprise north and south oriented locations. Mean annual temperatures and time series are interpreted regarding the processes explaining the observed variation.

Main findings

- *Locations with snow retention due to mid-steep slope (45–70°) and micro topography show lower mean annual temperatures than snow-free locations.*
- *The temperatures within open clefts are colder than the rock temperatures in similar situations most likely due to ventilation effects.*
- *Both effects are stronger in radiation exposed faces and are on the order of 1–3 °C cooling.*

Citation

Hasler, A. Gruber, S. Haeberli, W. 2011. Temperature variability and thermal offset in steep alpine rock and ice faces. The Cryosphere 5. 977–988.

Paper published in THE CRYOSPHERE in November 2011

Temperature variability and offset in steep alpine rock and ice faces

A. Hasler, S. Gruber, and W. Haeberli

Glaciology, Geomorphodynamics and Geochronology, Department of Geography, University of Zurich, Switzerland.

Received: 8 February 2011 – Published in The Cryosphere Discuss.: 1 March 2011
Revised: 12 October 2011 – Accepted: 14 October 2011 – Published: 10 November 2011

ABSTRACT

The thermal condition of high-alpine mountain flanks can be an important determinant of climate change impact on slope stability and correspondingly down-slope hazard regimes. In this study we analyze time-series from 17 shallow temperature-depth profiles at two field sites in steep bedrock and ice. Extending earlier studies that revealed the topographic variations in temperatures, we demonstrate considerable differences of annual mean temperatures for variable surface characteristics and depths within the measured profiles. This implies that measurements and model related to compact and near-vertical bedrock temperatures may deviate considerably from conditions in the majority of bedrock slopes in mountain ranges that are usually non- vertical and fractured. For radiation-exposed faces mean annual temperatures at depth are up to 3°C lower and permafrost is likely to exist at lower elevations than reflected by estimates based on near-vertical homogeneous cases. Retention of a thin snow cover and ventilation effects in open clefts are most likely responsible for this cooling. The measurements presented or similar data could be used in the future to support the development and testing of models related to the thermal effect of snow-cover and fractures in steep bedrock.

KEY WORDS: bedrock permafrost; rock face, ice face, thermal offset

1. Introduction

Steep rock and ice faces cover a large proportion of the area of high mountain ranges (Gruber and Haeberli, 2007) and permafrost and ice-cover, which both are dependent on climatic conditions affect slope stability and hazards endangering human lives and infrastructure in alpine regions (Haeberli et al., 1997). For the estimation of such hazards, especially with respect to climate change, knowledge about the thermal state and evolution of these faces is important. How- ever, only limited temperature datasets from steep bedrock permafrost and ice flanks exist: (a) Less than a hundred time series of high-alpine rock (near-) surface temperatures measurements exist (Gruber et al., 2004; Pogliotti et al., 2008; Allen et al., 2009; PERMOS, 2010; Wegmann et al., 1998; Coutard and Francou, 1989; Matsuoka, 2008; Matsuoka and Sakai, 1999); (b) only few boreholes for temperature measurements in steep bedrock permafrost exist in the Euro- pean Alps (PERMOS, 2010; Noetzli et al., 2010; Wegmann, 1998); (c) no empirical study on the temperatures of steep ice faces is known to the authors. One use of the surface temperature measurements is the validation of distributed surface energy balance models to extrapolate rock face temperatures in space and time and to assess permafrost distribution (Gruber et al., 2004; Noetzli et al., 2007). Further, the long-term time series of these temperatures serve as a proxy for the permafrost conditions in steep bedrock (PERMOS, 2010).

In this study we address the question how representative surface temperature measurements

are and whether systematic deviations (thermal offsets) between the mean annual rock/ground surface temperature (MAGST) and the permafrost temperature below exist. We investigate the variability of rock temperatures and thermal offsets and their dependence on surface and near-surface characteristics. As a special case of surface characteristics we additionally investigated the thermal condition in a thin (< 10 m) ice cover of a steep rock face, which usually are called *ice faces* and that indicate underlying permafrost. We analyse mean annual temperatures and thermal offsets derived from 17 shallow temperature profiles in bedrock, rock clefts and ice at Matterhorn and Jungfraujoch (Swiss Alps). The approach to analyse the dependency of subsurface temperatures on the different characteristics is descriptive-heuristic, hence we quantitatively describe differences (Sect. 4) and try to understand this observed variation in terms of the driving processes (Sect. 5).

2. Site description and data acquisition

2.1. Field sites

In this study, distributed temperature measurements from two permafrost field sites in the Swiss Alps – Matterhorn and Jungfraujoch – are analysed. The sites are located at similar elevation and in comparable topographic situations but differ concerning their geological structure and near-surface characteristics. In proximity of both sites rock falls of small to medium magnitude (≈ 1000–150'000 m^3) occurred within the last century. The Matterhorn is part of the main divide of the western Alps that marks the Swiss-Italian border. The Matterhorn field site (*mh*) is at the north-east ridge called Hörnligrat at an elevation of 3450 m a.s.l. and comprises both sides of the ridge with main orientations southeast and north (Figure 2). The bottoms of both rock faces are glaciated, on the south-eastern side by a large plateau causing strong reflection of solar radiation. Jungfraujoch (3500 m a.s.l.) is a mostly glaciated saddle of the northern Alpine range dividing the northern Pre-alps from the glaciated Aletsch basin. The "Sphinx" is an exposed rock ridge in the saddle with diverse tourist and research facilities. The measurement locations are on the northern and southern side of the Sphinx (Figure 3).

The mean annual air temperature (MAAT, average 1961–1990) is approximately –6.7 °C at the Matterhorn field site and –7.3 °C at the Jungfraujoch (Hiebl et al., 2009) and currently subject to an accelerating warming trend (Beniston, 2005). Except for some occasional rainfall in summer, all precipitation falls as snow, hence liquid water is mainly supplied by snow melt. Due to the location at the northernmost high-alpine ridge with corresponding orographic cloud formation, the Jungfraujoch receives less annual solar radiation and more precipitation than Matterhorn-Hörnligrat. The southern rock faces at both field sites experience extreme solar radiation due to reflection from the glaciers underneath, making strong daily cycles with positive rock surface temperatures common in clear-sky conditions during all seasons.

The structure at the two field sites differs mainly with respect to fracturation: Although metamorphic crystalline rocks prevail at both sites, the frequency and aperture of clefts is significantly different. At Jungfraujoch 5–20 clefts per meter and apertures of 0.5 mm to 3 cm are typical (Figure 4) while at Matterhorn clefts are less frequent (0.5–5 cl m-1) but have larger typical apertures (3–30 cm) (Figure 5). This difference affects the thermal properties of these rock masses, because the thermal parameters of the inter-joint rock mass are overprinted by the geometric setting of the discontinuities: Changes in water content and phase state within these discontinuities will influence the overall thermal conductivity in a near-surface layer more than what may be expected from the laboratory-derived thermal parameters of intact rock samples. The described difference in the cleft characteristics in similar topographic situation was an important motivation for the selection of the two complementary field sites.

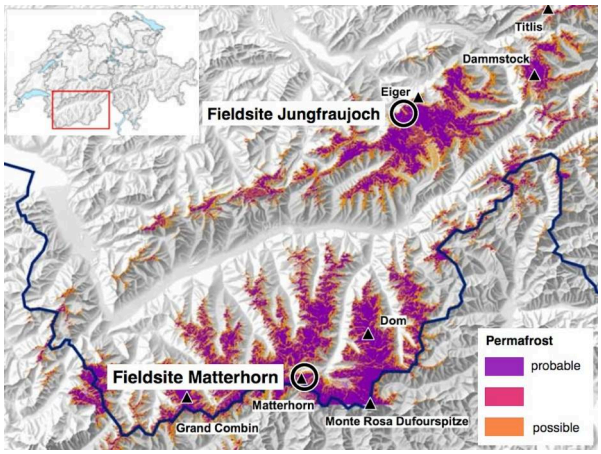

Figure 1: Location of the two field sites. The base map shows the potential permafrost distribution in the western Swiss Alps (FOEN 2006).

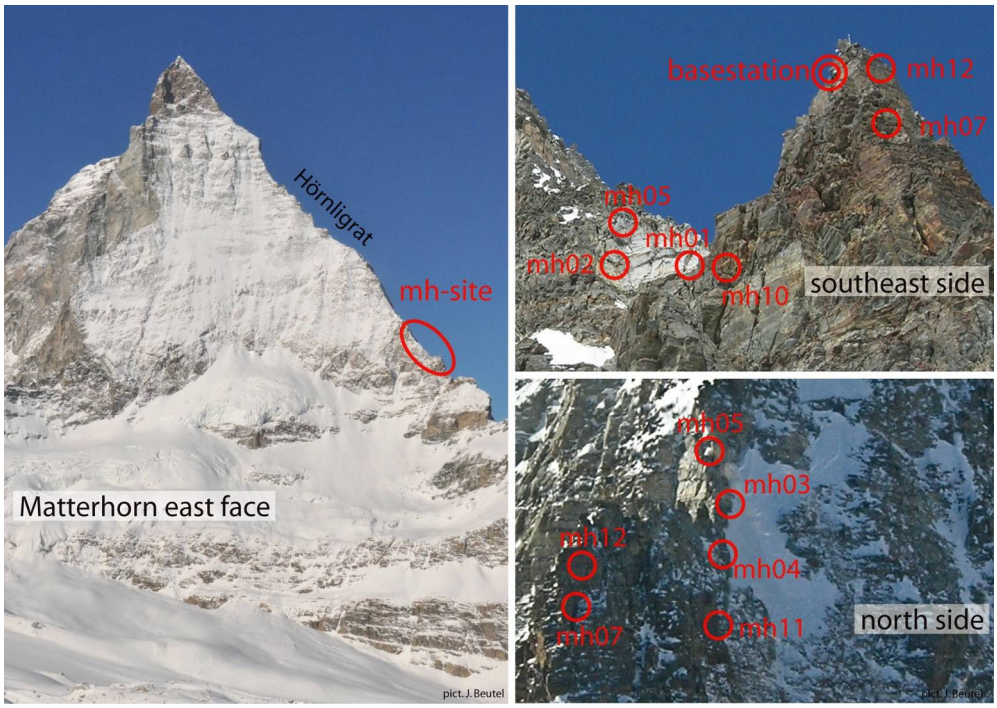

Figure 2: Overview of the Matterhorn field site at Hörnligrat. The circles with labels indicate the sensor locations. Note the thin snow cover in the Matterhorn east face (left picture taken in November 2009).

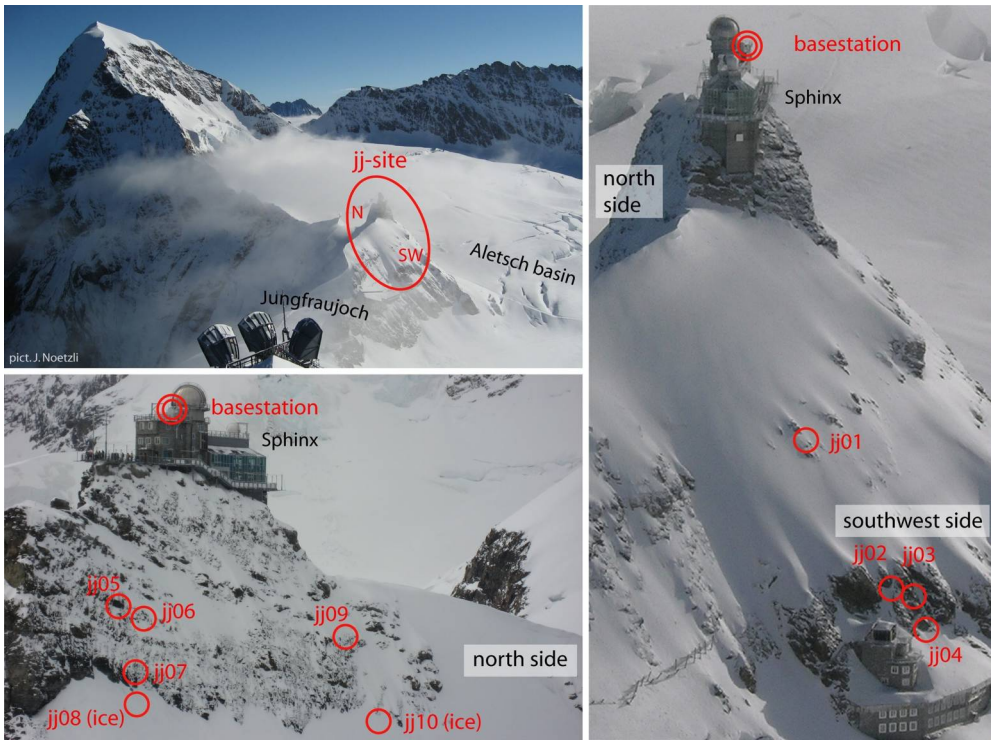

Figure 3: Overview of the Jungfraujoch field site around the Sphinx obervatory. The circles with numbers indicate the sensor locations. All pictures taken in October 2006.

2.2. Instrumentation

At both field sites, wireless sensor networks (WSNs) that record environmental parameters and transmit the data to an Internet server were installed. The conception and setup of these WSNs are described in detail by Beutel et al. (2009) and Hasler et al. (2008). Beside geotechnical and hydrological parameters, temperature measurements with totally 100 temperature sensing elements (YSI 44006 NTC-thermistors) where recorded with high temporal resolution since July 2008 at Matterhorn and since February 2009 at Jungfraujoch. Several differing sensors can be attached to one network node of the WSN, which is then termed sensor node, while the expression base station is used for the central node that transmits the data off the mountain. Sensor nodes are labelled with abbreviations of the field site (mh for Matterhorn and jj for Jungfraujoch) and a number for the location (Figure 1). Custom-built sensor rods measure the temperature and electrical resistance of the rock at four depths (0.1, 0.35, 0.6 and 0.85 m) in a 0.9 m deep boreholes, which are perpendicular to the surface (Hasler et al., 2008). Similarly, thermistor chains and thermistor–moisture chains measure four to eight temperatures within clefts or in ice faces. For the clefts, the precise physical context of the measured value is more complicated than for the other cases, because the temperature at the sensing element is influenced by the temperature of the air and the rock surface within the cleft or even by ice or percolating water. The measured temperatures within a profile are labelled *T1*–*T4/T8* with increasing depth (e.g. *T1* = 0.1 m and *T4* = 0.85 m for all sensor rods; cf. Table 1). The depth of these measurements is not exactly defined for all sensors and depends on the installation at each location (see Sect. 2.3). In addition to these multiplex sensors, rock surface temperatures (*Ts*) are measured with individual thermistors placed 2 cm below the surface in small inclined borings minimizing disturbance from solar radiation on the cables. Two sensor rods (jj04 and jj09) where not considered for this study due to malfunction.

2.3. Description of the sensor locations

Nine sensor nodes at Matterhorn and eight sensor nodes at Jungfraujoch perform cleft, rock, or ice temperature measurements relevant for this study (Table 1). At Matterhorn the sensors mh01, mh02, mh05, and mh10 are installed on the south-

Figure 4: Close-up of sensors in densly fractured rock at the south side of Sphinx, Jungfraujoch. The picture is taken in April 2007 after a periode with intense irradiation.

Figure 5: Fractures with large spacing and opening at Matterhorn Hörnligrat (pict. from November 2010).

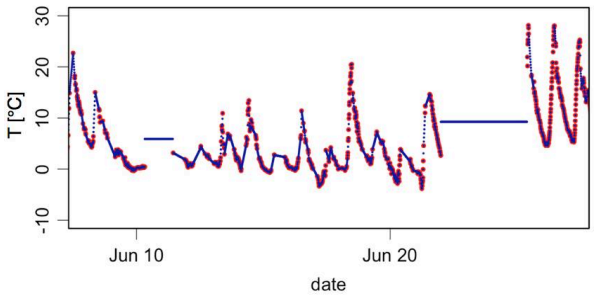

Figure 6: Example of gap-filling with original values (red) and the resulting dataset after gap filling (blue). Note that the data in this graph (mh01; *T1*) is a worst case concerning gap frequency.

Table 1. Type and orientation of measurement locations with depth of the thermistors

location	*type*	*aspect [°]*	*slope [°]*	*characteristics*	*depths of Ts (*), T1, T2, ... [m]*
mh01	cleft	95 (E)	75	intense solar radiation	0.02*, 0.1, 0.4, 0.7, 0.5
mh02	cleft	80 (E)	50	corner, often snow, wet	0.1, 0.3, 0.4 - 0.8 [6]
mh03	cleft	350 (N)	65	lower part snow	0.02*, 0.1, 0.4, 0.6 - 0.8 [5]
mh04	cleft	320 (N)	70	gully, often snow	0.05, 0.2, 0.2 - 0.5 [4]
mh05	cleft	90 (E)	60	small corner, often snow	0.1, 0.8, 1.8, 1.5
mh07	cleft	50 (E)	90	large ventilated cleft	0.1, 1, 2, 3
mh10	rock	140 (S)	90	int. solar rad., cleft at 1 m	0.02*, 0.1, 0.35, 0.6, 0.85
mh11	rock	340 (N)	70	occasionally snow, no clefts	0.02*, 0.1, 0.35, 0.6, 0.85
mh12	rock	45 (E)	85	snow free, clefts beside	0.02*, 0.1, 0.35, 0.6, 0.85
jj01	rock	215 (S)	30	often snow, wet	0.1, 0.35, 0.6, 0.85
jj02	rock	220 (S)	50	gully, often snow, wet	0.1, 0.35, 0.6, 0.85
jj03	rock	190 (S)	80	shaded, dry, small clefts	0.1, 0.35, 0.6, 0.85
jj05	rock	330 (N)	85	no macro clefts	0.1, 0.35, 0.6, 0.85
jj06	rock	335 (N)	75	large clefts at 0.15 and 0.4 m	0.1, 0.35, 0.6, 0.85
jj07	rock	330 (N)	75	limestone! occasional. snow	0.1, 0.35, 0.6, 0.85
jj08	ice	340 (N)	45	firn, 7 m from rock wall	0.7, 1, 1.4, 2.1, 2.8, 3.5, 4.2, 4.9
jj10	ice	330 (N)	45	firn, below single cliff	0.7, 1, 1.4, 2.1, 2.8, 3.5, 4.2, 4.9

* rock surface temperature (*Ts*) measured beside cleft or sensor rod
[X] number in brackets indicate number of thermistors in the given depth range without exact depth information

east side of the ridge that is exposed to intense solar irradiation, while mh07 and mh12 are on the ridge and the other sensors are in the shaded north face (Figure 2). At Jungfraujoch the locations jj01–jj04 are on the southwest slope and the other locations including the two ice boreholes are on the northern side of the Sphinx (Figure 3). The depths of thermistors (perpendicular to the surface) is indicated for all sensor rods and for cleft temperatures where it is clearly defined. Otherwise, an estimated depth-range and the corresponding number of thermistors is denoted (Table 1). The depths of the thermistor chains in the ice face are not constant with time as the face accumulates small quantities of ice (about 0.05–0.3 m a-1), however, the distance between sensors remains constant. Based on the installation depth of 0.3 m and the evolution of the amplitudes of the uppermost sensor, we estimate its average depth during the measured period as 0.7 m from the surface (Table 1). The location of the surface temperature measurements are in similar local orientations at 0.1–1 m distance from the boreholes of the sensor rods or from the clefts.

The rock temperature measurements at Matterhorn aim to record the thermal conditions in snow-free and compact rock as a reference for the cleft temperature measurements and comparison to RST-measurements in other areas. Therefore, near-vertical bedrock of the three main aspects that persist at this field site (NW, NE, SE) was instrumented with sensor rods. For the locations mh10 and mh12, however, no sufficiently large compact rock mass could be found and clefts exist in proximity of the boreholes (Table 1). At Jungfraujoch, the locations of the rock temperature measurements are selected to cover gradients in surface and near-surface conditions. For the two main aspects (N, S) different locations with respect to slope angle (snow retention), microtopography (water availability; only at S) and fracturation where selected (Table 1). The two sensors that failed are the snow-covered one in the north face (jj09) and the sensor in unfractured rock at the south side (jj04). As a consequence, the effect of snow cover in the northern face and difference caused by fracturation for the south side could not be assessed at this field site.

3. Data processing and quality

The raw data series contain invalid measurements or data gaps and the sampling interval of two minutes is slightly irregular. This demands a processing prior to the calculation of the main parameters of interest. These are the mean annual temperatures (MATs) and temperature offsets (TOs) within the profiles (definition see below). First, invalid data is filtered and the remaining data is aggregated to regular intervals. After this, data gaps are filled. As these processing steps but

also the characteristics and timing of the data acquisition introduce uncertainty into the computation of mean annual temperature an uncertainty analysis concludes this section.

3.1. Data validation, filtering and accuracy

In addition to the thermistors, each multiplex sensor measures temperature-stable reference resistors during each cycle of temperature measurements. Deviations in these reference values correlate with invalid temperature measurements if the source of error is within the data acquisition system and not at the sensing element itself. A threshold is applied on the reference values to filter invalid measurements from the raw data before averaging to ten-minute aggregates. This down-sampling does not lead to a significant loss of information because of the inertia of ground temperatures. Due to this down-sampling the resulting time series are usually continuous because invalid data is rare (with the exception of mh01). A second source of erroneous measurements is physical damage of thermistors due to water entry or mechanical distortion. This type of invalid data cannot be easily filtered automatically because it is typically indicated by a slow drift of values that can best be detected by visual inspection and manual masking of the time span concerned. A similar manual masking of erroneous values was applied to the surface temperature measurements by individual thermistors because no reference values for this data exists.

The supplier of YSI 44006 thermistors guaranties an interchangeability tolerance of ±0.2 °C over a temperature range from –40 °C to +120 °C but tests in an ice-water bath showed that 95 % of the thermistors are within a range of ±0.1 °C. A calibration of the assembled sensor could not be performed for logistic reasons, hence the accuracy of the installed system was not improved. Based on the stability of the reference resistors in the raw data we assume that the accuracy of a temperature measurement with the given setup including the effect of aggregation is ±0.2 °C for all sensors except jj03 with ±0.3 °C (Table 2).

3.2. Gap filling algorithm and mean annual temperature (MAT) calculation

Running arithmetic averages over 365 days are calculated and result in a continuous time-series of MAT values. These time-series are used to evaluate the uncertainty of the MAT value for one particular time window: In general the MAT presented is for the hydrological year 2010 (see below). Missing data within the considered time window affects the value of the resulting mean depending on the duration and timing of these gaps. In the data presented, we have: a) gaps of single or a few ten-minute values due to filtering of invalid data; and b) gaps of several days to weeks due to interrupted operation of the WSN. To minimize their effect on MAT calculation, a two-stage gap-filling algorithm was applied. For gaps shorter than 12 hours, missing values where estimated by linear interpolation of the nearest data points, longer gaps where filled with the average of the 30 days on each side of the gap. Figure 6 shows an example from mh01 before and after gap filling. For sensors mh03 to mh11, complete time series for more than a year are available and no gap filling was needed while in most of the other datasets 5–10 % of the data was missing. The effect of the gap filling on MAT was evaluated by introducing the same gaps into the complete time series; this showed that an approximation of the true MAT to better than ±0.1 °C was achieved with gap filling compared to ±1 °C if gaps contain no values. Sensors mh02 and mh12 contain larger gaps and therefore introduce a larger uncertainty into the MAT estimate (Table 2).

3.3. Definition and calculation of the temperature offset (TO)

For practical reasons we use the measured offset between the MAT at top and bottom of the profiles and call them *temperature offset* (TO). This parameter deviates from the *thermal offset* defined as the difference between the temperature below the active layer at the permafrost table (TTOP) and the MAGST (Burn and Smith, 1988). In fractured bedrock a quantification of the thermal offset is impractical, because of: a) highly variable MAGST; b) highly variable active layer thickness. The thermal offset is expected to be larger than our empirical TO in some cases. However, the values for offsets and MAT variability given in this study have an exemplary character and indicate possible ranges because many degrees of freedom exist in the possible variations of controlling parameters.

To quantify the temperature difference between the near-surface and greater depth, the MAT of *T4* is subtracted from the one of *T1* or for the ice face, *T8* from *T1*. Hence, positive differences indicate a higher MATs with depth while negative TO-values appear in situations where the subsurface is colder than the surface. As the MATs are continuous time-series (running annual

mean), the TO may be calculated for every day as well (c.f. Figure 7). The rock surface temperature measurements (*Ts*) are not considered for this calculation to avoid a mix of rock and cleft temperatures and to keep sensor rod measurements with and without *Ts* comparable. For mh02 *T6* is taken instead of *T4* because the MAT of the latter one is missing.

3.4. Uncertainty analysis of mean annual temperatures and temperature offsets

Three main sources of uncertainty (Table 2) affect our estimate of the MAT: (a) systematic measurement errors (U_{meas}), (b) data gaps (U_{gap}), and (c) the period for which the mean is calculated (U_{time}, U_{time_to}). U_{meas} is given by the measurement accuracy (section 3.1) because the bias from the measurement is systematic over the whole time series and is not significantly reduced by the averaging. For U_{gap} the values are estimated dependent on quantity of missing data in the averaging window (section 3.2) but lower values are chosen in case of the ice temperatures due to smooth time series and correspondingly better performance of the gap-filling algorithm. MAT calculations are influenced by the start and end date of the averaging window on the long term (inter-annual variation of MAT) but also on the short term (seasonal) if the temperature time series show strong weekly variations. Figure 7 shows the temperature time series and the seasonal variation of the MAT for the sensor rod at mh10 (rock). This variation is considered as uncertainty U_{time} for the comparison of the MATs because it is not correlated between locations. The MAT values for all sensors except jj01, mh04 and mh12 are calculated for 1 October 2009 to 1 October 2010 (Figure 7 black dots). The variation of the MAT is, however, influenced by data gaps, hence for three sensors the part of the time series with large gaps is excluded from the estimation of Utime that is performed by the difference of 2.5 and 97.5 % quantiles (Table 2). As the running annual means of the temperatures at different depth but at the same location are correlated (Figure 7), the temperature offset (TO) varies less over time. For that reason Utime_to is estimated as a measure of the uncertainty in temperature offset calculation, introduced by timing of the averaging interval, which is in most cases smaller than U_{time} (Table 2).

The total uncertainties of the MAT (U_{mat}) and the TO (U_{to}) are calculated by quadratic addition of the uncertainties according to the addition of spreads:

$$Umat = \sqrt{Umeas^2 + Ugap^2 + Utime^2} \quad (1)$$

$$Uto = \sqrt{2 \cdot Umeas^2 + Ugap^2 + Utime\_to^2} \quad (2)$$

Contrary to Eq. (1), the Umeas term is multiplied by a factor of two in Eq. (2) because the independent uncertainties of two temperature measurements contribute to U_{to}. U_{gap} of two measure-ments in the same profile are correlated and therefore their single consideration is a worst case. However this influence is negligible in most cases anyway (Table 2). The resulting uncertainties that are relevant for the interpretation of the MAT and the TO are listed in Table 2. These uncertainties are used in the following to evaluate if the MATs are significantly different and if significant TOs exists.

Table 2. Uncertainties of the MAT and the TO calculation

location	*Umeas*	*Ugap*	*Utime*	*Utime_to*	*Umat*	*Uto*
mh01	0.2	0.1	0.3	0.2	0.37	0.36
mh02	0.2	0.2	0.35	0.25	0.45	0.43
mh03	0.2	0	0.4	0.3	0.45	0.41
mh04	0.2	0	0.35	0.25	0.40	0.38
mh05	0.2	0	0.35	0.05	0.40	0.29
mh07	0.2	0	0.25*	0.05*	0.32	0.29
mh10	0.2	0	0.4	0.2	0.45	0.35
mh11	0.2	0	0.2*	0.1*	0.28	0.30
mh12	0.2	0.5	0.5	0.3	0.73	0.65
jj01	0.2	0.1	0.5	0.35	0.55	0.46
jj02	0.2	0.1	0.1	0.05	0.24	0.30
jj03	0.3	0.1	0.3	0.2	0.44	0.48
jj05	0.2	0.1	0.15	0.05	0.27	0.30
jj06	0.2	0.1	0.3	0.25	0.37	0.39
jj07	0.2	0.1	0.3	0.2	0.37	0.36
jj08	0.2	0.05	0.1*	0.05*	0.23	0.29
jj10	0.2	0.05	0.05*	0.02*	0.21	0.29

Umeas, *Ugap* and *Utime* (*Utime_to*) are the uncertainties introduced by the measurements, the gaps and the chosen averaging window. Values indicate the confidence interval on a 95 % level.
* only data after July 2009 was considered for the estimation because of large bias by gaps prior to this date

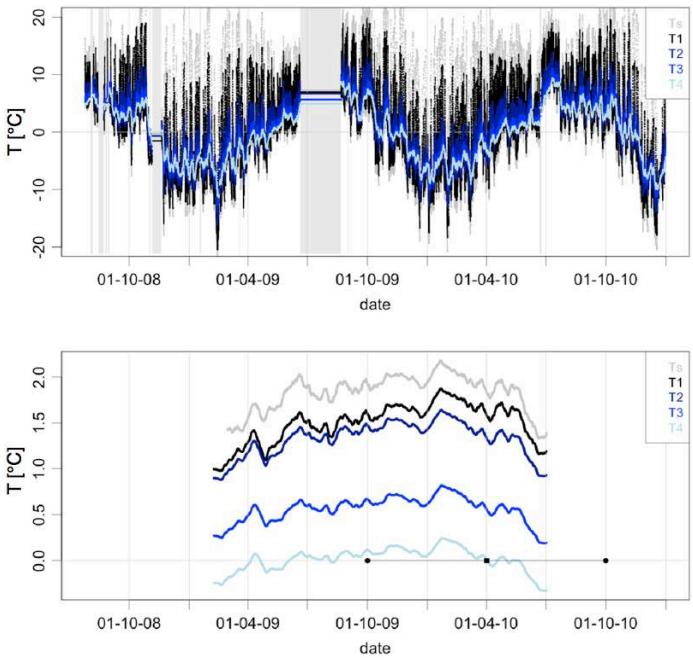

Figure 7: Time series from July 2008 to the end of 2010 of the rock temperature measurements (top) at mh10 with interpolated values in data gaps (grey bars) and corresponding running annual means (bottom) that are represented in the center of the averaging window. The black dots indicate this averaging window for one MAT with the quadrat showing the point in time of its representation. For most sensors this averaging window was chosen to minimize data gaps.

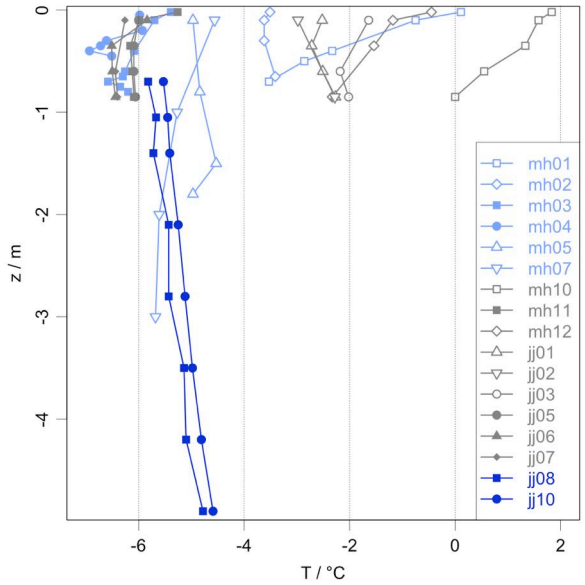

Figure 8: Mean annual temperature (MAT) profiles for clefts (light blue), rock (grey) and ice (dark blue) with depth z measured perpendicular to the surface. Solid symbols are shaded locations (north); hollow symbols are more exposed to solar radiation (south and east). Note that the uppermost MAT of mh01 to mh03 is a rock surface temperature (Table 1).

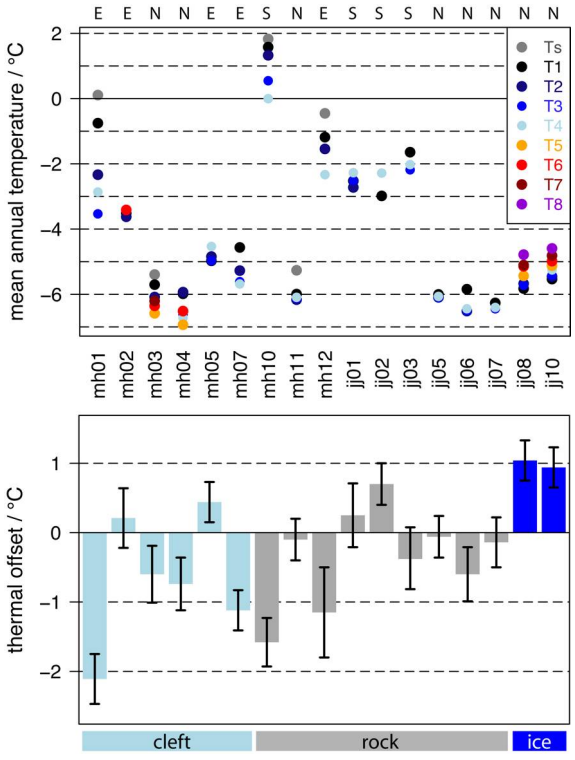

Figure 9: Mean annual temperature (MAT) and temperature offset (TO) between cleft top and within cleft (light blue); in shallow rock boreholes (grey) and in ice (dark blue). The black error bars show the uncertainties U_{to} of the temperature offset estimates on a 95% confidence level. The letters at the top indicate the main aspect of the locations (E=east, N=north, S=south). The location labels given in the middle of the figure help to read other attributes from Table 1. At the bottom, the location type is denoted, which corresponds to the colours of the bars from the thermal offset.

4. Results

4.1. Mean annual temperatures (MATs)

Figure 8 gives an overview of the MATs of the clefts, rock and ice ordered by location and type (colors). The representation as profiles with z being the distance from surface does not show the real distance between the sensors and lateral offsets in the thermistor position are masked in case of the cleft and ice temperatures. The MAT values from the north-oriented locations cluster around –6°C (Figure 8) and are slightly warmer (0.5–1.5 °C) than the MAAT (–6.7 to –7.3°C). Remarkable is the exact match in mean annual rock/ground temperature (MAGT) of mh11 and jj05, which are both in intact steep rock (Figure 8; for a better differentiation of these values see also Figure 8). The mean temperatures at the surface (MAGST) at the more sun-exposed locations are 1–8 °C higher than the shaded ones and the same is true for the near-surface cleft temperatures (MAT of *T1*) (Figure 8). The difference in MAGT between sunny and shaded locations is more pronounced at Matterhorn than at Jungfraujoch. This is because the south face MAGT at Matterhorn (mh10) is 3–4 °C higher for *T1* (0.1 m) and 2 °C higher for *T4* (0.85 m) than the ones at Jungfraujoch (jj01, jj02 and jj03) (Figure 8).

Cleft MATs of the east-oriented locations at Matterhorn are significantly lower than the MAGT at locations with comparable orientation: The cleft at mh07 is 4 °C colder at the top and 3 °C colder at depth than the rock at mh12 which is only a few meters above in the same face; the two clefts mh02 and mh05 are 2–3 °C colder than mh12 although they face more toward south; at depth, even the radiation-exposed profile mh01 is colder than mh12 (Figure 8). The MAT-profiles from the ice faces start around –5.5 °C near the surface and show a constant positive temperature gradient with depth of approximately +0.2 °C m^{-1} (Figure 8). The near-surface MAT in the ice is 0.2–0.8 °C higher than in the rock face just above the ice face, hence the difference found is marginal.

4.2. Temperature offsets (TOs)

Figure 9 shows the temperature offsets (TOs) from Matterhorn and Jungfraujoch. The difference in depth between the two thermistors that are used for the TO calculation is only constant for the rock temperatures (c.f. Figure 8), hence, the TO-values in Figure 9 are directly comparable for the rock measurements but smaller or larger depth ranges need to be considered for the cleft and ice temperatures.

In total, seven TOs are negative, four are positive and six lie within the uncertainty range (Figure 9). More than half (4) of the clearly negative TOs are detected within the clefts, the two most positive TOs consist of the ice face measurements. The locations with highest surface temperatures (mh01, mh10 and mh12) have most negative TOs and are all located at Matterhorn (2 in rock, 1 in cleft). From the rock temperatures at Jungfraujoch, only one sensor shows negative and one positive TO, whereas all the other sensors have no significant TO. This is in contrast to the Matterhorn data where seven out of nine cleft and rock sensors show a significant TO (Figure 9). A further regularity is, that all sensors with a slight or significant positive TO are located relatively flat and accumulate often a snow cover (cf. Table 1).

4.3. Seasonal temperature variation and inter-annual variability of MAT

To reveal some processes that are responsible for TOs and variations in MAT, a qualitative analysis of the time series from the measured data, the MATs and the smoothed temperature difference ($\Delta T = T4 - T1$) is presented in three examples. The data from jj05 serves as a reference for a rock temperature profile that has no significant TO (Figure 10): The 30-days running mean of ΔT has similar negative and positive amplitudes (±2 °C) and results in a TO close to zero if averaged over a year. This is also shown with the overlapping MATs that at the same time indicates the small seasonal variation (compare with U_{time} in Table 2). In Figure 11 and 12 two examples of time series are presented to illustrate, which periods of the year are responsible for the temperature offsets and what explains large variations of the MATs and TOs between different years: The time series of the cleft mh01 shows large seasonal variations and very large daily amplitudes in spring and summer that are not symmetrical with the temperatures at depth and cause a negative ΔT from March to November for both years (Figure 11). Similar seasonal patterns are found at all sensors with large negative TOs (mh07, mh10, mh12). In contrast, at jj01 (rock) positive temperatures and large daily amplitudes at T1 are limited to the snow free period in summer and the winter temperatures are smoothed by the snow cover (Figure 12). Because the snow-free periods differ between 2009 and 2010 and the temperatures at depth are buffered by thawing ground ice

(zero curtains), the summer ΔT varies strongly and the TO changes from positive to negative values (Figure 12).

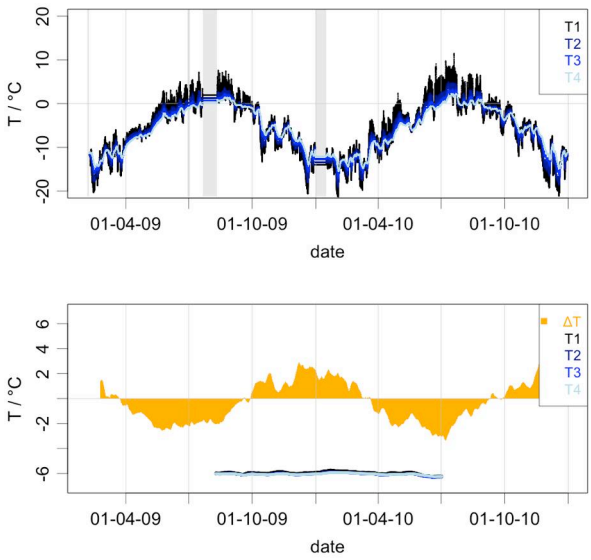

Figure 10: Time series of rock temperatures at jj05 (TO = 0 °C) measured every 10' (top) and the temperature difference ΔT = T4-T1 averaged over 30 days (bottom). Additionally the running MATs are ploted in lines similar to Figure 7 (bottom). Jj05 is a sensor rod at a shadowy location.

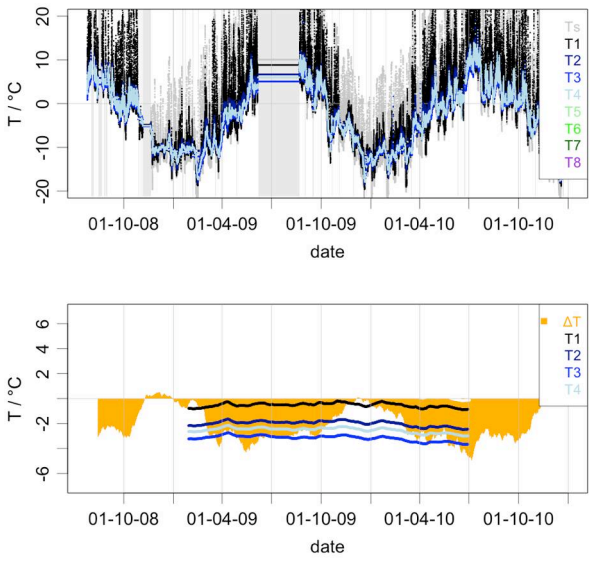

Figure 11: Time series of mh01 with measured temperatures (top) and the temperature difference ΔT averaged over 30 days as well as MATs (bottom). Mh01 is a cleft at a location with intense irradiation.

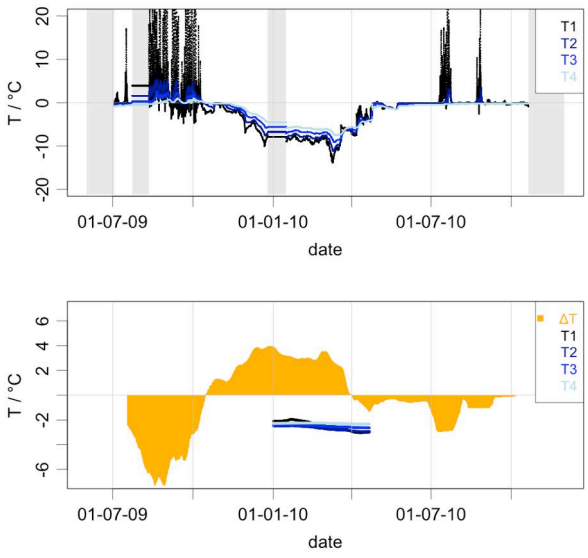

Figure 12: Time series of jj01 with measured temperatures (top) and the temperature difference ΔT averaged over 30 days as well as MATs (bottom). Jj01 is a sensor rod at a location that accumulates snow.

5. Discussion

5.1. Surface characteristics and temperature variability

Recent studies on the small-scale variability of mean annual ground surface temperatures (MAGST) in gentle mountain slopes, found a variability of 0.16–2.5°C within 10 m • 10 m footprints (Gubler et al., 2011) and 1.5–3.0°C over distances of 30 to 100 m (Isaksen et al., 2011). With the rough micro-topography typical for steep fractured bedrock, we expect MAGST-variabilities at the upper end of this range.

The general near-surface rock temperature pattern with a MAGT being slightly higher than the MAAT in shaded rock faces and several °C higher at radiation-exposed locations corresponds to other studies and reports from steep high-alpine bedrock (Coutard and Francou, 1989; Gruber et al., 2004; PERMOS, 2010). However, the temperatures are 2–3°C lower than the ones of Gruber et al. (2004) for this elevation in the Swiss Alps. The lower MAGTs at Jungfraujoch compared to Matterhorn may be explained partly by less direct solar irradiation due to more cloud cover determined by the more western orientation of the sensors with more convective cloudiness in the afternoon and the climatic situation (orographic clouds at the northern divide). The data

from the defect sensor jj04 (*T3* and *T4* have sufficient data to calculate annual means), however suggests that MAGT in the range of –0.5 °C occur at the south slope of Jungfraujoch as well. Hence, we assume other factors such as snow retention (jj01, jj02), cooling by melt water (jj02) and local shading (jj03, jj02) due to the micro-topographic situation as mainly responsible for the lower near-surface MAGTs at the Jungfraujoch south face (Table 1; Figure 4). The same cooling effect by local snow cover and more shading due to the concave micro-topography may be responsible for the lower cleft MATs at mh02 and mh05 in comparison with the near-surface MAT of mh01 that has the same orientation. This net cooling effect of the snow cover is in contrast to the net warming effect on more gentle slopes where thick snow cover cause a preponderance of "warming" by winter insulation over the "cooling" by increased albedo, emissivity and latent heat consumption (Keller and Gubler, 1993). In steep slopes at high elevation the thinner snow cover and summer snowfalls could result in a reverse effect (Pogliotti, 2011). This is supported by the data from jj01 showing that the surface remains snow-covered in the period with most intense solar irradiation (June and July) and that winter cooling indicated by upward heat fluxes (ΔT = +4 °C; larger than e.g. at jj05) is not prevented (Figure 12).

5.2. Non-conductive processes and near-surface temperature offsets

The variation of mean annual ground temperatures within the active layer is usually described with the thermal offset (see Section 3.3). This effect is well-known in arctic soils, and Gruber and Haeberli (2007) proposed three possible sources of thermal offsets making its importance also likely in steep fractured bedrock: 1) variable thermal conductivi-ty due to saturation and phase changes of pore water (thermal diode effect of rock); 2) changes of the heat transport across clefts as a consequence of freeze/thaw/runoff of cleft ice (thermal diode effect of clefts); 3) ventilation effects within loose block cover on less steep parts of rock faces. All these processes are expected to reduce temperatures at depth compared with MAGST and hence lead to lower TO-values in our measurements.

The comparably colder cleft temperatures at depth (Section 4.1) at locations without snow cover (mh01, mh07) need an alternative explanation (even though a part (≈0.5 °C) of the cooling with depth at mh01 may originate from lateral heat fluxes through the ridge). The large negative TOs of these clefts and the contrast to the rock surface temperature at mh01 point to strong non-conductive effects responsible for this cooling. Air ventilation is a likely source of cooling at depth because irradiation is reduced in open clefts and the temperature in the lower cleft approximates air temperature depending on the intensity of the sensible heat exchange similar to effects in coarse debris layers (Harris and Pedersen, 1998; Hanson and Hoelzle, 2004). A second cooling effect may be the latent energy consumption by the melt of snow that is deposited in larger clefts (cf. Figure 5). However, this process is only active if cleft temperatures are at 0 °C. The negative TO of 0.5–1.5 °C measured in rock (mh10, mh12, jj06) is well explained by the cooling within the clefts because all three boreholes are in proximity to open clefts (Table 1). Changes in thermal conductivity due to phase change of cleft and pore water (in case of jj06 the borehole crosses two clefts) could be an additional source of a negative TO at mh03 and mh06 (Gruber and Haeberli, 2007; Pogliotti et al., 2008). The seasonal pattern of ΔT (Section 4.3) fits best to the ventilation hypothesis for clefts because: a) the outward heat flux in winter would reduce ΔT (all sensors); b) radiation can not directly affect the upper most thermistor *T1* of the sensors mh01 (snow) and mh07 (shading) in winter; c) ventilation in winter is reduced due to snow in clefts (mh01, mh03, mh04). The other processes that are related to phase changes are more likely to produce a ΔT pattern that corresponds to freeze-thaw transitions. Slightly or significantly positive TOs occur all at comparably flat locations that are often snow-covered (Table 1). The described reduction of the local near-surface temperature and possibly the influence of sensible heat release at depth by percolating water (Hasler et al., 2011) explain the positive TOs except for the offset at jj02 where most likely small-scale 3D effect cause higher MAGTs at depth: A radiation exposed surface that is less snow covered is 0.8 from the drilling location and affects the measured temperature profile laterally (Figure 4).

5.3. Thermal regime in ice faces

In the ice face, near-surface temperatures do not significantly differ from the rock face above, hence the different albedo from the rock and ice (firn) surface has a minor effect at this shaded face. In contrast to the rock, however, the temperature gradient with depth is + 0.23 °C m^{-1} and results in a positive TO between 0.7 m and 5 m

depth. Possible sources of such positive TOs are a) stationary upward directed heat fluxes; b) transient effects of a surface cooling; c) lateral effects of the non-perpendicular drilling; d) advection of sensible heat by ice/firn motion (Luethi and Funk, 2001); e) latent heat release by percolation and refreezing water (Hoelzle et al., 2010). We exclude b), c) and d) as explanation for the observed offset because of the linear temperature profiles (Figure 8), no evidence for a surface cooling, the small lateral variability and the low ice flow velocity due to the proximity to the upper end of the ice face. In the present data we cannot identify a depth of maximal latent heat release (bent temperature profile), which should be typical for process e) (Figure 8). It is unclear whether this depth of heat release may be below the profile causing an upward heat flux, because little is known about the internal structure and permeability of such ice faces. Geothermal heat fluxes and 3D effects within the Sphinx ridge (Wegmann, 1998; Noetzli et al., 2007) driven by the warm south side and the infrastructure are more likely to explain the observed temperature profiles. Assumptions for the geothermal heat flux ($ht < 0.03$ W m^{-2}) and conductivity of porous ice ($\lambda > 1.5$ W m^{-1} K^{-1}) result in a significantly smaller temperature gradient ($dT/dz < 0.02$ °C m^{-1}). The lateral heat flux may be, however, ten times larger ($ht = 0.3$ W m^{-2}) due to the warm southern side and the heat introduced by the infrastructure within the ridge (Wegmann, 1998) induce a temperature gradient within the ice face in the order of 0.2 °C m^{-1}.

6. Conclusions and perspectives

The thermal conditions of steep bedrock permafrost and ice faces where studied based on 17 shallow temperature profiles. On the basis of two-year time series from two field sites in the Swiss Alps, we calculated the mean annual temperatures (MAT) and their temperature offsets (TO) within the profiles and analyzed them with respect to their micro-topographic situation, surface and near-surface characteristics. The main findings are:

- Differences in MAT and TO are highly significant with respect to the uncertainty introduced by measurement errors, data gaps and temporal variations.
- When using MAGST as an indication for the permafrost temperature in mountain faces, one needs to account for temperature offset, similar to the thermal offset in arctic lowland areas.
- The ice face investigated in this study has similar MAT as the rock beside and no clear evidence for TO by latent heat release from percolation effects was found.
- Snow cover likely reduces MAGST (2–3 °C) of moderately steep (45-70 °) locations in radiation-exposed faces at high elevation because it often persists for the period with most intense radiation (June).
- A ventilation effect of clefts causes negative TO and lower temperatures at depth (≈ 1.5°C) for strongly fractured near-vertical bedrock at radiation-exposed locations.
- Other processes such as thermal diode effects and local shading may support colder MAT but could not be quantified with the available data.
- Local warming within clefts by heat advection of percolating water shows minor effects on MAT, however, it should be considered in respect of rock stability.
- Summarizing the previous statements we postulate that radiation-exposed steep rock faces with intermitted snow patches and/or large fractures are up to 3 °C lower at depth than expected from MAGST at snow-free locations.

The lowering of ground temperatures in rock faces should be considered for the estimation of permafrost occurrence, which may in fact extend to lower elevations by several hundred meters in radiation-exposed faces than expected so far. Corresponding effects could be parameterized by the use of surface and near-surface characteristics that affect snow retention and ventilation. For an application and extrapolation of these findings the following may be reflected: a) the two effects should be considered to be complementary rather than cumulative, because snow reduces the efficiency of the ventilation; b) the ventilation effect depends on cleft aperture and frequency, hence near-surface characteristics need to provide information on this aspect; and c) the effect of snow cover could change with elevation due to a changed duration of the snow-free period. To estimate the latter, the near-surface temperature profiles may be used to calibrate the snow cover in a physically oriented permafrost models for steep bedrock: The measured gradients in the near-surface layer can serve as a direct estimate of the heat flux through the snow cover. As long as no further analysis and model-based spatial extrapolation of these findings is performed, we suggest to include up to 3 °C lower temperatures in radiation-exposed rock faces in the uncertainty indications of MAGT estimates.

Acknowledgements

We would like to thank the PermaSense team, J. Beutel, R. Lim, M. Yücel, I. Talzi, T. Gsell, M. Keller, L. Thiele and C. Tschudin, who made these challenging measurements possible. The presented research was funded within the project PermaSense by the Swiss Federal Office for the Environment (FOEN) and the Swiss National Foundation (SNF) NCCR-MICS. The fieldwork at Jungfraujoch was supported by the International Foundation High Altitude Research Stations Jungfraujoch and Gornergrat (HFSJG) and benefited from the friendly support of the Jungfrau Railways and their staff.

References

Allen, S.K., Gruber, S., and Owens, I.F.: Exploring steep bedrock permafrost and its relationship with recent slope failures in the Southern Alps of New Zealand. Permafrost and Periglacial Processes, 20, 345–356, 2009.

Beniston, M.: Mountain climates and climatic change: An overview of processes focusing on the European Alps. Pure and Applied Geophysics, 162, 1587–1606, 2005.

Beutel, J., Gruber, S., Hasler, A., Lim, R., Meier, A., Plessl, C., Talzi, I., Thiele, L., Tschudin, C., Woehrle, M., and Yuecel, M.: PermaDAQ: A scientific instrument for precision sensing and data recovery in environmental extremes. In *Proc. of the 2009 Int. Conf. on Information Processing in Sensor Networks*. IEEE Computer Society, 265–276. 2009.

Burn, C.R. and Smith, C.A.S.: Observations of the" thermal offset" in near-surface mean annual ground temperatures at several sites near Mayo, Yukon Territory, Canada. Arctic, 41, 99, 1988.

Coutard, J.P. and Francou, B.: Rock temperature measurements in two alpine environments: implications for frost shattering. Arctic and Alpine Research, 21, 399–416, 1989.

Gruber, S. and Haeberli, W.: Permafrost in steep bedrock slopes and its temperature-related destabilization following climate change. Journal of Geophysical Research, 112, F02S18, 2007.

Gruber, S., Hoelzle, M., and Haeberli, W.: Rock-wall temperatures in the Alps: modelling their topographic distribution and regional differences. Permafrost and Periglac., 15, 299–307, 2004.

Gubler, S., Fiddes, J., Gruber, S., and Keller, M.: Scale-dependent measurement and analysis of ground surface temperature variability in alpine terrain. The Cryosphere, 5, 431–443, 2011.

Haeberli, W., Wegmann, M., and Vonder Muehll, D.: Slope stability problems related to glacier shrinkage and permafrost degradation in the Alps. Eclogae Geologicae Helveticae, 90, 407–414, 1997.

Hanson, S. and Hoelzle, M.: The thermal regime of the active layer at the Murtel rock glacier based on data from 2002. Permafrost and Periglacial., 15, 273–282, 2004.

Harris, S.A. and Pedersen, D.E.: Thermal regimes beneath coarse blocky materials. Permafrost and Periglacial Processes, 9, 107–120, 1998.

Hasler, A., Gruber, S., Font, M., and Dubois, A.: Advective heat transport in frozen rock clefts - conceptual model, laboratory experiments and numerical simulation. Permafrost Periglac., 2011.

Hasler, A., Talzi, I., Beutel, J., Tschudin, C., and Gruber, S.: Wireless sensor networks in permafrost research: concept, requirements, implementation, and challenges. In *Proceeding of the Ninth International Conference on Permafrost*. Fairbanks, Alaska, USA, 669–674. 2008.

Hiebl, J., Auer, I., Böhm, R., Schöner, W., Maugeri, M., Lentini, G., Spinoni, J., Brunetti, M., Nanni, T., and Per ec Tadi, M.: A high-resolution 1961–1990 monthly temperature climatology for the greater Alpine region. Meteorologische Zeitschrift, 18, 507–530, 2009.

Hoelzle, M., Darms, G., and Suter, S.: Evidence of accelerated englacial warming in the Monte Rosa area, Switzerland/Italy. The Cryosphere, 5, 231–243, 2011.

Isaksen, K., Oedegard, R.S., Etzelmueller, B., Hilbich, C., Hauck, C., Farbrot, E., Hygen, H.O., and Hipp, T.F.: Degrading mountain permafrost in southern Norway: spatial and temporal variability of mean ground temperatures, 1999-2009. Permafrost and Periglacial Processes, in press 2011.

Keller, F. and Gubler, H.: Interaction between snow cover and high mountain permafrost, Murtel-Corvatsch, Swiss Alps. In *Proceedings of the Sixth International Conference on Permafrost*. 332-337. 1993.

Luethi, M.P. and Funk, M.: Modelling heat flow in a cold, high-altitude glacier: interpretation of measurements from Colle Gnifetti, Swiss Alps. Journal of Glaciology, 47, 314–324, 2001.

Matsuoka, N.: Frost weathering and rockwall erosion in the southeastern Swiss Alps: Long-term (1994-2006) observations. Geomorphology, 99, 353–368, 2008.

Matsuoka, N. and Sakai, H.: Rockfall activity from an alpine cliff during thawing periods. Geomorphology, 28, 309–328, 1999.

Noetzli, J., Gruber, S., Kohl, T., Salzmann, N., and Haeberli, W.: Three-dimensional distribution and evolution of permafrost temperatures in idealized high-mountain topography. J. Geophys. Res, 112, F02S13, 2007.

Noetzli, J., Gruber, S., and Poschinger, A.: Modellierung und Messung von Permafrosttemperaturen im Gipfelgrat der Zugspitze, Deutschland. Geographica Helvetica, 65: 2, 113–123, 2010.

PERMOS: Permafrost in Switzerland 2006/2007 and 2007/2008. Noetzli, J. and Vonder Muehll, D. (eds.). Glaciological Report (Permafrost) No. 8/9

of the Cryospheric Commission of the Swiss Academy of Sciences 2010.

Pogliotti, P.: Influence of Snow Cover on MAGST over Complex Morphologies in Mountain Permafrost Regions. PhD Thesis. Turin, Italy: Università degli Studio di Torino. 2011.

Pogliotti, P., Cremonese, E., Morra di Cella, U., Gruber, S., and Giardino, M.: Thermal diffusivity variability in alpine permafrost rock walls. In *Proceeding of the Ninth International Conference on Permafrost*. Fairbanks, Alaska, USA, pp. 1427–1432. 2008.

Wegmann, M.: Frostdynamik in hochalpinen Felswänden am Beispiel der Region Jungfraujoch - Aletsch. Mitteilungen der Versuchsanstalt für Wasserbau, Hydrologie und Glaziologie der ETH Zürich, 161, 1998.

Wegmann, M., Gudmundsson, G.H., and Haeberli, W.: Permafrost changes in rock walls and the retreat of Alpine glaciers: a thermal modelling approach. Permafrost and Periglacial., 9, 23–33, 1998.

Correspondence to:

1. Andreas Hasler, Department of Geography, University of Zurich, Winterthurerstr. 190, 8057-Zürich, Switzerland, andreas.hasler@geo.uzh.ch
2. Dr. Stephan Gruber, Department of Geography, University of Zurich, Winterthurerstr. 190, 8057-Zürich, Switzerland, stephan.gruber@geo.uzh.ch

Paper IV | Advection and cleft ice

Advective heat transport in frozen rock clefts - conceptual model, laboratory experiments and numerical simulation

Focus

Based on the typical characteristics of steep rock faces and studies of hydrothermal processes in other periglacial environments a conceptual model of advection and cleft-ice evolution was formulated. Simplified implementations of this model by a single cleft reproduced in the laboratory and a two-dimensional numerical model where used to asses this hydrothermal effects quantitatively.

Main findings

- *Ice aggradation at the initial percolation causes a rapid warming of the rock and preconditions it for later ice erosion.*
- *A large part of the applied sensible heat of percolating water results in cleft ice erosion and not in rock warming.*
- *For ice-filled clefts of approximately 1 cm width, the equilibrium between aggradation and erosion is in the range of 10–20 W/m sensible heat release along the ice surface.*
- *Large sensible heat inputs cause large erosion rates independently from rock temperature.*
- *For seasonal variable water percolation such as realistic for natural rock, the equilibrium between aggradation and erosion may be very sensitive to small changes in timing and magnitude of melt water supply.*

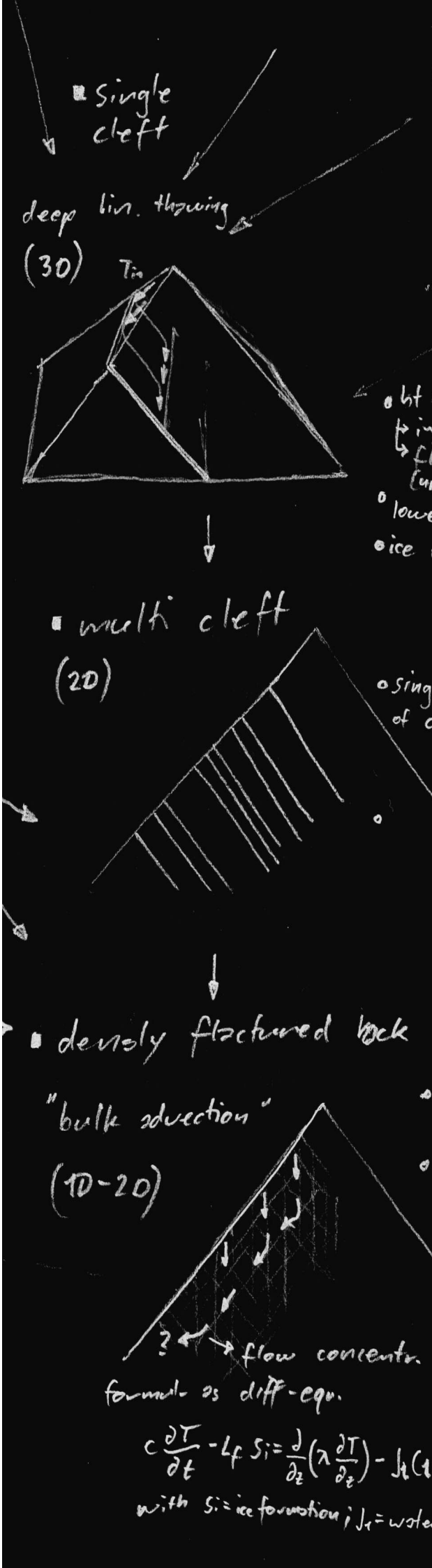

Citation

Hasler, A. Gruber, S. Font, M. Dubois, A. 2011. Advective heat transport in frozen rock clefts - conceptual model, laboratory experiments and numerical simulation. Permafrost and Periglacial Processes 22. 378–389.

Paper published in PERMAFROST AND PERIGLACIAL PROCESSES

Advective Heat Transport in Frozen Rock Clefts – Conceptual Model, Laboratory Experiments and Numerical Simulation

Andreas Hasler[1], Stephan Gruber[1], Marianne Font[2], and Anthony Dubois[2]

[1] Glaciology, Geomorphodynamics and Geochronology, Department of Geography, University of Zurich, Switzerland.

[2] Laboratoire M2C, UMR CNRS/INSU 6143, Université de Caen-Basse Normandie, France.

Received: 15 June 2010 – Accepted: 2 November 2011 – Published online: 13 December 2011

ABSTRACT

Advective heat transported by water percolating into discontinuities in frozen ground can rapidly increase temperatures at depth because it provides a thermal shortcut between the atmosphere and the subsurface. Here we develop a conceptual model that incorporates the main heat exchange processes in a rock cleft. Laboratory experiments and numerical simulations based on the model indicate that latent heat release can rapidly warm cold bedrock and can precondition it for later thermal erosion of the cleft ice by advected sensible heat. The timing and duration of water percolation both affect the ice level change because initial aggradation and subsequent erosion are of the same order of magnitude. The surplus of advected heat is absorbed by cleft ice loss and by runoff from the cleft so that this energy is not directly detectable in ground temperature records. Our findings suggest that thawing-related rockfall is possible even in cold permafrost if meltwater production and flow characteristics change significantly. Advective warming could rapidly affect failure planes beneath large rock masses and failure events could therefore differ greatly from common magnitude reaction-time relations.

KEY WORDS: bedrock; permafrost; advective heat transport; conductive heat transfer; laboratory experiment; numerical modeling; rockfall; climate change rock fall

INTRODUCTION

Mountain permafrost may be situated at high elevations above densely populated regions and in this steep topography it can condition debris flows or rockfalls which in turn may trigger greater hazards downvalley. Climate change is expected to modify this hazard potential (Haeberli et al., 1997) and to affect the links between permafrost-related mass movements and atmospheric conditions (Haeberli and Beniston, 1998; Geertsema et al., 2006; Harris et al., 2001; Harris et al., 2009). Key questions are whether an increasing number of extremely hot summers will lead to more rockfalls in steep bedrock terrain, as in the summer 2003 in the Alps (Gruber et al., 2004), and whether continued warming could cause large rock avalanches that differ markedly from historical events.

Both general thermal conditions and short-term thermal features must be comprehensively understood in order to investigate the temperature dependence of rock instability. In this context, it should be pointed out that: (1) the thermal conditions of recent rockfalls from permafrost areas are only known approximately and no correlation between these modelled rock temperatures and event frequency has been established (Noetzli et al., 2003; Fischer, 2010); and (2) much of the rockfall activity in the Alps in summer 2003 occurred earlier than the maximum active layer thickness predicted from heat conduction (Gruber et al., 2004). Given the hypothesis that these rockfalls relate to thermal conditions at the failure

planes, these two observations suggest that small-scale (cm–m) thermal anomalies caused by non-conductive effects may be significant.

Advective heat transport along clefts may be an important modifier of thermal and hydrological conditions and may influence the stability of ice-filled clefts in permafrost (Gruber and Haeberli, 2007). The quantification of this heat flux in steep, frozen bedrock is difficult because the physical processes are non-linear and natural conditions are heterogeneous and difficult to observe. For example, Hasler et al. (2011) measured significant thermal variability within the active layer of permafrost in steep bedrock, even on an annual basis, due to the cooling effects of thin snow cover and ventilation within clefts. Although short-term warming effects were measured in some clefts, they had minor impacts on average thermal conditions. Investigations of the local heterogeneity of rock temperatures using geophysical methods have also led to thawing corridors being detected and these were attributed to advective heat inputs from percolating water (Krautblatter and Hauck, 2007).

In this paper, laboratory and numerical experiments are presented in relation to a conceptual hydrothermal model of a rock mass containing a single cleft. These reveal the sensitivity of linear thaw (ice erosion) along clefts and corresponding local permafrost degradation, and form a basis for future investigations of cleft assemblies in fractured rock. The following research questions are addressed:

1) Which processes are important for advective heat transport in rock clefts at subzero temperatures?
2) What are the effects of advection on cleft-ice and on the temperatures around the cleft?
3) Which parameters govern the processes of advective heat transport?

The aim of the modelling is a semi-quantitative description of the thermal effects of advective heat transport in steep fractured bedrock with permafrost, rather than a direct prediction of the small-scale thermal field in nature. The latter cannot be undertaken at present because the necessary information (detailed surface and near-surface characteristics) is not available. However, the general sensitivity of clefts in bedrock permafrost to advective heat input can be assessed and this provides a means to understand the impact of extreme climatic events and mean annual temperature rise on the thermal, hydrological and mechanical conditions of steep bedrock with permafrost.

BASIS OF THE CONCEPTUAL MODEL

Hydrothermal processes in permafrost and seasonally-frozen ground comprise the phase change of water and the transport of latent and sensible heat by the motion of water and water vapour. The importance of these processes varies with water content, hydraulic permeability and gradient, and depends on the scale considered. Hence, the near-surface characteristics and (micro-) topographic situation are significant factors.

Hydrological properties of steep bedrock permafrost

High-alpine mountain flanks consist to large parts of bedrock with average inclinations between 40° and 70°. These rock masses contain discontinuities formed by the orogenesis and weathering processes. Clefts, being macroscopic discontinuities, have typical apertures in the rage of mm–dm, spacings of cm–m between each other in the shallow metres or decametres of steep bedrock (e.g. Hasler et al., 2011). These structural properties shape also the micro topography and lead to strong spatial heterogeneity of local aspect and slope angles. The hydrological properties of this steep bedrock differ from permafrost soils in gentle terrain, for which hydrothermal studies exist (cf. Kane et al., 2001; Boike et al., 2008), as the following: i) In unfrozen state, the water flow is dominated by the flow along open clefts and the water migration through the inter-cleft rock mass plays a minor role in low porosity rock (Dietrich, 2005). ii) Large hydraulic gradients (slope) and high permeability (macroscopic clefts) lead to mostly unsaturated conditions with preferential flow paths developed in the cleft system of the thawed near-surface layer. iii) In the permafrost body, the cleft-ice content is decisive for the hydraulic permeability. For point iii) it is often assumed that permafrost acts as an aquiclude in fractured bedrock or coarse-grained sediments as long as the pore space is saturated (Rist, 2007). Observations of ice filled clefts in the field (Gruber and Haeberli, 2007) indicate that this condition is often met in bedrock permafrost. Pumping experiments in fractured granite with and without permafrost support this hypothesis (Pogrebiskiy and Chernyshev, 1977). Nevertheless, thermally eroded and progressively deepening channels within the cleft ice cannot be excluded and deep-seated rock creep may render frozen fissures permeable by imposing geometry changes.

Our model assumes an initially ice-sealed permafrost body with percolation along preferential flow paths and lateral runoff on the cleft ice surface (Figure 1). Rapid percolation in relatively wide clefts results in minimal heat exchange for water within the unsaturated zone, causing an efficient heat transport to the cleft-ice level (cf. Rist and Phillips (2005) who observed similar effects in debris), which we can treat as a *heat-transport short-cut* between the surface (or atmosphere) and the ice level. The low depth of the water flow over the ice may, however, not be correct for very narrow clefts or clefts with sediment infill where heat exchange is expected to be less concentrated around the ice level. The temporal development of the ice level depends on available water and thermal conditions (see below). Water availability is limited during the cold season at high elevations, but in the spring, rock at several degrees below 0 °C may be subject to percolating meltwater (cf. Stähli et al., 1996; Boike et al., 1998; Scherler et al., 2010). For this reason, ice aggradation is expected during the early thawing season before ice erosion becomes dominant.

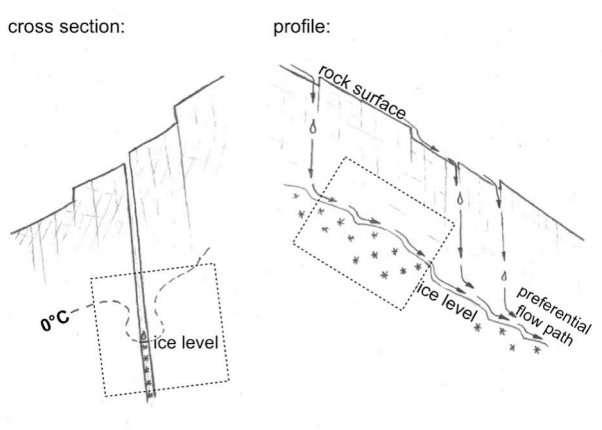

Figure 1: Sketch of hypothetical flow paths in the active layer or a talik within of bedrock permafrost. Left: Cross section through a rock cleft with the 0 °C isotherm in summer (thawing front). Right: Profile along a cleft with preferential percolation paths and runoff on the surface of the cleft ice. Dashed boxes: Domain of physical and numerical modelling.

Heat flow and cleft ice evolution fractured rock

Advective heat transport to the subsurface comprises heat uptake in a source area at or near the surface, heat transport by water percolation, and subsurface heat release. Heat uptake at the surface depends on various factors, causing a wide temperature range for the percolating water. Manual water temperature measurements at the rock surface at different sites and with differing weather conditions showed a range of 0.2–20 °C for flow rates of 5 to several hundred L h^{-1}, which correspond to a sensible heat inputs of 20–10 000 W (Hasler, 2011).

Part of this heat is used to warm the surrounding rock while the water percolates to the ice level. The water that arrives at the ice level with temperatures >0 °C may advect sensible heat (P_{adv}) because the temperature at a macroscopic ice-water interface equilibrates at 0 °C. This results in (1) warming by ΔT of the surrounding rock (and ice) mass with corresponding change in liquid water content of the porewater (ΔLWC); and (2) geometry change (mass loss/gain) of cleft ice as a function of the average cleft ice level (Δz) if the cleft aperture (d_{cl}) is constant (Figure 2). Accordingly, energy conservation in an advectively influenced cleft environment including conductive heat flux (P_{cond}) can be described as:

$$(P_{adv} + P_{cond}) \cdot t = \Delta T \cdot C_1 + \Delta z \cdot C_2 + \Delta LWC \cdot C_3 \quad (1)$$

with the left terms being the heat input for a given duration (t) and the right terms being the internal energy of the rock mass and latent energy change of cleft ice change and pore-ice change. The constant C_1 is the heat capacity of the volume with changed temperature and C_2 and C_3 are the cleft geometry (width, length) and pore water content multiplied with the latent heat of fusion (the general heat transport equation as a physical formulation of these processes may be found in the supporting material). The advected sensible heat (P_{adv}) tends to zero when water that percolates into the cleft is at or close to 0 °C, but heat transport still takes place when latent heat of ice

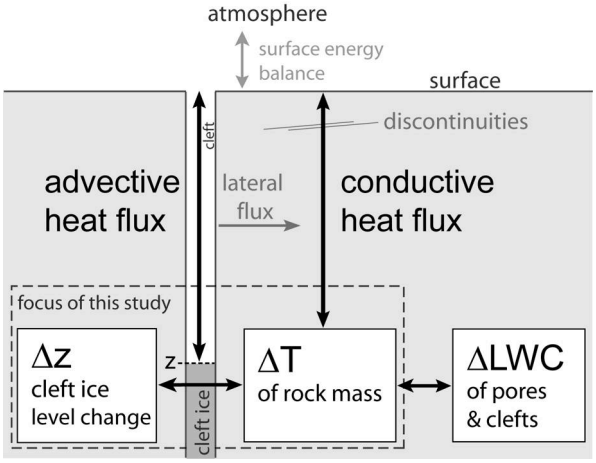

Figure 2: Conceptual model of heat flux components in bedrock with a cleft intersecting the surface and containing ice up to the level z. The advective heat transport along the cleft and the heat conduction in the rock mass result in changing rock temperature (ΔT) and liquid water content (ΔLWC) at depth and/or in a change of the ice level (Δz).

aggradation is released ($\Delta z > 0$) and absorbed by cold rock (ΔT) around the cleft. If ice is eroded by P_{adv}, latent heat is consumed and exported from the system as runoff ($\Delta z < 0$). Liquid pore water content (ΔLWC) and cleft ice geometry (Δz) are both reservoirs of latent energy but differ in their reversibility and feedbacks: Liquid water that stays in place after melt will refreeze at the end of the thawing season and ground temperatures below the freezing transition indicate the enthalpy of the system and are inter-annually comparable. This is true for the pore water because we consider the average pore water content (LWC+pore ice) as constant due to the low hydraulic permeability of most rock types. Mass loss of cleft ice, which is much more mobile, reveals the enthalpy change and exports the advected energy with the eroded ice volume. Such geometry changes are essential because the melt-interface will be at a new depth for subsequent thawing events modifying hydraulic and thermal conditions and changing the sensitivity to future thawing events. Hence, permafrost degradation is not necessarily visible in ground temperature but changes in ground ice content need to be considered. Thereto a quantification of the heat release and its effect rock warming (ΔT) and ice level (Δz) will be performed in the following.

METHODS AND MODEL SETUP

Our conceptual model of heat exchange was examined by focussing on a single cleft (Figures 1 and 2) using a combination of numerical analyses with a two-dimensional finite element model and physical experiments with an artificial cleft between two granite blocks in a cooling chamber.

The numerical model was formulated from the conceptual model with a heat conduction scheme and a moving ice-water interface. The fluid-dynamics of the flow on this interface and the corresponding heat exchange with the ice and surrounding rock were parameterized with heat transfer coefficients. The laboratory experiment dimensions were chosen based on typical cleft dimensions (Hasler et al., 2011) and initial numerical experiments to estimate the volume being thermally influenced by the cleft within the given time frame.

Experimental runs initially took place with constant heat inputs into the cleft (stationary experiments). These were used to calibrate the heat transfer coefficients to fit the observed ice level changes. The numerical model was then used to investigate ice erosion and rock warming by systematically varying advective heat input, rock temperature, and cleft size. In addition, a combined forcing by transient surface temperature and advection (cyclic experiments) was applied to the laboratory experiments to simulate thawing after a cold time period. Finally, scale effects and variable advective heat inputs were investigated numerically.

Numerical model

COMSOL Multiphysics software was used to solve the two-dimensional heat-conduction equation and the moving boundary of the ice-water interface (Stefan-Problem). The model geometry corresponded to a cross-section perpendicular to a cleft and consisted of the two rock sub-domains and simplified rectangular cross sections of the water flow-body and the ice within the cleft (Figure 3). The rock and ice sub-domains had an initialization temperature T_{rock} *(initial condition)*. The *driving variables* of the model were either the flow Q and mean water temperature T_w or the advective heat source P_{adv}, and the upper and lower boundary conditions (T_{up}, T_{bot}). Heat flux through the lateral boundaries was set to zero corresponding to the insulation in the laboratory experiments (Figure 3). To simplify the model, porewater was neglected (ΔLWC=0) and the rock was considered homogeneous and isotropic, corresponding to low-porosity rock and the laboratory settings (see below). To achieve stable model operation and a correct solution of the heat exchange at the moving boundaries (ice-water interface), the mesh was refined toward the cleft and model time steps were limited to 10 or 20 seconds. Both stationary and cyclic experiments are transient model runs and the term *stationary* refers only to the conditions of the driving variables (no steady-state modelling).

Flow characteristics (laminar or turbulent flow) along the ice surface in the cleft define the rate of heat exchange at the fluid-solid boundaries (water-ice and water-rock). Epstein and Cheung (1983) give a review of flow characteristics, heat exchange and interface instabilities on ice–water interfaces. Based on their model of simple phase change in an externally forced fluid flow, we used a heat transfer coefficient h_{int} as input to the phase change boundary. For initial modelling, standard values for h_{int} for a laminar flow of water were taken from literature (2000 W m^{-2} K^{-1}). However, positive feedbacks between the interface geometry and the flow are known to lead to turbulence and higher coefficients (Gilpin et al., 1980). Because the geometry of the rectangular flow cross-section in the model does not accurately represent real flow heights and geometry,

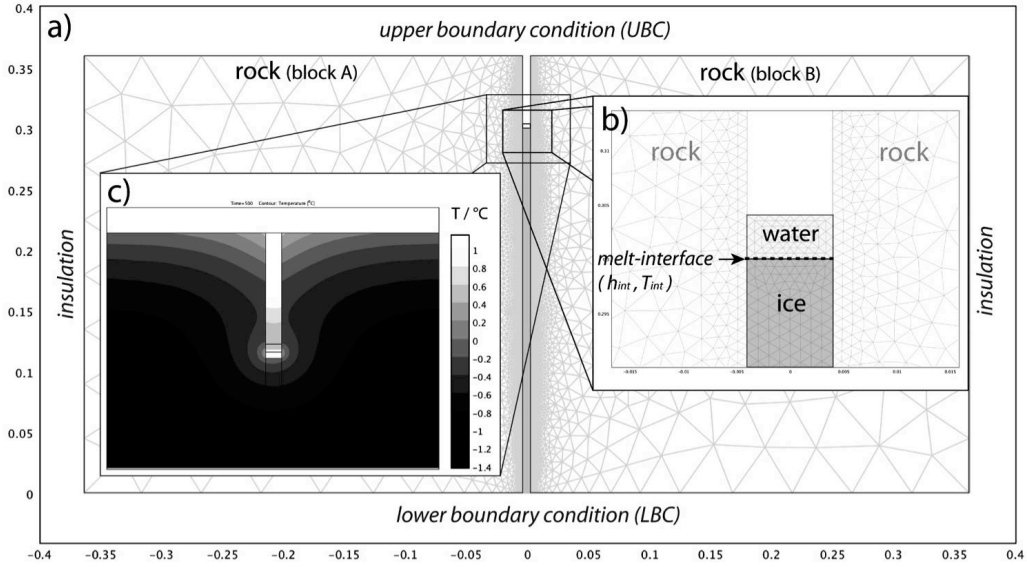

Figure 3: Geometry and mesh of the 8 mm cleft mode and sample results: a) overview of whole model; b) close-up of ice-water interface within the cleft; c) sample result at the end of a 500 seconds model run. The temperature at the melt-interface (ice-water) T_{int} is defined as 0 °C if a water flow is applied. The resulting heat flux discontinuity forces the interface movement (*dz/dt*).

the lateral heat transfer coefficient h_{side} is different from h_{int}. This difference is considered by a scaling factor *sf,* which includes the effect of real flow height ($sf = h_{side} / h_{int}$).

The ice geometry change of the cleft ice is implemented via the *moving mesh application mode* of COMSOL. The melt-interface, that is the upper boundary of heat conduction in the ice sub-domain, is set constant to zero degrees Celsius and coupled to the water sub-domain via the heat transfer coefficient h_{int}. The resulting heat flux discontinuity $(\Delta q_i = q_{i\_up} - q_{i\_down})$, is divided by the volumetric latent heat of fusion *(Lf)* and defines the velocity of the vertical displacement of the melt-interface *dz/dt*. The displacement of the interface is averaged over the cleft width (d_{cl}) to avoid lateral mesh deformation:

$$\frac{dz}{dt} = \frac{\Delta q_{i\_mean}}{Lf} = \int_{-d_{cl}/2}^{d_{cl}/2} (q_{i\_up} - q_{i\_down}) dx \Big/ (d_{cl} \cdot Lf) \quad (2)$$

Therefore the model reproduced the movement of the mean ice level but not the shape of the melt-interface. The water sub-domain was shifted according to the melt-interface velocity. The ice sub-domain was deformed by the interface movement at the top and kept stable at the lower boundary.

The output of the model consisted of the temperature field, heat flux density and ice geometry for each time step. Heat fluxes through the boundaries of the water sub-domain and the velocity of the melt interface (*dz/dt*) were extracted as single values once they were in equilibrium (constant) or as a time slice if they were changing significantly. Model operation was verified by a visual check of the distributed model outputs, by an evaluation of maxima and minima within the solutions and by cross-checking of the calculated heat fluxes and ice erosion rates.

Laboratory experiments

The laboratory experiments were conducted in the climate chamber that can be controlled between outside air temperature and approximately –20 °C. It is subject to fluctuations due to regulation and defrosting of the refrigerator. Strong ventilation prevents air stratification inside the cooling chamber and increases heat exchange at exposed surfaces. Additionally, a basal cooling plate controls the bottom temperature. Harris et al. (2008) describe the cooling room with the basal cooling plate in detail.

The single-cleft model simulates the heat advection by water flowing along an ice surface within a frozen rock cleft and corresponds to the volume element shown in Figure 1. The vertically dipping cleft is formed by two inclined granite blocks with a spacing (d_{cl}) of approximately 4 and 8 mm, which is filled with ice (water frozen *in situ*) up to a defined initial ice level (Figure 4).

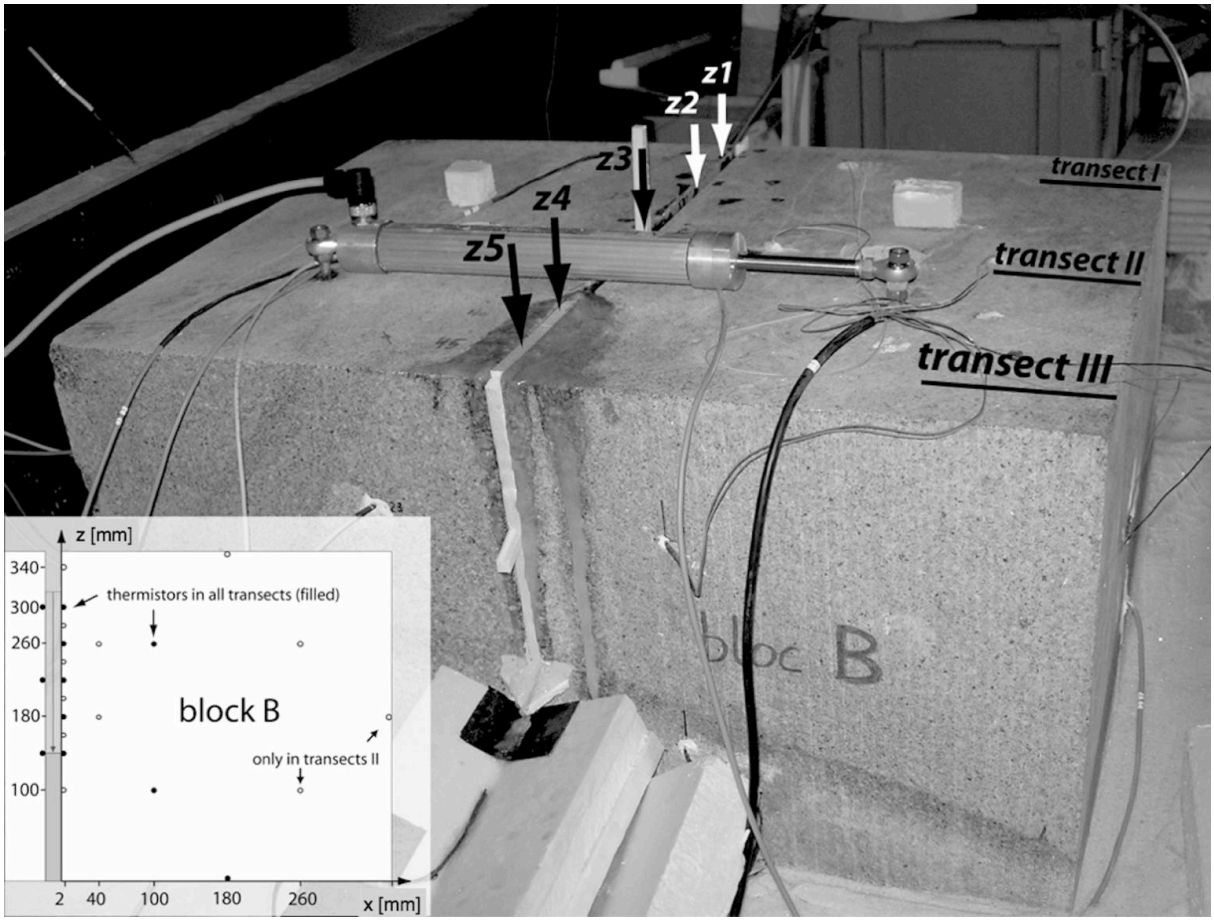

Figure 4: Setup of the laboratory experiment: Two granite blocks (0.36 * 0.36 * 0.5m) form a cleft of approximately 8 mm (and 4mm) width. The water flows from the backside to the front, where it is captured by a styrolen arrow and the water temperature is measured with a thermistor before it leaves the experiment (front). On top, a crackmeter is mounted across the cleft to record cleft aperture. Ice levels are measured at five positions along the cleft (z1 to z5); small figure: dots indicate where rock temperatures are measured within the three transects (I-III); label of thermistors are given according to x-coordinate and z-coordinate (e.g. 2_340 is the upper most thermistor near the cleft).

The ice level is kept parallel to the surface (α=12°) or at an inclination of α=3° or α=30° for the stationary experiments and at 12° as initial condition of the cyclic experiments. A controlled water flow Q of temperature T_w flows along the cleft. The granite blocks are insulated at their sides to minimize the lateral heat flux through these boundaries. The temperature at the surface (T_{up}) is controlled by the cooling room, and the bottom is kept at a constant temperature (T_{bot}) by the basal cooling plate. Granite with a low porosity (< 0.5 %) and homogenous characteristics was used to minimizes anisotropy and latent heat effects of pore water (ΔLWC close to 0). Sawed cleft surfaces lead to a reduced roughness and a more constant cleft width compared to natural situations. This setting allows a quantification of ice volume changes by simple ice level measurements but may lead to more regular flow conditions than in natural clefts. Water was cooled to the input temperature T_{win} by a looped copper tube in an ice-water bath and the flow rate was regulated by a mechanical dosing valve. The stability of Q and T_{win} was low due to feedbacks between flow and water temperature and could not be easily controlled to the desired input temperature.

Experiments are defined by *input parameters* specified for each run and *result variables* are recorded. Input parameters are the initial model temperature (T_{rock}) and *driving variables* T_{win}, Q, T_{bot} and T_{up}. Result variables are the ice level changes Δz and temperatures within the model. The vertical distance of the ice level to the block surface is manually measured at five positions (50, 150, 250, 400 and 450 mm form the inlet side) using a ruler with a precision of ±2 mm. These raw values are used to calculate the respective ice levels z1 to z5 and average ice level change Δz. The spatial distribution of rock temperatures is measured by a total of 50 thermistors placed in three transects (I=50 mm, II=250 mm and III=450 mm from inlet) perpendicular to the cleft, at 2, 40, 100 and 260 mm from the cleft

(Figure 4). These temperatures are labelled according to the distance from the cleft and the height (z-axis) (Figure 4). Thermistors at the rock surface, the sides and bottom of the block provide boundary temperatures of block B (Figure 4; right block). Cleft aperture d_{cl} is surveilled with a crack meter at the top of the blocks and the output water temperature T_{wout} is measured in the funnel below the model (Figure 4).

A 60-channel *Agilent 34970A* data acquisition system was used together with negative temperature coefficient thermistors (YSI-44031) having an absolute accuracy of ±0.05 °C around the calibration point of 0 °C. Thermistors were calibrated before the instrumentation in a double coated ice-water bath. The measurement accuracy of the water temperatures T_{win} and T_{wout} is ±0.2 °C due to the influence of ambient temperature for the lowest flow rates and better if Q>10 L h^{-1}. Water flow was measured using multi-purpose *Digmesa FHKSC flowmeters*. The sensors have an absolute accuracy of only ±20% but better relative accuracy for temporal variations. Values are recorded every 10 seconds for stationary experiments and every minute for cyclic experiments.

Calculation of heat input P_{adv} and latent heat flux P_{lat}

To link laboratory experiments and numerical modelling, the two main heat fluxes need to be defined considering the geometrical setting and the measured parameters. The sensible advected heat flux P_{adv} is calculated by the cooling of the water within the cleft $(T_{win}–T_{wout})$ multiplied with Q, the heat capacity of water C_w in J m^{-3}K^{1}.

$$P_{adv} = Q \cdot (Tw_{in} - Tw_{out}) \cdot C_w \qquad (3)$$

If Q is in L h^{-1} (as here) a divider of 3.6*10^{6} should be added to (3) to obtain Watt. For not constant fluxes and temperature differences such as the case in some laboratory experiments, P_{adv} needs to be calculated for each point in time and averaged subsequently.

The latent heat flux P_{lat} is deduced from the erosion rate dz/dt multiplied by the cleft width d_{cl}, the length of the cleft l and the latent heat of fusion Lf:

$$P_{lat} = Lf \cdot 0.917 \cdot d_{cl} \cdot l \cdot \frac{dz}{dt} \qquad (4)$$

For the non-standart units used here, (4) needs to be multiplied with 6*10^{-5} to obtain Watt. The factor 0.917 applied on Lf arrises from the lower density of ice. For the 2-dimensional modelling these values of the heat fluxes are devided by the length l of the experiment.

Model runs and calibration

The advection experiment consists of two main phases (stationary and cyclic) with several runs each. Detailed information in the settings of the laboratory experiments is provided in the supporting material (Table 1). For the stationary laboratory experiments this variation is not strictly systematic due to limitations in the control of Q and T_{win}, however rock and water temperatures and heat input cover the following range: T_{win} varies between 0 and 6 °C, Q is in the order of 4 to 60 L h^{-1} and T_{rock} is in the range of -1 to -6 °C. This does not span all possible values in nature at the near-surface but is realistic for the conditions at some meter depth in alpine permafrost. The numerical simulations of the stationary experiments reproduce these settings for model calibration before systematic variation was applied to analyze the sensitivity of the ice erosion and rock warming on these settings. A detailed list and graph of the cyclic experiment settings is also included in the supporting material. For these experiments the surface temperatures fluctuated for all cycles between -4 and +4 °C and water flow (Q) of a total volume V_w was applied after a time delay Δt. Q is limited to approximately 5 L h^{-1}, hence the duration of the advection event depends mainly on the applied water volume V_w. The water temperature was kept as constant as possible around 2 °C for all experiments and only V_w and Δt are variable for the cyclic experiments (supporting material).

The heat transfer coefficient h_{int} and the scaling factor sf of the numerical model depend on the flow conditions, which result from the flow rate, the cleft width and the inclination of the ice surface. Assuming Reynolds Numbers in the order of 10^{2} to 10^{3} derived from average flow velocity observations in the laboratory, we expect laminar flow for this open channel situation. However, the observed step formation of the melt-interface and the retrograde erosion at the model outlet indicate the presence of local turbulence. To estimate the scaling factor we neglect these features and used a simple approximation of the flow height based on the flow velocity measurements. A linear function is used to parameterize this scaling factor dependent on the flow Q and the cleft width d_{cl} (supporting material). The value of the scaling factor has minor influence on the model results. The heat transfer coefficient h_{int} was determined by two different calibration procedures (supporting material). Both methods provide parameters in the same order of magnitude. A linear function for the flow dependent heat transfer coefficient is used for each cleft size

(see supporting material). If T_w is used as driving variable, errors of h_{int} propagate proportionally to the resulting erosion rate and warming of ice. For model runs driven by P_{adv} the influence of h_{int} is only significant when erosion rates are close to zero. P_{adv} is used as driving variable for all experiments, except for the analysis of the scale effects.

RESULTS

Laboratory experiments

Several qualitative and semi-quantitative observations were made during the experiments that are important for interpretation of the quantitative results. One to four steps, 2-5 cm high, formed in the cleft ice surface with the exception of when the ice was inclined at only 3°. These irregularities affected those stationary experiments with strong erosion as well as cyclic experiments. Frontal erosion of the ice occurred at the lower side of the cleft (water outlet; close to *z5*) and an over-deepening of the ice-water interface developed at the water inlet (at *z1*). This required sealing the upper side of the cleft to avoid water loss. Some ice remained on the lateral cleft surfaces at low rock temperatures so the entire cleft ice volume within *dz* was not subject to melt. These observations indicate the importance of flow conditions for local ice erosion rates and the potential for warm water to cause rapid ice-erosion. For each stationary experiment, water temperatures within the cleft were measured intermittently, indicating a linear temperature decrease along the cleft. The cleft width (d_{cl}) did not change significantly as long as the model remained frozen.

The results of one stationary experiment are shown in Figure 5a. The advective heat flux according to equation (3) and the erosion rate in the middle (z3) of the experiment were constant (black line). The higher erosion rate at z5 resulted from frontal erosion at the experiment outlet. The near-cleft temperatures (at z = 300 and 280 mm) increased until the ice level and corresponding water flow reached the level of the thermistor. Subsequently, the temperature dropped again with a slightly lower gradient. When two thermistors were passed by the erosion surface, the time between two temperature peaks indicates the erosion rate at this transect (Figure 5a). For the experiment shown, this value corresponds well with the manual measurements of ice erosion.

The average ice erosion rate based on all ice level measurements was calculated for stationary experiments. These rates depend on cleft width, advective heat input and initial rock temperature (Figure 5b). The number of experiments is not sufficient to quantify these relations empirically, but Figure 5b indicates that the erosion rate correlates with the applied advective heat for similar cleft widths and initial rock temperature (T_{rock}). The lines in Figure 5b indicate the maximum erosion calculated by equation (4) assuming that all heat is transformed into ice melt (P_{lat}/P_{adv} = 1). Erosion rates exceeded this theoretical limit in one experiment (Figure 5b; *stat_13*: red square at 47 W). The water temperature had a further influence on the erosion rate because higher water temperatures at the same P_{adv} (larger T_{win} and smaller flow Q) resulted in more ice erosion (P_{lat}/P_{adv} is larger). However, this effect was minor compared to the influence of P_{adv} and T_{rock}. The inclination α also had an influence on flow conditions (h_{int} in the model) and modified the heat input P_{adv} (supporting material). This explains the observed frontal erosion and may control the along-cleft form of the ice level.

The input parameters and other variables of interest in one cyclic experiment are shown in Figure 6a. The near-cleft temperatures at the ice level showed an abrupt increase when water was applied. A significant modification of the conductive warming was also observed at the thermistors at 40 mm distance to the cleft. The applied advective heat per cycle is proportional to the water volume V_w (light blue area) if the water temperature remains constant as intended for all experiments. This was not the case and T_{win} was significantly different from 2 °C for some cycles (Figure 6a). However, V_w and Δt were used as common settings that define cycle classes and the variability in T_{win} affected the spreads (boxplot) in ice erosion per cycle within these classes (Figure 6b; supporting material). Step formation in the ice surface accumulating over several cycles may have been a further reason for the large spreads. Nevertheless, a qualitative dependency of the ice erosion on V_w and Δt is apparent, with the timing of the applied advective heat and the amount of heat of comparable importance (Figure 6b).

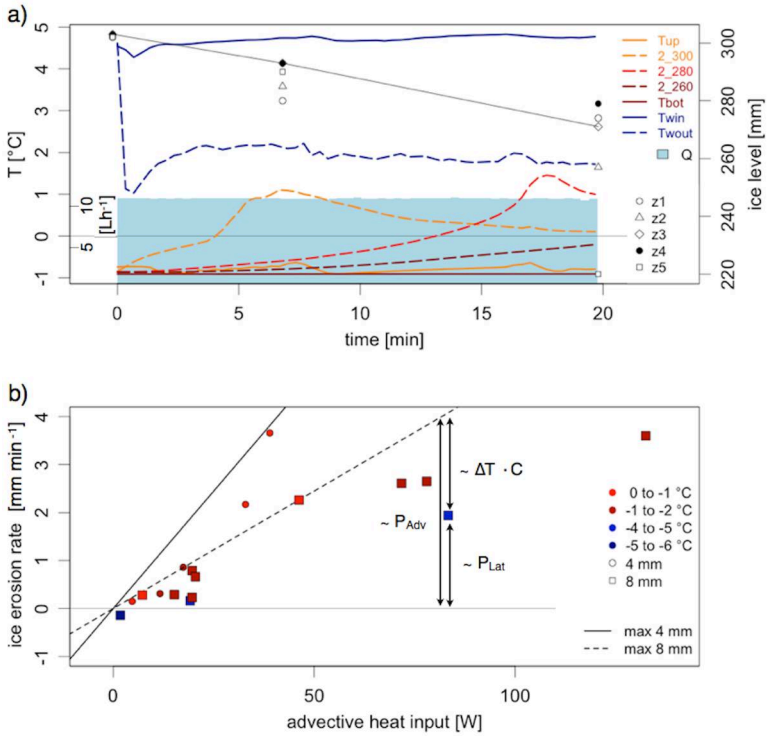

Figure 5: Results from the stationary laboratory experiments: a) measured driving variables (T_{up}, T_{bot}, T_{win}, Q), rock temperatures of transect II near the cleft (2_300, 2_280, 2_260), and ice levels (*z1-z5*) at the example of experiment stat_5 (4 mm cleft, Q=12 L h^{-1}, T_{win}=4.7°C). The line for *z3* indicate an erosion rate of 1.6 mm/min. The time difference between the two peaks indicates 20 mm erosion in 11 minutes (1.8 mm/min); b) ice erosion rates for different cleft sizes (point shape) as a function of applied advective heat flux P_{adv} ; point colours indicate rock temperature at experiment start; the lines correspond to the maximal erosion rates when all applied energy is used for ice melt only: P_{lat} of one experiment is proportional to the distance from 0 mm/min erosion and the distance to the corresponding line is proportional to the advective warming of the rock (example by arrows).

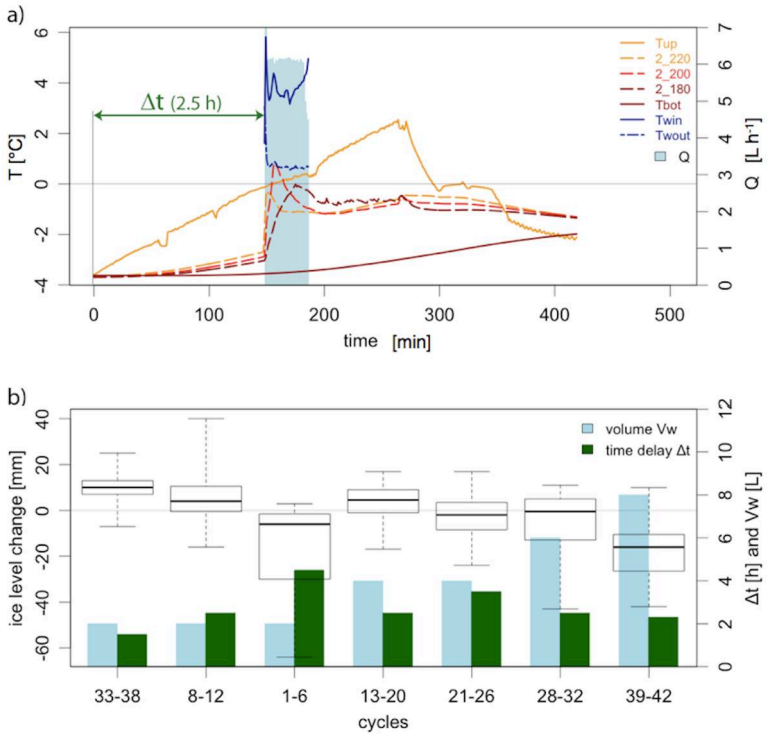

Figure 6: Results from the cyclic laboratory experiments: a) boundary conditions, flow Q, water temperatures (T_{win}, T_{win}), and near-cleft rock temperatures for warm period of cycle 30; b) ice erosion per cycle, ordered by applied water volume V_w and time delay Δt. The box plot indicates the spread (variance (box) and extreme values (whiskers)) of all the ice level changes (z1 to z5) of the different cycles with similar settings.

Numerical model results

Figure 7 shows the near-cleft rock temperatures for a model run with P_{adv} and T_{rock} settings similar to those of the laboratory experiment stat_5. The amplitudes and time lags for two modelled temperatures (m_300 and m_280) correspond well with those for the thermistors 2_300 and 2_280 in the experiment. It should be noted that these temperatures were not used for the calibration of h_{int} (supporting material) so this accord indicates that the model is operating correctly. In experiment stat_5, the ratio P_{lat}/P_{avd} was 20 W/33 W, while the modelled ratio for the corresponding settings is 19.2 W/33.3 W.

The evolution of the modelled ice level (Δz) for different P_{adv} and T_{rock} = –3 °C is shown in Figure 8. For large heat inputs (P_{adv} > 20 W) the ice erosion starts within seconds after model initialization. If P_{adv} is low, however, significant ice aggradation occurs. Similar aggradation was observed in the laboratory experiments (Figure 5b; negative erosion rate). The aggradation is greatest at the start of the advective heat flux due to the large sensible heat flux toward the sub-zero cleft environment. For simulations with moderate heat input (10 W > P_{adv} > 5 W; for 8mm cleft) ice aggrades during the first seconds or minutes, and is subsequently eroded or remains at a constant level if the heat flow for rock warming (ΔT) balances P_{adv} (Figure 8). The time until the heat fluxes are in equilibrium and *dz/dt* becomes constant is referred to as equilibration time (Δt_{eq}).

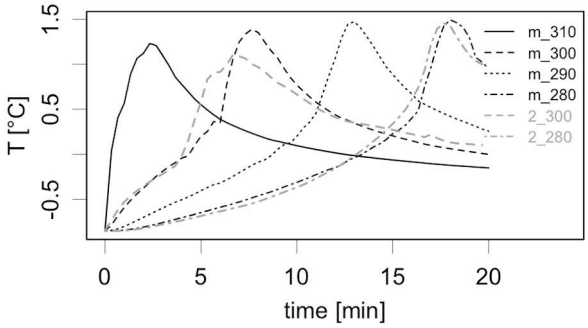

Figure 7 Numerical model results (*m_310, ..., m_280*) and measured (transect II: *2_300, 2_280*) near-cleft rock temperatures (2 mm from cleft surface) in a 4 mm wide cleft. The settings correspond to experiment stat_5 (T_{rock} = -0.85 °C, P_{adv} =33 W).

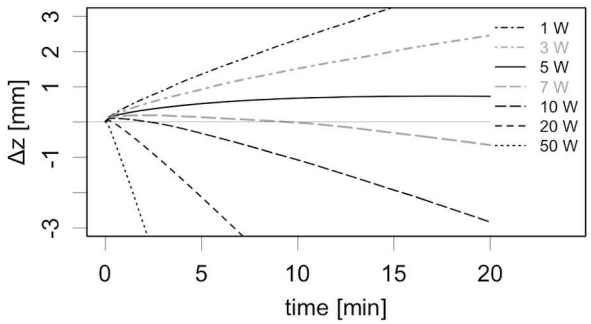

Figure 8 Modeled ice levels change Δz for various P_{adv} (legend) with d_{cl} = 8 mm and T_{rock} = -3 °C. The ice level change becomes linear (constant erosion rate) after a stabilization time that is shorter for large P_{adv}.

SYNOPSIS AND DISCUSSION

Ice erosion, aggradation and stable conditions for constant heat input

A first step towards quantitative understanding of heat advection in frozen rock clefts is to quantify Δz and ΔT for a constant P_{adv}. Figure 9 shows the modelled equilibrium ice erosion rates *dz/dt* that result from a heat input P_{adv} to a rock cleft at a given bulk temperature T_{rock}. Equilibrium is reached after Δt_{eq} = 200-4000 seconds. Ice erosion increases nearly linearly with the heat applied for rock temperatures ranging from 0 to -5 °C. The relative difference of *dz/dt* between different rock temperatures decreases with P_{adv} (Figure 9). This suggests that cleft ice is eroded independently of the temperature of the surroundings for large P_{adv} once the erosion equilibrium is reached (after Δt_{eq}). The decreasing influence of T_{rock} is caused by the larger ratio P_{lat}/P_{adv}, which results from smaller thermal gradients between the water and the warmed cleft surface at the water-rock interface while the ice surface remains at 0 °C. The erosion rates are of the same order of magnitude as those for the stationary laboratory experiments (Figure 5). In cases where the cleft orientation deviates strongly from the modelled vertical case, less heat is consumed by ice melt (smaller P_{lat}/P_{adv}) due to a larger contact area of the flow cross-section and the cleft surface, and possibly because of ice remaining at the upper cleft surface.

A multiple linear regression analysis was used to describe the ice erosion rate $dz/dt(P_{adv}, T_{rock})$ after Δt_{eq} for an 8 mm near-vertical ice-filled cleft of 0.5 m length:

$$\frac{dz}{dt}\left[mm/\min\right] = (0.05 + 0.04 \cdot P_{adv} + 0.1 \cdot T_{rock}) \qquad (5)$$

with the numerical values of P_{adv} in W and T_{rock} in °C. This linear approximation is represented by the lines in Figure 9 for the results from the numerical model. The quality of both the approximation and the numerical model results is low for small erosion rates and heat inputs due to larger relative errors. Even though an extrapolation with equation (5) to stable conditions of the ice level

(6.25 W) coincides with the erosion rates of small P_{adv} values in Figure 8, much time is needed for these rates to reach equilibrium. The laboratory experiment with small advective heat inputs and cold rock temperatures indicates a similar range (equation (5) with -5 °C: 11.3 W; Figure 5b: interpolation from squares ≈ 10 W). Even though equation (5) is based on only a few results from the numerical model it describes the dependency of the two main parameters P_{adv} and T_{rock}. A Pearson's correlation coefficient of 0.94 was obtained when it was applied to all laboratory experiments (all cleft sizes). Hence, equation (5) can be used to provide a rough estimate of ice erosion for clefts approximately 1 cm wide, and to eliminate the length of the considered cleft, the heat input per length unit (W m^{-1}) can be calculated by replacing the coefficient of 0.04 by 0.02 (multiplying by 0.5 m). In the supporting material the effect of variable heat input is discussed and can be summarized that a variable heat input causes slightly more ice erosion than a constant one and that this variability is more important if the heat input is small (close to stability conditions).

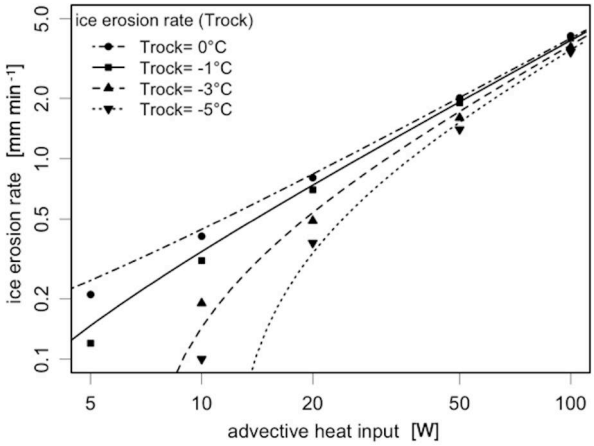

Figure 9 Modeled ice erosion rates *dz/dt* in dependence of the advective heat input (P_{adv}) and for different rock temperatures (legend) in an 8 mm wide cleft. The points are the results from the numerical model, the lines indicate the approximation by the linear function (5). The relative difference of the erosion rate decreases with larger advective heat input. This corresponds with more heat used for ice melt regarding the applied heat (P_{lat}/P_{adv}). The residuals between linear approximation and model results appear larger for small erosion rates due to the logarithmic representation.

Dependency of erosion rate on timing of advection and conduction

Advective heat inputs into a cleft are usually accompanied by conductive heat from the surface. Depending on the geometric situation and the surface condition (bare rock vs. snow cover) this conductive warming has differing influences on the rock temperature around the ice level. The cyclic laboratory experiments indicate that the erosion of the cleft ice during a thawing event depends on the sum of applied advective heat but is also sensitive to changes in the time lag Δt between the start of surface warming and the start of heat advection (Figure 6b). As the data quality of these experiments is limited, these results were analyzed using equation (5). The small applied heat flux (P_{adv} = 14 W) results in a rock temperature of -5.7 °C for stability. The rock temperatures around the cleft ice level before percolation (Figure 6a) were in the range of -2 to -5 °C and erosion occurred after initial aggradation. The time until the aggraded ice was completely eroded is in the order of 3 to 30 min and is very sensitive to changes in P_{adv} and T_{rock}. If the duration of the applied flux is short, a net aggradation instead of net erosion takes place (see cycles 33–38, 8–12 and 13–20 in Figure 6b).

The amount of heat conducted through the rock that reaches the cleft ice level after a given time depends on the latter's depth. If the ice were to aggrade over several cycles it would reach a level where heat conduction warms the rock more rapidly and aggradation would decrease or cease. Erosion does the opposite, moving the thawing front in the cleft to colder levels and resulting in a reduced rate of erosion. That leads to stabilization of the ice level after repeated similar cycles as was observed in the laboratory for cycles 8–12 (while a decrease in erosion per cycle occurred for cycles 39–42, as shown in the supporting material). In the field, this means that the ice level represents a hydrothermal equilibrium if conditions are similar on an inter-annual basis and if the ice level is at a depth of a few meters where annual cycles are present and the temperatures decrease with depth when sensible heat advection occurs. If the cleft ice erodes to a level where thermal gradients become reversed, similar hydrothermal conditions would lead to progressive thawing over the years until the lateral heat loss of the percolating water (Figure 2) is large enough to reduce the heat input at the cleft ice level. This indicates that relatively small climatic variations resulting in changed inputs of water could significantly alter cleft ice conditions.

Scaling of conductive and advective heat transport

The cleft size d_{cl} influences advective heat exchange by modifying the flow cross-section for a given discharge (changed *sf* in the model) and the ice erosion rate changes because the latent heat used for erosion depends on d_{cl} (ice volume). In the laboratory, a constant P_{adv} causes less ice erosion and less sensible warming if d_{cl} is increased because more ice volume needs to be eroded for a given Δz (see Figure 5b).

If the whole experiment is scaled by a factor *f* and Q is multiplied by f^2 (proportional to the surface supplying the cleft with water of temperature T_{win}), the ice erosion rate remains in the same order of magnitude. For a modelled cleft with d_{cl} = 80 mm, for example, the erosion rate dz/dt increased by only 50% compared to one with d_{cl} = 8 mm. This change is caused by an increase of P_{lat}/P_{adv} at larger dimensions. If the heat input in the up-scaled experiment lasts for factor *f* longer (time scaling of *f*), the ice level change relative to the experiment scale remains in the same order of magnitude (e.g. increased by the 50% from the above example). For the situation including conductive heat flux (cyclic experiments) the time scaling of the two processes is not similar: in an up-scaled situation, the conductive heat wave needs f^2 more time to propagate from the surface to a depth increased by the factor *f* (cf. model result in Figure 3c). This different time scaling of the advective and conductive regime (*f* vs. f^2 respectively) does not allow a direct scaling of the cyclic experiments to annual cycles of a larger volume. The cyclic laboratory experiments, therefore, illustrate the processes but do not provide a quantitative basis for up-scaled conditions. In contrast, the stationary experiments can be transferred to other scales and allow estimates of ice erosion and rock warming in larger clefts.

CONCLUSIONS

Several specific conclusions can be reached from this study:

(1) Advective heat transport by percolating water is a highly efficient process to transmit heat from the surface to the level where clefts become impermeable. The conceptual model suggests that heat exchange with the surrounding rock takes place mainly in the area of the cleft ice level as the water accumulates there and runs off laterally. Progressive thaw of cleft ice conceals the effect of warming events by export of latent heat making them not directly detectable in ground temperature records. As a consequence the local degradation of permafrost along rock clefts may be at least partially hidden from thermal monitoring.

(2) More than half of the advected sensible heat is consumed by phase change of the cleft ice erosion while the minor part results in rock warming. The findings from the laboratory experiments and the numerical models indicate that ice erosion occurs even in cold rock if the applied heat along a cleft is large enough (>28 W m^{-1} for -6 °C and >12 W m^{-1} for -3 °C in a 8 mm cleft). This ice erosion occurs only after the cold rock has locally warmed due to the latent heat released by ice aggradation during initial percolation. For large advective heat inputs the rock temperature has only a minor effect on the erosion rate. Conversely, percolation with only a small heat input into a cold rock cleft results in ice aggradation.

(3) The main parameters that govern ice erosion and rock warming in a frozen cleft are the advective sensible heat input (resulting from water flow rate and water temperature) and rock temperature. Other factors, such as scale effects, water temperature alone (for the same heat input) and the variability of the flow, slightly alter the ratio between energy used for ice erosion and rock warming but do not strongly modify the absolute values. Laboratory experiments simulating melt water input during a thawing event indicate that the timing of the initiation of the sensible heat advection relative to conductive warming from the surface is important. Given the small heat fluxes applied during these experiments, this effect is attributed to ice aggradation during initial water percolation.

A general conclusion is that rockfall, if related to the warming and ice erosion in clefts, is not necessarily limited to areas with relatively warm permafrost. This may account for the low correlation observed between modelled permafrost temperature and rockfall occurrence. Further the study shows that heat applied from the surface by advection may reach failure planes at depth more rapidly and cause events of a greater magnitude than would be expected based on the assumption of conductive heat transfer.

Studies with hydro-thermal models, as well as geophysics in steep bedrock may contribute to a better understanding of permafrost degradation relating to ground ice loss. Of particular interest would be the coupling of such models with meteorological data so that the sensitivity of clefts to different meteorological situations could be assessed and compared to observed rockfall activity.

LIST OF TERMS

α	inclination of the ice surface along the cleft [°]
ΔLWC	change in liquid pore water content [%]
Δt	time delay between start of warming and applied advection in cyclic experiments [h]
Δt_{eq}	equilibration time needed until the ice erosion rate remains constant [s]
ΔT	temperature change of rock (and ice) in the considered volume [°C]
Δz	cleft ice level change [mm]
C_w	heat capacity of water (volumetric; liquid water): 4.18 MJ/m^3 K
d_{cl}	cleft width (aperture) [mm]
dz/dt	ice erosion rate (positive values for $\Delta z<0$) [mm/min]
h_{int}	heat transfer coefficient for water–ice interface [W/m^{2}K]
Lf	latent heat of fusion (volumetric; liquid water): 334 MJ/m^3
l	length of cleft in experiment; constant: 0.5 m
P_{cond}	conductive heat flux [W]
P_{adv}	advective heat flux [W]
P_{lat}	latent heat flux due to cleft ice change (Δz) [W]
Q	water flow (flow rate) [L/h]
q	heat flux [W/m^2]
sf	scaling factor for the sideward heat transfer coefficient (water–rock) ($sf=h_{side}/h_{int}$)
T_w	mean water temperature in the cleft (empirically: $(T_{win}+T_{wout})/2$) [°C]
T_{win}	water temperature at the inlet [°C]
T_{wout}	water temperature at the outlet [°C]
T_{rock}	initial or undisturbed rock (and ice) temperature [°C]
T_r, T_{r_x}	measured rock temperature within the physical model (laboratory) [°C]
T_{up}	temperature of upper boundary (surface in laboratory) [°C]
T_{bot}	temperature of lower boundary (bottom) [°C]
V_w	applied water volume in the cyclic experiments (L)
$z1$–$z5$	cleft ice level along the cleft at 50–450 mm from the inlet [mm]
z	ice level (in general, modelled, averaged)

ACKNOWLEDGEMENTS

We would like to thank Jean-Louis Lagarde, Hansueli Gubler, Jean-Claude Ozouf and Wilfried Haeberli for their advice, many interesting discussions and for sharing their long experience in geomorphdynamics, environmental physics and (lab-) instrumentation. The team of the morphodynamic laboratory CNRS-M2C in Caen (FR), friendly welcomed and supported the first author during the experiments: Thank you! The presented research, was mainly funded by the Swiss Federal Office for the Environment (FOEN) via the project PermaSense and additionally supported by the SNF NCCR-MICS. M. Fabrice Freret and M. Bernard Legentil, Carrières de Montjoie, Av. De Bischwiller, 14501 Vire Cedex France, are thanked for their availability, their advices and the accurate cutting of the granite blocks used for the laboratory experiment.

REFERENCES

Boike, J. Hagedorn, B. Roth, K. 2008. Heat and water transfer processes in permafrost-affected Soils: A review of field-and modeling-based studies for the Arctic and Antarctic. In *Proceeding of the Ninth International Conference on Permafrost*. , Fairbanks, Alaska, USA pp. 149–154.

Boike, J. Roth, K. Overduin, PP. 1998. Thermal and hydrologic dynamics of the active layer at a continuous permafrost site (Taymyr Peninsula, Siberia). *Water Resources Research* **34**(3): 355–363.

Dietrich, P. 2005. *Flow and Transport in Fractured Porous Media* Springer.

Epstein, M. Cheung, FB. 1983. Complex freezing-melting interfaces in fluid flow. *Annual Review of Fluid Mechanics* **15**: 293–319.

Fischer, L. Purves, R. Huggel, C. Noetzli, J. Haeberli, W. On the influence of geological, topographic and cryospheric factors on slope instabilities: Statistical analyses of recent Alpine rock avalanches. submitted to *Natural Hazards and Earth System Sciences*.

Geertsema, M. Clague, JJ. Schwab, JW. Evans, SG. 2006. An overview of recent large catastrophic landslides in northern British Columbia, Canada. *Engineering geology* **83**(1-3): 120–143.

Gilpin, RP. Hirata, T. Cheng, KC. 1980. Wave formation and heat transfer at an ice-water interface in the presence of a turbulent flow. *Journal of Fluid Mechanics* **99**(3): 619–640.

Gruber, S. Haeberli, W. 2007. Permafrost in steep bedrock slopes and its temperature-related destabilization following climate change. *Journal of Geophysical Research* **112**: F02S18.

Gruber, S. Hoelzle, M. Haeberli, W. 2004. Permafrost thaw and destabilization of Alpine rock walls in the hot summer of 2003. *Geophysical Research Letters* **31**(13): L13504.

Haeberli, W. Wegmann, M. Vonder Muehll, D. 1997. Slope stability problems related to glacier shrinkage and permafrost degradation in the Alps. *Ecologae Geologicae Helvetiae* **90**(3): 407–414.

Haeberli, W. Beniston, M. 1998. Climate change and Its impacts on glaciers and permafrost in the Alps. *Ambio* **27**(4): 258–265.

Harris, C. Arenson, LU. Christiansen, HH. Etzelmüller, B. Frauenfelder, R. Gruber, S. Haeberli, W. Hauck, C. Hölzle, M. Humlum, O. 2009. Permafrost and climate in Europe: Monitoring and modelling thermal, geomorphological and geotechnical responses. *Earth Science Reviews* **92**(3–4): 117–171.

Harris, C. Davies, MCR. Etzelmueller, B. 2001. The assessment of potential geotechnical hazards associated with mountain permafrost in a warming global climate. *Permafrost and Periglacial Processes* **12**(1): 145–156.

Harris, C. Kern-Luetschg, M. Murton, J. Font, M. Davies, M. Smith, F. 2008. Solifluction processes on permafrost and non-permafrost slopes: results of a large-scale laboratory simulation. *Permafrost and Periglacial Processes* **19**(4): 359–378.

Hasler, A. 2011. *Thermal conditions and kinematics of steep bedrock permafrost*. PhD Thesis. Zurich, Switzerland: University of Zurich.

Hasler, A. Gruber, S. Haeberli, W. 2011. Temperature variability and thermal offset in steep alpine rock and ice faces. *The Cryosphere Discussion* **5**: 721–753.

Kane, DL. Hinkel, KM. Goering, DJ. Hinzman, LD. Outcalt, SI. 2001. Non-conductive heat transfer associated with frozen soils. *Global and Planetary Change* **29**(3–4): 275–292.

Krautblatter, M. Hauck, C. 2007. Electrical resistivity tomography monitoring of permafrost in solid rock walls. *Journal of Geophysical Research* **112**: F02S20.

Noetzli, J. Hoelzle, M. Haeberli, W. 2003. Mountain permafrost and recent Alpine rock-fall events: a GIS-based approach to determine critical factors. In *Proceedings of Eighth International Conference on Permafrost*. , Zürich, Switzerland pp. 827–832.

Pogrebiskiy, MI. Chernyshev, SN. 1977. *Determination of the Permeability of the Frozen Fissured Rock Massif in the Vicinity of the Kolyma Hydroelectric Power Station (Oshenka Vodopronishaemosti Merzlogo Greshinovatogo Massiva Gornkh Porod Uchastka Kolmskoy ges)* Cold Regions Research and Engineering Laboratory Hanover NH.

Rist, A. Phillips, M. 2005. First results of investigations on hydrothermal processes within the active layer above alpine permafrost in steep terrain. *Norwegian Journal of Geography* **59**(2): 177–183.

Rist, A. 2007. *Hydrothermal processes within the active layer above alpine permafrost in steep scree slopes and their influence on slope stability*. PhD Thesis. University of Zürich, Switzerland.

Scherler, M. Hauck, C. Hoelzle, M. Stähli, M. Völksch, I. 2010. Meltwater infiltration into the frozen active layer at an alpine permafrost site. *Permafrost and Periglacial Processes* **21**(4): 325–334.

Stähli, M. Jansson, P. Lundin, L. 1996. Preferential water flow in a frozen soil – a two-domein model approach. *Hydrological Processes* **10**(10): 1305–1316.

Correspondence to:
Andreas Hasler, Department of Geography, University of Zurich, Winterthurerstr. 190, 8057 Zürich, Switzerland, andreas.hasler@geo.uzh.ch

Supporting Material

General heat transport equation

Equation 1 derived by the time can be written as the general heat transport equation for a porous rock mass (neglecting pore water migration) containing partly permeable clefts with Q being the water flow through the cleft, T_w the water temperature, C_w the volumetric heat capacity of water, K_r the thermal conductivity of the rock, Lf the latent heat of fusion of water, V_{por} the pore volume, sat the water saturation of the pores and C and T the heat capacity and temperature of the considered volume element:

$$C_w \cdot Q \cdot \nabla T_w + \nabla \cdot (K_r \cdot \nabla T) = \frac{\partial CT}{\partial t} + Lf \cdot \nabla \cdot Q + Lf \cdot V_{por} \cdot sat \cdot \frac{\partial LWC}{\partial t} \quad (6)$$

In (6) the cleft ice mass change is expressed by mass gain or loss in the cleft water flow assuming that the liquid cleft water is not retained. This formulation does not address the Stefan Problem because the heat exchange between the water and the ice is not expressed. Thereto we need a formulation, how efficiently sensible heat is transformed into latent heat. This is expressed by (2) in the formulation of the numerical model.

Sensitivity analysis, parameterization and calibration of the numerical model

The model parameters, influencing the model output to different extents, are grouped in four categories: The *internal model parameters* and the *material parameters*, are set to constant values for all experiments. The *heat exchange parameters* being the heat transfer coefficient h_{int} and the scaling factor sf. Finally there are the *input parameters* (*initial condition* (T_{rock}, α, d_{cl}, and initial ice level) and the time dependent *driving variables* being the heat input (T_w and Q or P_{adv}) and conductive boundary conditions (T_{ro} and T_{bot})). Their effect on the model output is presented in the results section and they are not subject to this technical sensitivity analysis.

Internal model parameters have no physical meaning and are prescribed with high/low values (K_w =100 W m^{-1} K^{-1}, C_w = 1000 J kg^{-1} K^{-1}) to set the whole water sub-domain to uniform temperature. The parameter h_{conv} couples the input variable T_{w_mean} to the sub-domain and is set to 10^8 W m^{-3} K^{-1}. The model results are not sensitive these values. The material parameters, the heat capacity and the thermal conductivity were set to C_i = 1.93 MJ m^{-3} K^{-1} and K_i = 2.2 W m^{-1} K^{-1}, for ice and to C_r = 2.4 MJ m^{-3} K^{-1} and K_r = 3.2 W m^{-1} K^{-1} for rock (Cermak and Rybach, 1982). Rock parameters varying ±30% cause no significant change of ice erosion rates but the sensible heat flux from water to the rock P_{sides} is slightly modified. This may influence the results in situations where the melt-interface is nearly stable and when the model is driven by P_{adv}. Ice parameters are regarded as invariable for the temperature range considered.

The scaling factor was derived from the estimated flow heights of the laboratory experiments. Travel-time measurements from inlet to outlet are converted into flow velocities (v_f). This values in the order of 0.1–0.5 m/s is used to estimate the flow height and scaling factor correspondingly:

$$sf \approx Q/(v_f \cdot d_{cl}^2) \quad (7)$$

A linear parameterisation function for sf is fitted through estimated ratios of the flow height over cleft aperture (Figure S1a).

The heat transfer coefficient h_{int} is deduced in two ways: 1) For a given T_w, h_{int} is adjusted until the modelled interface velocity in the model corresponds to the ice erosion rate dz/dt (averaged over the middle three measurements z_2, z_3 and z_4); and 2) P_{adv} is used as driving parameter and h_{int} is adjusted to reach the measured values for T_w. The first procedure is sensitive to errors in the ice level measurements, whereas the second depends on sf and provides inaccurate values in case of strong frontal erosion (erosion of the cleft ice at outled). For the experiments with 3° inclination, we used only the first procedure because of significant frontal erosion. For all other experiments, method two provided more consistent results, which were used to calculate linear regressions (Figure S1,b). The heat transfer coefficient increases with inclination and Q except for the 3° inclination and are approximated by the linear funtion: h_{int} =2300 + Q*90 (Figure S1,b). The accuracy of the absolute values of h_{int} is limited due to the data quality of the lab measurements but this is relevant only if T_w is used as driving variable.

Overview of experimental runs

The laboratory experiment consists of two phases with several runs each (Table 1). Prior to the actual advection experiment, test and calibration runs where conducted (Table 1) to check sensor calibration in situ and to evaluate rock thermal parameters for use in the numerical model. In the first stationary phase, ice erosion is observed and the warming of the rock is recorded every 10 seconds. The cyclic experiments of the second phase simulate the combination of a conductive heat wave from the rock surface with advective heat input at the melt interface. Values are recorded

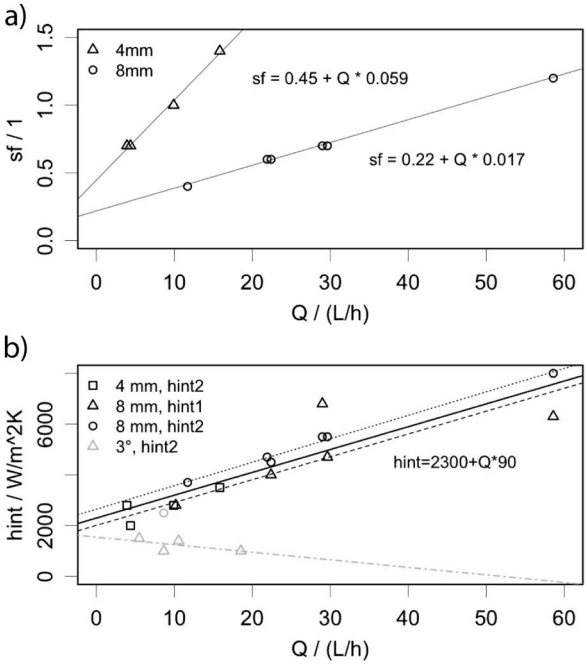

Figure S1 Numerical model parametrization: a) estimated scaling factor between downward and sideward heat transfer coeficient (sf = h_{int}/h_{side}) based on flow height estimates; b) heat transfer coefficient h_{int} is fitted to the observed with values deduced from the lab experiments.

every minute. Aggradation and erosion of the cleft ice during these *thawing cycles* are observed only by their integral effect on the ice level as it is evaluated once per cycle. In Figure S2 all the ice level measurements at the end of each thawing phase. The ice level change for cycles with same settings (V_w and Δt) vary strongly because the water temperature was different between cycles (1.5–3.5 °C). Further the ice level change depends on the depth of the ice level within the experiment because of the damping and latency of the conductive heat wave with depth. this may lead to a stabilization of the ice level after many cycles with similar parameters. This effect is adumbrated for the cycles 9–13 and 29–33 (Figure S2).

Variable versus constant heat input – numerical sensitivity study

The applied water flow and temperature does not remain constant over time in nature and the question, if variable $P_{adv}(t)$ has similar effects as its temporal mean (P_{adv_mean}), is essential for a transfer of results to natural situations. As an extreme case of variable advection we discuss the effect of a pulsed heat input in comparison to a constant P_{adv}: Δt_{adv} is the duration of water being applied to the cleft and Δt_{dry} is the time period with no water in the cleft and with possible negative temperatures at the melt interface. Comparisons of the modelled pulsed heat input with P_{adv_mean} (averaged advective heat input) show that P_{lat} and the corresponding ice erosion are larger in the pulsed case (Figure S3). This is explained by the fact that the ratio P_{lat}/P_{adv} does not remain constant: With P_{adv} being larger than P_{adv_mean} less of the heat applied is used to warm the rock and, consequently, more heat is available for ice melt. This causes a large relative difference of dz/dt if the ice level is nearly stable (Figure S3; *const5W* vs. *puls10W*). With cyclic heat input where P_{adv} remains positive ($cycl$ = 10 ± 8 W) and water is always available for refreezing, there is no significant increase of dz_i/dt compared to constant

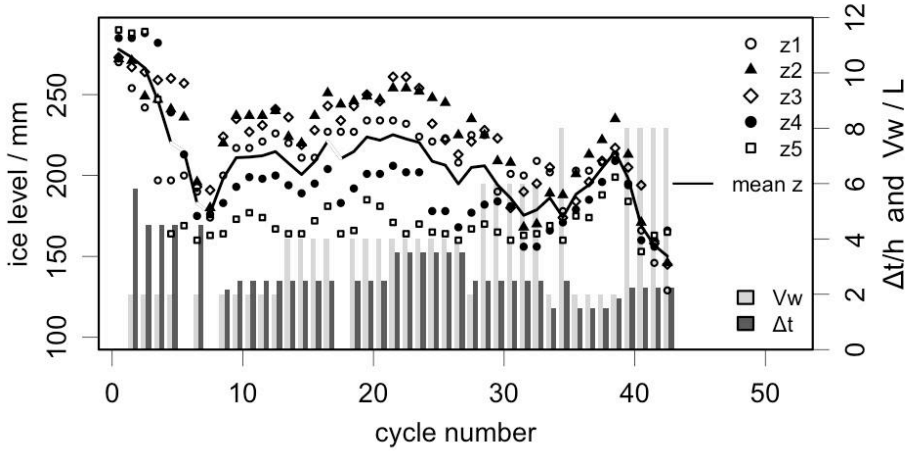

Figure S2 Results of the cyclic experiments: Ice levels of all cyclic experiments with corresponding applied water volume Vw and time delay from start of warming to start of water discharge Δt.

Table 1. Experimental runs of the laboratory experiments

phase	run	d_{cl} [mm]	α [°]	Q, (V_w) [L/h]	T_{win} [°C]	T_{bot} [°C]	T_{up} [°C]	duration, (time delay)	dz/dt [mm/min]
calibration & preparation	therm. test	3	12	0	-	0	0	1 d	
	temp. step	3	12	0	-	-10	-10	1 d	
	initial freez	3	12	0	-	-10	-10	1 d	
stationary experiments	stat3_1	3.6	12	4.5	5.92	-1	-1	21 min	1.33
	stat3_2	3.6	12	4.4	0.97	-1	-1	73 min	0.11
	stat3_3	3.6	12	3.9	1.7	-1	-1	38 min	0.25
	stat3_4	3.6	12	9.8	2.2	-1	-1	24 min	0.54
	stat3_5	3.6	12	11.7	4.69	-1	-1	20 min	1.78
	stat3_6	3.6	12	15.8	3.4	-1	-1	11 min	1.59
	stat9_1	8.7	12	8.3	0.79	-5	-6	32 min	-0.23
	stat9_2*	8.7	12	11.5	1.71	-5	-6	42 min	0.22
	stat9_3	8.7	12	11.6	1.61	-5	-6	30 min	0.02
	stat9_4	8.7	12	19.7	5.29	-5	-6	25 min	1.47
	stat9_5	8.7	12	21.9	5.07	-1.5	-1.5	8 min	2.83
	stat9_6	8.7	12	29.6	4.19	-1.5	-1.5	9 min	2.52
	stat9_7	8.7	12	29	2.63	-1.5	-1.5	8 min	2.27
	stat9_8	8.7	12	58.6	4.53	-1.5	-1.5	7 min	4.05
	stat9_9	8.7	12	10.2	2.03	-1.5	-1.5	46 min	0.51
	stat9_10*	8.7	12	4.9	-0.13	-1.5	-1.5	22 min	-0.06
	stat9_11	8.7	12	18.5	1.44	-1.5	-1.5	30 min	0.1
	stat9_12*	8.7	3	10.3	1.38	-1.5	-1.5	56 min	0.14
	stat9_13	8.7	3	5.5	1.13	-1.5	-1.5	102 min	0.11
	stat9_14	10	3	8.6	1.83	-1.5	-2	80 min	0.1
	stat9_15	10	30	8.5	1.9	-1.5	-2	92 min	0.66
cyclic experiments	cycl. 1-6	10	free	5, (2L)	2	-5	-4 to 4	1d, (4.5h)	
	cycl. 8-12	10	free	5, (2L)	2	-5	-4 to 4	1d, (2.5h)	
	cycl. 13-20	10	free	5, (4L)	2	-5	-4 to 4	1d, (2.5h)	
	cycl. 21-26	10	free	5, (4L)	2	-5	-4 to 4	1d, (3.5h)	
	cycl. 28-32	10	free	5, (6L)	2	-5	-4 to 4	1d, (2.5h)	
	cycl. 33-38	10	free	5, (2L)	2	-5	-4 to 4	1d, (2.5h)	
	cycl. 39-42	10	free	5, (8L)	2	-5	-4 to 4	1d, (2.5h)	

* = runs are not considered for analysis because of irregularities in Q or T_{win}
for cyclic experiments Q and T_{win} are given as nominal values but they slightly vary
dz/dt is calculated by averaging z2, z3, and z4 to exclude disturbances from inlet and outlet.
α = free indicates that the ice surface is not levelled between cycles.

heat input (Figure S3) The faster start of ice erosion of the simulations with cycles is due to the higher initial values of P_{adv} during the first half period. As water percolation and sensible heat supply under natural conditions will show clear diurnal and annual cycles, these thermal effects of variable advection have to be considered. If water percolation stops completely for some time, larger erosion rates compared to the ones of P_{adv_mean} have to be expected. To the current state of knowledge, we also have to expect this effect for longer time scales than modelled. This may significantly modify the ice erosion in cases where P_{adv_mean} is in the order of stable conditions. In these cases, the interruption of the advection has to be represented in a model of heat advection . For simulations with significant average erosion or variations without ebbing of the flow, the use of an averaged heat input is appropriate.

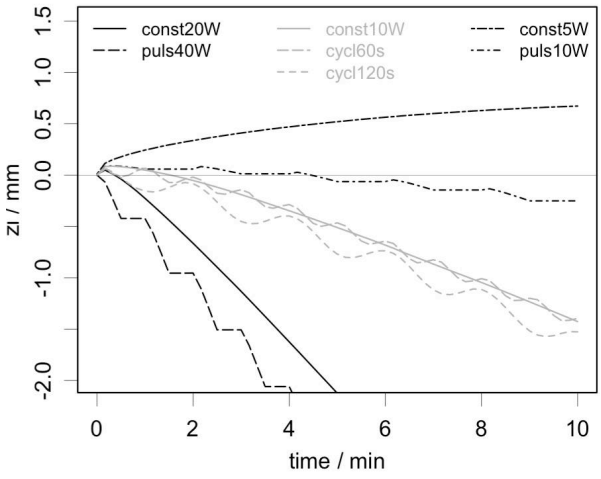

Figure S3 Ice level evolution of the numerical model with constant, pulsed (1:1 ratio) and cyclic 10 ± 8 W (sinusoidal) heat input with Trock= –3 °C. The label of the pulsed heat input corresponds to the maximum value, hence puls40W has same average as const20W

Paper V | Rock kinematics

Kinematics in steep bedrock permafrost

Focus

Cleft dilatation and shearing records from the Matterhorn field site are analysed in regarding the evolution of respective cleft temperatures and rock temperatures near-by. Extracted patterns are discussed with respect to existing explanations of rock movements and hypothesis on the relevant processes for permafrost bedrock are formulated.

Main findings

- *Cleft expansions negatively correlated with temperature prevail at all clefts and are consistent with other measurements in permafrost bedrock.*
- *An abrupt change to an unexpected summer opening occurred at some clefts synchronically with intense snow-melt and lasts until refreeze. Increased shearing activity is observed during similar time span.*
- *We argue for a thermo–mechanical forcing responsible for the negatively temperature-correlated movements. Ice segregation is not likely to cause the observed patterns.*
- *The movements of the melt-period are likely caused by a reduction of the mechanical cleft strength that is related to melt water percolation.*

Citation

Hasler, A. Gruber, S. Beutel, J. (accepted). Rock kinematics in steep bedrock permafrost. Journal of Geophysical Research.

Paper accepted for JOURNAL OF GEOPHYSICAL RESEARCH

Kinematics of steep bedrock permafrost

Andreas Hasler[1], Stephan Gruber[1], and Jan Beutel[2]

[1] Glaciology, Geomorphodynamics and Geochronology, Department of Geography, University of Zurich, Switzerland.

[2] Computer Engineering and Networks Laboratory, ETH Zurich, Switzerland.

ABSTRACT

The mechanisms that control climate-dependent rock fall from permafrost mountain slopes are currently poorly understood. In this study, we present the results of an extensive rock slope monitoring campaign at the Matterhorn (Switzerland) with a wireless sensor network. A negative dependency of cleft expansion relative to temperature was observed at all clefts for the dominant part of the year. At many clefts this process is interrupted by a period with increased opening and shearing activity in the summer months. More specific, this period lasts from sustained melting within the cleft to the first freezing in autumn. Based on these empirical findings we identify two distinct process regimes governing the cleft motion observed. Combining current theories with laboratory evidence on rock slope movement and stability, we postulate that i) the negative temperature-dependency is caused by thermo-mechanical forcing and is reinforced by cryogenic processes during the freezing period and, ii) the enhanced movement in summer originates from a hydro-thermally induced strength reduction in clefts containing perennial ice. It can be assumed that the irreversible part of the process described in (i) slowly modifies the geometric settings and cleft characteristics of permafrost rock slopes in the long-term. The thawing related processes (ii) can affect stability within hours or weeks. Such short-term stability minima may activate rock masses subject to the slow changes and lead to acceleration and failure.

KEY WORDS: Bedrock permafrost; rock kinematics; cleft dilatation; slope instability; climate change impact

1. Introduction and problem statement

Steep bedrock in high-alpine regions such as the European Alps is influenced by seasonal frost or permafrost. Permafrost degradation and changes in the thermal and hydrological regime in these areas as a result of changing climatic conditions can directly affect manmade infrastructure, cause increased rock fall activity or trigger natural disasters via process chains [*Haeberli et al.*, 1997]. The hypothesis that such climate related processes are relevant to alpine geomorphodynamics and rock destabilisation is supported by a) the exceptional rock fall that occurred in the hot summer of 2003 in the European Alps [*Gruber et al.*, 2004], b) the correlation of regional rock fall activity with warm decades in the past century [*Fischer*, 2010; *Ravanel and Deline*, 2010] and c) the presence of ice at the failure surface of high-alpine rock falls as reported by [*Gruber and Haeberli*, 2007; *Pirulli*, 2009; *Fischer et al.*, 2010]. The processes linking climate change and rock fall in high-alpine regions and the role of permafrost in rock fall release are currently poorly understood but several studies focus on physical processes and phenomena that are closely related. These studies state that ice formation processes are an efficient contribution to rock weathering and fracture widening [*Hallet et al.*, 1991; *Matsuoka*, 2001a; *Coussy*, 2005; *Murton et al.*, 2006] and that the pore ice content influences the geotechnical properties of intact rock [*Mellor*, 1973]. Furthermore, changes in ice temperature and geometries affect the mechanical properties of the rock discontinuity [*Davies et al.*, 2001; *Guenzel*, 2008] and so permafrost degradation can modify the hydraulic permeability leading to a possibile build-up in hydrostatic pressure within previous-

ly ice-sealed fractured rock and its down-slope hydrological regime [*Haeberli et al.*, 1997]. Fischer, [2010] discussed different factors that contribute to the stability of high alpine slopes and arranges them in a continuum between *disposing factors* and *trigger factors*. Accordingly, lithology, structure and topography of rock slopes are dominating factors for the disposition to rock fall but they remain rather constant within the timescales considered in the discussion of climate change impact (decades to millennia). Further, rock fatigue and sub-critical fracture propagation [*Atkinson,* 1982; *Kemeny,* 2003] can lead to rock weakening and failure without the presence of an obvious trigger. In contrast, glaciers, ice faces, permafrost and hydrothermal conditions within rock faces are directly influenced by climate change and subject to the corresponding response times. Related mechanisms are well suitable candidates to explain the variation of event frequency that is related to climatic fluctuations and extreme climatic events. Therefore, these factors are essential for the understanding of recent and future development of hazards originating from high-alpine bedrock.

In this study we focus on steep high-alpine rock faces that were not subject to recent glacier or ice retreat. We aim to identify the processes of thermal and hydrologic control on deformation and related rock fall. Rock movements are not necessarily only pre-failure deformations but may be part of slow moving instabilities (rock creep) or reversible (quasi-elastic) movements. The investigation of the mode and evolution of these slow deformations allows drawing conclusions on the driving forces and processes of an event [*Braathen et al.*, 2004]. In this study we have analysed the seasonal evolution of deformation with high temporal resolution considering spatial movement modes such as toppling, buckling and sliding [*Cruden*, 2003] qualitatively where clear geomorphic evidence exists. For this purpose, an analysis of the relative deformations (dilatation and shear) in rock clefts and the temperatures in the active layer of permafrost rock faces at Matterhorn Hörnligrat (Swiss Alps) has been performed. We use the term *cleft* for open rock fractures that experience opening (joints) or shearing (shear-fractures; faults). Most deformation in hard brittle rock occurs along these

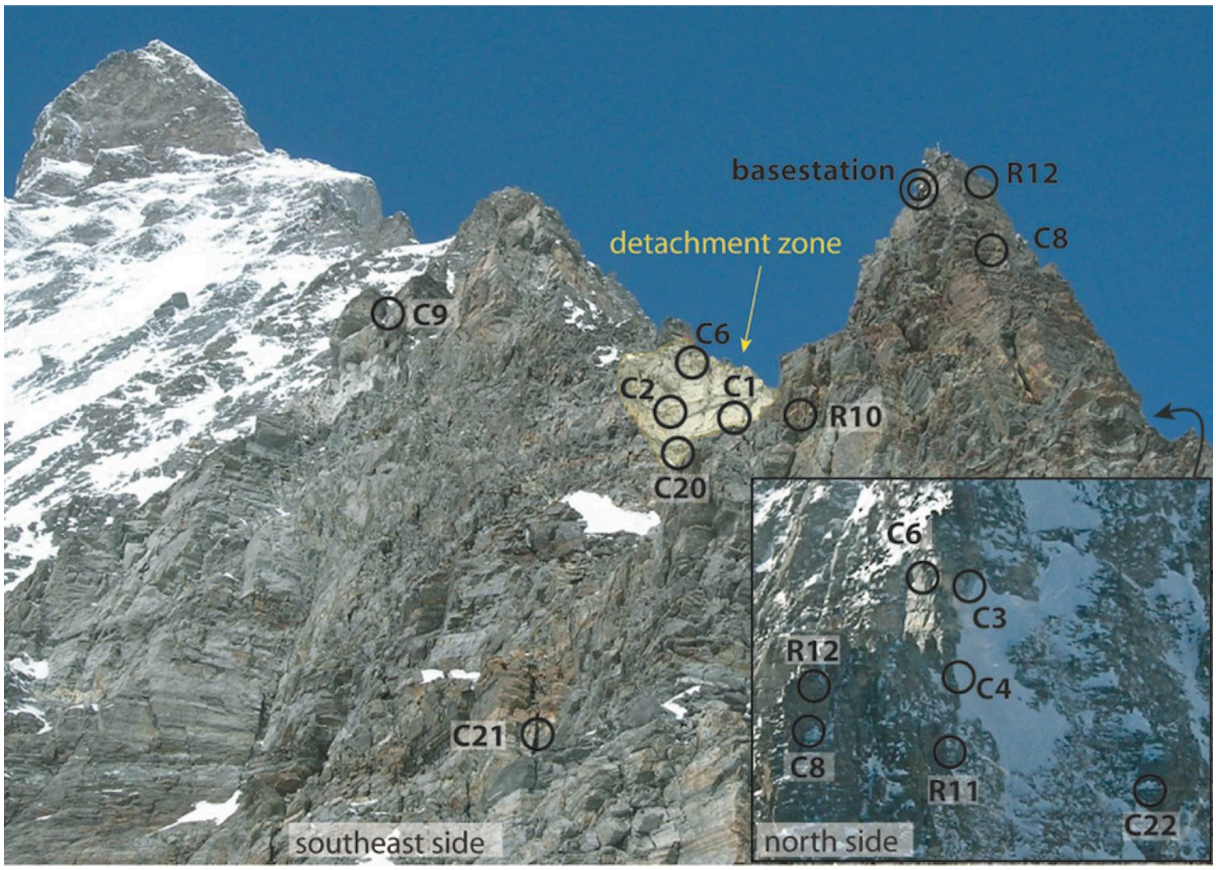

Figure 1: Overview of the Matterhorn Hörnligrat site from south-east and north-east (small picture). The circles with labels indicate the sensor locations. C stands for cleft (expansion and temperatures) and R stands for shallow rock boreholes (temperatures and electrical resistance).

(pre-existing) discontinuities and causes relative movements of the blocks of rock [*Eberhardt et al.*, 2004]. At high-alpine sites with differing mechanical and lithological settings similar movements with cleft expansion in autumn and contraction in springhave been observed [*Matsuoka*, 2001a, 2008; *Nordvik et al.*, 2010; *Wegmann and Gudmundsson*, 1999]. Because of these apparent similarities we expect common mechanisms which are not masked by geological circumstances.

In the first part of this paper we describe the situation, measurement setup and results derived from two and a half years of recordings of temperatures and cleft movements in the active layer of steep bedrock permafrost (Section 2–4). We then elaborate on typical patterns observed, correlations found within this data and develop hypotheses about the driving mechanisms behind the empirical findings (Section 5). This hypothesis-generating approach follows that of *Matsuoka* [2001a, 2008] but differs regarding the clefts dimensions and rock masses considered.

2 Site description

2.1 Topographic and climatic situation

The summit of Matterhorn, 4478 meters high, is part of the main divide of the western Alps that marks the Swiss-Italian border. The north-eastern ridge also known as the Hörnligrat is one of the most famous ascents in the Alps attracting more than a thousand alpinists per year. In July 2003 a rock fall occurred at the base of the ridge near the top of the so-called second couloir and 84 climbers had to be evacuated (pers. com., B. Jelk, regional safety officer). The ice-filled clefts observed immediately after the detachment of this rock fall, the strong fracturing, the large gradient of surface thermal conditions and the suspected deformation in proximity of the detachment zone motivated the selection of this site. In October 2007 a first installation of temperature sensors and geo-technical instruments was performed within and near the detachment zone [*Hasler et al.*, 2008]. An extension of this initial deployment was undertaken in June 2010 resulting in aninstrumentation with a cluster of 17measurement devices distributed across the site (Figure 1).

The field site is located at an elevation of 3500 m a.s.l. and comprises both sides of the ridge with main orientations south-southeast and north-northwest at the given elevation (Figure 1). The northern side contains small ice fields within a steep heterogeneous rock face, which is dominantly snow-free accumulating a thin snow cover only sporadically in winter. On the south side, snow patches develop during winter in couloirs and on rock bands, which are partly debris covered (Figure 2). These snow patches on the south side disappear in spring/summer completely. The bottom of both rock faces is glaciated, on the south-eastern side leading into a plateau formed by the Furgg glacier. The mean annual air temperature (MAAT, average 1961–1990) is –6.7°C [*Hiebl et al.*, 2009] and the typical annual precipitation is assumed to be greater than 1000 mm/a although accurate estimates are difficult to obtain due to the proximity to the meteorological divide and a large elevation difference to the next meteo station (Zermatt) operated by the Swiss Meteorological Service. Except for some occasional summer rainfalls the dominant precipitation falls as snow hence liquid water is mainly supplied to the site by snow melt.

2.2 Geology and structure

Geologically, the main part of the Matterhorn summit consists of gneiss and amphibolite of the Dent Blanch nappe [Pleuger, 2007]. The site is 30–100 m above the interface with the underlying Tsaté series of the Combin zone (mainly Bündnerschiefer and ophiolite) [Pleuger, 2007]. The lower part of the Hörnligrat (<3800 m a.s.l.) is strongly fractured but the rock in the northern face shows many lichens, indicating a rather low erosive activity. Typically, cleft spacing is 0.2–2 m with apertures of 3–30 cm. The most dominant cleft family (see A in Figure 2) is oriented parallel to the ridge and dips nearly vertical. These clefts have an extent of 3–40 m. Several signs of toppling movements lateral to the ridge are visible. This tilting of (free standing) rock pillars and flakes differs from slope toppling situations because the shearing movement at the contact with the neighbouring blocks only dominates in the root zone of the blocks [compare e.g. *Savage and Varnes*, 1987]. Further up the ridge close to location 9 (Figure 1), these near-vertical clefts cluster into two separate families, one dipping at 75° southeast and the other dipping at 75° northwest. A second cleft family is visible near-horizontal corresponding with the schistosity of the amphibolite (see C in Figure 2). The cleft families B and D are inclined with respect to family C but also perpendicular to the ridge (overlap with C in Figure 2a). The mineral orientation of the gneiss builds the weakness planes for these clefts. The

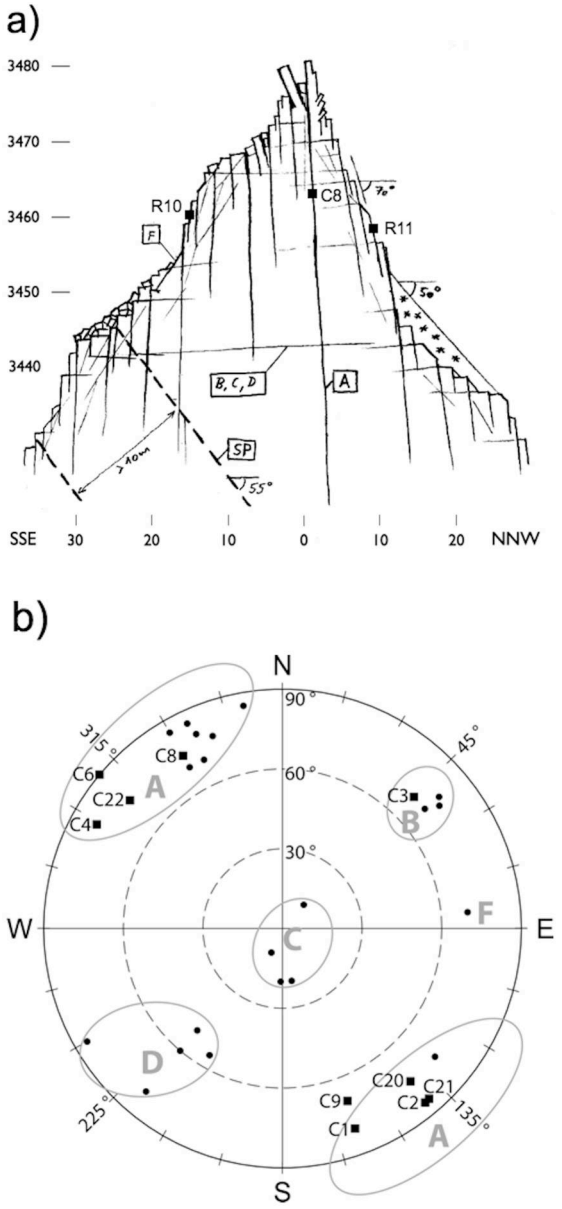

Figure 2: Geometry and structural situation of the installation site (3440–3480 m a.s.l.) at the Matterhorn Hörnligrat. **a)** profile sketch through the ridge (A–F = cleft families; SP = faults beneath the installation site; left scale elevation; bottom scale distance from ridge [m]). **b)** polar plot (upper hemisphere) of the cleft orientation (normal) of 21 sampled clefts (dots) and the clefts instrumented with crack meters (squares and sensor labels) with corresponding cleft families (A–F).

extent of the clefts and free surfaces of these families is 0.1–2 m. Often their extent is limited by the clefts of family A. Faults with more than ten meters spacing dip 55° north-westerly. Their shearing direction could not be assessed because the offset of the bedding is not obvious. In addition to the cleft families described there are inferior surface-parallel clefts and free surfaces visible although they could not be assigned to a particular family. The only surface with such an orientation and a significant persistence in proximity of the rock fall zone is the detachment surface itself (see F in Figure 2 and Figure 3).

2.3 Rock fall of summer 2003

The Matterhorn rock fall of 2003 had a decisive influence on the field site therefore a brief description of this event is provided: The summer 2003 in Switzerland was approximately 3°C warmer than the long term average and was characterized by a long period with very little precipitation [*Gruber et al.*, 2004]. A total volume of 1000–2000 m^3 of rock detached in two distinct events on 15 and 16 July respectively. The early timing within the year (little advanced thawing front) and no obvious triggering such as heavy precipitation is characteristic for the exceptional rock falls in this summer [*Gruber et al.*, 2004]. The rock mass detached at the southern side of the ridge above a small saddle (Figure 1). The base of the detached rock mass is located at the top of a couloir and does not show a sliding plane. Lateral detachment surfaces correspond to a cleft of the family B and the main failure plane F (Figure 2). The first event (15 July) comprised the lower right hand part of the rock mass whereas a pillar remained in the corner between B and F until it collapsed less than a day later. At the failure plane ice was observed shortly after the second event took place (Figure 3).

3 Measurement setup

3.1 Instrumentation

Acquiring distributed long-term measurements in harsh and high-alpine regions is challenging and needs an appropriate measurement setup. This was realized by the development and application of a wireless sensor network (WSN) at the Matterhorn field site [*Talzi et al.*, 2007; *Hasler et al.*, 2008; *Beutel et al.*, 2009]. Two distinct features makea wireless sensor network a most suitable measurement system for high-alpine applications are i) the reduced sensitivity to environmental influences such as lightning, rock and ice fall due to reduction in cabling and ii) the transmission of data from the measurement site in real time. While data are typically analysed using batch processing the latter might not seem so important yet it has been found that more important than transmitting the sensor data is the capability to analyse the system health and data integrity with very short delay. Especially when compared to traditional data logging equipment this later fact

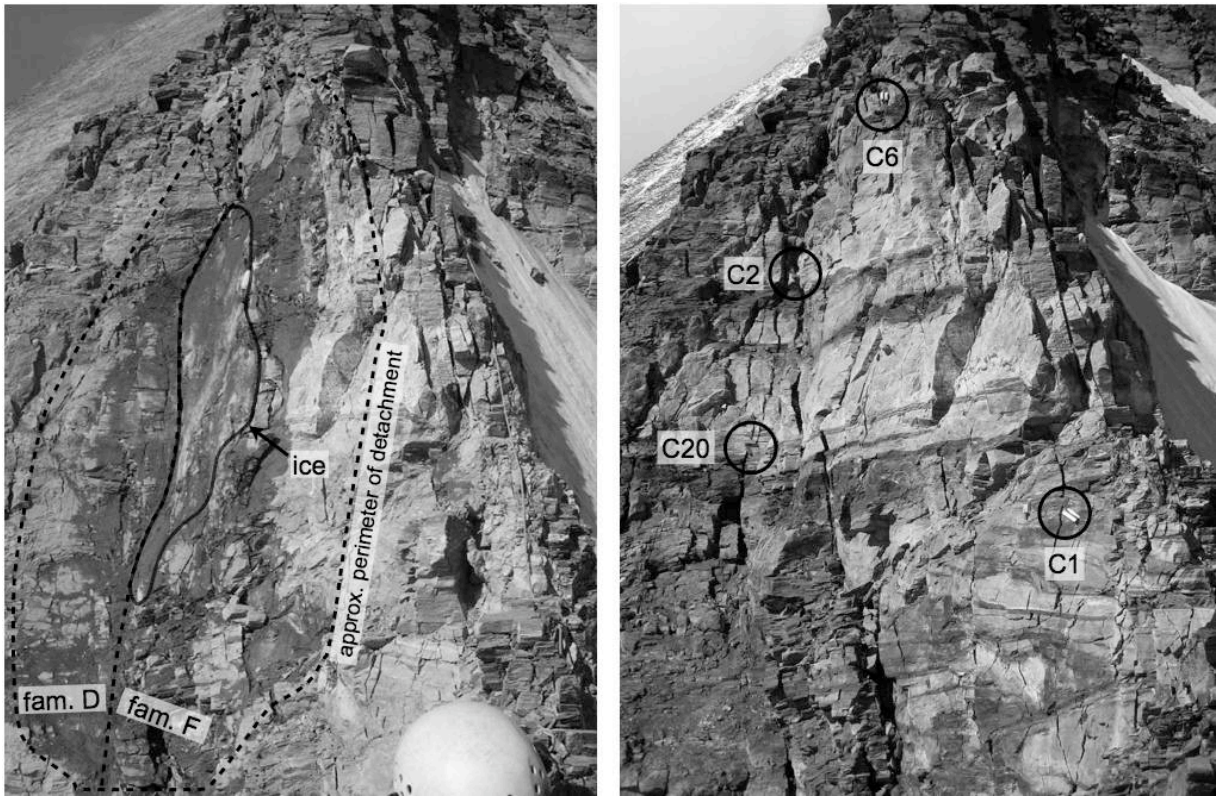

Figure 3: Close-up of the detachment zone of the rock fall in summer 2003. a) Detachment zone some hours after the 2nd rock fall on 16 July 2003 (photography. B. Jelk). b) Detachment zone with sensor locations in August 2010. The failure surface consists of different surfaces of the family F where ice was visible after the event in 2003 and a cleft of the family B.

allows controlling and reacting upon quality changes in the experimental setup.

In this WSN system autonomous miniature battery powered sensor nodes are fitted with standard commercial and customized sensors. The sensor nodes form an ad-hoc wireless network optimized for longevity and reliability. All data is transmitted to a central base station where it is aggregated, time stamped using a UTC referenced clock and sent over a long-distance link to a database server. Furthermore the PermaDozer system applied at the Matterhorn site [*Beutel et al.*, 2009] contains storage layers that allow every component to collect and aggregate sensor values autonomously should parts of the system (wireless links, base station, server) be unavailable, e.g. due to weather, snow fall or maintenance.

At Matterhorn Hörnligrat three sensor rods (rigid multi-thermistor chains), four thermistor chains, two thermistor–moisture chains and eight individual thermistors record rock and cleft temperatures (Table 1). Seventeen crack meters (*ForaPot crack meters, ForaTec*) measure the dilatation and shearing of clefts and in two clefts stress and pressure sensors are installed. The crack meters contain an internal reference temperature sensor allowing compensating thermal errors in the distance measurements. The locations of the sensor nodes are labelled *C* or *R* for cleft and rock respectively followed by a number. At two locations (C6 and C8) two sensors nodes are installed at the same cleft accommodating a multitude of sensors, however this is not represented in this labelling for simplicity reasons. For each location the thermistors (or temperature time series) are labelled with *T* followed by a number. Crack meters are labelled with *Cr1, Cr2* and *Cr3* depending on the number of axes instrumented with crack meters at a given location.

Custom-built sensor rods measure the temperature of the rock at four depths (T1–T4: 0.1, 0.35, 0.6 and 0.85 m) installed in a 1 m deep borehole [*Hasler et al.*, 2008]. Similarly, the thermistor chains and the thermistor–moisture chains measure four to eight temperatures (and on the latter two resistances as an indicator of the presence of liquid water) within clefts (Table 1). The depth of these measurements depends on the installation at each respective location, reaching a maximum of 4 m. Additionally individual thermistors that measure the surface temperature (*Tsurf*) were placed at 2 cm depth in small borings. In two cases, an additional thermistor measures the temperature found within a cleft (C2, C9 in Table 1).

The crack meters are anchored at both sides of the cleft within a distance of some cm from the cleft using chemical anchors and protected by a steel shield against simple pebble, ice fall and excessive solar irradiation (Figure 4). For locations instrumented with a single crack meter only the component normal to the cleft is measured (cleft expansion). By instrumenting a crack with two crack meters the shearing (cleft- and surface-parallel translation, approximately in dipping direction) is measured (Figure 4). As a perpendicular mounting is most likely not possible the actual values are calculated based on the measurement values and corrective angles measured during installation. The sideward shearing is measured by a third crack meter at location C9 but is not considered for analysis here due to the short time series available. Further measurements such as the water pressure and cleft-ice compression stress (perpendicular to cleft surface) could not detect any valuable records so far and as a result was not considered for analysis in this study either. However, the functionality of the pressure measurements was verified and visual inspection confirmed that no ice or water table built up at the position of the sensors. Meteorological data and images from the detachment zone as well as individual instruments are recorded automatically at the nearby base station [*Beutel et al.,* 2009]. The meteorological data recorded covers only a limited time span as will be explained later, does not include solid precipitation, i.e. snow and was mainly used to check the validity of an extraolation of precipitation events from the meteorological station in Zermatt.

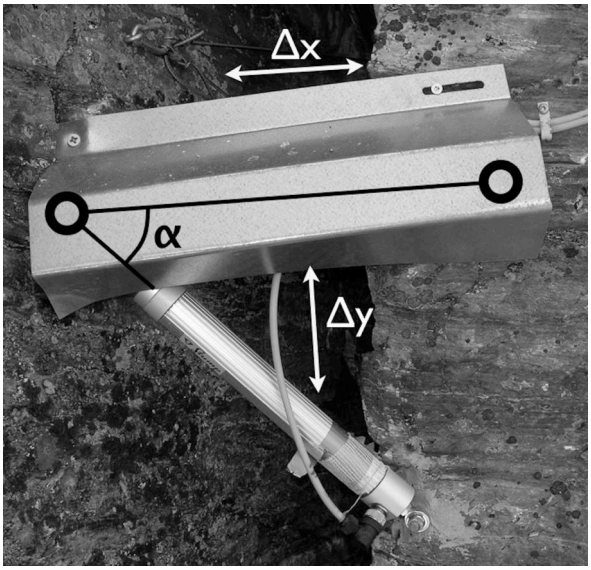

Figure 4: Instrumentation with two crack meters at C8; the crack meter *Cr1* is hidden under the protection shield and directly measures the dilatation component *Δx*; the visible crack meter *Cr2* is used to compute the component *Δy* parallel to the cleft.

3.2 Measurement locations

The general characteristics of the measurement locations are described in Table 1. In the following the spatial relation of the individual locations is briefly described (see also Figure 1): All clefts instrumented with crack meters except for C3 are running parallel to the ridge (family A, Figure 2). The cleft of C1 cuts across the detachment surface (Figure 3). It is approximately 2 m deep and 4 m long and exposed to strong solar radiation. In summer 2010 the position of the crack meter located at this cleft was changed from crossing the cleft to a position not crossing the cleft to determine the accuracy and repeatability of an instrument mounted on a portion of solid rock, i.e. at a known non-moving position (see below). Sensor C2 is located in the corner of the detachment (Figure 3) and measures one of a series of clefts with debris and clay infill. The upper part of this corner accumulates snow during winter. At the top of the detachment zone sensor C6 monitors a cleft, which divides the ridge with thermal influence coming from both sides of the ridge. Figure 3 also shows C20 located in the lower left part of the detachment surface at a cleft parallel to the one of C2. On the north side of the ridge C3 and C4 are installed in proximity of the detachment zone (Figure 1). The cleft of C3 is perpendicular to the other clefts and divides the north-western rock flake of the steep ridge limiting the detachment.

The crack meter C8 and a sensor rod (R12) are located at the north-easterly oriented face of a tower 50 m northeast of the detachment zone (Figure 1). This tower is divided by a big cleft that extends to a depth of about 40 m. C8 is installed across this cleft at 8 m from the top and R12 is drilled into compact rock at 4 m from the top to record the temperature evolution in this rock mass. Two other sensor rods are installed on both sides of the ridge between the tower and the detachment zone to survey the thermal conditions found in a south-easterly exposition (R10) and a north-westerly facing cliff (R11). Their distances to the ridge are 15–20 m, hence more than 20 m rock mass lie between both sides and reducing the effect of large lateral heat fluxes in the ridge [*Noetzli et al.,* 2007] on the temperature profiles recorded.

Additionally, on both the north and south sides of the ridge a cleft is instrumented at a larger distance away from the ridge and the detachment zone: The location C21 is on the south side at a large cleft separating a 20 m high and 7 m

Table 1. Site characteristics and instrumentation.

location description						sensor node description						
location	character	cleft size		orientation		crack meters (X/mm)			temperatures			
		op / cm	*ext / m*	*dir /°*	*dip /°*	*Cr1*	*Cr2*	*Cr3*	*SR*	*TC*	*TM*	*Ts*
C1	intense radiation	5 / 0	3	160	80	50				x		x
C2	concave, wet	15	10	140	85	50				x		c*
C3	north side	7	6	45	70	150				x		x
C4	saddle north	3	3	300	80	50				x		x
C6	top detachment	4	>5	310	90	100	200				x	
C8	large tower	15	40	330	75	100	150				x	
C9	leaning tower	20	20	160	70	100	200	200				c**
R10	rock south side	free s.		S	90				x			x
R11	rock north side	free s.		N	70				x			x
R12	rock large tower	free s.		E	90				x			x
C20	below C2	5	>5	140	75	100	150					
C21	south low	15-30	20	140	85	100	150					
C22	north low	1	5	310	75	100	150					

Cleft size contains the opening (*op;* if not free surface) and the lateral extent (*ext*) of the cleft. The *cleft orientation* describes the direction and dipping angle of the cleft planes (compare Figure 2). For the *crack meters*, the numbers indicate the measurement ranges of the present instruments. *Temperatures* shows the type of temperature sensor: *SR* = sensor rod; *TC* = thermistor chain; *TM* = thermistor–moisture chain; *Ts* = individual temperature sensor measuring the surface temperature (*x*) or the temperature in a cleft (*c** in neighbouring cleft, *c*** in cleft of crack meters).

thick rock mass from the slope (Figure 1). Water is supplied from the melt of a snow patch above and seasonal ice is observed close to the surface in this cleft. Tilted blocks at the top of the cleft indicate an outward movement of the rock mass. Since no cleft of the same extent as at C21 was found on the north side, C22 is installed at a similar situation but with smaller cleft dimensions. Sensor C22 is located 40 m from the ridge in the north face. In contrast to the south side, no geomorphic indication of large movements exist here and the water supply is smaller due to the thermal conditions and geometric settings. Finally, a last sensor C9 is installed 100 m above the detachment zone at a tower located in the southeast face (Figure 1). This tower apparently leans toward the ridge. A niche from a small rock fall is visible at the tower basement forming an overhang. The southward dipping cleft (C9 in Table 1), dividing the tower from the face, is instrumented with three crack meters to resolve for all three axes. Its topographic position on a spur prohibits the supply of larger quantities of melt water.

3.3 Data quality

The reliability and quality of the expansion and shearing time series measured is essential for the interpretation whereas the measurement accuracy of the temperature measurements is less critical because in our context the main uncertainty arises from high spatial heterogeneity. It is thus sufficient to state that the absolute accuracy requirement for the temperature measurements is ±0.2°C [*Hasler et al.,* 2011a].

The test setup for the crack meters is similar to the one of *Matsuoka* [2001a]: Both anchor points of the instrument at location C1 are mounted on intact rock without a cleft in between (except for one micro fissure) and the movements measured by the instrument are analysed. These data are compared to results from the same crack meter mounted across a cleft prior during an earlier period in time revealing the effect of changing temperatures on the rock mass and instrument respectively (Figure 5). The expansion-temperature relation (*dx/dT*) measured for the cleft-crossing installation (Cr1 and T1 data measured before 25 June 2010) is -10 µm/°C. The same relation measured for the intact rock installation (after 25 June 2010) is +0.2 µm/°C, but with a lower correlation because of shifts found between different periods following this trajectory (Figure 5). The typical linear thermal expansion coefficient for crystalline rock is in the order of $5 \cdot 10^{-6}$/°C, which means that the expansion of a rock mass of the size between the anchor points (150 mm) is approximately +0.7 µm/°C. The lower expansion measured (+0.2 µm/°C) agrees well with this theoretical value because the rock at the surface needs to deform elastically constrained by against the lower rock

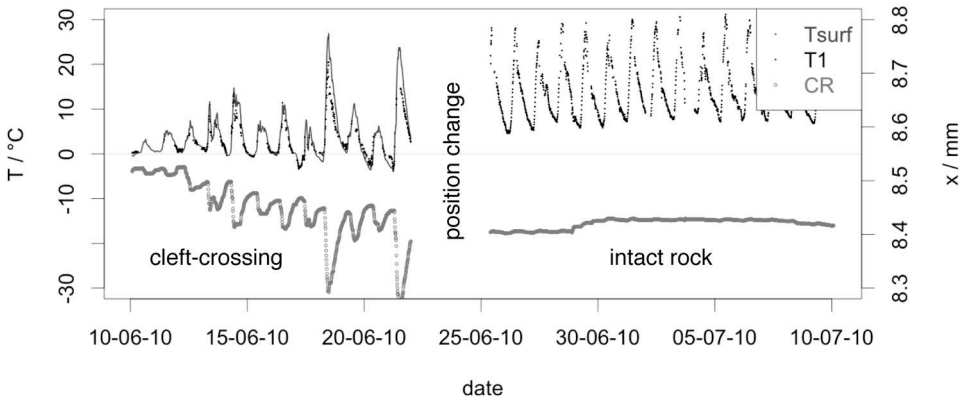

Figure 5: Validation of crack meter measurements at C1. Time series of rock surface temperature (*Tsurf*) and top cleft temperature (*T1*) and crack meter expansion *(CR)* for the instrument installed across the cleft (June) and in intact rock (July).

masses with less (diurnal) temperature amplitude inducing thermal stresses preventing free deformation. The shift of the crack meter extension on intact rock (Figure 5) may originate from inelastic distortion and stress field variations on a larger scale. This result indicates that the internal temperature compensation of the crack meter works well and a relative measurement accuracy of better than ±0.1 µm/°C can be assumed resulting in an absolute crack meter accuracy of ±5 µm over a temperature range of 50°C and across a measurement range of 50 mm. An elongation of the crack meter from 50 to 200 mm range results in a linear decrease of the total accuracy of ±20 µm, which is well below the signals anticipated. On the multidimensional measurements, the accuracy of the movement component Δy parallel to the cleft may be lower than Δx perpendicular to the cleft because it is calculated by subtraction (error propagation) and depends on the angle between the two crack meters (α in Figure 4): We assume an accuracy of Δy of ±100 µm for all sensors except for C6 (err.Δy = ±12 µm; α = 90°).

Consistent time series of data from the sensors initially installed in 2007 (C1–C8 and R10–R12) start in July 2008. Prior to this date only fragmentary data from early tests exists which are not used in this study. From July 2008 to November 2010 the dataset has several gaps due to technical problems (Figure 6). In the summer of 2009 a data gap over a period of two months is a result of a breakdown of the WSN due to a software error. The crack meter measurements at location C4 are only available from the summer of 2010 onwards due to mechanical damage to the sensor that was only discovered then. Another substantial gap is the one of location C6 in the spring of 2010. The sensors installed during the extension of the field site in June 2010 (C9, C20–C22) have delivered continuous time series since except for location C9, which contains two small gaps in autumn 2010. The values of crack meter C8, experienced a bias due to a short circuit in another sensor attached to the same sensor node that was disassembled upon detection of this problem in June 2010. Analysis revealed the main problem to be a drop in the reference voltage that could be corrected by multiplying the raw values by a factor of 2.1 of the crack meter time series of location C8 prior to June 23, 2010. The behaviour of the data of location C8 prior to the data gap in summer 2009 could not be explained satisfactorily and so these data are not considered for the analysis.

The on-site meteorological time series cover autumn 2009 and summer 2010 and detailed image data is available from pictures automatically taken several times per day over large parts of the whole measurement period.

All the data are sampled every 2 minutes and aggregated to 10 minute averages as a base for the analysis presented here. This aggregation produces deviations smaller than 0.1°C from the instantaneous raw values even for signals with a large short-term variation.

4 Results

4.1 Rock and cleft temperatures

The temperature measurements in clefts and shallow rock boreholes show differing diurnal and annual amplitudes depending on their location and depth. In order to illustrate the seasonal temperature evolution at the field site three temperature time series from the bottom of the shallow boreholes and clefts are presented in Figure 6a. This data however conceals the fact that the diurnal temperature fluctuations at the rock surface at locations exposed to direct solar radiation exceed

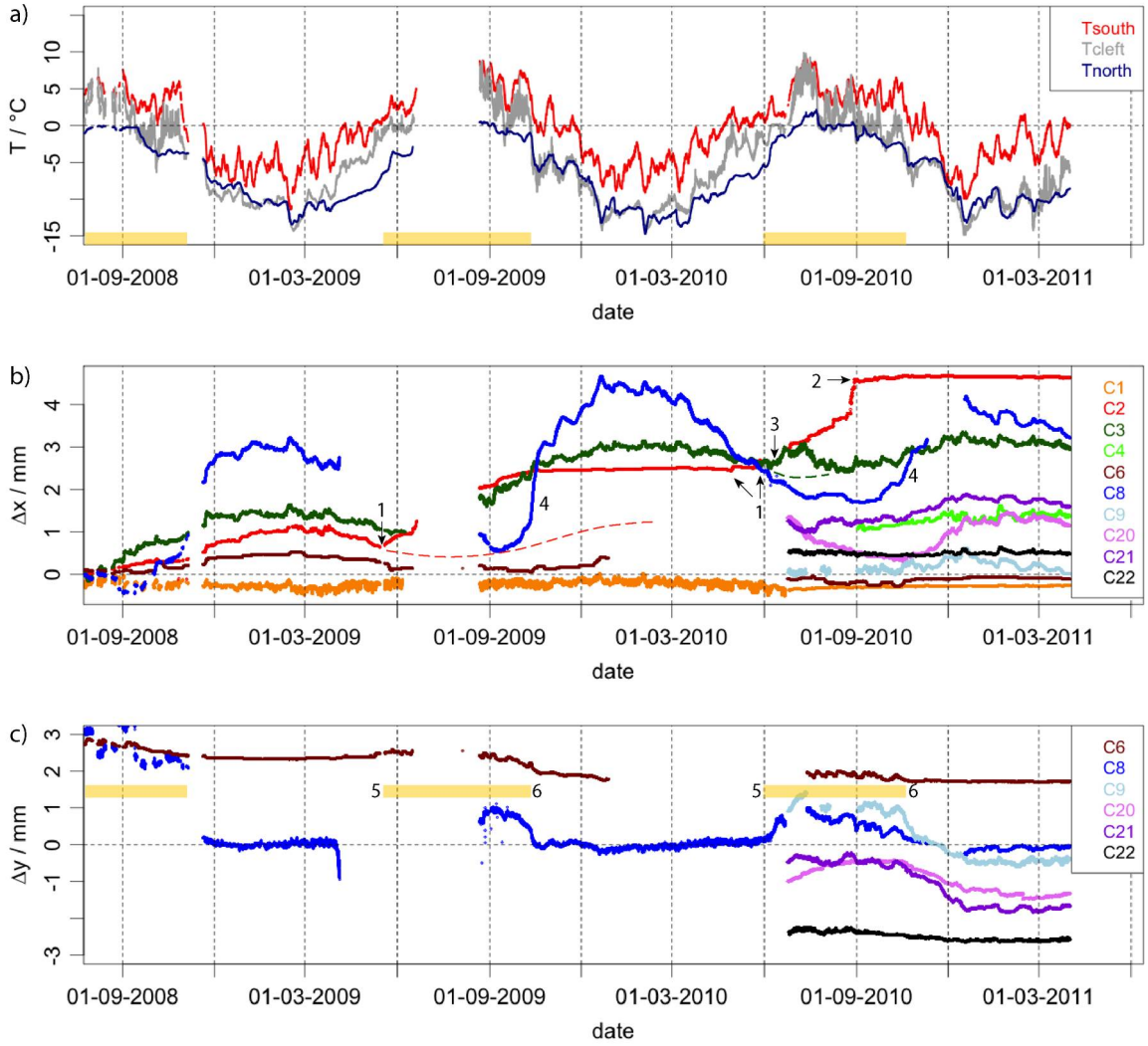

Figure 6: Overview of thermal conditions and cleft movements at the Matterhorn Hörnligrat showing patterns negative correlated with temperature during the cold season and enhanced shearing in summer: a) rock temperatures on southeast and northwest side at 0.85 m depth and cleft temperature at 2 m depth, the yellow bars indicates $T_{cleft} \geq 0°C$; b) cleft expansion Δx; c) shearing Δy with positive signs for upward movement of the valley-side rock mass (see Figure 4). The numbers indicate events of special interest that are described in the text.

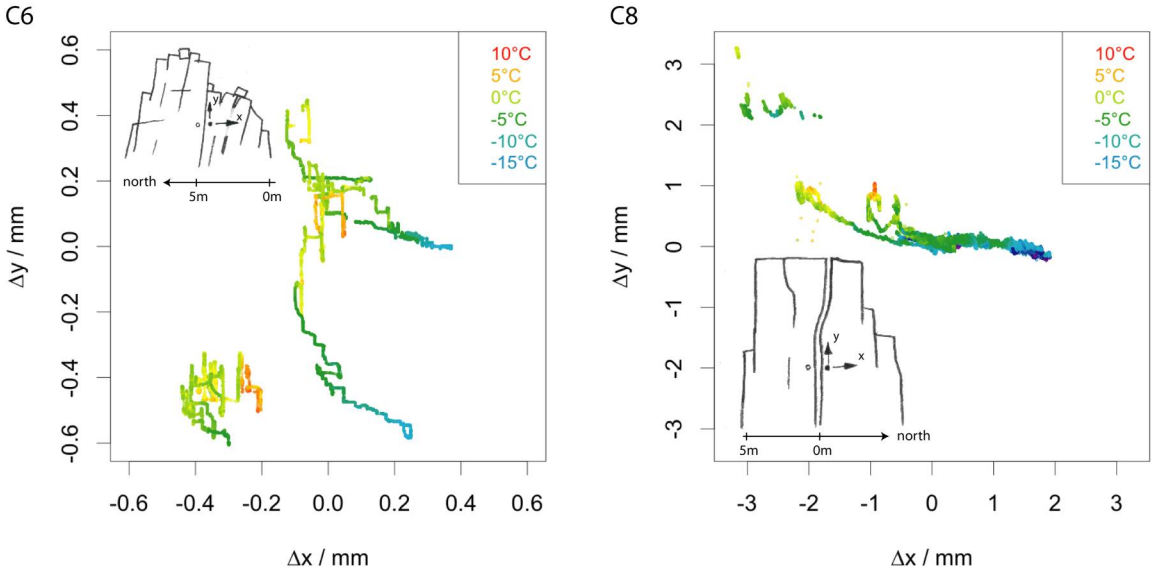

Figure 7: 2D-movement pattern with cleft temperature (color) at C6 and C8. The shearing component Δy is the position of the right mass relative to the other side of the cleft.

the amplitude found in the annual fluctuations (e.g., Figure 5). The difference between the rock temperatures southeast (T4 at R10) and northwest (T4 at R11) of the ridge is approximately 6°C on average (Figure 6) with a mean annual ground temperatures (MAGT) of 0°C and -6°C respectively. The temperature data derived from the southeast aspect has larger weekly amplitudes with the two temperature curves running almost in parallel with respect to annual fluctuations. The cleft temperatures (C6-T4) have larger annual amplitudes with strong diurnal signals found in some time periods (Figure 6). This is observed for all measured clefts even though the extent of periods with large diurnal fluctuations varies with the cleft location and measurement depth within this specific cleft. This reflects that the recorded cleft temperatures are a mix of air temperatures, rock surface temperatures in the cleft and the temperature of a possible cleft infill (snow, ice, water and debris). Therefore, the imprecisely defined physics of the measurement setup in the cleft and the varying conditions need to be considered here: The accuracy of the data is reduced by a possible bias introduced by the setup (e.g., conduction along cables, ice formation on sensors) inherently difficult to quantify. On the other hand, the high correlation found in data derived from several temperature sensors mounted within a single cleft ($r > 0.86$ for all cleft temperatures) demonstrates that an interpretation with respect to the thermal evolution of the cleft can be performed. For the detailed analysis of the cleft movements the temperature with the highest correlation to the expansion at the respective cleft is adopted within this study. These are the surface temperature for cleft C1 (C1-Tsurf), the temperature at 0.5 m depth for cleft C2 (C2-T6) and for cleft C3 the one at 0.6 m depth (C3-T4). The movements at C8 are analysed in relation with the rock temperatures at 0.85 m depth (R11-T4).

4.2 Cleft kinematics

4.2.1 General patterns of the cleft expansions

An overview of all measured cleft movements is provided in Figure 6b/c. The illustration 6b shows expansion relative to the initial values of each data series allowing a joint visualisation and not the total aperture of the cleft given in Table 1. For the first year (July 2008 to June 2009) all cleft expansions show a negative dependency on temperature but with differing amplitudes and attenuation over time: A negative correlation with the annual temperature evolution prevails at C2, C3, C6 and C8 (Figure 6b). The peak-peak values of these annual amplitudes are in the range of 0.5 to 4 mm. In contrast, C1 shows diurnal cycles with amplitudes of about 0.2 mm (see also Figure 5). Equally, at C3 and for a limited time between February and April 2009 at C2 short-term cleft movements overlay the lower frequency signals of the annual cycle. After the data gap in summer 2009, these general patterns are visible again except for C2, which almost stagnates during the entire winter after leaving the expected negatively temperature-correlated path (dashed red line in Figure 6b). Of the five clefts with measurements available for more than two years, three clefts (C2, C3 and C8) experience net-expansions in the order of 1–2 mm/a; at C1 and C6 the expansions are reversible. The irreversible openings were composed to large parts by deviations from the observed negative dependency occurring in summer (C2, C3) or an enhanced opening during the freezing period (C8). Both periods are described and discussed in more detail below. The sub-annual time series from the sensors installed in June 2010 adumbrate the following: a) the negative dependencies on temperature during winter was similar to the ones of the other clefts; b) during summer and

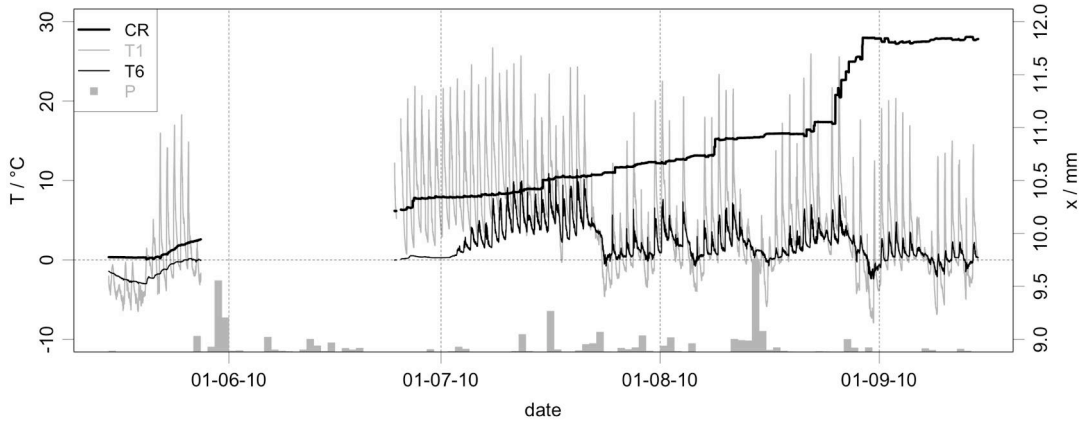

Figure 8: Cleft expansion with step-wise opening at C2 in summer 2010 and corresponding cleft temperatures. *CR* is the crack meter expansion*; T1* is the temperature at cleft top; *T6* at 0.6 m depth; *P* is the diurnal precipitation in Zermatt (qualitative indication: maximal value is 62 mm).

autumn these dependencies varied between locations (different delays); c) C22 in the north face showed a minor dilatation.

4.2.2 Cleft shearing and 2-dimensional movements

For the shearing motions, a seasonal difference is evident: In the long shear time series from C6 and C8, significant activity was limited to the warm periods. At C6 the active time span was from May to mid-October in the year 2009 and stopped at about the same date in 2010 (Figure 6c; 5=start, 6=stop). The values however stagnated with an offset found between successive winters. The shearing of the cleft at location C8 stopped at the same time in both years (the start could not be evaluated for the year 2009). In contrast to C6, the shearing component in C8 returned to the same position in the two autumns. A direct comparison of the timing of this activity is not possible due to diverse gaps in the two data sets (Figure 6c). The shearing time series of C9 and C21 show large movements in summer and autumn and rather constant values in winter while at C22 only minor shearing activity was observed (Figure 6c). The shearing at C20 followed the annual temperature fluctuations with a delay (positively temperature-correlated).

In Figure 7 the 2-dimensional movement patterns of C6 and C8 are shown. The two components correspond to the dilatation (cleft-perpendicular) and the shearing in the (near-) dipping direction (Figure 4). As both clefts are near-vertical and the shearing is plotted on the ordinate, the graphs can be interpreted as the translatory movement of the rock mass relative to the other side of the cleft (cf. sketches in Figure 7). In case of C6 the relative movement of the southern block is plotted and for C8 for the northern block with the colors signify the cleft temperature. The transition from shearing to opening was similar for both cases but the inter-annual offset is larger on the y-axis for C6 and on the x-axis for C8. This indicates, that the cleft at C6 had a small trend in shearing (<0.5 mm/y), while C8 had a trend in opening (1–1.5 mm/y).

4.2.3 Summer expansions

At C2 the non-reversible movement was composed of two expansions of 2 mm each that occur in summer when the cleft temperature was at or above 0°C (Figure 6a/b). The temperature dependency of this summer expansion deviates visibly from the negatively temperature-correlated

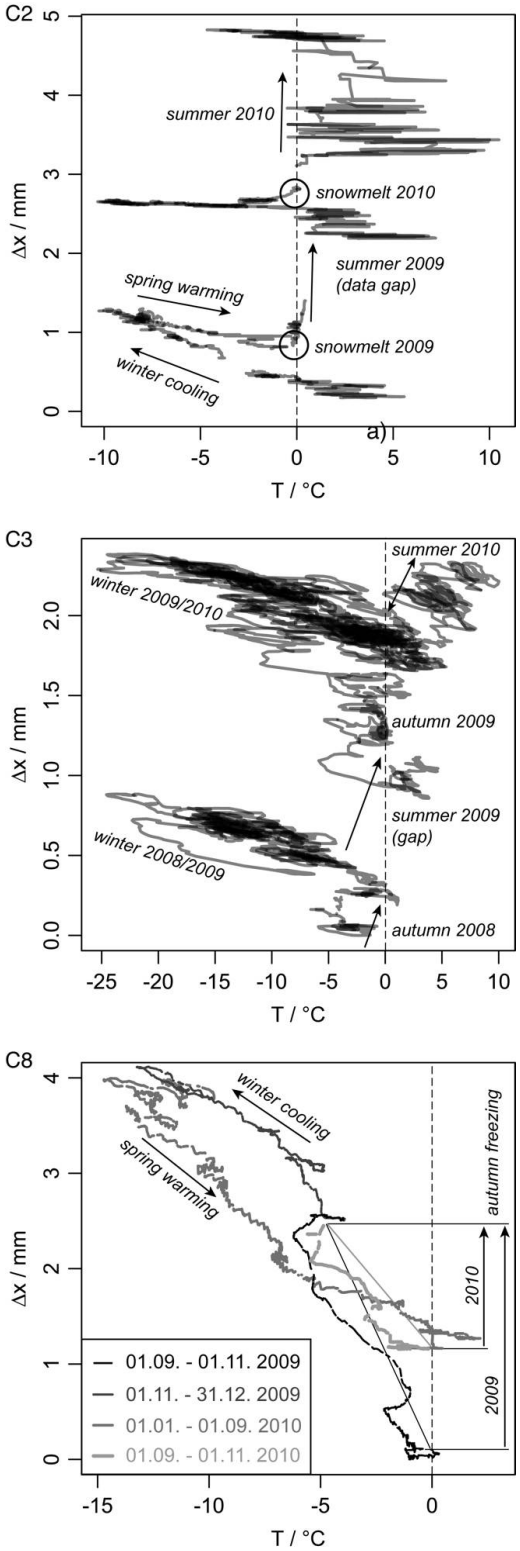

Figure 9: Cleft expansion as a function of temperature $\Delta x(T)$ at C2, C3 and C8. For C2 the correlation between Δx and the plotted cleft temperature *T6* (0.6 m depth) has a Pearson's coefficient of r=–0.95 for the first winter. For C3 the correlation between Δx and *T4* (0.5 m) has an r=–0.82 for winter 2008/2009 and an r=–0.84 for winter 2009/2010. Δx of C8 is plotted against the rock temperature *T4* (0.85 m) of R11 and has an r=–0.91 over the whole time span. The lines are transparent to visualize overlapping; for C8 the line style varies by period (legend).

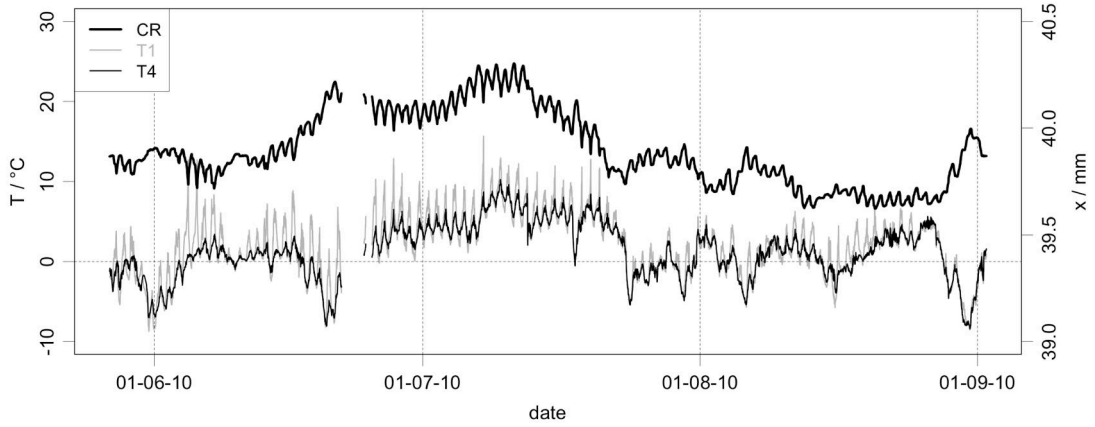

Figure 10: Cleft expansion and cleft temperatures at C3 in summer 2010. *CR* is the crack meter expansion; *T1* is the temperature at cleft top; *T4* at 0.5 m depth. End of June the cleft expansion changes from negatively temperature-correlated to positive dependency from temperature for one month.

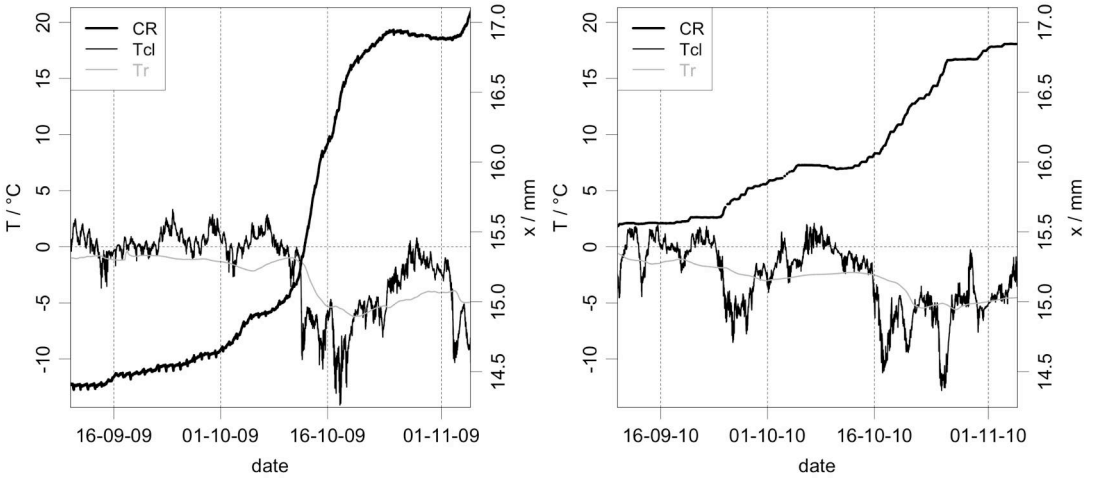

Figure 11: Cleft expansion at C8: comparison of 2009 and 2010 autumn freezing.*CR* is the crack meter expansion; *Tcl* is the cleft temperature in 2 m depth at C8; *Tr* is the rock temperature in 0.85 m depth on the north side (R11).

expansions described above. This second movement mode started in early summer when thawing occurred inside the clefts (Figure 6b, 1) and abruptly stopped with the first freezing at the end of August (Figure 6b, 2). In 2010 a first melt event led to some expansion but continued expansion was initiated with a second melt period followed by sustained positive cleft temperatures. Figure 8 shows a detailed time series of this summer expansion and cleft temperatures at C2. The start of this expansion was simultaneous with the first significant positive temperatures measured at the top of this cleft. With a delay of four days the temperatures within the cleft reached 0°C and remained at or above this temperature for the most part of the following three months (Figure 8; for the gap compare Figure 6a). The movement mode was a stepwise expansion (motion time < minutes) with plateaus found in between. The steps occurred in the afternoon in most cases (78% of the 32 distinct steps that are larger than 0.01 mm). There is no correlation of the steps with the timing of significant precipitation events (Figure 8). A significant increase in the number of steps occurred at the end of August before cleft freezing terminates the movement (Figure 8). In Figure 9 the cleft expansions are plotted against the temperatures found within the clefts. The partly reversible expansion for C2 of the winter 2008/2009 was not repeated in the following winter with the whole opening process found in this cleft occurring while the cleft temperature at 0.6 m depth was larger than 0°C (Figure 9, C2). The minor dependency of the cleft expansion on the positive temperatures is illustrated in Figure 9 by the horizontal stripes that are shifted upward (offsets of the trajectories) when steps occurred. No dependency between the expansion rate (dx/dt) and the temperature could be determined.

During the data gap of the summer 2009 an expansion occurred at C3 continuing during the freezing period of the north side in September (Figure 6a/b). An opening in summer 2010 showed a deviation from the negative correlation with the cleft temperature typically found (Figure 6b; C3 and green dashed line) and being reversible in contrast to the situation at C2. The transition from the negative to positive temperature-correlation occurred around mid-June but without a visibly abrupt regime change (Figure 10). It ended with a temperature drop in the cleft on 24 July. The diurnal fluctuations remain negatively correlated with diurnal temperature variation for the entire warm period. The movement mode was continuous without steps such as those found at C2 (Figure 10). In the diagram showing the expansion versus temperature (Figure 9) this behaviour does not lead to an offset and the trajectories being generally negative inclined.

4.2.4 Autumn freezing period

The major opening events in the data (except the summer opening) coincide with a rapid temperature drop (Figure 6a/b). Noticeable are the expansions at C8 during the initial autumn freeze periods of 2 and 1 mm each, occurring within a few days (Figure 6b, 4). A comparison of the two opening events in 2009 and 2010 is shown in Figure 11. The initial aperture at the beginning of September differed by 1 mm only between the two years. The cleft temperature evolution in 2009 was characterized by values that remained around 0°C until October 10th and then dropped by 10°C within just a few hours. In the following two weeks the temperature fluctuated around –10°C (Figure 11). The temperature drop in 2010 was less sudden. A first intense freezing event occurred already end of September, followed by slightly positive temperatures before the temperatures finally decrease below zero degrees (Figure 11). The difference in expansion and expansion rate between these two periods is not proportional to the slight difference observed in the net temperature decrease for these two years. Despite the dependency of the cleft expansion on the lower rock temperatures (Figure 11) the expansion-temperature relation was not constant over time and shows a path dependency (Figure 9). In 2009 a larger gradient is visible in the expansion-temperature relation than in 2010. For the other clefts a clearly increased expansion during autumn freezing was not observed.

5 Discussion

5.1 Measurement patterns and correlations

Based on the preceding description of cleft kinematics, we identify two main regimes of movement. The first one persists for most of the year and at some locations is replaced by the second regime for a variable period (a few weeks to months) when the cleft temperatures are above 0°C. In the following discussion we call these a) the *temperature-correlated dilatation regime* and b) the *enhanced expansion and shearing regime*. While the temporal extent of these periods differs between the clefts, their general characteristics and relation to temperature are similar and discussed below.

5.1.1 Temperature-correlated dilatation regime

This period is characterized by the predominance of a negative correlation of the cleft expansion with temperature. It occurred at all clefts during winter except at C2 where the negative correlation was limited to the winter 2008/2009. The thermal cleft expansion gradient *dx/dT* differs between locations and shows variations both over time and with the path direction (opening/closing). Table 2 presents an overview of these gradients. The basis of these gradients is a qualitative interpretation of the expansion versus temperature plots and a regression analysis performed between these two variables (see Figure 9 for C2, C3 and C8). The Pearson's correlation coefficient for the two cleft dilations C1 and C6 is $r = –0.85$ (Δx vs. *Tsurf*) and $r = –0.38$ (Δx vs. *T4*). The gradients span almost two orders of magnitude and correspond with the annual amplitudes. At C8 where the cleft dimension is bigger than at the other clefts (see Table 1) the gradient was largest. At C1, the cleft which issmallest in dimension, the least temperature dependent dilatation values were recorded. However, the gradients at the clefts C2 and C6 should not be mistaken as the relative lateral movement of the larger rock mass because here only one cleft

Table 2. List of average gradients of cleft expansion gradients

sensor	expansion gradient / (mm/°C)
C1	-0.01 (diurnal fluctuations)
C2:	-0.1 (opening), -0.05 (closing; 2008/2009)
C3:	-0.02 to -0.04
C6:	-0.04 mm/°C (with no sensitivity on T in between)
C8:	-0.2 (general), -0.5 (freezing 2009), -0.3 (freezing 2010)

within a series of clefts was actually measured. For the interpretation of the larger movements at C8 we have to consider that i) the measurement location was situated above the root zone of the cleft in a large tower and hence the signal measured may be amplified relative to its origin by a tilting component (see sketch in Figure 7) and ii) the exceptionally large gradient of0.5 mm/°C was restricted to the freezing period of autumn 2009 (Figure 9).

Characteristic for all measurements is the absence of significant shearing, a fast reaction to changes in near-surface temperature and a continuous movement mode during the negatively temperature-correlated dilatation regime. At a seasonal scale this correlation exists with regard to the temperatures at depth or a smoothed surface temperature with a minor dependency on short-term temperature fluctuations existing at some locations. This leads to the assumption that one could describe the cleft dilatations observed with a regression model that considers short-term variation and long-term evolution of the near surface rock or cleft temperatures. Modification of the crack meter regression model of *Nordvik et al.* [2010] (Equation 6) with a temperature record that reflects the seasonal variations (taken from depth or smoothed) instead of a sinusoidal explanatory function, may reveal a larger temperature dependence of cleft movements. Different time series analysis, such as the cross correlation function or a correlation analysis of the two signal decompositions of temperature and cleft expansion, may be able to quantify these dependencies and their variation over time in more detail - once longer time series of data are available.

5.1.2 Enhanced expansion and shearing regime

In subsection 4.2 two main features are described that we subsume under this regime: The first is the *summer expansion* that is initiated by isothermal/positive temperatures in clefts and the second is the *enhanced shearing*. In summer the cleft movement departed from the characteristic path of the negatively temperature-correlated dilatation regime in one of the components of the cleft movement. In 2010 this became visible between end of May and mid-June for all locations subject to this regime. Figure 12 illustrates the coincidence of this behaviour with snow melt for C2. Mostly snow-free conditions in spring 2010 were first reached at the end of April with subsequent snow fall leading to a temporal extent in snow cover (Figure 12, left). On 21 May some last snow patches remained in clefts, but disappeared over the next couple days. Simultaneously, cleft temperatures rose up to 0°C and summer expansion commenced (Figure 12). At C6 the reaction of the cleft temperatures to the snow melt near the surface was observed ten days later. At the same time the shearing activity started at C8 and the transition to summer expansion took place at C3 (Figure 6). The regime change is clearly identified before the summer maxima of the exceptionally warm period of July 2010. The highest activity of the stepwise opening of C2 was observed after this warm period and no coincidence of such opening events with precipitation was found (see Section 4 and Figure 8). The retardation of snow melt a few days after precipitation possibly masks a dependency between precipitation and opening activity. For the large movements at the end of August (Figure 8) such a connection to recent precipitation is unlikely because the last snow fall had occured 12 days before. A spatial interpretation of the movement and its extent at C2 was not possible because the cleft movement was only measured in one dimension. The upward shearing of the lower cleft (C20) in July and August can be possibly attributed to a toppling movement of the southern rock mass.

So far we have stated patterns and correlations, but not causal relationships between the thermal, hydrological and meteorological conditions described and the cleft movements. In the following, we discuss possible explanations for the two regimes and formulate hypotheses about which (combination of) physical mechanisms described in literature could explain the phenomena observed.

5.2 Hypothesis I – thermo-mechanical and cryogenic forcing of cleft dilatations

Cleft expansions that are negatively temperature-correlated have been observed at various permafrost sites [*Wegmann and Gudmundsson*, 1999; *Matsuoka*, 2008, 2001a; *Nordvik et al.*, 2010] and at some rock slopes in non-permafrost areas [*Watson et al.*, 2004; *Gischig et al.*, 2011b; *Mufundirwa et al.*, 2011]. For permafrost bedrock, ice formation processes (*cryogenic processes*) such as ice segregation [*Wegmann and Gudmundsson*, 1999] or the volumetric expansion of bulk freezing of cleft water [*Matsuoka*, 2001a] have been inferred as the driving processes of these movements. In contrast, the opening during cooling and stagnation or re-closing during warming is attributed to elastic deformation of rock due to stress caused by the thermal dilata-

tion of near-surface rock layers (thermo-mechanical forcing) [*Watson et al.*, 2004; *Gunzburger et al.*, 2005; *Gischig et al.*, 2011a]. We postulate a combination of these physical processes to explain the observed negatively temperature-correlated cleft movements because none of the processes suffice individually.

Wegmann and Gudmundsson [1999] assumed ice segregation as the explanatory process based on the correlation between borehole extensometer strain rates (dx_{Ex}/dt) of fractured rock and a calculated freezing rate in the corresponding temperature profile. Significant freezing rates found for positive rock temperatures (see Figure 8.2 in *Wegmann* [1998]) justify some suspicion and point to a shortcoming in their method: The calculation of the freezing rate is especially sensitive to thermal parameter estimation if large temperature gradients ($|dT/dt|$) occur. Possibly, the postulated dependency of the strain rate on the freezing rate only results from the inherent correlation between dT/dt with the strain rate (or the cleft expansion rate) of the negatively temperature-correlated regime. However, for porous sedimentary rock, ice segregation has been proven as the driving process for rock fracturing, ice lens formation and corresponding frost heave in laboratory experiments [*Akagawa and Fukuda*, 1991; *Murton et al.*, 2001]. With the low permeability of (frozen) crystalline rock and a cryogenic suction of about 15 kPa [*Fukuda*, 1983] we cannot explain the fast reaction of cleft movements to the surface temperature changes observed by a segregation process. This is supported by the fast response of micro-seismic activities on rapid temperature drop recorded at another permafrost site at the Matterhorn [*Amitrano et al.,* 2010]. Furthermore, the negative temperature dependency at strongly negative or positive temperatures does not correspond to the pattern of ice segregation (compare to Figure 6 of *Matsuoka and Murton* [2008]) and the water supply for a long term cleft ice growth (mm to cm) through meters of frozen rock is limited by low permeability and hydraulic gradient. *Matsuoka* [2001b] discussed this discrepancy between laboratory experiments with porous sedimentary rock and the field conditions in hard, fractured rock. He argues that the hydraulic and thermal conditions differ strongly between clefts and the inter-cleft rock masses and

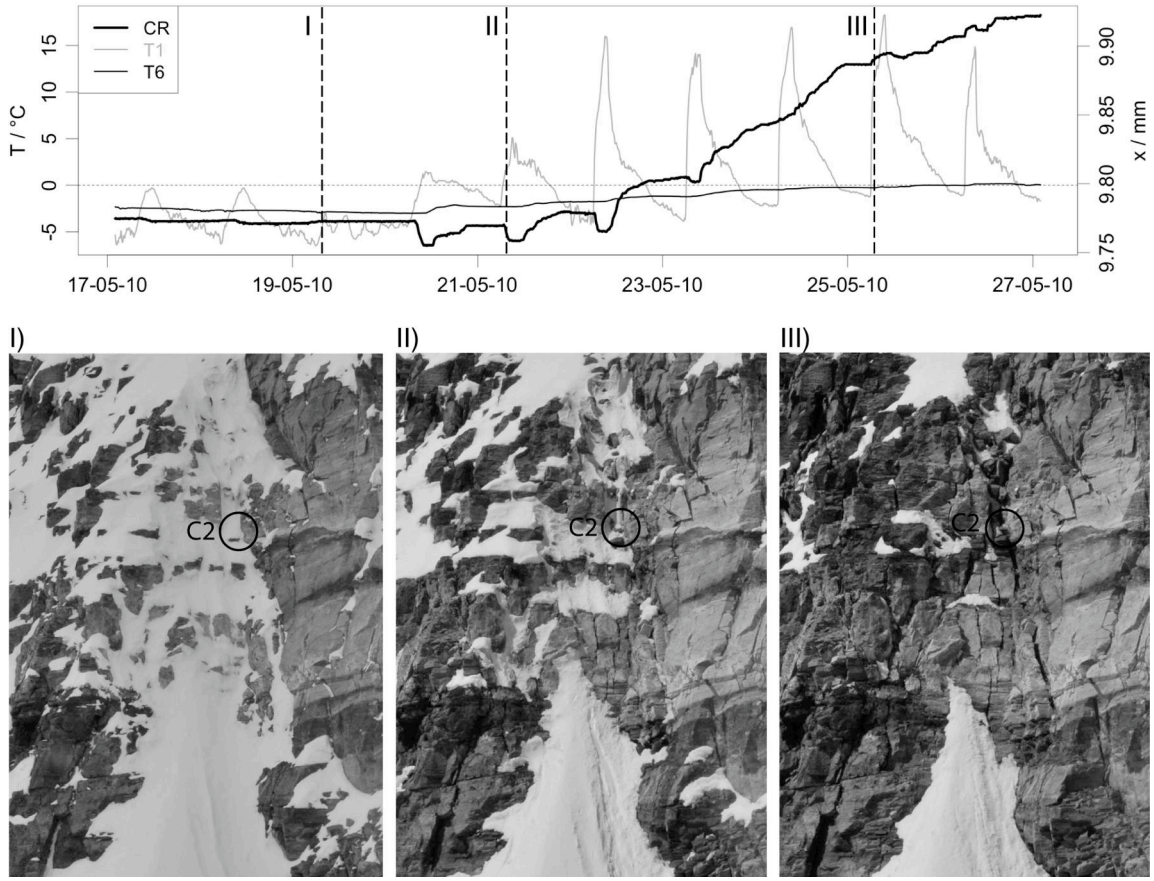

Figure 12: Transition to snow free conditions in the detachment zone around C2 during initial melting 2010. The time series with crack meter expansion (*CR*) and temperatures (*T1, T6*) from C2 contains indications (I-III) of time when pictures are taken: I) May 19th, 9:45 am; II) May 21st, 8:45 am; III) May 25th, 8:45 am. *T1* is measured at cleft top; *T6* at 0.6 m depth.

therefore, laboratory results cannot simply be applied to the widening of pre-existing macro-fractures. The coincidence of short-term cleft expansion and freezing at the cleft top of clefts 2-5 mm wide in the Japanese and Swiss Alps where attributed to freezing-induced volumetric expansion on the order of 9% instead of ice segregation [*Matsuoka*, 2001a, 2008]. Here one part of the negatively temperature-correlated cleft expansion may be attributed to a similar process, the exceptional large opening during autumn freezing (e.g. C8). This however requires the retentions of liquid water within the cleft prior to freezing. Even though a hydrologically closed situation is unlikely for large clefts, cleft infill (debris and clay or snow) might serve as a retention substrate. Volumetric expansion (and possible ice segregation within the cleft infill) during freezing progression can cause expansive stress on the cleft walls and support opening.

To explain the seasonal and also the short-term cleft expansion from the Matterhorn, the concept of a thermo-mechanical forcing is more convincing. This concepts explains the negatively (and positively) temperature-correlated movements across discontinuities by the thermal expansion and contraction of near-surface inter-cleft rock masses [*Watson et al.,* 2004, *Gischig et al.,* 2011a]. This thermally induced stress and reactive (cleft-) movement propagates several tens of metres into the rock to depths where only minor annual temperature fluctuations exist. The particular trajectories and possible amplification of such relative cleft movements, depend on the geometric (topographic and structural) settings that mask the influence of gravity together with the mechanical conditions of the clefts. Despite the variation of these parameters from site to site and corresponding differences in the reversibility and phase of the recorded movements, common annual temperature dependent patterns point toward similar driving processes. *Gischig et al.*, [2011b] applied coupled thermal mechanical finite element models for compact and fractured rock to reproduce deformations from a post-failure rock slope in Randa (Swiss Alps). With respect to this approach an important characteristic is the absence of high variations in water pressure within the cleft system, which would modify the stress normal to the cleft and change the effective friction. The absence of high (variations in) water pressure reveals the temperature dependency of the movements because in this case they are not dominated by rock hydrology. Similar vadose hydrological conditions were observed by *Watson et al.* [2004] in an unstable rock slope at Checkerboard Creek (Canada) showing temperature dependent movements. The lack of liquid precipitation during most of the year and partial ice sealing of clefts may lead to analogue reactions of many permafrost areas to temperature fluctuations.

Therefore, we hypothesize that the negatively temperature-correlated regime of the cleft dilatations presented here is caused by thermo-mechanical forcing and that the additional (enhanced) expansion in autumn is caused by ice formation processes in a substrate that retains liquid water. A similar combination of thermo-mechanical forcing and ice formation is known to be the driving mechanism for the formation of ice-wedge polygons in arctic permafrost [*Lachenbruch*, 1962]. These two processes differ with respect to the timing of ice formation and the influence of gravity. However, the example of ice-wedging illustrates the importance of ice formation in combination with thermally induced movements. Ice formation prohibits a re-closing by its frozen cleft infill and causes an inter-annual accumulation of movements even if the geometric setting would lead to reversible movements.

5.3 Hypothesis II – hydro-thermally caused shear strength reduction

The regime of enhanced opening (C2, C3) and shearing (C6, C8) cannot be plausibly explained by Hypothesis I: It contradicts the general trend of cleft contraction in summer following the negative temperature-correlation. Furthermore, a higher cryogenic activity due to melt water supply in the clefts, analogous to the summer frost heave in porous rock [*Murton et al.*, 2001] or spring freezing expansion [*Matsuoka*, 2008], would limit itself after a few days due to the concentrated release of latent heat along the cleft – resulting in local warming [*Hasler et al.,* 2011b]. As an alternative explanation, we suggest a change in the resistive forces against gravity and thermally induced stress.

According to the formulation of Terzaghi, stress in hard, fractured rock acts on discontinuities and intermediate rock bridges – overcoming their frictional strength and cohesion (and in some cases tensile strength) if irreversible deformation occurs [*Erismann and Abele*, 2001]. Depending on the persistence of the discontinuities and the spatial movement mode the importance of these resistive forces varies [*Eberhardt et al.*, 2004] and time-dependent processes such as sub-critical fracture growth [*Atkinson*, 1982] may

play a decisive role for rock fall release. For transient effects on the resistive strengths in permafrost bedrock, changes in temperature and hydrology are possible explanations. In contrast to dry clefts, frozen cleft infill causes significant cohesion or possibly even short-term adhesion (i.e. tensile strength) that is sensitive to temperature [*Krautblatter*, 2009] while the build-up of a hydrostatic pressure reduces the normal stress and correspondingly reduces the shear strength of clefts. These two mechanisms of strength reduction of clefts in permafrost areas may be responsible for thawing related increase of cleft movements and are discussed in the following.

The tensile strength and cohesion of intact, water saturated rock increases with lower sub-zero temperatures [*Mellor*, 1973]. Furthermore, laboratory experiments show that the shear strength of an ice-filled cleft becomes minimal if the temperature approaches 0°C and (brittle) failure at the rock-ice interface occurs [*Davies et al.*, 2001; *Ladanyi*, 2006; *Guenzel*, 2008]. The transfer of laboratory results to field situations is problematic as the time scales considered in the laboratory are on the order of minutes to hours as compared days to months in the field. As the compensation of stress in ice-filled clefts depends on ductile ice deformation rates [*Guenzel*, 2008; *Ladanyi*, 2006] similar deformation rates as detected in the laboratory would result in unrealistic large deformations in the field (>> cm/y). This means that the effect of pure ice infill cannot stabilize an open cleft under long-term mechanical stress [*Krautblatter*, 2009]. The stabilizing effect must be attributed to the prevention of water pressure build-up at depth [*Gruber and Haeberli*, 2007] or to additional friction by rock-rock contacts due to fracture roughness or debris and clay infill, which both show a dependency on sub-zero temperatures [*Krautblatter*, 2009; *Ladanyi*, 2006].

The enhanced expansion and shearing described above shows similarities with the seasonal pattern of permafrost creep in rock glaciers [*Arenson et al.*, 2002; *Perruchoud and Delaloye*, 2007; *Ikeda et al.*, 2008]. Similarly to the temperature-dependent reduction of the internal friction of a rock-ice mixture in rock glaciers, the warming of cleft-ice or frozen cleft infill may be responsible for enhanced toppling and sliding movements of large blocks in rock slopes. The shearing recorded in summer can be explained by such a reduction of the shear strength in the (steeply dipping) clefts found between individual blocks. Because the thermo-mechanically induced stress is not constant over time (Hypothesis I), additional short-term stress is withstood by the ice (ductile deformation). The reduction of shearing movements recorded during winter corresponds to such a mechanism. The sudden change in the shearing regime points to a warming caused by water percolation and related heat release or water pressure build-up. The same is true for the rapid response of the summer expansion at C2 and constant temperatures at 0°C (zero-curtain) which indicate water percolation. In contrast, at C3 a gradual response to the rock warming and the absence of a zero-curtain indicates no water percolation. The clefts at this northern oriented location are influenced by warming due to heat conduction in the rock that may cause changes in the cleft strength. In the case of C2, where we assume a gravity driven instability, the temporal movement during the summer expansion phase does not show a simple correlation with temperature or precipitation once the enhanced opening is triggered. Time-dependent processes such as sub-critical fracture propagation [*Kemeny*, 2003] or stick-slip shear failure [*Byerlee*, 1970] appear to be involved in these movements. However their occurrence during the thawing seasons and the clustering of large movements (slips) in the afternoon may indicate that the conditions for these processes are not independent from temperature.

Even though it is unclear if some of these warming-related movements will climax in a significant failure event, common mechanisms with pre-failure deformations are likely. The response to thawing within hours to weeks in the near-surface cleft may be an explanation for the early timing of rock fall in the European Alps in the hot summer of 2003 [*Gruber et al.*, 2004]. At the same time, the strong sensitivity to water percolation could be a reason for no clear correlation between rock fall activity and warm permafrost conditions [*Noetzli et al.*, 2003; *Fischer*, 2010]. In bedrock permafrost, the direct response of rock stability to short-term warming seems to be characteristic of only one type of rock fall release. Alternative mechanisms, such as the accumulation of an irreversible part of cleft expansion (temperature-correlated dilatation regime) or freezing related mechanisms could be relevant in other situations.

6 Conclusions

The interaction of physical processes that govern rock fall hazard from permafrost mountain slopes is poorly understood at present. In this study we have used high-resolution temperature and cleft

movement records from the Matterhorn Hörnligrat (Switzerland) to analyse the interaction between the thermal conditions and the relative movements at these large open fractures. The movements observed at 10 clefts show differences in amplitude and response time but commonality in patterns: During most of the year the cleft expansion is negatively correlated to the rock or cleft temperature with an occasionally increased expansion rate in autumn. Conversely opening occurs at two clefts in summer when minimal cleft aperture would be expected according to the described negative correlation. The initiation of this summer opening is synchronised to snow melt and stops with the first intense freezing in autumn. Significant shearing activity is restricted to this time span as well. The response of both movement types to the thermal conditions at the near-surface is within hours to a few weeks.

Based on the review and discussion of existing explanations for rock and cleft movements we state the following two hypotheses on the physical processes that cause movement of large clefts in permafrost bedrock:

I Temperature-correlated cleft expansion mainly originates from thermo-mechanical forcing and from cryogenic processes within the cleft driving increased autumn dilatation.

II Shearing and exceptional expansion that occur during the melting season are explained by a (shear-) strength reduction of rock–rock contacts, the rock–ice interface or ice-cemented infill within clefts. This is caused by a) conductive warming and b) melt water percolation with related hydrostatic pressure build-up or/and latent heat release.

In view of rock slope failure in permafrost the processes in I are relevant as disposition factors. The accumulation of irreversible movements modifies the geometrical setting of large blocks and can slowly bring them to a critical state. Clefts influenced by such large movements would not be permanently ice-sealed and thus may be more sensitive to water percolation. Ice segregation is an unlikely explanation for the recorded movements (Subsection 5.2) however it could play an important role in fracture propagation and the development of planes of weakness in frozen rock [*Hallet et al.*, 1991]. This effect is expected to be very inert in fine porous hard rock [*Matsuoka*, 2001b] with time-scales in the order of decades to centuries and is therefore not measurable with our current setup.

Hypothesis II concerns mechanisms that can modify slope stability rapidly. It is likely that the postulated decrease in the mechanical strength of clefts is involved in the release of warming-related rock fall from permafrost slopes. Where the stability of rock masses is critical due to the geological, structural and topographic settings such short-term variations of strength parameters can trigger failures. The fast response of both the movements derived from the time series data presented here and rock fall activity observed [*Gruber et al.*, 2004] points to the high importance of the hydrothermal processes. Even though different mechanisms are assumed (see Section 5.3) to link water percolation and stability their sensitivity to snow melt and liquid precipitation is similar. The investigation of the evolution and movement mode of such warming related rock movements with respect to the thermal and hydrological conditions at the shearing planes may be a key for the understanding of summer rock fall from permafrost areas.

Notations:

x	expansion of the cleft perpendicular crack meter [mm]
Δx	cleft expansion minus to initial value (x_0): $\Delta x = x\text{-}x_0$ [mm]
Δy	cleft shearing in dip direction parallel to cleft surface [mm]
dx/dt	expansion rate [m/s]
dx/dT	thermal cleft expansion gradient [mm/°C]
dT/dt	temporal derivative of temperature (warming rate) [°C/s]

Acknowledgements

We would like to thank the PermaSense team, R. Lim, M. Yücel, I. Talzi, T. Gsell, M. Keller, L. Thiele and C. Tschudin who made this challenging measurement possible. Thanks to P. Pogliotti and L. Fischer for the support with the geological interpretation in the field and V. Gischig and J. Moore for the discussions and their advice. The research presented within the project PermaSense was funded by the Swiss Federal Office for the Environment (FOEN) and the National Competence Center on Mobile Information and Communication Systems NCCR MICS of the Swiss National Science Foundation (SNSF).

References

Akagawa, S., and M. Fukuda (1991), Frost heave mechanism in welded tuff, *Permafrost Periglac. Process., 2*(4), 301–309.

Amitrano, D., M. Arattano, M. Chiarle, G. Mortara, C. Occhiena, M. Pirulli, and C. Scavia (2010), Microseismic activity analysis for the study of the rupture mechanisms in unstable rock masses, *NHESS, 10*, 831–841.

Arenson, L., M. Hoelzle, and S. Springman (2002), Borehole deformation measurements and internal structure of some rock glaciers in Switzerland, *Permafrost Periglac. Process., 13*(2), 117–135.

Atkinson, B. K. (1982), Subcritical crack propagation in rocks: theory, experimental results and applications, *J. Struct. Geology, 4*(1), 41–56.

Beutel, J. et al. (2009), PermaDAQ: A scientific instrument for precision sensing and data recovery in environmental extremes, in *Proceedings of the 2009 Int. Conference on Information Processing in Sensor Networks*, pp. 265–276, IEEE Computer Society.

Braathen, A., L. H. Blikra, S. S. Berg, and F. Karlsen (2004), Rock-slope failures of Norway, type, geometry deformation mechanisms and stability, *Nor. Geologisk Tidskr.*, *84*(1), 67–88.

Byerlee, J. D. (1970). The mechanics of stick-slip, *Tectonophysics, 9*(5), 475–486.

Coussy, O. (2005), Poromechanics of freezing materials, *J. Mechanics and Physics of Solids, 53*(8), 1689–1718.

Cruden, D. M. (2003), The shapes of cold, high mountains in sedimentary rocks, *Geomorphology*, *55*(1–4), 249–261.

Davies, M. C. R., O. Hamza, and C. Harris (2001), The effect of rise in mean annual temperature on the stability of rock slopes containing ice-filled discontinuities, *Permafrost Periglac. Process., 12*(1), 137–144.

Dramis, F., M. Govi, M. Guglielmin, and G. Mortara (1995), Mountain permafrost and slope instability in the Italian Alps: the Val Pola landslide, *Permafrost Periglac. Process., 6*(1), 73–81.

Eberhardt, E., D. Stead, and J. S. Coggan (2004), Numerical analysis of initiation and progressive failure in natural rock slopes – the 1991 Randa rockslide, *Int. J. Rock Mechanics and Mining Sciences*, *41*(1), 69–87.

Erismann, T. H., and G. Abele (2001), *Dynamics of rockslides and rockfalls*, Springer.

Fischer, L., F. Amann, J. R. Moore, and C. Huggel (2010), Assessment of periglacial slope stability for the 1988 Tschierva rock avalanche (Piz Morteratsch, Switzerland), *Eng. Geol., 116*(1–2), 32–43.

Fischer, L. (2010), Slope instabilities on perennially frozen and glacierised rock walls: multi-scale observations, analyses and modelling, PhD Thesis, University of Zurich, Zuerich, Switzerland.

Fukuda, M. (1983), The pore water pressure profile in porous rocks during freezing, in *Proceedings of the 4th Int. Conference on Permafrost*, pp. 322–327. Washington DC, USA.

Gischig, V. S., J. R. Moore, K. F. Evans, F. Amann, und S. Loew (2011a), Thermomechanical forcing of deep rock slope deformation: 1. Conceptual study of a simplified slope, Journal of Geophysical Research, 116(F4), F04010.

Gischig, V. S., J. R. Moore, K. F. Evans, F. Amann, und S. Loew (2011b), Thermomechanical forcing of deep rock slope deformation: 2. The Randa rock slope instability, Journal of Geophysical Research, 116(F4), F04011.

Gruber, S., and W. Haeberli (2007), Permafrost in steep bedrock slopes and its temperature-related destabilization following climate change, *J. Geophys. Res.*, *112*, F02S18.

Gruber, S., M. Hoelzle, and W. Haeberli (2004), Permafrost thaw and destabilization of Alpine rock walls in the hot summer of 2003, *Geophysical Research Letters*, *31*(13), L13504.

Guenzel, F. (2008), Shear Strength of Ice-Filled Rock Joints, in *Proceeding of the 9th Int. Conference on Permafrost*, pp. 581–586, Fairbanks, Alaska, USA.

Gunzburger, Y., V. Merrien-Soukatchoff, and Y. Guglielmi (2005), Influence of daily surface temperature fluctuations on rock slope stability: case study of the Rochers de Valabres slope (France), *Int. J. of Rock Mechanics and Mining Sciences*, *42*(3), 331–349.

Haeberli, W., M. Wegmann, and D. Vonder Muehll (1997), Slope stability problems related to glacier shrinkage and permafrost degradation in the Alps, *Ecologae Geologicae Helveticae*, *90*, 407–414.

Hallet, B., J. S. Walder, and C. W. Stubbs (1991), Weathering by segregation ice growth in microcracks at sustained sub-zero temperatures: Verification from an experimental study using acoustic emissions, *Permafrost Periglac. Process., 2*(4), 283–300.

Hasler, A., S. Gruber, and W. Haeberli (2011a), Temperature variability and thermal offset in steep alpine rock and ice faces, *The Cryosphere, 5,* 977–988, doi: 10.5194/tc-5-977-2011.

Hasler, A., S. Gruber, M. Font, and A. Dubois (2011b - in press), Advective heat transport in frozen rock clefts - conceptual model, laboratory experiments and numerical simulation, *Permafrost Periglac. Process*.

Hasler, A., I. Talzi, J. Beutel, C. Tschudin, and S. Gruber (2008), Wireless sensor networks in permafrost research: concept, requirements, implementation, and challenges, in *Proceeding of the 9th Int. Conference on Permafrost*, pp. 669–674, Fairbanks, Alaska, USA.

Hiebl, J., I. Auer, R. Böhm, W. Schöner, M. Maugeri, G. Lentini, J. Spinoni, M. Brunetti, T. Nanni, and M. Per ec Tadi (2009), A high-resolution 1961–1990 monthly temperature climatology for the greater Alpine region, *Meteorologische Zeitschrift*, *18*(5), 507–530.

Ikeda, A., N. Matsuoka, and A. Kääb (2008), Fast deformation of perennially frozen debris in a warm

rock-glacier in the Swiss Alps: an effect of liquid water, *J. Geophys. Res.*, *113*(F1), F01021.

Kemeny, J. (2003), The time-dependent reduction of sliding cohesion due to rock bridges along discontinuities: A fracture mechanics approach, *Rock Mechanics and Rock Engineering, 36*(1), 27–38.

Krautblatter, M. (2009), Detection and quantification of permafrost change in alpine rock walls and implications for rock instability, PhD Thesis, Rheinischen Friedrich-Wilhelms-Universität Bonn, Bonn, Germany.

Lachenbruch, A. H. (1962), *Mechanics of thermal contraction cracks and ice-wedge polygons in permafrost*, Geological Society of America New York.

Ladanyi, B. (2006), Creep of frozen slopes and ice-filled rock joints under temperature variation, *Canadian J. of Civil Engineering*, *33*(6), 719–725.

Matsuoka, N. (2001a), Direct observation of frost wedging in alpine bedrock, *Earth Surf. Processes Landforms*, *26*(6), 601–614.

Matsuoka, N. (2001b), Microgelivation versus macrogelivation: towards bridging the gap between laboratory and field frost weathering, *Permafrost Periglac. Process., 12*(3), 299–313.

Matsuoka, N. (2008), Frost weathering and rockwall erosion in the southeastern Swiss Alps: Long-term (1994-2006) observations, *Geomorphology*, *99*(1–4), 353–368.

Matsuoka, N., and J. Murton (2008), Frost weathering: recent advances and future directions, *Permafrost Periglac. Process., 19*(2), 195–210.

Mellor, M. (1973), Mechanical properties of rocks at low temperatures, in *Proceedings of the 2nd Int. Conference on Permafrost*, pp. 334–344, Yakutsk, UdSSR.

Mufundirwa, A., Fujii, Y., Kodama, N., and J. Kodama (2011), Analysis of natural rock slope deformations under temperature variation: A case from a cool temperate region in Japan, *Cold Reg. Sci. Technol., 65*(3), 488–500.

Murton, J. B., J. P. Coutard, J. P. Lautridou, J. C. Ozouf, D. A. Robinson, and R. B. G. Williams (2001), Physical modelling of bedrock brecciation by ice segregation in permafrost, *Permafrost Periglac. Process., 12*(3), 255–266.

Murton, J. B., R. Peterson, and J. C. Ozouf (2006), Bedrock fracture by ice segregation in cold regions, *Science*, *314*(5802), 1127.

Neaupane, K., T. Yamabe, and R. Yoshinaka (1999), Simulation of a fully coupled thermo-hydro-mechanical system in freezing and thawing rock, *Int. J. of Rock Mechanics and Mining Sciences*, *36*(5), 563–580.

Noetzli, J., S. Gruber, T. Kohl, N. Salzmann, and W. Haeberli (2007), Three-dimensional distribution and evolution of permafrost temperatures in idealized high-mountain topography, *J. Geophys. Res.*, 112.

Noetzli, J., M. Hoelzle, and W. Haeberli (2003), Mountain permafrost and recent Alpine rock-fall events: a GIS-based approach to determine critical factors, in *Proceedings of 8th Int. Conference on Permafrost*, pp. 827–832, Zürich, Switzerland.

Nordvik, T., L. H. Blikra, E. Nyrnes, and M. H. Derron (2010), Statistical analysis of seasonal displacements at the Nordnes rockslide, northern Norway, *Eng. Geol.*.

Perruchoud, E., and R. Delaloye (2007), Short-term changes in surface velocities on the Becs-de-Bosson rock glacier (western Swiss Alps), *Proceedings HMRSC-IX*, *43*, pp. 14–15.

Pirulli, M. (2009), The Thurwieser rock avalanche (Italian Alps): Description and dynamic analysis, *Eng. Geol.*, *109*(1–2), 80–92.

Pleuger, J., S. Roller, J. M. Walter, E. Jansen, und N. Froitzheim (2007), Structural evolution of the contact between two Penninic nappes (Zermatt-Saas zone and Combin zone, Western Alps) and implications for the exhumation mechanism and palaeogeography, International Journal of Earth Sciences, 96, 229-252.

Ravanel, L., and P. Deline (2010), Climate influence on rockfalls in high-Alpine steep rockwalls: The north side of the Aiguilles de Chamonix (Mont Blanc massif) since the end of the'Little Ice Age', *The Holocene*.

Talzi, I., A. Hasler, S. Gruber, and C. Tschudin (2007), PermaSense: investigating permafrost with a WSN in the Swiss Alps, in *Proceedings of the 4th Workshop on Embedded Networked Sensors*, pp. 8–12, ACM Press New York, NY, USA.

Savage, W. Z., and D. J. Varnes (1987), Mechanics of gravitational spreading of steep-sided ridges («sackung»), *Bulletin of Engineering Geology and the Environment, 35*(1), 31–36.

Watson, A. D., D. P. Moore, and T. W. Stewart (2004), Temperature influence on rock slope movements at Checkerboard Creek, in *Proceedings of the 9th Int. Symposium on Landslides*, pp. 1293–1298.

Wegmann, M. (1998), Frostdynamik in hochalpinen Felswänden am Beispiel der Region Jungfraujoch - Aletsch, *Mitteilungen der Versuchsanstalt für Wasserbau, Hydrologie und Glaziologie der ETH Zürich*, *161*.

Wegmann, M., and G. Gudmundsson (1999), Thermally induced temporal strain variations in rock walls observed at subzero temperatures, *Advances in Cold-Region Thermal Engineering and Sciences*, 511–518.

Andreas Hasler, Department of Geography, University of Zurich, Winterthurerstr. 190, 8057-Zürich, Switzerland, andreas.hasler@geo.uzh.ch

Dr. Stephan Gruber, Department of Geography, University of Zurich, Winterthurerstr. 190, 8057-Zürich, Switzerland, stephan.gruber@geo.uzh.ch

Dr. Jan Beutel, Computer Engineering and Networks Laboratory, ETH-Zurich, Gloriastr. 35, 8092-Zürich, Switzerland, j.beutel@ieee.org

Appendix

Technical documentation

This technical documentation gives an overview of the contribution to the PermaSense data acquisition infrastructure by the author. Even though it is kept more simple in layout and text than the rest of this thesis, it illustrates the benefit from a comprehensive understanding of the data acquisition, which was important for this thesis. The physics of the sensing variables and electronically induced effects need to be considered for data processing and analysis for the non-standard setup and sensors used in this study.

A extended version of this documentation including all available schemes and lists is available at: http://www.permasense.ch/data/sensordocu.pdf

A technical documentation regarding all aspects of the PermaDAQ-infrastructure is provided by the technical partners.

A.1 Wireless sensor network – hardware setup

Sensor rods and thermistor chains

The *sensor rods* and *thermistor chains* consist of a mechanical and electronical assembly of 6–14 individual sensing elements (or configurations). In the case of the sensor rod (SR) these sensing elements are four thermistors (YSI–40006) and four electrode pairs (conductive foam) that measure the direct current (DC) resistance of the rock as indicator of its liquid water content (see Publication I; Figure 3). Additionally, the resistance between electrodes at different depths is recorded, but the electronical setup does not support meaningful measurements for the extremely high resistances of this configuration. The sensor rods are placed in near-surface borings with a diameter of 14mm that are drilled perpendicular to the rock surface. A bayonet mounting-tool allows the placement below the surface to avoid direct radiation on the sensor rod. The position of the in-rod electronics at the tip of the sensor rod minimizes measurement errors due to temperature fluctuations (see Publication I; Figure 3). The thermistor chains (TC) measure six to eight temperatures along a cable that is placed within a rock cleft or in a borehole within steep ice faces. A sight variation of the thermistor chain is the so-called *moisture chain* (TM) that record four temperatures and two resistances of the medium around the cable (simple detection of liquid water).

This three sensor types are electronically very similar and contain the same custom circuit board with two assembly options. Different measurement channels of the senor elements are switched by the internal electronics of the sensor rod (multiplexer). The measurement signal is transmitted by a DC-voltage to the sensor interface board (SIB) in the network nodes. Beside the real measurements, *reference resistors* within the sensor electronics are recoded as independent references. For details on the sensor electronics (circuit board, schemes) and the logging schemes see the extended version of this documentation (sensordocu.pdf).

Other sensors such as single thermistors or the test setup for self-potential measurements are not presented in this section. The operation of individual thermistors was applied successfully at the Matterhorn field site. Electronically the measurement principle corresponds to the single-ended voltage dividers used within the sensor rods. The self-potential measurements did not provide useful results.

Applied standard sensors

The geotechnical sensors used at the Matterhorn deployment are:

a) *ForaPot Crackmeter, ForaTec*: Potentiometric distance sensor that are anchored at the two sides of a cleft and that provide an analogue output signal linearly dependent on the cleft aperture/shear
b) *Earth pressure cell 3500, Geokon*: Piezometric stress sensor that translate a stress acting on the measurement plane into a DC-voltage proportional to the stress
c) *Water level transducer 26W, Keller*: Digital stand-alone sensor that calculates the water level from the difference between two piezometric pressure sensors (air, water) and provide digital conversions via RS-485

An overview of these sensors is provided in Figure 19. All the sensors are connected with water-tight connectors (*Souriau*) to the sensor interface board (SIB) in the network nodes. The SIB was designed to provide the stable supply voltage and signal interfaces to these and other standard sensors and allows a flexible combination of different sensors with one network node. All these sensors except the stress sensor where operated successfully, but the pressure sensors did not provide useful information of the hydrological cleft conditions because no water table or ice built-up at the sensor locations. The crackmeters are protected by a shield the reduce the impact of debris fall, snow loading and radiation on the sensors (Figure 20). Further, cables are kept as short as possible to reduce environmental impact.

Figure 19: *Overview of applied sensors: Water / air pressure sensor (WP), crackmeter (CR), earth pressure cell (EP), and sensorrod (SR). Other sensors (TC/TM/SP) are not shown.*

Network nodes

The hardware of the network nodes comprises the WSN-platform (communication electronics), the sensor interface, power-supply, electro-mechanical parts (antenna, connectors) and the mechanical setup. For the WSN-platform the commercial platform *TinyNode (Shockfish)* was used (see Dubois-Ferrière et al., 2006). The sensor interface and power management (and some additional functions: e.g. system reset; memory extension) are implemented with the SIB. This SIB was developed by an engineering company (*AOT*) based on a user system specification that includes the experience of the first generation network nodes (Talzi et al. 2007) and the extended requirements by the geotechnical sensors (see above). For a technical description of the SIB see Publication II. The power supply is provided by a Lithium-Thionylchlorid non-rechargeable battery (*Saft LSH-20*), which provides stable voltage at very low temperatures for low-power use. Options for external power supply exist. The mechanical setup consists of a rugged aluminum housing (*Bopla*) and a stainless steel protective shoe (Figure 20). This double protection against environmental impact was very successful and no network node experienced serious damage for the whole operation period. The protective shoe has additionally the function to allow a fast node exchange without any tools and reduced the impact of lightnings because the galvanic coupling between housing and protective shoe is low. The shoe was enhanced between the first and the second generation regarding the performance to exchange nodes. The downward orientation of the connector and the antenna (Figure 20) minimizes the impact on these sensitive parts and avoids water entry if the sealing is broken.

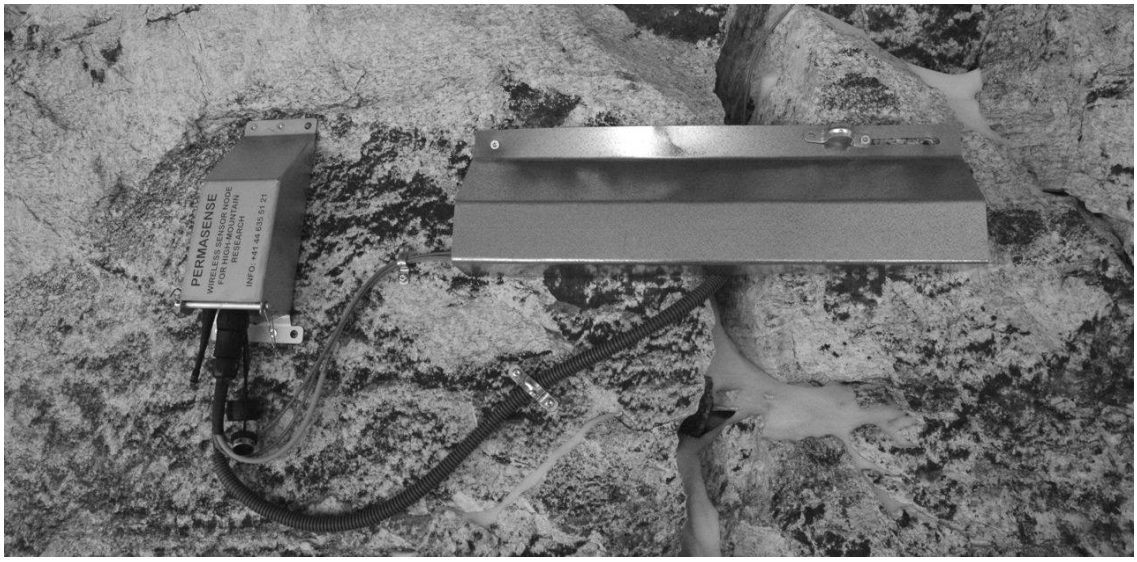

Figure 20: *Sensor node consisting of the network node inside of the protective shoe (left), a crack-meter below the shield (right) and a thermistor chain inside the cleft (dark cable).*

A.2 Data management and data processing

An overview of the steps of the data acquisition was given in Chapter 3. These are: 1) physical sensing, 2) data logging, 3) data transmission, 4) pre-processing, and 5) archiving. Here we leave out the intermediate parts of the data acquisition (logging and data transmission) because the author made only minor contributions to these parts. Instead the focus is on the pre-processing and archiving with respect to the access to this data by geo-scientists. Processes, which are currently not included in the pre-processing of the PermaDAQ infrastructure are described in a subsequent subsection (Data cleaning, aggregation, and merging). These process may be included in the pre-processing within PermaDAQ in the future. At the end of this section the applied analysis tools for off-line processing are outlined.

Data structure, pre-processing, and data access

The data arrives divided into different data packets at the data backend server: For each point in time of the logging 2–5 data packets are generated and transmitted to the server which runs a software for data streaming (GSN: see Publication II). The types of data packets are *MUX1* and *MUX2* for the multiplexer data (sensor rods, thermistor chains, and moisture chains), *ANL* for the other analogue measurements (crackmeters, individual thermistors, and earth pressure cells), and *DIG* for the digital water table sensors. A fifth sensor data packet type (*DIFF*) for the self-potential measurements exists but is not described for the further processing. The same is true for the health data that monitors parameters of the network nodes.

In a first step, these system specific processes are performed and the data is dumped into a SQL database. In a second step this raw data is converted into physical units (°C, mm, MPa, …) based on meta-information of the attached sensors and assigned to the measurement locations. This converted data is stored in a second database that is accessible for the users with separate tables for each data packet type. This data base contains many tables that most are not used for the data access. The relevant tables start with *matterhorn* or *jungfraujoch* and have a suffix for the sensor type. E.g. the table *matterhorn_sensorrod1* contains all data from *MUX1* of the sensor rods at Matterhorn. For details see the extended version of this documentation (sensor_docu.pdf). For the crackmeter data there are 5 sub-types with separate tables. Each table is for a certain combination of sensors attached to the 4 channels of the analog-digital converter (ADC) (Table 2). There are 4 letters representing the sensors attached to the 4 channels of the ADC. E.g. *nctn* means that channel 0 and 3 has no sensors connected, on channel 1 is a crackmeter, and on channel 2 there is a thermistor. Table 1 provides the primary meta data that is needed for the access of this data. The data is accessed by mySQL commands. Automated routines for this data access are implemented for the R data analysis software and are described in the next subsection and the extended documentation. Alternatively tools to export csv-files are provided by the data front-end on http://data.permasense.ch/.

Table 1. Primary meta-information for data access:

pos	MUX	ANL	DIG
jj01	SR		
jj02	SR		
jj03	SR		
jj04	SR		
jj05	SR		
jj06	SR		
jj07	SR		
jj08	TC		
jj09	SR		
jj10	TC		
mh01	TC	nctt	
mh02	TC	nctt	
mh03	TC	nctt	
mh04	TC	nctt	
mh05	TM	EP	WP
mh06		tctc	
mh07	TM	EP	WP
mh08		nctc	
mh09		ccct	
mh10	SR	ntnn	
mh11	SR	ntnn	
mh12	SR	ntnn	
mh13		SP	
mh20		ccnn	
mh21		ccnn	
mh22		ccnn	

Data merging, filtering, and aggregation

For an efficient analysis the data should be ordered by sensor node because the ease direct extraction of time series and cross-correlations. The data may be identified by the sensor node and the sensing element label (e.g. *mh01 – TC_T3* stands for thermistor 3 of sensor node 1 at Matterhorn). To get the data in that order, the data from the same sensor node in the different tables (see above) needs to be merged. Because the different data packets (MUX1, MUX2, …) have slightly different timestamps for the measurements of the same logging cycle, a simple merging by time is not possible. Two possibilities to do this merging are implemented for different data types: a) for the MUX data the sample number and the timestamp is used for merging; b) the data is first aggregated to regular timestamps and merged subsequently. The more intensive version a) is required by the filtering algorithm for the MUX data. This filtering applies the values of the *reference resistors,* which are measured together with the real measurements (see Hardware setup): If the reference values is not within a defined range (see sensor_docu.pdf) the data is considered as invalid and not used for the analysis. For all non-MUX sensors a visual control and a masking of the invalid data is applied (see Table 2).

The temporal resolution of the raw data is currently 2 min allowing down sampling and aggregation of the data. The current implementation with mySQL by the query generation routines makes an average over the interval [t–($intv$/2) : t+($intv$/2)] (with t = timestamp and $intv$ = aggregation interval in minutes) and assigns the values to the timestamp. The level of aggregation (or measurement interval) depends on the characteristics of the data and the purpose the data use (Hall, 1997). With increasing size of the averaging interval the amplitude of the

time series is less represented in the dataset and the values deviate more from the effective temperature measured at this point in time (Figure 21). For the rock surface temperature (2cm) with strong radiation influence and large daily amplidudes, such as at position mh10 (Figure 21), precise representation of the raw values an short term fluctuations is given on a aggregation with a granularity of 10 minutes or smaller, while the daily evolution and amplitude is still well represented on a 30 minutes level. Larger averaging windows are not suitable to represent surface temperature variations on rock and underestimate temperature peaks. For temperatures at greater depth larger aggregation intervals may be suitable and allow data reduction if non-conductive effects can be neglected.

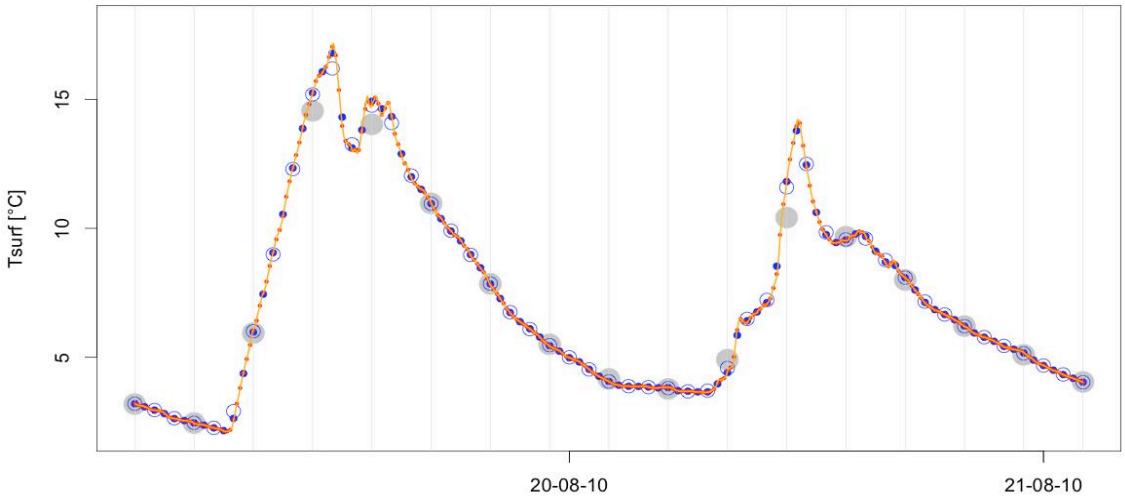

Figure 21: *Effect of aggregation levels on the example of Tsurf of mh10: raw data (orange line), 10 min av. (red), 30 min av. (blue), 1 hour av. (blue circle) and 3 hours av. (grey). Co-centric circles indicate good representation of the instantaneous value.*

The difference (ΔT) between down sampling by averaging or by linear interpolating for 10 min intervals at mh10 has a standard deviation stdev(ΔT1) is 0.032 °C, stdev(ΔT2) is 0.013 °C and stdev(ΔT3) is 0.005 °C. Hence, with a ten minutes interval the aggregated data is valid for both, representation of the instantaneous value and mean of the 10 minutes time period.

Analysis tools

The analysis tools used for this thesis comprises diverse plotting routines for time series, cross-correlations, 2–dimensional movement patterns and spectral analyses that are implemented in R (sensor_docu.pdf) and comparison between modeled and measured temperatures assuming conductive heat flux (*DeltaCon*) that is written in the interactive development language IDL. Further, functions to fill data gaps for mean annual temperature calculation (MAT) where applied (Publication III). The procedure of the time series and cross-correlation plots are described in Publication III and V.

A spectral analysis was applied in earlier studies for the detection of non-conductive heat fluxes (Hinkel and Outcalt, 1993). Examples for such an application is given in Appendix A.6. There a short time fourier transformation (STFT) is used to calculate the power spectrum of the frequencies within 2-day windows that are shifted with 12 hours increments. The tool DeltaCon calculates the temperatures of the two intermediate thermistors of the sensor rods (SR_T2,

SR_T3) for a point in time based on the measured temperatures of the previous time step and the uppermost and lower most temperature. The temperature difference of the modeled and measured temperatures at SR_T2, SR_T3 is converted into a source term of the non-conductive heat flux (Gerber, 2010). Both methods, the spectral analysis and DeltaCon, produce comparable results, but DeltaCon is restricted to temperature profiles with clearly defined depths of the thermistors (Appendix A.6). Contrary, DeltaCon gives a rough indication how large the non-conductive heat fluxes are.

A.3 Data quality

During the testing phase and two years of operation of the PermaSense WSNs, diverse evaluations of the data quality have been undertaken. Some of these results are contained in Beutel et al. (2009), Hasler et al. (2008) or internal reports (Hasler and S. Gruber, 2009). An complete quantitative data evaluation can not be presented within this study because of the lack of automated data checking algorithms (visual control is still one of the most reliable methods) that would be necessary to treat this amount of data. Here different aspects of the data quality and characteristics are illustrated in an exemplary manner. The basic terms used hereto are:

- *Absolute accuracy* in the sense of how correct the measurement quantity at the sensing element is represented in the dataset (measurement error).
- *Stability* or *relative accuracy* means how much the measurement value is independent of effects other than the measurement quantity within a time series. (In contrast to other definitions, here relative accuracy is not used for the accuracy between different sensing elements, because this corresponds quite much to the absolute accuracy in this case (measurement errors are little dependent).
- *Representativity* of a measurement says how good a measured value at the sensing element represents the physical quantity to be measured in the undisturbed situation (physical effect of the instrumentation). This effect may also be considered in the therm absolute accuracy (or better *total accuracy*) in many studies, but it is rarely addressed explicitly.
- *Precision* means the number of digits with which the data is measured, stored, transmitted or represented. Note that measurement precision (ADC-resolution) may differ from transmission/representation precision.

The reliability of the system is evaluated by the completeness of the data and by the time delay with which the data was delivered to the data backend, the first being essential for an environmental science instrument and both being important for environmental monitoring and early warning.

Temperature measurements

The following quality analysis is the basis for the application of the temperature data in Publication III and V. A summary of this analysis in contained in the respective publications.

The internal references of the sensor rods and the thermistor chains (Appendix A.1) are used as an indicator of proper functionality of the measurement and for the quantification of the measurement accuracy and stability. The stability of these references has two different characteristics that are valid for the measurements as well: First, fluctuations within a consistent measurement series caused by temperature fluctuations and electronical “noise”. Second, an offset between series with exchanged hardware (different WSN-nodes in different *deployments*). Figure 22 shows two examples of this reference stability of a thermistor chain and a sensor rod. The fluctuations due to temperature variations (mh03) lie within 20 mK and the offset due to different nodes attached (before and after June 23th) is below 5 mK. Both values are clearly

smaller than the range of the thermistor accuracy defined by the supplier (± 0.2°C; no successful calibration was made). Some single measurements of the thermistorchain show higher deviations that may be caused electronically. If they exceed a tolerance of 2±0.15 °C the sample is filtered (section A.2). The raw data is transmitted with a two-byte precision resulting in a 1.3 mK resolution (horizontal stripes in Figure 22). The resulting absolute accuracy of the measurement system itself is ± 0.3°C. Relative accuracy within a time series is clearly better in case of non-occurrence of electronical instabilities.

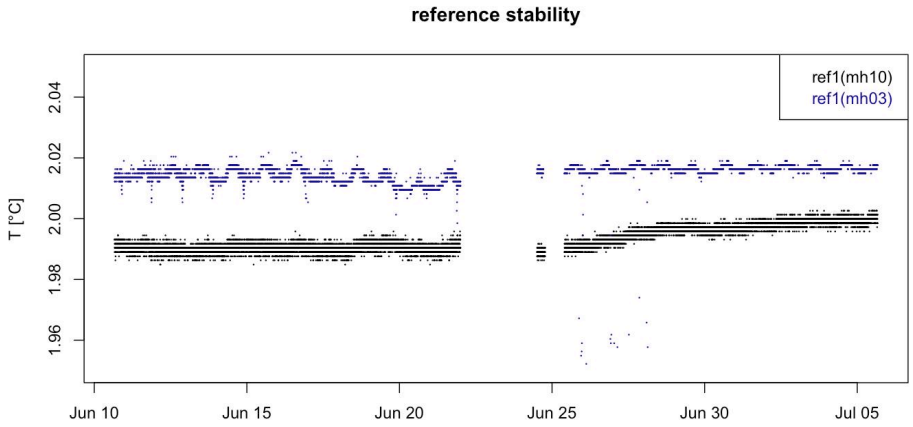

Figure 22: *Stability of reference values during node exchange at June 23th 2010 of thermistorchain mh03 (blue) and sensorrod mh10 (black).*

The representativity of a temperature measurement depends strongly on the physical sensor design and the thermal parameters of the measurement media. The high heat capacity of rock and the proximity (< 1mm) of the thermistor to this *thermal mass* increases the representativity of the measurement. The effect of direct thermal coupling through the thermistor wires can be neglected with the given sensor design (wires are lead from inside towards the surface; smaller gradients), but heat may be transmitted from the bypassing wires to the thermistor. This influence may be relevant only for the upper most sensor of the sensorrod. Numerical modeling of this setup would help to quantify this source of error. So done for the laboratory experiments (with slightly different setup), the error was smaller than 0.01°C for a 10°C cable temperature disturbance at 10cm distance. For the measurements of the cleft temperatures, the representativity is much lower. First, the thermistor chain measures a mix between cleft air temperature and cleft surface temperature, and second, disturbances through the wires will affect the measurements much more due to bad thermal connection with the measurement media (in case of ice infill significantly better). Thus, the cleft temperature must be interpreted with an uncertainty in the range of ± 2°C.

Rock resistance

In terms of accuracy and precision the rock resistances measured by the sensorrods have similar characteristics as the temperature measurements as they are electronically identical. This means that the absolute accuracy is ± 1 kΩ if the measured value is 1 MΩ but the accuracy decreases dramatically for large resistance values (± 200 MΩ at 1 GΩ; upper limit of range). The representativity of the resistance measurements depends on the contact resistance of the

electrodes and on local heterogeneities of the rock between these electrodes. In contrast to ERT-surveys the contact resistance is directly added to the rock resistance (serial connection). Pre-tests with the applied conductive foams showed, that contact resistances are below 5 kΩ if installed on a clean rock surface. Because of the in-hole installation of the electrodes, the cleanness of the contact can hardly be controlled. Temperature-resistivity gradients for intact porous rock in frozen state lies in the range of 20–40 %/°C cooling (Krautblatter, 2009). Larger temperature dependency in the measured data (Appendix A.8), indicate that the measurements on the north side of Jungfraujoch (jj05–jj09) are influenced by variations of the contact resistance or micro clefts between the electrode pair.

Cleft movements:

The potentiometric dilatation measurements have little electronic sources of errors as they do not contain any electronics and thermal changes of the total potentiometer resistance are compensated by the bridge circuit measurement design. Hence, the electronical accuracy depends only on effects on the sensor interface board (SIB) that are in the order of the measurement precision (CR-range/65000 = 15 ppm = 0.8–5 µm). Effects due to thermal expansion of the materials are compensated mechanically within the instrument.

Errors due to rapid change in irradiation (leading not equilibrated instrument temperatures) are analyzed by changing the crackmeter mh01 from being mounted across the cleft to a setting with both displacement anchors at the same side of the cleft on an intact rock mass (Publication V). Figure 23 shows this change from across-cleft to intact-rock dilatation, illustrating the good thermal stability of the crackmeter measurements even with enormous temporal temperature gradients (≈ 10 °C/h at 2 cm from rock surface). While the linear expansion of the cleft was -6 µm/°C, the on over the approximately 150mm intact rock between the anchors is +0.1 to +0.2 µm/°C for daily temperature fluctuations. This dilatation signal may be explained by thermal expansion of the rock, hence no significant measurement error is detected (Publication IV). This is clearly better than the supplier's specification 5 ppm/°C (being 0.25 µm/°C for 50 mm CR-range) even for this very fast temperature fluctuations.

No node change at position mh01 was performed since the modification of the crackmeter position, therefore its effect could not be quantified with this stable time series. Never-the-less time series from other sensors (see: Supplementary material) indicate no significant offsets in the crackmeter data when node changes where performed. In analogy with the sensorrod data, this offset is assumed to be in the order of the measurement precision (15 ppm). Hence, the crackmeter accuracy is ±3 to ±18 µm (±50 ppm of the measurement range, 50 to 300 mm CR-range).

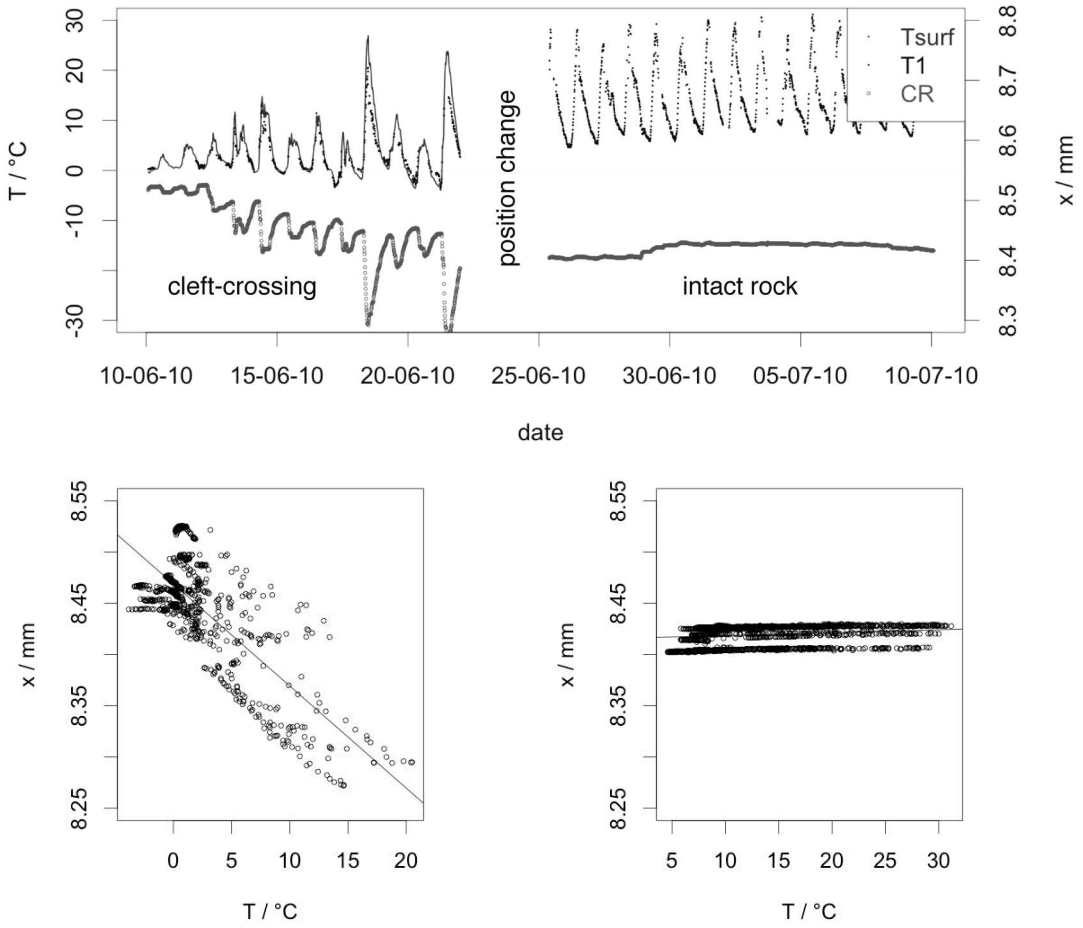

Figure 23: Stability of crackmeter measurements: Time series of dilatation and cleft temperatures and instrument Temperature before (top – June–July 2010) change from cleft to plain rock (Figure 5 in Publication V); dilatation (ΔCR) as a function of the surface temperature (Tsurf) in June 2010 (bottom left) and July 2010 (bottom right).

Hydrological and geotechnical sensors

The hydrological and geotechnical sensors placed in two clefts where not frozen in or flooded during the two years of measurements available. This corresponds with observations made in several site visits. Because this series are not used for the analysis in this study, an evaluation of the data quality is passed. Just the functionality of these sensors is briefly summarized: The digital hydrological sensor measuring air and water pressure (and the temperature of both sensing elements) did register reliable values for the whole time the system was operating (Figure 24). The pressure within the cleft (water sensor) and at the rock surface (air pressure) follow each other closely, hence, no water column is detected.

In contrast, the earth pressure cell did not register reasonable values. This is on one hand due to the missing ice aggradation around the sensor, but the analysis of the values indicates an additional technical problem: An error in the logging routine writes the channels 0–2 instead of channel 1–3 of the ADC to the respective data fields. Hence, the instrument temperature (measured as controlling parameter) of the earth pressure cell is written into the field for the stress data (EP_P) with the conversion for the latter parameter. However the instrument temperature and earlier tests in the laboratory indicate that this problem could be corrected

easily and that future operation of this sensor type will be successful.

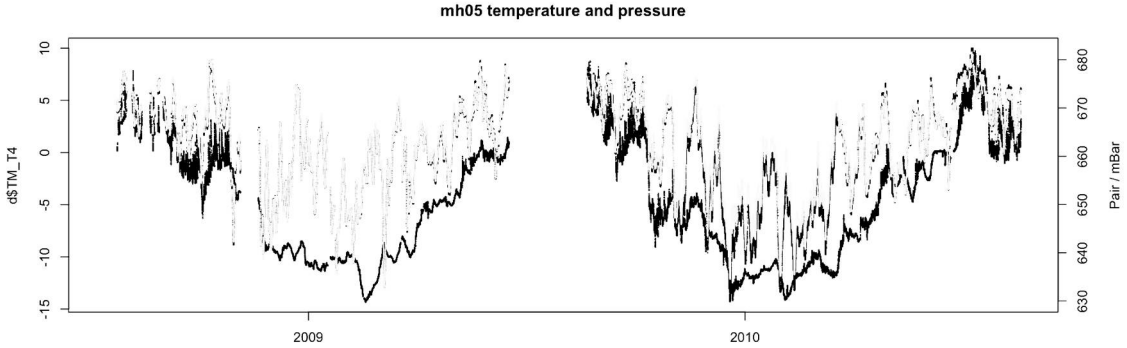

Figure 24: *Hydrological measurements at mh05: temperature of the moisture chain T4 (black), air pressure (dark grey) and cleft water pressure in 3 m depth (light grey). The air and water pressure are closely correlated.*

A.4 Data integrity

For geo-science it is often important to have continuous time series over long (multi annual) time spans. Three types of missing data may be distinguished in our system: a) A sensor node fails regarding data logging or transmission and all measurements for the given time span is missing. b) The sensor rod (or thermistor chain) fails and invalid data is transmitted. c) One individual sensing element fails due to physical damage. This section gives an overview of the available data and illustrates the evolution of the system performance of the WSN in terms of data delivery. Further a list of the failed sensing elements (e.g. thermistors) is provided.

Overview of data integrity

In Figure 25 the data integrity of each sensor node is illustrated with respect to the type a) and b) data gaps. The failure of individual sensing elements is not considered in Figure 25. Hence, the grey area shows how much of the data acquisition is correct in terms of measurements, logging and transmission. The black lines show how fast the data is available (assuming proper transmission from the base station to the server and correct server operation; this is usually the case).

Four sensor nodes (mh09, mh20, mh21, and mh22) were installed in summer 2010 and have no data prior to this date (Figure 25). The low values at mh01 are explained by a malfunction of the sensor rod and consecutive filtering. Due to the high sampling rate interpolation of the missing values is still possible. Sensor node jj01 shows a data gap since October 2010 due to snow cover on the network node (Figure 25). This data will be automatically delivered in spring when connection is re-established. In summer 2010 this “flushing” function worked properly after a base station failure (transmission delay of all jj nodes). The sensor rod at jj09 has most likely an error in the addressing of the multiplexer of the sensor rode (wrong pin connection) and much of the data is filtered due to this (Figure 25). Since summer 2010 only two gaps of each about one month exist (mh08, mh09). These two network nodes run out of power and were replaced. This low power situation was detected in advance by system monitoring tools (http://data.permasense.ch/) but weather conditions and availability of personnel are the reasons for these gaps. Regarding the transmission delay the data is available with only 30–120 seconds delay since summer 2010. The current status of data integrity and system behavior is very satisfying.

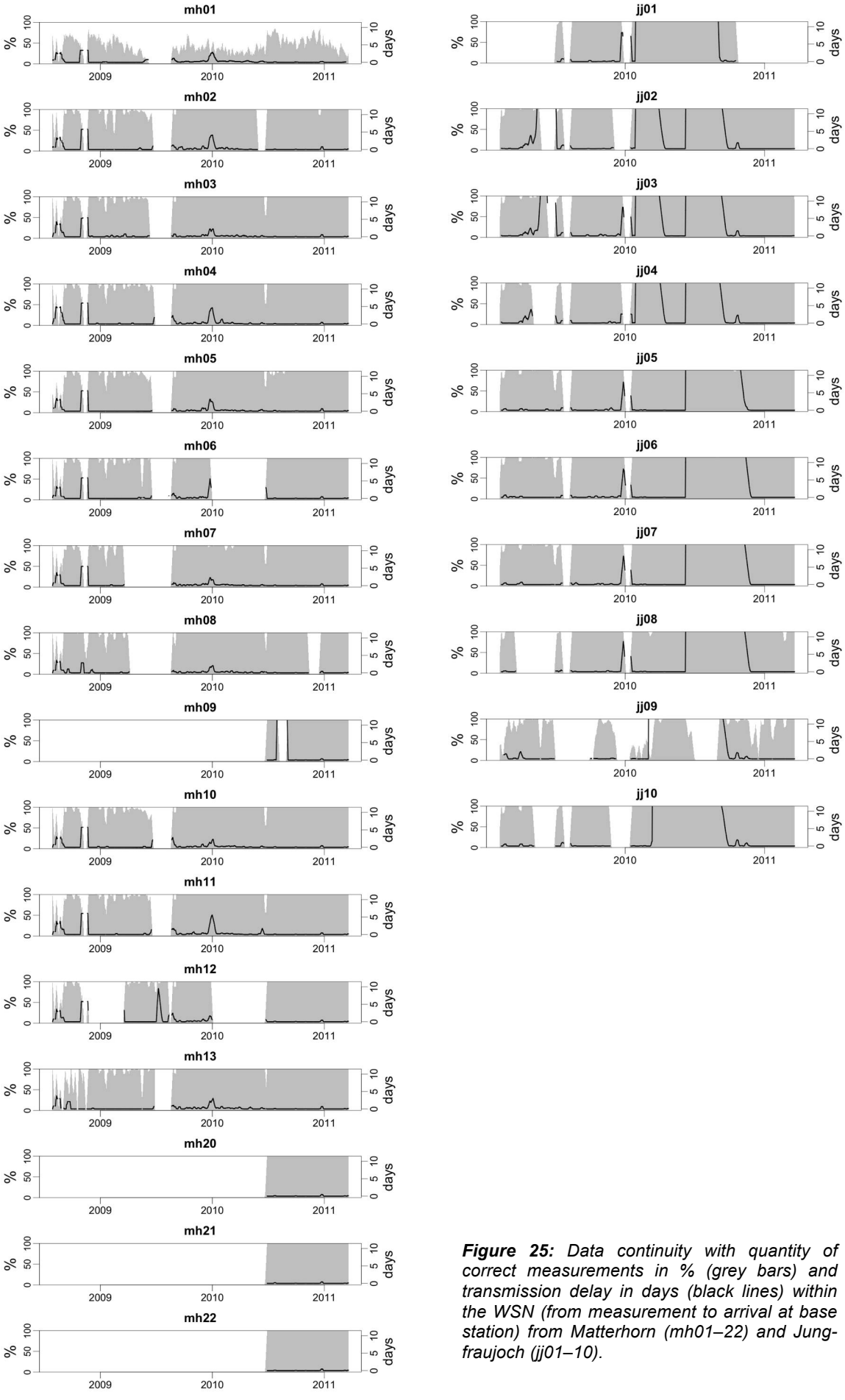

Figure 25: *Data continuity with quantity of correct measurements in % (grey bars) and transmission delay in days (black lines) within the WSN (from measurement to arrival at base station) from Matterhorn (mh01–22) and Jungfraujoch (jj01–10).*

Overview of sensor failures and data gaps

Table 2 summarizes the gaps in the data from Jungfraujoch and Matterhorn. All the three mentioned types (a, b, c) of missing data is considered. The information about broken thermistors of Table 2 is used to filter this invalid data because no automatic detection is possible in these cases.

Table 2. Notes of data gaps and broken thermistors:

Matterhorn:	**Jungfraujoch:**
all mh nodes: gaps from mid June 2009 to mid August 2009 (except mh12) and in Nov. 2008 mh01 instability of sensor rod for whole period	all jj nodes: gaps in Aug 2009 and Jan 2010 Hardware error at jj09 (wrong addressing, pin connection mistaken)
mh01: gap in Tsurf after exchange June 2010 mh02: gap in Tsurf after exchange June 2010 mh03: gap in Tsurf after exchange June 2010 mh04: no Tsurf after exchange June 2010, broken thermistor mh04: no CR before June 201o mh06: gap in CR from Jan to June 2010 mh07: long gap before June 2010 mh08: gap in CR from April to August 2009, gap in CR after exchange June 2010, gap in October 2010 mh09: gap in July and August 2010 mh12: gap in MUX Nov. 2008 to March 2009 and Jan. to June 2010	large gaps at jj01, jj08 and jj10
broken thermistors: mh02: T3, T4, T7, T8 mh12: T3	broken thermistors: jj02: T2, T3 jj03: T2 (occasionally) jj04: T1, T2 jj07: T2

Supplementary material

A.5 Melt water temperatures on steep bedrock

To estimate the order of magnitude of sensible heat uptake and transport into the cleft system, a few water temperature measurements where performed: At three different field sites the temperature of snow melt water flowing at the rock surface was measured manually at one given point in time (Table 3). The measurement accuracy is ±0.1 °C. The flow rate was estimated by visual observation and has a high uncertainty, however the water temperature is well above zero even for large flow rates (Table 3). The estimate of the advected sensible heat (relative to 0 °C) includes the uncertainty of this estimation because it is calculated by the flow rate and the water temperature.

The ten measurements are taken in radiation exposed faces but with different weather conditions. The Galenstock measurements are taken at a day with extreme solar radiation, which corresponds to water temperatures up to 20 °C (Table 3). In contrast, the cloudy weather during the Jungfraujoch measurements led to minimal warming and water temperatures close to 0 °C. The Matterhorn measurements were performed with sunny conditions (but less reflection from snow compared to Galenstock) and showed warmer temperatures again. The water temperatures show a dependency from the runoff length at the surface with strongest warming at the first couple of meters.

This limited measurements support the assumption that melt water temperatures depend highly on the radiation conditions and to minor extent on the flow path length. The range of this temperatures is extremely large and reaches from 0.2–20 °C.

Table 3. Melt water temperatures in radiation exposed rock faces.

date	time	location	elevation, aspect	weather	flowp., l / m	discharge / (L/h)	Twater / °C	Psens / W
14.6.2009	13:00	Galenstock	3240, SW	sunny	d, 0.1	≈10	2.4	≈30
14.6.2009	14:55	Galenstock	2900, SW	sunny	d, 10	≈10	19	≈200
14.6.2009	15:00	Galenstock	2900, S	sunny	d, 4	≈10	20	≈200
14.6.2009	15:10	Galenstock	2900, S	sunny	d, 1.5	≈100	11	≈1000
14.6.2009	15:30	Galenstock	2850, SW	sunny	c, 30	≈1000	11	≈10000
2.7.2009	17:00	Jungfraujoch	3450, S	clouded	c, 4	≈100	0.2	≈20
2.7.2009	17:00	Jungfraujoch	3450, SE	clouded	d, 3	≈100	0.3	≈30
22.6.2010	10:20	Matterhorn	3450, SE	sunny	d, 1.5	≈10	6	≈70
22.6.2010	10:30	Matterhorn	3450, S	sunny	c, 4	≈5	11	≈60
22.6.2010	10:40	Matterhorn	3450, S	sunny	c, 12	≈5	13	≈70

flowp. = flow path: d = disperse flow; c = channeled flow;
l = length of flow path since snow patch on rock surface
Psens = sensible advective heat flux if the water would be cooled to 0 °C (without freezing) in clefts
note: latent heat released if water would completely freeze in clefts is proportional to discharge (Q):
Plat = Q [L/h] * 93 [Wh/L] = x [W], hence it is similar to sensible heat release from cooling by 93 °C

A.6 Sensible and latent heat advection in field data

Gerber (2010) investigated the PermaSense data from Jungfraujoch regarding to advective heat transport. Beside visual observation a analysis tool that calculates the heat sink/source necessary to fit a one dimensional heat conduction scheme to the observed temperature profile (Hasler 2007, DeltaCon – Model description, unpublished documentation). The resulting non-conductive effects where analysed to identify processes that cause this thermal "disturbance". Figure 26 shows an example of short-term disturbances caused by release of latent heat in a temperature time series and the corresponding heat sources.

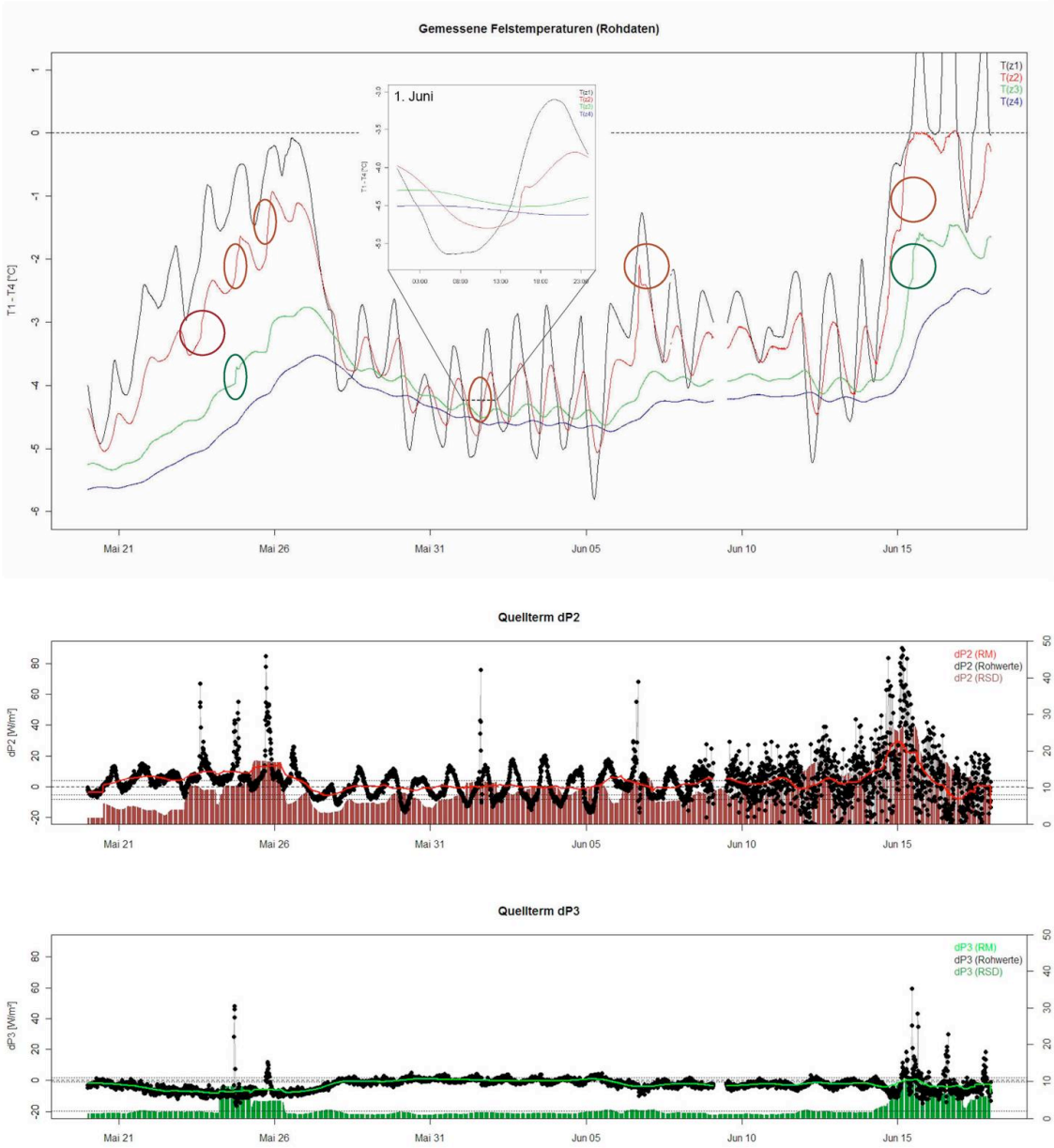

Figure 26: *The percolation of water into clefts of the profile jj06 at Jungfraujoch in spring 2009: Top: rock temperatures of the sensor rod (0.1, 0.35, 0.6, 0.85 m depth) with indication of non-conductive events; middle / bottom: heat source (released energy) at the two depths (dP2= 0.35 m; dP3=0.6 m) by non-conductive processes. Figure from Gerber (2010).*

With spectral analysis (see A.2), similar patterns of advective events are detected (Figure 27). Additionally, this method can be applied to temperatures that are not within a borehole because no physical model (heat conduction) is required for the analysis (Figure 28).

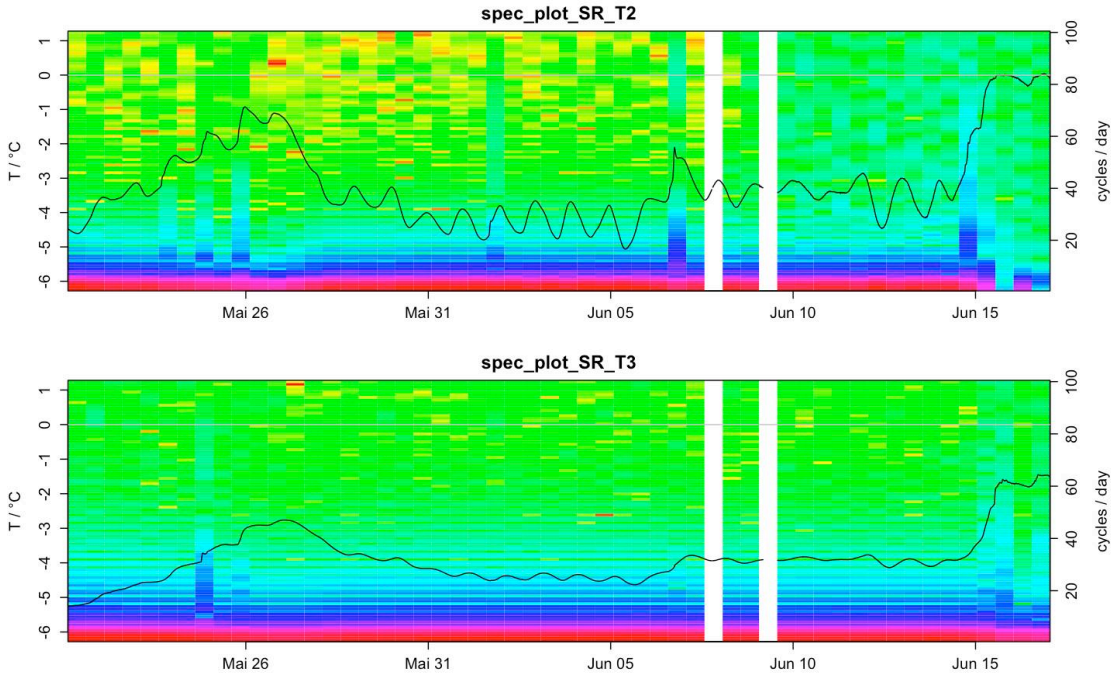

Figure 27: *Power plot (red=high, green=low) of the spectral analysis with corresponding temperature curve (jj06) included. The same advective events as in Figure 26 are detected (more power at higher frequencies: blue bars). Top: at 0.35 m depth (T2); bottom: at 0.6 m depth (T3).*

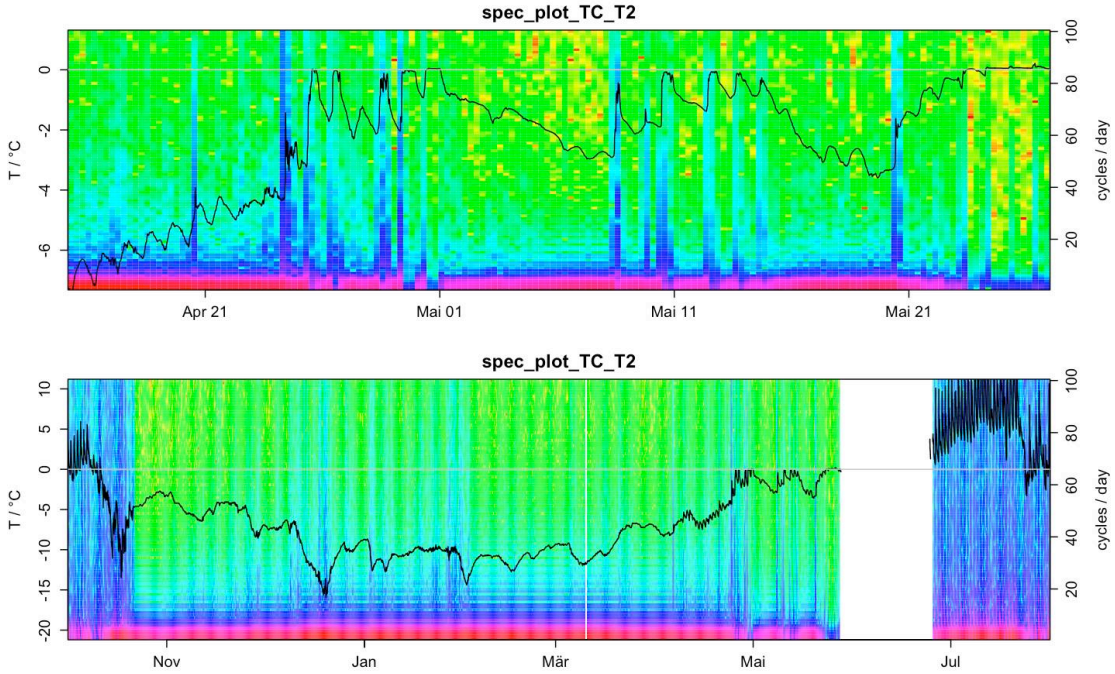

Figure 28: *Spectral analysis from temperature in cleft mh02 (top: April–May 2010, bottom: Nov. 2009 to July 2010). Latent heat release (blue stripes) and zero curtains (no magenta) is clearly visible during thawing season (top). Note that the two advective events (27 April and 20 May) coincide with the initiation of summer cleft opening at mh02 (compare Publication V). The method provides also good overview of snow-free period (bottom: bluish area).*

A.7 Thermal diode effect in intact rock – numerical experiments

Temperature dependent thermal conductivity at subzero temperatures causes unbalanced in- and outward ground heat fluxes. This effect, called "thermal diode effect", is well investigated for different arctic soil types but only a few studies investigate this for bedrock (e.g. (Pogliotti et al., 2008). Lacking a containment of this effect in intact rock, a brief model study was conducted:

For a one dimensional heat conduction scheme (within the finite element solver COMSOL) a temperature dependent thermal conductivity was parameterized as the following:

a) A freezing characteristics of porous rock with a freezing range between -0 and -5 °C (Mottaghy and Rath, 2006).

b1) Weighted geometric mean for conductivity (homogeneous pore space) (Sass et al., 1971)

b2) Weighted harmonic mean for conductivity (idealized schistosity perpendicular to heat flux; strongest possible effect)

c) Upper boundary (surface temperature) -1±15 °C, insulated lower boundary.

3 % porosity and 100 % saturation were assumed. This is a high porosity for crystalline rock and realistic values will most likely be between lower. The present calculations with parametrization b2) is an upper boundary of possible thermal diode effects in rock and realistic values ia and ib.

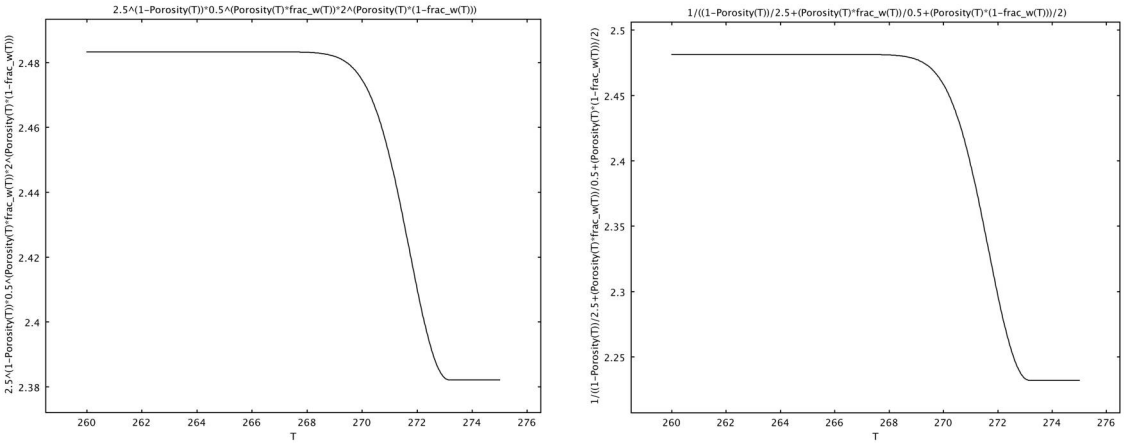

Figure 29: *Temperature dependent thermal conductivity for b1 (left) and b2 (right).*

Thermal offset between surface and 1 m depth after 365 modeled daily cycles are for

b1: -0.175 °C

b2: -0.45 °C

In respect to pure phase-change effects these are maximal values, however other effects such as the seasonal variation in pore saturation are not considered in this calculations.

A.8 Freezing of pore water – Resistivity measurements

The sensor rods measure rock resistance and temperature in four depths (Appendix A.1, Publication I). The resistances are transformed into rock resistivity by multiplying R with a constant factor resulting from the geometrical setup: σ = R*0.01 m (assuming homogeneous half space). The resistivity σ shows a clear temperature dependency on subzero temperatures (Figure 30) caused by phase change of the pore water, which is used in ERT sounding to estimate rock temperature (e.g. Krautblatter et al. 2009). Field verifications of this relation with in-situ rock temperature measurements rarely exist. We measured these two parameters, however the simple direct current setup for the resistivity measurements is sensitive on contact resistance. Not all of the 10 sensor rods record reasonable resistivity values (0.5-1000 kΩm) and may be influenced by ice at the contacts (e.g. jj05 in Figure 30) or micro fissures between the electrodes (Figure 31; σ1vsT1).

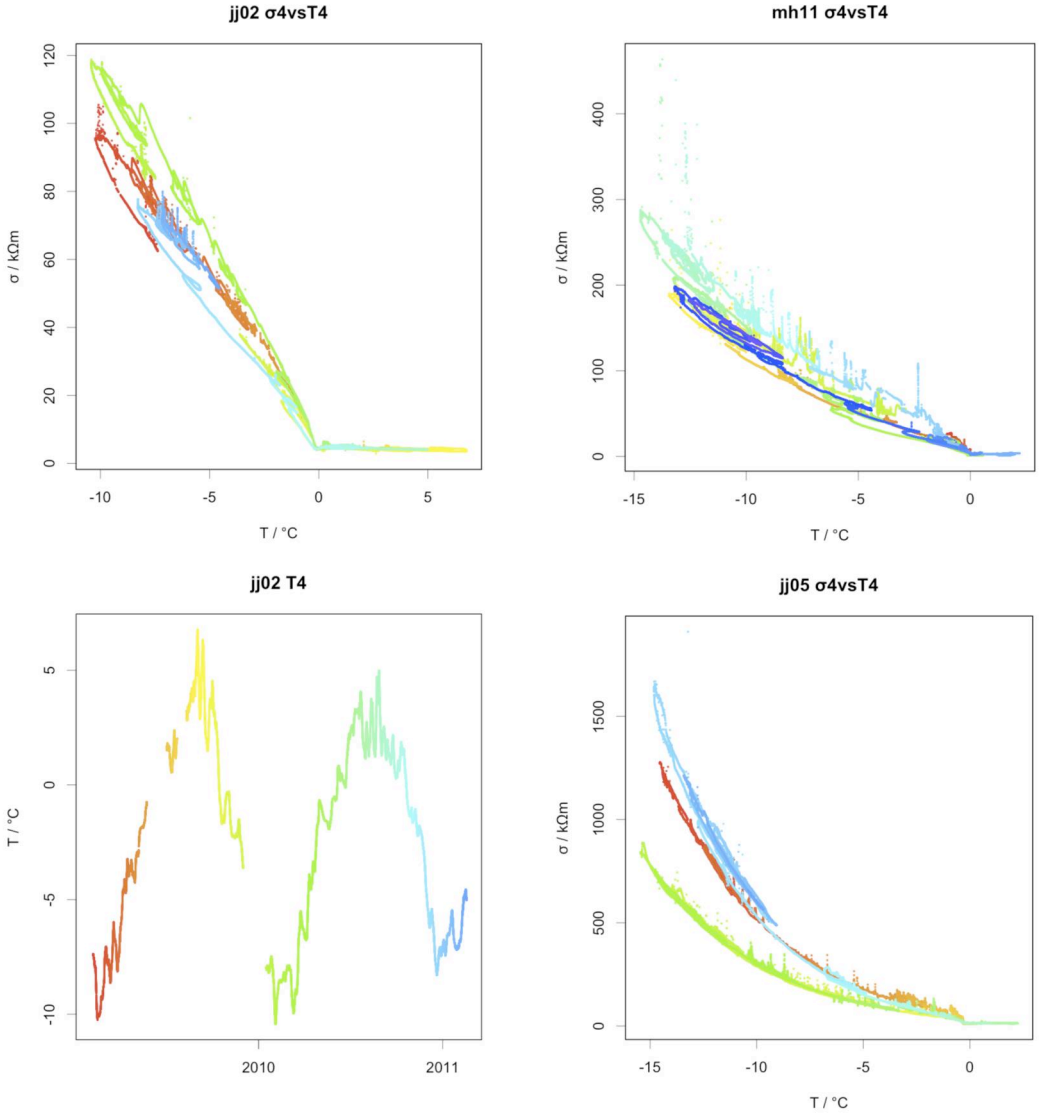

Figure 30: *Rock resistivity at three different locations in 0.85 m depth and temperature time series at one of these location (bottom left). Colours are time-dependent for visualisation of inter-annual differences in T–R paths.*

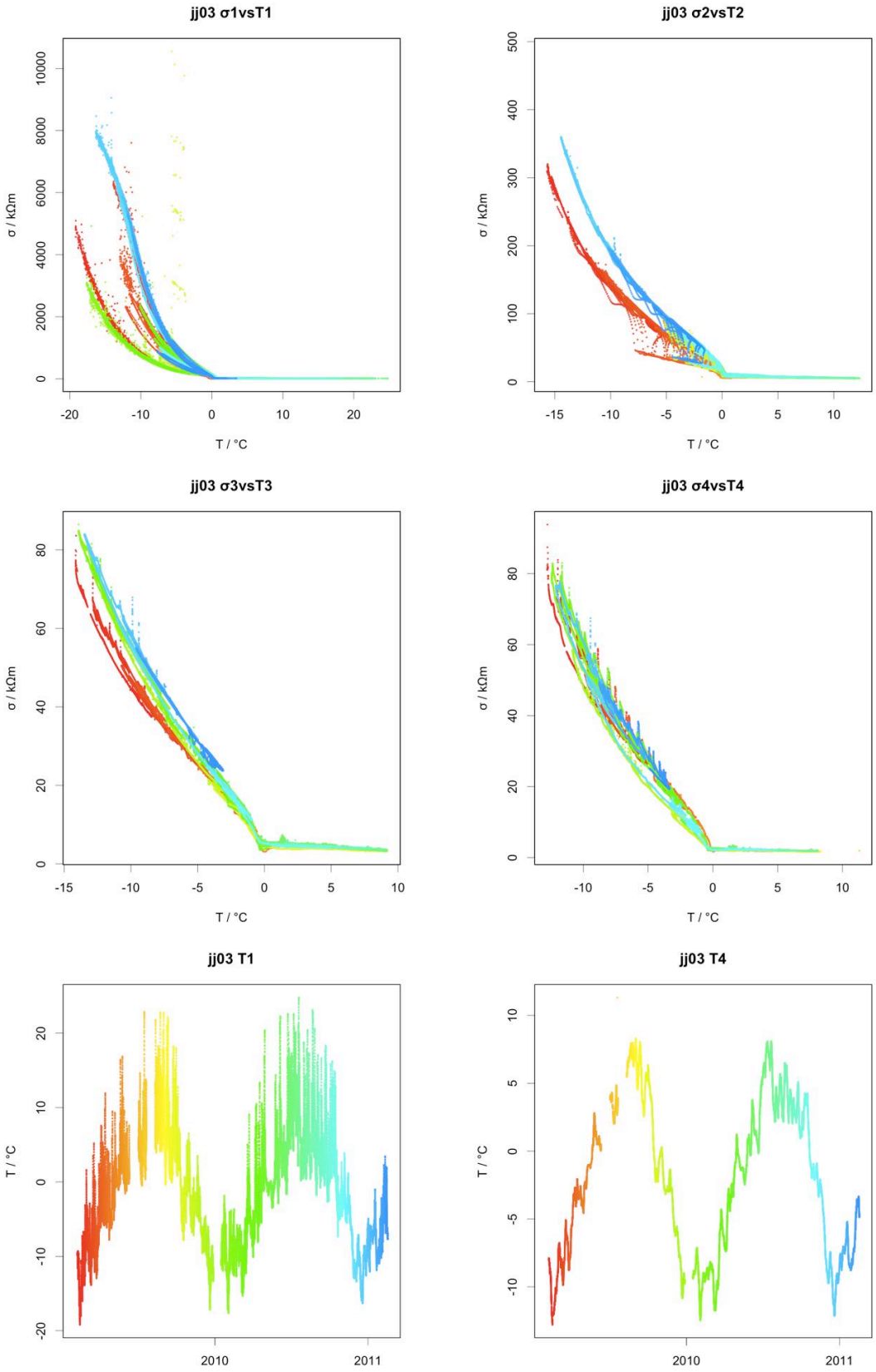

Figure 31: *Rock resistivity-temperature plot for jj03 in four depths and two temperature time series. Colours are time-dependent for visualisation of inter-annual differences in T–R paths.*

A.9 Frost cracking – evidence from field measurements?

The crackmeter extension on rock without macro cleft but a fissure with a diameter smaller than 0.5 mm (mh01) is of interest beyond its validation purpose for the crackmeter stability (Publication V, Appendix A.3). It shows an occasional shift that occurs simultaneous with freezing events (Figure 32). Otherwise the gradients with temperature are very small and slightly positive (Publication V). This freezing expansion may to one part by freezing of water in the fissure and is possibely related to expansion of the rock due to pore water freezing. This effect has been identified in saturated concrete (Kaufmann, 2000) and is shown in Figure 33. A similar set up on intact rock (no fissures at all) may give further insights if this effect is detectable in rock und natural conditions.

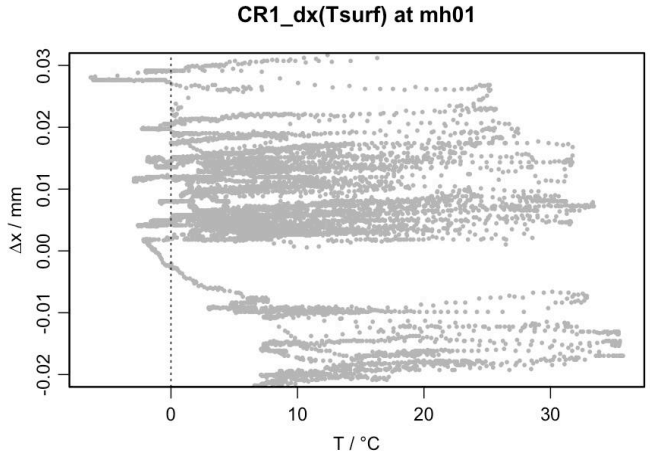

Figure 32: *Thermal expansion measured at the Matterhorn field site on rock with a micro-cleft < 0.5 mm (mh01).*

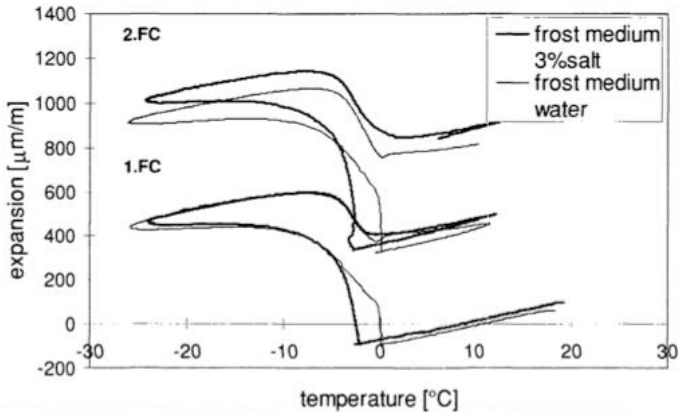

Figure 33: *Thermal expansion of vacuum saturated concrete with freeze-thaw cycles (Kaufmann, 2000; Figure 28).*

Personal bibliography

Publications that are part of this thesis (Part B: Publications) are marked with a roman number (I–V).

Publications with peer review:

II: Beutel, J. Gruber, S. **Hasler, A.** Lim, R. Meier, A. Plessl, C. Talzi, I. Thiele, L. Tschudin, C. Woehrle, M. Yuecel, M. 2009. PermaDAQ: A scientific instrument for precision sensing and data recovery in environmental extremes. In Proceedings of the 2009 International Conference on Information Processing in Sensor Networks. IEEE Computer Society. 265–276.

V: **Hasler, A.** Gruber, S. Beutel, J. (accepted). Rock kinematics in steep bedrock permafrost. *Journal of Geophysical Research*.

IV: **Hasler, A.** Gruber, S. Font, M. Dubois, A. 2011. Advective heat transport in frozen rock clefts - conceptual model, laboratory experiments and numerical simulation. *Permafrost and Periglacial Processes*.

III: **Hasler, A.** Gruber, S. Haeberli, W. 2011. Temperature variability and offset in steep alpine rock and ice faces. *The Cryosphere 5*. 977–988.

I: **Hasler, A.** Talzi, I. Beutel, J. Tschudin, C. Gruber, S. 2008. Wireless sensor networks in permafrost research: concept, requirements, implementation, and challenges. In Proceeding of the Ninth International Conference on Permafrost, Fairbanks, Alaska, USA. 669–674.

Krautblatter, M. Huggel, C. Deline, P. **Hasler, A.** 2011. Research perspectives for unstable high-alpine bedrock permafrost: measurement, modelling and process understanding. *Permafrost and Periglacial Processes*.

Ramos, M. **Hasler, A.** Vieira, G. Hauck, C. Gruber, S. 2009. Drilling and installation of boreholes for permafrost thermal monitoring on Livingston Island in the maritime Antarctic. *Permafrost and Periglacial Processes*.

Talzi, I. **Hasler, A.** Gruber, S. Tschudin, C. 2007. PermaSense: investigating permafrost with a WSN in the Swiss Alps. In Proceedings of the 4th workshop on Embedded networked sensors, New York, USA. 8–12.

Publications without peer review:

Beutel, J. Gruber, S. Gubler, S. **Hasler, A.** Keller, M. Lim, R. Talzi, I. Thiele, L. Tschudin, C. Yücel, M. 2009. The PermaSense Remote Monitoring Infrastructure. In Proceedings of the Snow Science Workshop, Davos, Switzerland.

Beutel, J. Gruber, S. **Hasler, A.** Lim, R. Meier, A. Plessl, C. Talzi, I. Thiele, L. Tschudin, C. Woehrle, M. 2009. Demo:Abstract: Operating a sensor network at 3500 m above sea level. In Proc. of the 8th Int. Conf. on Information Processing in Sensor Networks (IPSN).

Hasler, A. 2009. Permafrost-Bohrarbeiten in der maritimen Antarktis. Geosciences Actuel, 2009/1. 16–19.

Unpublished reports:

Hasler, A. Gruber, S. 2009. PermaSense II: Zusammenfassender Schlussbericht an das Bundesamt für Umwelt.